The G305 star forming complex: a panoramic view of the environment and star formation

by

Luke Hindson

A thesis submitted to the University of Hertfordshire in partial fulfillment for the degree of Doctor of Philosophy

in the
Center for Astrophysics Research
Science and Technology Research Institute

May 2012

"If you wish to make an apple pie from scratch, you must first invent the universe."

Carl Sagan

Abstract

This thesis presents molecular line and radio continuum observations of the giant molecular cloud (GMC) complex known as G305. The energy input from high-mass stars in the form of powerful winds and ionising radiation is one of the primary feedback mechanisms in GMCs. This feedback is thought to play a dual role both dispersing and destroying the natal environment but also sweeping up and compressing molecular gas and potentially triggering new episodes of star formation. Despite their importance to the evolution of GMCs and galaxies as a whole, the physical processes behind the formation and evolution of high-mass stars remains poorly understood. We therefore set out to obtain wide-field observations of the ionised and molecular environment to study the impact of high-mass stars on the evolution of G305.

Observations conducted with the Mopra telescope of the molecular gas traced by NH_3 in the (1,1), (2,2) and (3,3) transition and CO (^{12}CO, ^{13}CO and C^{18}O $J = 1$–0) reveals the reservoir for future star formation in G305 and allows the physical properties and kinematics of the region to be studied. We identify 15 large molecular clouds and 57 smaller molecular clumps towards G305. The physical properties of the molecular gas are consistent with G305 being amongst the most massive a vigorous star forming regions in the Galaxy. We find a total molecular gas mass of $\sim$ 2.5–6.5 $\times$ 10^5 M$_\odot$ indicating that there is a large reservoir for future star formation. By considering virial equilibrium within the molecular clumps we discover that only 14% of the molecular clumps in G305 are gravitationally unstable, however these clumps contain > 30% of the molecular mass in G305 suggesting there is scope for considerable future star formation.

To study the ionised environment towards G305 we have obtained some of the largest and most detailed wide-area mosaics with the Australia Telescope Compact Array to date. These radio continuum observations were performed simultaneously at 5.5 and 8.8 GHz and by applying two imaging techniques we are able to resolve HII regions from the ultra-compact to classical evolutionary phase. This has allowed high-mass star formation within G305 to be traced over the extent and lifetime of the complex. We discover that more than half of the observable total ionising flux in G305 is associated with embedded high-mass star formation around the periphery of a central cavity that has been driven into the molecular gas by a cluster of optically visible massive stars. By considering the contribution of embedded and visible massive stars to the observed radio continuum we suggest that more than 45 massive stars exist within G305.

Combination of these two studies and recent and ongoing star formation provides the most in depth view of G305 to date and allows the star formation history and impact of high-mass stars to be investigated. We find compelling morphological evidence that suggests triggering is responsible for at least some of the observed high-mass star formation and construct a star formation history for the region.

Acknowledgements

First and foremost, I would like to thank my supervisor Dr Mark Thompson for giving me the opportunity to pursue a career in astronomy, for providing me with support and guidance throughout my PhD, sending me away to the other side of the world and being the good cop. I would also like to thank my co-supervisor Dr James Urquhart for all of his support, for teaching me some of the finer points about a life in astronomy and being the bad cop.

I would never of reached this point without the constant and unquestioning love and support of my mother and father, Karen and Adrian. I could not of asked for better role models. Although he has passed away I would especially like to thank my grandfather for helping to develop my inquisitive nature and love of science and astronomy. This thesis is a testament to his positive and lasting influence on my life. I am eternally grateful to Kathryn for her support, patience, understanding and love despite the occasional observing trip to the other side of the world and long hours at the office. I would also like to thank all of my friends, especially my bru Rob for keeping me sane, helping me to grow and making my time at university such a memorable experience.

Contents

List of Figures

List of Tables

Chapter 1

Introduction

1.1 Introduction

The visible universe is dominated by stars, looking up at a clear night sky, we see only a few thousand of the hundred billion that constitute our Galaxy, the Milky Way, just one of the innumerable galaxies in the universe. Stars are the building blocks upon which these galaxies are constructed. The study of how they form, how different environmental effects influence mass distribution and star formation rates are important parameters that can allow us to determine the structure and evolution of galaxies.

Work in the last two centuries has culminated in our understanding that stars are not unchanging point like sources of steady light but transient objects that are born, evolve and die, some in spectacular supernova. The accepted theory is that stars are born from the collapse of dense cores of dust and gas, composed of mostly hydrogen, and at their core are undergoing nuclear fusion due to the massive pressures and temperatures. When the hydrogen fuel runs out, depending on the mass, stars can end their lives as cooling white dwarfs or explode in violent supernova that briefly outshine even their host galaxy, returning heavy elements to the universe. However, it is only in the last century that the evidence has become convincing that stars are presently forming by the collapse of diffuse interstellar matter in our Galaxy and others, and it is only in recent decades that we have begun to gain some physical understanding of how this happens. Our understanding of the lives of stars and the impact they have on their surroundings is still incomplete; there are many questions yet to be answered.

Currently one of the most intensely discussed topics in star formation is that of massive (high-mass) stars. Whilst a broad understanding of the formation and evolution of low-mass stars, such as our Sun, has been developed high-mass stars remain poorly understood. This is because limitations and complex physical processes complicate the observational and theoretical study of high-mass stars. This is a vexing problem; high-mass stars play a pivotal role in astrophysics and may be one of the most important driving forces behind the evolution of galaxies in stark contrast to their low-mass counterparts, which are comparatively quiet in their formation and evolution. When high-mass stars are born and throughout their short lives, a large portion of their energy returns to the star-forming region from which they were born in the form of powerful winds, outflows, high-energy radiation and finally supernovae. Recent studies have found that this energy input has a significant impact on the evolution of the local environment driving the dispersal of the molecular material and potentially enhancing or quenching star formation (cf. Zinnecker & Yorke 2007). To understand the physics of the evolving universe on both small and large scales it is essential we first understand the nearest examples of massive star formation.

Our best tool with which to peer into the murky regions within which massive stars form are observations of the (sub)millimetre, infrared and radio wavelengths where the copious amount of dust and gas that obscure other wavelengths is relatively transparent. Previous observations at these wavelengths have often been restricted to single star-forming sites observed at high-resolution and sensitivity or conversely large area surveys of lower resolution and sensitivity. These studies, although useful, have obvious limitations. Observations of entire star-forming regions at high-resolution and sensitivity and at multiple wavelengths are required in order to develop a proper understanding of the formation, evolution and impact on the natal environment. Recent improvements in instrumentation make such observations practical for the first time, allowing the mapping of entire star-forming regions in unprecedented detail and multiple wavelengths and so allowing the investigation of the star formation mechanism(s) and history of high-mass star-forming regions.

The rest of this chapter will review the status of our knowledge of the star formation process and environment relevant to the understanding and completion of this thesis.

1.2 Molecular clouds

From observations of stars, it is apparent that they are composed mainly of hydrogen; therefore it is logical to assume that we will find stars forming towards areas that contain substantial condensations of dense hydrogen gas. Hydrogen is found in its atomic (HI), molecular (H_2) and ionised (HII) states with the densest condensations of hydrogen found to be predominantly in H_2 form within complexes of molecular clouds which are the largest cohesive entities found within the spiral arms of galaxies. It is within these giant molecular clouds (GMCs) that new generations of stars form. In Fig. 1.1 the well-known star-forming cloud the Eagle Nebula is presented, a region of our Galaxy where stars are currently forming out of dust and molecular gas. This stunning three colour image was taken with the Hubble Space Telescope (HST) and is comprised of three filters designed to detect light generated by predominantly Sulphur ions

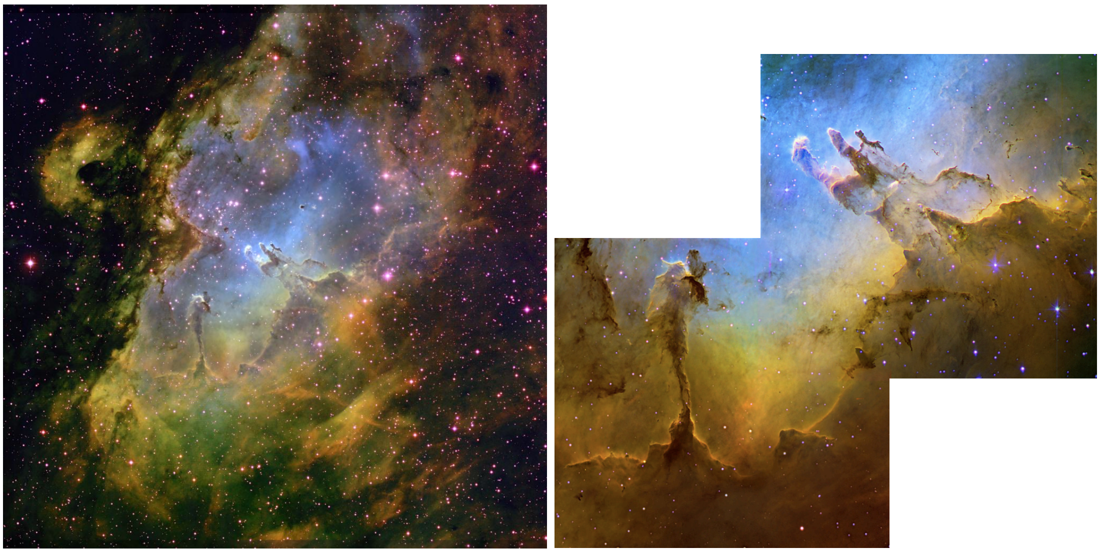

FIGURE 1.1: A three-colour image of the famous Eagle Nebula taken with the Hubble Space Telescope. Over densities in the molecular material results in the prominent pillars that can be seen extending into the centre of the nebula and provides an excellent environment in which star formation can take place.

as red, light from hydrogen atoms as green and light from doubly-ionised oxygen as blue. Ultraviolet light from newly formed stars near the nebula is pumping energy into the gas clouds, causing them to glow in visible light and sculpting the gas into columns and pillars. It is within dense regions such as these that the environment is conducive to star formation.

1.2.1 Molecular cloud composition

Studies (Bergin & Tafalla, 2007; Rathborne et al., 2009) and reviews (Blitz, 1991, 1993; Shu, Adams & Lizano, 1987; Evans, 1999; Williams, Blitz & McKee, 2000) have found molecular clouds of several distinct types but all consist of dense molecular gas ($\sim$ 99%) and tiny dust grains ($\sim$ 1%), approximately $\sim 0.1\,\mu$m in size. This dust is an important component as it is able to efficiently radiate away energy and thus cooling the cloud, act as a catalyst providing a surface upon which complex molecules can form (Gould & Salpeter, 1963) and shield the environment from photoionising radiation. This dust is also responsible for absorbing and scattering radiation when it lies between an emission source and the observer known as extinction ($A_{\rm V}$).

At high enough surface densities ($\sim 10\,{\rm M}_\odot\,{\rm pc}^{-2} \sim 2\times10^{-3}\,{\rm g\,cm}^{-2}$ Krumholz, McKee & Tumlinson 2009) dust and gas provides a shielded environment, which allows the formation of H_2 and a wide range of delicate complex molecules (Fig. 1.2) such as Carbon Monoxide (CO) and ammonia (NH_3), which would otherwise be destroyed by the action of starlight (photodissociation). These clouds are dominated by H_2 $\sim$ 90% and helium (He) $\sim$ 10% however, $\sim$ 118 types of molecules have been detected in dense molecular clouds. Detection of these molecules provides a means to trace the various physical conditions within the parent cloud that give rise

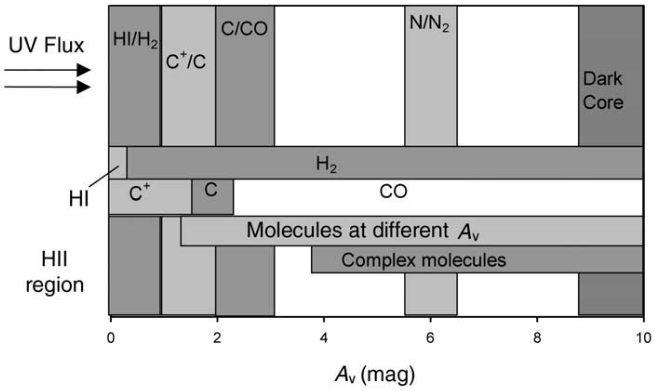

FIGURE 1.2: Schematic model of the various chemical transitions within a GMC.

to their formation. Molecules have different excitation conditions and critical densities required for formation and so the study of the molecular emission allows us to infer the physical and chemical properties of the molecular cloud.

Molecular clouds are also associated with ionised gas in the form of HII regions, ionised boundary layers (IBLs) and diffuse ionised regions. The boundary between the ionised and neutral environment is a transition region known as the Photo Dissociation Region (or Photon-Dominated Region, or PDR) and is rich in complex molecules. It is within PDRs that the UV radiation is able to excite Polycyclic Aromatic Hydrocarbons (PAHs) in emission, which emit strongly in the mid-infrared (Fig. 1.2).

1.2.2 Molecular cloud physical properties

Molecular clouds have a wide range of physical properties with masses and sizes, ranging from less than $10\,M_\odot$ and ~ 1 pc for the smallest clouds, up to the most massive GMCs of $> 10^6\,M_\odot$ on scales of > 100 pc. Molecular clouds are found to have volume averaged H_2 number densities ranging from $< 50\,\mathrm{cm}^{-3}$ for GMCs to $> 10^5\,\mathrm{cm}^{-3}$ for dense cores of size 0.03–0.1 pc (Vázquez-Semadeni et al., 2007). The temperatures in molecular clouds are relatively constant, with kinetic temperatures of $\sim$ 10–15 K, suggesting that radiation is efficiently transported out of the cloud, although temperatures larger by a factor of a five are observed towards sites of star formation (Zinnecker & Yorke, 2007). It is the excitation of atoms, ions and at low temperatures principally CO molecules through collisions and the subsequent emission of radiation that is responsible for efficiently cooling the cloud as long as the medium remains optically thin (Dyson & Williams, 1997).

Structurally, molecular clouds are complex with filamentary and clumpy structure on many different scales. The Eagle nebula (Fig. 1.1) provides an excellent example of the hierarchical structure. This complex structure results in a broad classification scheme (Table. 1.1) based on

Classification	Size (pc)	Temperature (K)	Density (cm^{-3})	Line width (km s^{-1})	Mass ($M_\odot$)
Complex	~ 10–60	10–15	100–500	5–15	10^4–10^6
Cloud	3–20	15–40	10^2–10^4	1–10	10^2–10^4
Clump	0.5–3	30–90	10^3–10^5	0.3–3	10–10^3
Core	$\lesssim 0.5$	30–200	$> 10^5$	0.1–0.7	0.1–10

TABLE 1.1: Classification scheme resulting from the typical physical parameters for molecular material in the ISM.

the observed hierarchy and physical properties. Following this classification scheme the base unit of a molecular cloud is a core, a small ~ 0.1 pc gravitationally bound region that may go on to form individual stars, cores are found within molecular clumps, larger over-dense regions that in turn are found within a molecular cloud, which may consist of a number of clumps and a single complex may contain a number of molecular clouds. This classification scheme for molecular clouds is adopted throughout the work presented here. For completeness, molecular clouds are also sometimes described in terms of self-similar fractal dimensions (Williams, Blitz & McKee, 2000).

1.2.3 Molecular cloud formation and evolution

The physics of the formation of molecular clouds is one of the major unsolved problems of the interstellar medium. It is not yet known what the dominant formation mechanism is, or even what the relative importance of gravity, radiation and magnetic fields is in the cloud formation process. In principle molecular clouds could form in either a "bottom-up" or "top-down" process. In the bottom-up scenario smaller clouds combine in inelastic collisions (Kwan, 1979), a slow process that would mean destructive processes from star formation would prevent GMCs from attaining higher mass once star formation has commenced. In the case of top-down, large-scale self-gravitating instabilities condense out of the wider ISM (Elmegreen, 1979), however quite how this happens is still a topic of debate. Several scenarios are put forward including; compression of the diffuse ISM by a supernova and expanding HII regions, magneto-rotational instability and large-scale gravitational instability in the galactic disk. In the case where converging flows atomic material in the diffuse ISM collides and becomes molecular and gravitationally unstable. The initial turbulence of converging flow and subsequent cloud formation may then be able to seed the first stars, which form before the global collapse of the cloud (Vázquez-Semadeni, 2010).

Broadly speaking the evolution of a molecular cloud goes through the following stages: cloud formation, cloud core formation, protostellar collapse followed by the onset of star formation, which results in the dispersal of the cloud (Elmegreen, 2007; Vázquez-Semadeni, 2010). However, the exact physical process responsible for each stage, corresponding time scales and in particular how star formation propagates through molecular clouds is still poorly understood. Traditionally molecular clouds have been thought of as virialised structures in the ISM with relatively long lifetimes and a significant delay before star formation occurs (Dyson & Williams, 1997). On the other hand recent studies have suggested that molecular clouds are transient features that begin forming stars shortly after they themselves form, and are non-equilibrium entities (Vázquez-Semadeni et al., 2006; Mac Low & Klessen, 2004).

Very few molecular clouds are known that are not actively forming stars ($< 10\%$) (Blitz, 1993), and the most massive and dense GMCs all contain newly formed stars. Statistically this suggests that these clouds are young (< 3 Myr) This would suggest that there cannot be any significant time between the formation of a massive dense molecular cloud and the onset of star formation and so any period of quasi-static evolution is unlikely. This view is consistent with the irregular and often wind blown appearance of molecular clouds (Fig. 1.1).

Despite having a global evolutionary picture of GMCs it remains unclear how star formation propagates through a GMC on local scales. In particular, the role the first generation of massive stars plays in triggering, regulating and terminating subsequent star formation is uncertain (Blitz, 1993). The need to understand and parameterise the dense clumpy nature of GMCs is evident, particularly with regard to variations on a cloud to cloud basis.

1.3 Star Formation

The previous section provides an overview of the environment in which stars form, the remainder of this chapter is concerned with the details of how stars form and specific issues concerning high-mass stars.

Before looking at how stars form, it is useful to define what a star is and how different stars are classified. A main sequence (MS) star is a luminous body of gas under hydrostatic equilibrium in which the force of gravity, acting towards the centre of mass is balanced by the internal pressure of the star. The luminosity is generated by the fusion of hydrogen within the core of the star, which provides the thermal pressure support against gravity. The simplest way to classify stars is by mass, since the greater the mass the higher the temperature and the more luminous a star will be, giving rise to differing formation and evolution tracks. In this way, stars divide into three categories, low-, intermediate-, and high-mass stars. In general stars are separated into the following categories: low-mass from 0.1–2.0 $M_{\odot}$, intermediate-mass between $\sim$ 2–7 $M_{\odot}$ and high-mass (or massive stars) above 8 $M_{\odot}$. With this broad definition of what a star is and how they are classified we now examine how they form.

1.3.1 How do stars form

Gravity plays the dominant role in star formation, its ceaseless action of drawing material towards the centre of mass is able to compress molecular clouds from a density of $10^2\,\mathrm{cm}^{-3}$, by more than three orders of magnitude into a molecular clump of $> 10^5\,\mathrm{cm}^{-3}$. Given the right conditions this compression continues and goes on to form a star of mass density $10^{24}\mathrm{cm}^{-3}$, an increase of some 20 orders of magnitude.

Under the influence of gravity alone molecular clouds would be expected to collapse in their global free-fall times (Shu, Adams & Lizano, 1987) given by:

$$t_{\mathrm{ff}} = \left(\frac{3\pi}{32G\rho}\right)^{0.5} = 3.4 \times 10^7 n^{-0.5}\ [\mathrm{yrs}] \tag{1.1}$$

where G is the gravitational constant, ρ is the average density and n is the number density. In a typical molecular cloud ($n > 50\,\mathrm{cm}^{-3}$) the free-fall time is $t_{\mathrm{ff}} < 5 \times 10^6$ yrs, giving a lower limit to the timescale for stellar evolution. However, molecular clouds are thought to survive up to 30 times longer than this (Blitz & Shu, 1980; Williams & McKee, 1997). Moreover, if molecular clouds were to collapse, on such time scales the observed rate of star formation would be $250\,\mathrm{M}_\odot\,\mathrm{yr}^{-1}$ (Lada & Kylafis, 1999) considerably higher than the observed value of approximately 1–3 $\mathrm{M}_\odot\,\mathrm{yr}^{-1}$ (Chomiuk & Povich, 2011). Several internal support mechanisms have been proposed to counteract gravity, slowing the collapse of molecular gas and accounting for the longer observed lifetime of molecular clouds and the inefficiency of the star formation.

1.3.1.1 Turbulence

The observed line widths of molecular emission within GMCs is often found to contain a significant non-thermal component thought to arise from random non-thermal motions of parcels of gas within the cloud that broadens observed spectral lines through the Doppler effect (see Appendix B Section B.5.4). The sound speed in the gas is typically $\sim 200\,\mathrm{m\,s}^{-1}$ (Ossenkopf, Klessen & Heitsch, 2001) and velocity dispersions of up to 10 times this are measured, which implies that there are substantial supersonic motions within the gas. This turbulence is thought to have a dual role, both creating over densities in the molecular cloud and also supporting these over-dense regions against collapse termed the gravo-turbulent fragmentation model (Mac Low & Klessen, 2004; Krumholz, 2011). Turbulence is thought to decay on a dynamical or crossing time of a cloud, defined as the cloud size divided by a typical turbulent velocity, through shock waves that efficiently radiate away the kinetic energy. This means that turbulence must be continuously driven to maintain the observed velocity dispersion most likely by stellar feedback such as outflows, supernovae and expanding HII regions. It is now widely held that collapse is inhibited primarily by supersonic motions (Mac Low & Klessen, 2004), rather than magnetic fields (Shu, Adams & Lizano, 1987)

1.3.1.2 Magnetism

The magnetic fields that thread the Milky Way are also present within molecular clouds and could have a significant impact on the formation and evolution of stars (Crutcher, 1999, 2005). Within a molecular cloud, magnetic fields are able to trap electrons and ions around the field lines these collide with the neutral material and the resultant drag works to counteract gravity perpendicular to the direction of the field lines. This process is known as ambipolar diffusion and allows the magnetic flux to be redistributed until eventually gravity can overcome the magnetic field and collapse to form stars. The importance of magnetic fields is still a topic of debate, the exact processes by which they form, evolve, and affect star formation is yet to be understood. This ambiguity mainly arises due to the inherent difficulty in observing Zeeman splitting or polarisation properties, and so empirical evidence is scarce.

1.3.1.3 Thermal pressure

The thermal pressure in a molecular cloud originates from the kinetic temperature of the gas. This kinetic temperature is due to the ejection of photoelectrons from dust grains because of the background UV radiation field, or heating by low-energy cosmic rays. However, observations of molecular clouds find temperatures on the order of 10 K (Roman-Duval et al., 2010) due to efficient transfer of radiation (Vázquez-Semadeni, Gazol & Scalo, 2000). This results in a low thermal pressure, certainly too low to support the cloud against collapse. However, on small scales, such as in pre-stellar cores, thermal pressure becomes the most important force in opposing gravitational collapse.

1.3.2 The star formation process

Any incipient or induced density enhancement in a molecular cloud will attract additional mass through gravity and grow until gravity is able to overcome any support mechanisms. The density enhancement's self-gravity attracts more and more material to the centre of mass, leading to the formation of an over-dense region, known as a molecular clump. In the absence of any support the molecular clump would then be expected to quickly collapse into a cluster of stars, however as mentioned above support mechanisms account for the extended life time of clumps and so a clump will continue to accrete large amounts of material (10 - 1000 $M_{\odot}$).

Beyond a critical length and mass limit, a clump will undergo collapse regardless of the thermal pressure support and undergo star formation. These limits are known as the Jeans length ($R_{\rm J}$) and Jeans mass ($M_{\rm J}$):

$$
\begin{aligned}
M_{\rm clump} > M_{\rm J} &\equiv \left(\frac{5k_{\rm B}T}{G\mu m_{\rm H}}\right)^{3/2}\left(\frac{3}{4\pi\rho_0}\right)^{1/2} \\
R_{\rm clump} < R_{\rm J} &\equiv \left(\frac{15k_{\rm B}T}{4\pi G\mu m_{\rm H}\rho_0}\right)^{1/2}
\end{aligned}
\tag{1.2}
$$

where ρ_0 is the mean density of the gas, μ is the mean molecular weight and $m_{\rm H}$ is the atomic mass of hydrogen. Above these limits, a clump will be gravitationally unstable and will collapse. For a typical clump ($T = 30\,{\rm K}$ and $\rho_0 = 10^3\,{\rm cm}^{-3}$) the Jeans mass is $\sim 200\,{\rm M}_{\odot}$. Despite only including thermal pressure to oppose gravity the $R_{\rm J}$ and $M_{\rm J}$ provide an approximate estimate of whether a cloud is gravitationally unstable. An important feature of $R_{\rm J}$ and $M_{\rm J}$ is that they are dependent on the density and temperature ($M_{\rm J} \propto \rho^{-1/2}T^{3/2}$) on both local and global scales.

Once the Jean's criterion is satisfied a clump will effectively collapse in free-fall providing it remains optically thin thus allowing heat, generated by the release of gravitational potential energy in collapse, to be efficiently radiated away. This is achieved by the coupling of the dust and gas, allowing heat to be efficiently radiated away and maintaining a temperature of $\sim 10\,{\rm K}$ over a wide range of densities. Since the temperature remains constant but the density increases locally within the collapsing clump the Jeans mass must also decrease, thus any incipient or turbulence induced density enhancements in the collapsing clump independently satisfy the Jeans equations and collapse on a local scale. This leads to fragmentation of the initial clump into a large number of smaller, denser molecular cores.

At some critical point a dense core is unable to maintain a high enough level of radiative transfer as the medium becomes optically thick and the collapse goes from being isothermal[1] to adiabatic[2]. This causes the temperature to rise as the heat imparted from gravitational potential energy is unable to escape, which results in an increase in the thermal pressure, this is able to counteract gravity and results in an increased Jeans mass and thus the cessation of fragmentation. Towards the centre of the core, collapse is slowed or halted altogether resulting in a core where the internal pressure balances gravity (hydrostatic equilibrium). As the core collapses, any initial angular momentum is magnified (conservation of angular momentum) and so a rotating spherical core is formed surrounded by a more slowly rotating envelope of dust and gas called a pre-protostellar core.

[1]An isothermal process is a change of a system, in which the temperature remains constant: $\Delta T = 0$ and $Q \neq 0$.

[2]An adiabatic process is where a system exchanges no heat with its surroundings: $\Delta T \neq 0$ and Q = 0.

The envelope of material surrounding the core is essentially in free-fall towards the hydrostatic pre-protostellar core, this material encounters the surface and generates a shockwave known as the accretion shock. This in turn generates a significant amount of heat transferred from the kinetic energy of the in-falling material and provides most of the core's luminosity. Whilst the core is opaque to its own radiation the accreting material on the surface is still able to freely radiate away its energy. As material continues to accrete onto the central core the temperature and pressure continue to rise whilst the radius of the star decreases until a temperature of $\sim$ 2000 K is reached, when the molecular hydrogen begins to disassociate via collisions in an endothermic reaction. This results in a drop in pressure destroying the previously stable state of hydrostatic equilibrium and the core collapses. At this stage, the core is referred to as a protostar and is now visible in the infrared.

The protostar is now in the main accretion phase, material continues to accrete from the rotating envelope. Angular momentum continues to be conserved which would be expected to result in a cut-off in the accretion process as the rotation speeds reach values so high that the accreting material exceeds the escape velocity. Through magnetic fields and rotation a bipolar molecular outflow is established which ejects material with velocities up to 100 km s^{-1} from the poles of the accreting protostar that can travel for many parsecs. This ejection is perpendicular to the accretion disk and is thought to rotate (Chrysostomou et al., 2008) so provides a means to remove the angular momentum from the system, reduce the rotation velocity and allow accretion to continue. To continue growing in mass a forming star requires both accretion and ejection of material and so the final mass depends on the accretion rate vs. the ejection rate.

When the protostar has accreted sufficient mass and the central core has reached $\sim 10^6$ K the protostar begins to burn deuterium (^{2}H). At this point, the star has accreted most of its mass from the surrounding disk that is eroded by radiation pressure and stellar winds. Most of the surrounding medium has been swept away by the bipolar outflows and the star becomes optically visible as a pre MS star. The star then continues to contract and evolve onto the MS.

The star formation process is very inefficient, the Galactic star formation efficiency (SFE), that is how much mass is actually transformed from molecular gas into stars, is $\sim$ 2% (cf. Vázquez-Semadeni 2010). The SFE of various star-forming regions is between 2–17% (Williams & McKee, 1997; Tachihara et al., 2002) and the range is thought to be due to different star formation histories. The star formation rate (SFR) in the Galaxy is also low, on the order of only $\sim 2\,M_{\odot}\,yr^{-1}$ (Chomiuk & Povich, 2011). This low efficiency and rate of star formation can be attributed to either the star formation process being inherently inefficient or very slow. Either molecular cloud formation and star formation are slow and gradual processes or it is a transient phenomenon that occurs on short time scales but inefficiently. It remains unclear what processes control the SFR/E in molecular clouds.

There are two main scenarios that attempt to explain evolution of GMCs and account for the low SFE. These scenarios concern the impact of stellar feedback (mainly from massive stars) on the star-forming clouds. In the first scenario stars quickly disrupt their parent clouds by dispersal and/or photoionisation, before the gaseous mass of the cloud is completely converted into stars (Whitworth, 1979; Williams & McKee, 1997). In this case, the SFR of active star-forming sites may be large for brief periods of time and then halted by the very first stars. In the second scenario, the role of stellar feedback is to drive turbulent motions within the GMC, which opposes its self-gravity, allowing it to remain in a state of quasi-equilibrium for times significantly longer than its free-fall time (Krumholz, Matzner & McKee, 2006). In this case the SFR is suppressed by supersonic turbulence which both opposes the global collapse while promoting collapse on local scales.

Recent work has tended to lend weight to the idea that molecular clouds are dynamically evolving and transient objects that form and disperse in a few dynamical times (e.g. Pringle, Allen & Lubow 2001) and star formation occurs in a single crossing time at all scales. Feedback processes from principally massive stars work as the catalyst that drive the dissipation of a molecular cloud, through powerful stellar winds and radiative heating, however as they do so they may provide the increase in pressure that may trigger the formation of new stars (Elmegreen, 1998). This is opposed to the classical view where molecular clouds are in a state of quasi-equilibrium, surviving for times much larger than their free-fall times supported by strong magnetic fields that are able to slow the rate of star formation.

Molecular clouds do not appear to survive for long after they begin forming stars since the age span of the associated young stars and clusters is never more than $\sim 10^6$ yrs about the dynamical crossing time of a large GMC. Moreover, stars and clusters older than $\sim 10^6$ yrs no longer have any associated molecular gas (Leisawitz, 1989). Star formation in a molecular cloud is therefore evidently a fast process and it always occurs in a time comparable to the crossing time of the associated cloud or core. Soon after the first stars form the cloud is destroyed, or becomes unrecognisable, perhaps being destroyed by stellar feedback as opposed to being supported by the injected turbulence. Whether the molecular cloud is dispersed by stellar feedback or it is brought into a state of quasi-static equilibrium is still uncertain.

1.4 High-mass stars

The previous section concentrated on a general overview of star formation. In the following section, massive stars are discussed in more detail with particular attention being paid to the key differences between high- and low- mass stars, how high-mass stars interact with the environment and reveal their presence.

1.4.1 Differences between low- and high- mass stars

In comparison to low-mass stars, high-mass stars are rare, evolve on much shorter time scales, have significantly higher temperatures and interact with the environment to a greater degree.

High-mass stars are rare compared to low-mass stars, this can be seen from the initial mass function (IMF), which describes the mass distribution of a newly formed population of stars described by a power law:

$$\xi(M) = \xi_0 M^{\alpha_{\rm IMF}} \tag{1.3}$$

where ξ_0 normalises the distribution and $\alpha_{\rm IMF}$ can be fitted take a range of values, such as the three part Kroupa IMF (Kroupa, 2001) where $\alpha_{\rm IMF} = -0.3$ for $m < 0.08$, $\alpha_{\rm IMF} - 1.3$ for $m < 0.5$ and $\alpha_{\rm IMF} = -2.3$ for $0.5 < m$ (Bastian, Covey & Meyer, 2010).

Unlike low-mass stars, high-mass stars reach the MS whilst still deeply embedded in dense molecular material and continue to accrete material even after the star has turned onto the MS and fusion is taking place. Mathematically this is represented by the Kelvin-Helmholtz time ($t_{\rm KH}$), an estimate of the time it takes for a star to contract onto the MS, being less than the free-fall time, $t_{\rm KH} < t_{\rm ff}$, where $t_{\rm KH}$ is given by:

$$t_{\rm KH} \approx \frac{GM_*^2}{R_* L_*} \text{ [yrs]} \tag{1.4}$$

where R_* is the stellar radius and L_* is the stellar luminosity. For a 1 $M_\odot$ star this time is relatively long $t_{\rm KH} \approx 3 \times 10^7$ yrs, in comparison for a massive star of 50 $M_\odot$ ($L_* \approx 10^4$ $L_\odot$) collapse takes place extremely rapidly $t_{\rm KH} \approx 10^4$ yrs. This compounds the observation of their formation and early evolution as they remain embedded in dust and gas for up to 10% of their main-sequence lifetime.

Another key difference is that high-mass stars have significantly higher surface temperatures ($\sim 3 \times 10^4$ K), hence luminosity of 10^4–10^6 $L_\odot$ and produce copious amounts of high energy UV photons with energies > 13.6 eV. Therefore, high-mass stars are able to ionise the surrounding molecular material resulting in an HII region that indicates the presence of massive star(s) through radio continuum emission and Balmer lines. For massive stars, the luminosity can be so great that the radiation pressure exceeds the gravitational attraction that should slow, or even halt and reverse, the in-falling material from the accretion envelope (Wolfire & Cassinelli, 1987). For this reason a massive star should cease accreting material once fusion has switched on and it has turned on to the MS thus preventing them from growing in mass. If this were the case then the highest mass that could be attained by a star is $\sim$ 20–40 $M_{\odot}$ (Kuiper et al., 2010), which is clearly not the case as stars of up to 300 $M_{\odot}$ have been observed (Crowther et al., 2010).

A great deal of theoretical work has been carried out in recent years in an effort to resolve the issue of radiation pressure in massive star formation. The solution appears to lie in understanding the three-dimensional radiation-hydrodynamics of the collapse of a massive pre-stellar core (Krumholz et al., 2009). Simulations in this case model the accretion of material onto the pre-stellar core through a non-axisymmetric disk affected by gravitational and Rayleigh-Taylor instabilities that channel material on to the star. Filaments that form in the disk are found to self shield against radiation, while allowing radiation to escape through optically thin bubbles hence accretion is able to continue. These simulations are strengthened by the use of typically observed starting conditions (Beuther et al., 2007) and recent observations confirming the presence of disks and outflows around B stars (e.g. Shepherd & Churchwell 1996b,a; Zhang et al. 2001; Beuther et al. 2002). These results also help explain the observed multiplicity of massive stars because of instabilities in the accretion disk leading to the formation of a companion star.

Unlike low-mass stars, the vast majority of high-mass stars are observed to be parts of clusters or runaway stars that have been expelled from clusters (Lada & Lada, 2003). However, this assumption is still unclear: 4 ± 2% of O stars are not observed to be associated with a cluster, nor can they be considered runaways indicating that massive stars are able to form in isolation (Krumholz & Tan, 2007; de Wit et al., 2005).

Finally, disruption of the birth cloud occurs as the first high-mass stars form, evolve, and influence their environment via strong winds, powerful outflows, UV radiation and eventually supernovae. In this way, massive stars have a significant impact on the surrounding GMC structure, being able to move or photo-evaporate and dissipate the surrounding molecular gas and so driving the evolution of the GMC. The most massive stars end their lives as supernovae after $\sim$ 5–8 Myr (Bertelli et al., 1994; Martins, Schaerer & Hillier, 2005) and destroy any molecular material in their immediate vicinity (Herbig, 1962) but may trigger star formation at greater distance (Elmegreen & Lada, 1977; Zavagno et al., 2006). The end products of massive star formation are either gravitational bound OB stars in a dense OB cluster or loose unbound OB associations both with an associated co-spatial population of lower mass stars.

1.4.2 Theoretical models of high-mass star formation

Two main models dominate the theory of massive star formation, these are called monolithic collapse and competitive accretion (Zinnecker & Yorke, 2007). In both theories, a star initially forms when a gravitationally bound dense gas core collapses; the crucial distinction lies in what happens next. The idea behind monolithic collapse is that massive star formation is a scaled up version of low-mass star formation, where the final mass of the star is determined by the mass in the molecular core and that accretion of material outside of the initial core contributes little to the final mass (McKee & Tan, 2003; Padoan et al., 2005). Alternatively, the competitive accretion model predicts that the final mass is determined through environmental processes such as a central location or the merging of protostars, and thus the final mass is strongly dependent on the accretion of material outside of the initial collapsing core that is not initially gravitationally bound to the core. Details of these two models are given below.

1.4.2.1 Monolithic collapse

In the monolithic collapse and disk accretion model (Yorke & Sonnhalter, 2002), also known as the turbulent core model, the formation of a massive star is similar to that of a low-mass star. The massive star forms from a collapsing massive core that is thought to be initially supported by turbulence (McKee & Tan, 2003). The massive core is prevented from fragmenting, which would result in a number of lower mass stars, due to radiative heating on scales of around the size of a pre-stellar object (Krumholz & Tan, 2007). This model suggest that the relationship between the mass of the core and the mass of the resultant star is linked to the initial mass of the clump in which they form and any bulk motions of the embryo star is followed by its protostellar envelope. The accretion of the material from the dense core onto the star is facilitated by the formation of a disk around the star and a molecular outflow is formed, which is able to transfer the angular momentum away from the star.

1.4.2.2 Competitive accretion

Competitive accretion and runaway growth, a theory first suggested by Bonnell et al. (1997) (see also Bonnell et al. 2001; Bonnell, Vine & Bate 2004) uses the clustered nature of high-mass stars to explain their formation. According to this theory the protostar's accumulated mass depends very much on the size of its first accretion domain, the location in the cluster within which it is forming and potentially the time in which it forms. Stars that form early on near the centre of proto-clusters have the ability to accrete more mass. This is because at the centre of the cluster the gravitational potential is greatest and so the forming star will have access to all the gas that slowly falls into the centre of it. Here a major difference arises between the two models; whereas in monolithic collapse the mass of the star is linked to its initial clump mass, in competitive accretion all stars start out much smaller than the typical stellar mass ($0.5\,\mathrm{M}_{\odot}$) and may accrete mass from various parts of the parent cloud and move relative to the gas, so only gas in the protostellar disk is bound. Thus, stars that form in such a potential will be forced to compete for the available mass in the proto-cluster and their location in the cluster will determine in a high degree their resulting mass. This leads to a hierarchical substructure of the cluster where a massive protostar is formed in its centre with increasingly lower mass stars surrounding it. Competitive accretion is supported by the observation that almost all massive stars form in a cluster and that the more massive stars are found towards the centre surrounded by low and intermediate mass stars. However, this mass segregation could be an observational effect (Ascenso, Alves & Lago, 2009) caused by overcrowding towards the core of the cluster leading to incompleteness issues and all clusters appearing to be mass segregated.

In this scenario, the massive stars had accretion histories that were privileged at every stage from Jeans instability protostellar birth to location and density in the gas cloud, i.e. all factors affecting accretion were more favourable than the average. The most rare and massive of them probably formed in the most favourable conditions by runaway accretion until their gas reservoir was exhausted or dissipated

1.4.2.3 Stellar mergers

Stellar collisions and mergers are also proposed as part of the competitive accretion model. This model was originally developed to solve the problem of radiation impeding accretion and to account for the high-density of massive stars in clusters. It is plausible that collisions may occur in the centre of very dense clusters in which case the radiation could be overcome. However, the problem remains that high-mass or intermediate mass stars are still needed to be present to facilitate the creation of increasingly more massive stars (Zinnecker & Yorke, 2007) and very high and unobserved stellar densities are required > 10^8 $M_\odot$ pc^{-3}.

These models have been at the centre of a debate lasting a decade with numerous arguments and counter arguments being presented. Recently both monolithic collapse and competitive accretion models appear to be converging with fewer and fewer observable differences with both models now predicting circumstellar disks and outflows. The main observable difference is found in the kinematic motions of the protostars within the dense clumps and fragmentation length scales (Pillai et al., 2011). Future detailed observations should be able to identify a correct star formation model.

1.5 Observable tracers of high-mass star formation

As previously mentioned, direct observations of the environment and processes associated with massive star formation are complicated. However, massive stars betray their presence through their impact on the surrounding environment, which can be observed, and provide a “signpost” to massive star formation. While an evolutionary paradigm for massive stars has yet to be fully constructed, Evans et al. (2002) and Massey (2003) outline the observational features that such a theory must accommodate (Fig. 1.3).

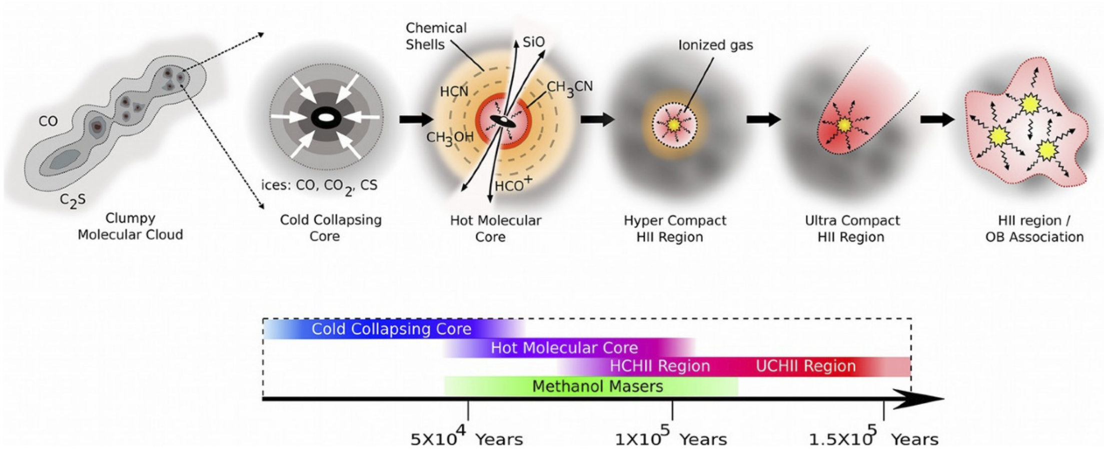

FIGURE 1.3: Proposed observable sequence of massive star formation, with proposed time line and tracers (Purcell, 2006).

1.5.1 Dust

The dust grains that exist in the ISM are responsible for the absorbing and scattering radiation in the optical and UV regime giving rise to interstellar extinction. The dust grains absorb high frequency radiation from embedded objects and re-radiate it at far-infrared and (sub)mm wavelengths. Thus dust grains provide a good diagnostic of the location of massive protostars and stars through thermal black body continuum radiation (Appendix B Section B.6.1.1). Observing the thermal emission associated with dust at a range of frequencies allows the environment from cold dense condensations to hot cores to be probed uncovering some of the earliest stages of star formation (Lumsden et al., 2002).

1.5.2 Hot molecular cores

Hot molecular cores (Fig. 1.3) are dense, compact regions of warm molecular gas detected towards sites of massive star formation. Hot cores are sites of rich molecular line emission caused by high temperatures sublimating the icy molecular mantles from dust grains. They have diameters of < 0.1 pc, particle densities of $> 10^7\,\mathrm{cm}^{-3}$ and temperatures of 100–250 K (Cesaroni, Walmsley & Churchwell, 1992). It is thought that they are heated by a central massive protostar (Molinari et al., 1996), which is likely to be surrounded by an accretion disk. They are usually found to be associated with massive bipolar outflows, or externally from nearby star formation. Masers have also been detected towards many hot molecular cores, indicating the presence of the early stages of infall and outflow (Longmore et al., 2007a).

1.5.3 Astrophysical masers

Masers are compact sites of intense molecular line emission where the radiation emitted from certain atomic and molecular transitions is massively amplified via stimulated emission (Elitzur, 1992). In order for masing to take place the following conditions must be satisfied; the gain medium must have coherent velocity and high-density, the masing transition must contain a high energy meta-stable transition and there must be an exciting source to "pump" the system into population inversion (see Appendix B Section B.5.5). Masers are used to study kinematics, determine accurate parallax distances, and probe the magnetic fields, age and physical conditions in the immediate surroundings. A brief outline of masers commonly observed towards GMCs is presented below; more information may be found in reviews by Ellingsen et al. (2007) and Elitzur (1992).

Hydroxyl (OH) masers are observed in a wide range of environments, such as around evolved stars, regions of massive star formation, and the interface between supernova remnants, HII regions and molecular material. Of particular interest to this study is the fact that OH masers are often observed towards UC HII regions and may form within the circumstellar material of YSOs and so trace an advanced stage of star formation (Bloemhof, Reid & Moran, 1992).

Water (H_2O) masers are thought to be collisionally excited by gas shocked in the outflows and accretion disks of protostars (Elitzur, 1992) and trace regions of both high- and low- mass star formation. These masers are rarely detected centred on stellar sources even at infrared wavelengths suggesting they trace young, deeply embedded stellar sources and outflows (Genzel & Downes, 1977).

Methanol (CH_3OH) masers are split into two classes (Menten, 1991): class I are found offset from star-forming regions by up to a parsec whilst class II are found in close proximity to infrared sources, OH masers and HII regions. Class II methanol masers are frequently found in the directions, or projected against, the edge of UC HII regions and appear to be almost exclusively associated with the earliest stages of massive star formation with a statistical age of $< 10^5$ yrs (Harju et al., 1998; Caswell, 2009; van der Walt, 2005).

The study of masers has become popular in recent years as they may provide a diagnostic tool with which to gauge the evolution of star formation (Ellingsen et al., 2007). This is because masing transitions may preferentially form in the environments of specific evolutionary epochs of star formation. This scenario is attractive but the association of masers with star formation is still poorly understood due to the large overlap of masers present in different stages of stellar evolution. Nevertheless, a tentative timeline has been suggested for the evolutionary stages of maser emission with Ellingsen et al. (2007) presenting a "straw man" evolutionary sequence through statistical analysis. It is important to stress that this area of maser research is still young and that unbiased searches have only just begun and so any statistical analysis is limited.

To summarise, in relation to this work masers provide a means to trace star formation and whilst the exact epoch is unknown, they nevertheless provide an excellent tool to identify regions of ongoing star formation.

1.5.4 Outflows

Molecular outflows are ubiquitous in low-mass star formation and have been studied in some detail (Bachiller, 1996; Lada, 1985; Fukui et al., 1993). Molecular outflows are powered by the release of gravitational potential energy of a protostar with an accretion disk and are driven by the conservation of angular momentum. Therefore, molecular outflows are a direct indication of ongoing star formation and an important contribution to turbulence and dynamics in star-forming regions (Hartmann, Ballesteros-Paredes & Bergin, 2001). It is also suggested by these studies that molecular outflows are common in massive star-forming regions with recent systematic surveys for outflows toward such regions showing a detection rate of molecular outflow phenomena as high as 90%, confirming that outflows are also common in massive star-forming regions (Shepherd & Churchwell, 1996b; Beuther et al., 2002; Arce et al., 2007; Zhang et al., 2001). Outflows have a broad range of properties with physical sizes ranging from 0.1–5.0 pc and velocities that span tens of km s^{-1}. Observations have shown that molecular outflows can have an impact on their cloud at different distances from a few thousand AU to several parsecs.

1.5.4.1 Outflow identifiers

The spectral profile of emission from molecular gas associated with an outflow has distinct non-Gaussian emission in the wings of the profile. This is a result of the fast flowing ($\sim 10\,\mathrm{km\,s^{-1}}$) outflowing material which Doppler shifts the emission from the quiescent cloud velocity extending the spectral line profile in the wings.

Optically thick ^{12}CO emission is one of the best tracers of outflows and generally the $J = 2$–1 or 3–2 transition is preferred as it is preferentially excited in the warmer regions were outflows occur and generally has increased spatial and velocity resolution. A number of methods are commonly used to search for outflows. These all involve identifying the characteristic kinematic signature of outflows via identification of: i) non-Gaussian line-wings in single spectra (Shepherd & Churchwell, 1996b; Hatchell, Fuller & Richer, 2007; Hatchell & Dunham, 2009; Curtis et al., 2010; Graves et al., 2010) ii) clear deviations from the quiescent cloud velocity in position-velocity (PV) diagrams (Zhang et al., 2001; Graves et al., 2010) iii) or via visualisation in three-dimensional (PPV) space (Borkin et al., 2008; Arce et al., 2010) iv) resolved outflow motions in renzograms (Shepherd & Churchwell, 1996b; Hatchell, Fuller & Richer, 2007).

The first of these methods allows the automated detection of outflows based on a broadened spectral profile identified through a set of criteria generally set to identify emission above a given threshold at a particular velocity from the systematic velocity of the cloud. The advantage of this method is that it can be automated and removes the subjectivity commonly encountered in outflow identification. The drawback of this method is that regions of complex velocity structure can easily generate false-positive detections. The second method, PV diagrams, allows the identification of structures where deviations from the systematic cloud velocity are easily visible. This method is somewhat subjective, requires high-resolution and is complicated when the region observed has a range of systematic velocities. More recently, improvements in imaging techniques and data processing has made three-dimensional analysis practical (Arce et al., 2010). A three-dimensional analysis is perhaps more intuitive than the methods above and efficient for searching large areas however, it is subjective and as will be shown, identification via this method is difficult when observing ^{12}CO J = 1–0. Renzograms are images in which integrated velocity channels are assigned contour levels and colours based on their velocity range. This allows the identification of spatially resolved outflows but can be complicated by projection effects (Hatchell, Fuller & Richer, 2007).

1.5.5 HII regions

As mentioned in Section 1.4.1 massive stars have high surface temperatures and luminosities, a consequence of this is that they generate radiation that is able to ionise the surrounding neutral environment. To completely photo-disassociate H_2 a star must generate UV photons with energies > 11.2 eV and to photo-ionise hydrogen (HI) > 13.6 eV. It is thought that only stars of spectral type B3 and earlier are capable of producing sufficient ionising flux (Lyman continuum photons) (Crowther & Conti, 2003) to produce an HII region. The physics behind the generation and evolution of HII regions is discussed in more detail in Appendix B.

There are four classes of HII regions that are commonly described in the literature; hyper compact (HC) ultra compact (UC), compact and classical. The different classification arises from the expansion of the HII region and corresponding difference in physical properties highlighted in Table. 1.2. HII regions can be identified through observations of the thermal Bremsstrahlung and recombination line emission at radio and optical wavelengths respectively.

When a massive star begins generating Lyman continuum photons, the initial expansion of the HII region is rapid as the ionisation front moves through the ISM. The flux of photons decreases as $1/r^2$ with distance and the rapid expansion phase ends when the rate of ionisation is balanced by recombination. The number density in the ionised gas doubles and the temperature within the HII region rapidly reaches equilibrium at $\sim 10^4$ K and the resulting pressure gradient between the hot gas and surrounding cool gas causes further expansion at the sound speed in the HII

HII region	R (pc)	n_e (cm^{-3})	EM (pc cm^{-6})	M_{HII} (M$_\odot$)	Age Myr
Hypercompact (HC)	$\lesssim 0.01$	$\gtrsim 10^6$	$\gtrsim 10^{10}$	$\sim 10^{-3}$	-
Ultracompact (UC)	$\lesssim 0.1$	$\gtrsim 10^4$	$\gtrsim 10^7$	$\sim 10^{-2}$	$\lesssim 0.1$
Compact	$\lesssim 0.5$	$\gtrsim 10^3$	$\gtrsim 10^7$	~ 1	$\sim$ 0.2–0.4
Classical	~ 10	~ 100	$\sim 10^2$	$\sim 10^5$	> 1

TABLE 1.2: The classification scheme of HII regions drawn from the varying physical properties radius (R), electron density (n_e), emission measure (EM), ionised gas mass (M_{HII}) and Age (Davies et al., 2011; Kurtz & Hofner, 2005; Comeron & Torra, 1996).

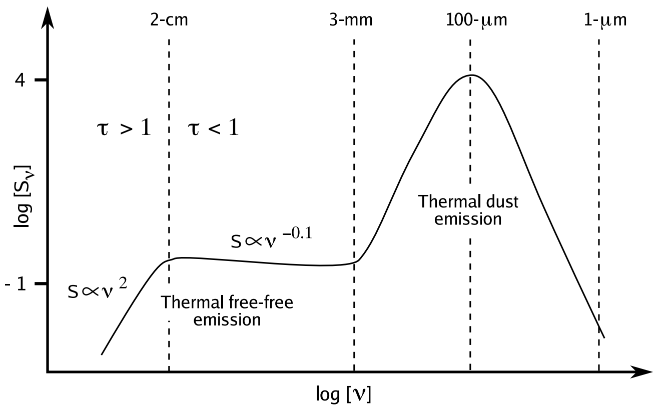

FIGURE 1.4: Spectral energy distribution from a spherical, homogenous and isothermal UC HII region. At wavelengths longer than $\sim$ 3 mm the emission is dominated by thermal free-free emission from the ionised gas. Between 3 mm< λ < 3 cm the emission is optically thin and $S \propto \nu^{-0.1}$. At wavelengths longer than 3 cm the free-free emission is optically thick and $S \propto \nu^2$. The turnover frequency corresponds to 5–15 GHz. At wavelengths shorter than 3 mm the emission is dominated by thermal emission from relatively warm ($\sim$ 30 K) dust.

region. A result of these temperatures and ionisation is that the HII regions drive shocks into the molecular environment.

1.5.5.1 Ultra compact HII regions

One of the key aims of this work is to identify UC HII regions, one of the earliest observable indicators of the presence of high-mass star(s), through observations of their radio continuum emission. Whilst the UC HII phase is essentially part of the evolutionary sequence of HII regions there are several problems unique to this evolutionary stage that must be addressed.

The spectral energy distribution (SED) of a characteristic UC HII region located in the Galactic plane is presented in Fig. 1.5.5.1 and demonstrates the contribution of free-free and thermal dust continuum emission. The thermal dust emission arises from a shell of dust that surrounds the ionised gas that absorbs radiation, which it then re-emits in the infrared. The free-free component is the result of thermal Bremsstrahlung emission generated by the electrostatic interaction between electrons and ions in the HII region. It is clear that the best wavelengths with which to directly identify UC HII regions in the Galaxy lies in the infrared and radio regime where emission is brightest and unobscured by intervening dust and gas.

An extensive study of UC HII regions has been carried out by Wood & Churchwell (1989a,b) using the Infrared Astronomical Satellite (IRAS) point source catalogue (PSC). The IRAS wavebands cover the spectrum in four windows centred at 12, 25, 60 and 100 μm, effectively sampling the far-infrared black body component of the UC HII SED. Peaking at 100 μm, the SED of UC HII regions appear significantly reddened compared to other objects in the IRAS PSC. This prompted Wood and Churchwell to search the Galactic plane using colour cuts within the IRAS PSC ($\log f_{25}/\log f_{12} > 0.57$ and $\log f_{60}/\log f_{12} > 1.3$) in search of UC HII regions.

The dynamical age of an UC HII region can be estimated by taking the typical size (0.1 pc) and sound speed in an ionised medium (10 km s^{-1}) to be $\sim 10^4$ yrs. The statistical argument suggests that there are $\sim$ 17000 O stars and if the age is taken to be $\sim 10^4$ yrs (< 2% of the lifetime of a O star) then approximately 300 UC HII regions should be expected within the Milky Way. Number estimates however reveal many more UC HII regions, such as the 75 UC HII detected in Wood & Churchwell (1989a) in a region spanning only $\sim 40°$ in longitude, assuming this is representative of the distribution across the entire Milky Way on the order of $\sim$ 700 UC HII regions in the Galaxy are expected. If this is the case, a massive star can spend $\sim$ 10 % of its MS lifetime in the embedded phase. Since the main-sequence life time is $\sim 10^6$ yrs we can estimate the lifetime of an UCHII to be $< 10^5$ yrs (Comeron & Torra, 1996; Davies et al., 2011) an order of magnitude longer than the dynamical time.

There are far too many observed UC HII compared to the youthful dynamical state the difficulty then is why do UC HII regions appear to be so prevalent and small? One explanation is that infall quenches the expansion and so ionising Lyman continuum photons are consumed through ionising this fresh matter or that the estimate of UC HII regions by Wood & Churchwell (1989a,b) may suffer from considerable contamination from low-mass stars (Churchwell, 2002) and YSOs. In addition the limited resolution of IRAS ($\sim 2'$) suggests there may be significant contamination of colour selected UC HII regions by compact HII regions, which would appear unresolved at distances greater than $\sim$ 4 kpc and have colours indistinguishable from UC HII regions.

1.6 Triggered star formation

First proposed more than 30 years ago triggered (or induced) star formation is thought to be a result of the interaction between massive stars and their environment. The classical model for triggering given by Elmegreen & Lada (1977) is that an advancing pressure front, caused by an HII region, induces collapse in a density enhancement that was either already present in the surrounding molecular cloud or was swept up by the advancing pressure front. If the triggered star(s) happen to be massive, this process may repeat producing another generation of stars and this sequential process would continue until there is no material left to form stars. In this way massive stars are thought to be able to directly impact the star formation efficiency (SFE) and rate (SFR) either enhancing through triggering or quenching through dissipation of the reservoir for star formation and so driving the evolution of their host GMC.

1.6.1 Models

There are three distinct means of triggering star formation discussed in the literature: the direct compression of pre-existing molecular condensations in a process known as radiative driven implosion (RDI), the accumulation of gas into a ridge or shell that can then collapse into star-forming cores known as the collect and collapse (C&C) process and cloud-cloud collisions. In the first and second case expanding HII regions (or supernova) generated by massive stars are thought to be the main driving force and so are described in more detail below.

1.6.1.1 Collect and Collapse

The C&C model for triggered star formation was developed by Elmegreen & Lada (1977) in part due to the observations of sequential bursts of star formation and the sequence of spatially distinct OB subgroups in nearby OB associations (Blaauw, 1964). In this theory as soon as the first massive stars form their ionising radiation and winds begin to disperse the immediate surroundings thus terminating star formation in the direct vicinity of the massive star. Further away the ionisation and shock fronts produced by the HII region sweep up and compress neutral material into an increasingly massive and dense shell of cool gas. If the expansion continues for long enough the surface density of the shell increases to the point where it becomes self gravitating, the shell is then expected to fragment and collapse possibly forming a new generation of massive, low and intermediate mass stars. This process continues as long as subsequent generations of massive stars are formed (Whitworth et al., 1994) until the wave of propagating star formation reaches the edge of the molecular cloud and thus can explain the sequences of subgroups seen in OB associations.

According to this model low-mass stars are expected to be systematically older than the associated OB stars, which show a large age spread, corresponding to the total lifetime of the cloud (low-mass stars are expected to form spontaneously). It is also expected that the youngest massive stars have the largest fraction of low-mass stars as these regions have had more time to form low-mass stars. If the region is uniform, there should be an age sequence spreading out from the initial site of massive star formation. If C&C is taking place observations should reveal an over density of molecular gas in the vicinity of HII regions in the cloud where the dense gas has been swept up and stars formed in the process should retain a velocity component moving away from the driving source.

1.6.1.2 Radiative Driven Implosion

An alternative triggering mechanism is described by the RDI model. In this model as the ionisation front of an HII region expands into a nearby molecular cloud it drives a shock wave into the cloud (Lefloch & Lazareff, 1994) at the interface between ionised and neutral material. This generates enhanced inward pressure that is able to trigger the formation of new, gravitationally unstable, dense cores or it may compress pre-existing cores leading to the formation of a new generation of stars. The UV radiation from the nearby OB star(s) photo-ionises the surface of the neutral material and any over-dense regions will persist leading to a bright rim pointing towards the source of the ionising radiation. The photo-ionised surface causes gas to be swept away radially from the OB star resulting in clouds developing a cometary appearance.

This model predicts that the low-mass stars should be younger than the massive stars that initiate the formation and there may be a gradient in the low-mass population since objects closer to the massive stars where triggered first. In order for shocks to be driven into the molecular cloud the pressure of the HII region must be larger than the molecular gas.

1.6.2 The role of triggering

Triggering may be an important process in regulating star formation in a molecular cloud. Evidence of both C&C and RDI triggering mechanisms has been found in several carefully selected cases (e.g. Deharveng, Zavagno & Caplan 2005; Zavagno et al. 2006; Thompson, Urquhart & White 2004; Urquhart et al. 2007b) but the specific mode and overall importance of triggering to star formation and the evolution of GMCs has yet to be determined. This is because it is difficult to determine whether star formation has been triggered or if the dissipation of molecular material by the massive star by photo-evaporation has simply exposed stars that were already forming spontaneously.

Further insight into triggering can be gained by determining the star formation history (SFH) of GMCs, this allows a plausible sequence of cause and effect to be established by comparing age estimates of shock waves and star formation, agreement between these times adds weight to any triggering scenario. The average SFE in the Milky Way (3–6% Evans et al. 2009) and other galaxies (5% or less e.g. Rownd & Young 1999) appears to be insensitive to anything but the molecular surface density which suggests that triggering is one of many processes that lead to gravitational collapse and star formation (Elmegreen, 2007). Large sample, statistical studies of triggering (Thompson et al., 2012) are just beginning to provide strong evidence of triggering.

Theoretical models and simulations (Dale, Bonnell & Whitworth, 2007; Dale & Bonnell, 2011; Haworth & Harries, 2012; Miao et al., 2009; Bisbas et al., 2011) are beginning to incorporate more and more of the physical processes that occur within GMCs to test the viability of massive star formation models and feedback. By modelling ionising radiation, winds and shocks in molecular clouds with realistic conditions, simulations are beginning to replicate observations and provide insight into high-mass star formation and triggering. Further observational study is required to provide realistic physical conditions and comparisons to these theoretical models.

1.7 Motivation

The broad aim of this work is to compare the global molecular and ionised environment of the GMC G305 with the associated stellar populations and ongoing star formation. This is in an effort to characterise the environment in which massive stars form and determine the star formation history to assess the impact of high-mass stars on the evolution of G305. High-mass stars form in clusters, which in turn form within extended star formation complexes. In order to understand the relationship and complex interplay between different populations and epochs of star formation and the environment, detailed, multi-wavelength observations across entire GMCs are required to disentangle the complex star formation history. With this in mind, this work aims to address the following questions:

- What are the physical conditions that give rise to massive stars?
- What is the relationship between the molecular and ionised environment, ongoing and recent star formation?
- Do massive stars propagate through GMCs?
- To what degree does the energy input from massive stars affect the evolution of GMCs?

To answer these questions we set out to characterise the molecular and ionised environment and compare this to the recent and ongoing star formation within the GMC designated G305 (Chapter 2). This work is part of a wider collaboration performing an in depth multi-wavelength analysis of all evolutionary stages in G305 from the molecular reservoir, pre-stellar, protostellar and YSOs to the optically visible massive stars and the ionised environment they create. This includes; HST observations of the two central clusters in G305 (Danks 1 and 2; Davies et al. 2012), APEX LABOCA 870 μm dust maps, far-infrared observations as part of the *Herschel* Infrared GALactic plane survey (Hi-GAL) survey (Molinari et al., 2010a).

The work presented in this thesis is centred around three wide-area observations of the G305 complex using the Mopra telescope and Australia Telescope Compact Array (ATCA) at millimetre and radio wavelengths respectively. The first of these observing projects uses the Mopra telescope and millimetre spectroscopy to reveal the dense molecular environment and star formation traced by NH_3 and H_2O masers. The second data set is also obtained with Mopra but traces CO to study the more diffuse molecular material and kinematics. Finally, radio continuum observations were carried out using the ATCA to uncover the small- and large-scale ionised environment towards G305.

This is an opportune time to carry out such a study for two reasons. First there has recently been a number of improvements in instrumentation, discussed in the following chapters, that allow high sensitivity and angular resolution, wide-area mapping to be performed in a practical amount of time. Secondly, a number of surveys such as the H_2O Southern Galactic Plane Survey (HOPS) (Walsh et al., 2008), Co-Ordinated Radio 'N' Infrared Survey for High-mass star formation (CORNISH) (Purcell, Hoare & Diamond, 2008), Millimetre Astronomy Legacy Team 90 GHz (MALT90) survey (Foster et al., 2011) and Hi-GAL at a range of wavelengths that cover a large portion of the Galactic plane are being carried out or published that will provide similar quality multi-wavelength data sets across a large number of GMCs. Now is an excellent time to exploit these improvements in instrumentation to construct a high-quality multi-wavelength dataset of G305 to investigate massive star formation and provide a case study for future surveys

1.8 Structure of this thesis

In Chapter 2 a description and literature review of G305, the GMC chosen for this study, in addition to the motivation behind why this region was chosen is presented. In Chapter 3 Mopra telescope wide-area maps of the dense environment traced by NH_3 and lower density environment traced by CO are presented as well as newly detected H_2O masers. Chapter 4 presents ATCA 3 and 6 cm observations of the small- and large-scale radio continuum emission uncovering the ionised environment towards G305. The comparison of the molecular and ionised environment as well as the star formation history and an in depth discussion is presented in Chapter 5. Finally, Chapter 6 presents a summary and conclusions of this thesis and the potential for future work.

Chapter 2

G305 Complex

2.1 Introduction

The target of this study is the G305 star-forming complex a GMC located in the Galactic plane at $l \approx 305.4^\circ$, $b \approx 0.1^\circ$ and extending over $\sim 1\overset{\circ}{.}0 \times 0\overset{\circ}{.}8$ in angular scale. In this chapter we present a literature review of the G305 complex.

2.2 Morphology

The first mention of G305 is in the survey of 70 star-forming regions in the Southern Galactic plane by Goss & Shaver (1970) and Shaver & Goss (1970) with the Parkes radio telescope at 5000 MHz and 408 MHz (Fig. 2.1, top). These low-resolution ($4'$) radio continuum observations reveal the general radio structure to be a complex collection of five bright thermal radio sources indicative of HII regions embedded within a region of extended low surface brightness radio emission. The G305 complex is found to have a composite flux at 5000 MHz of $\sim$ 200 Jy making it the tenth brightest star-forming region in the sample of Goss & Shaver (1970). These single dish observations prompted interferometric follow-up with the Fleurs synthesis telescope (Jones et al., 1984) at 1415 MHz (Fig. 2.1, bottom). At a higher resolution of $20''$ the radio emission reveals the substructure of the thermal radio sources in G305 to be distinct sources with bright compact cores, shells and diffuse boundary layers.

One of the most revealing wavelengths with which to study a star-forming region is in the infrared where the radiation, re-emitted by the heated dust and excited PAHs present in GMCs, is able to penetrate any obscuring cold interstellar dust and gas. The *Spitzer* space telescope Galactic Legacy Infrared Mid-Plane Survey Extraordinaire (GLIMPSE) (Benjamin et al., 2003; Churchwell et al., 2009) maps mid-infrared emission across the Galactic plane at 3.6, 4.5, 5.8

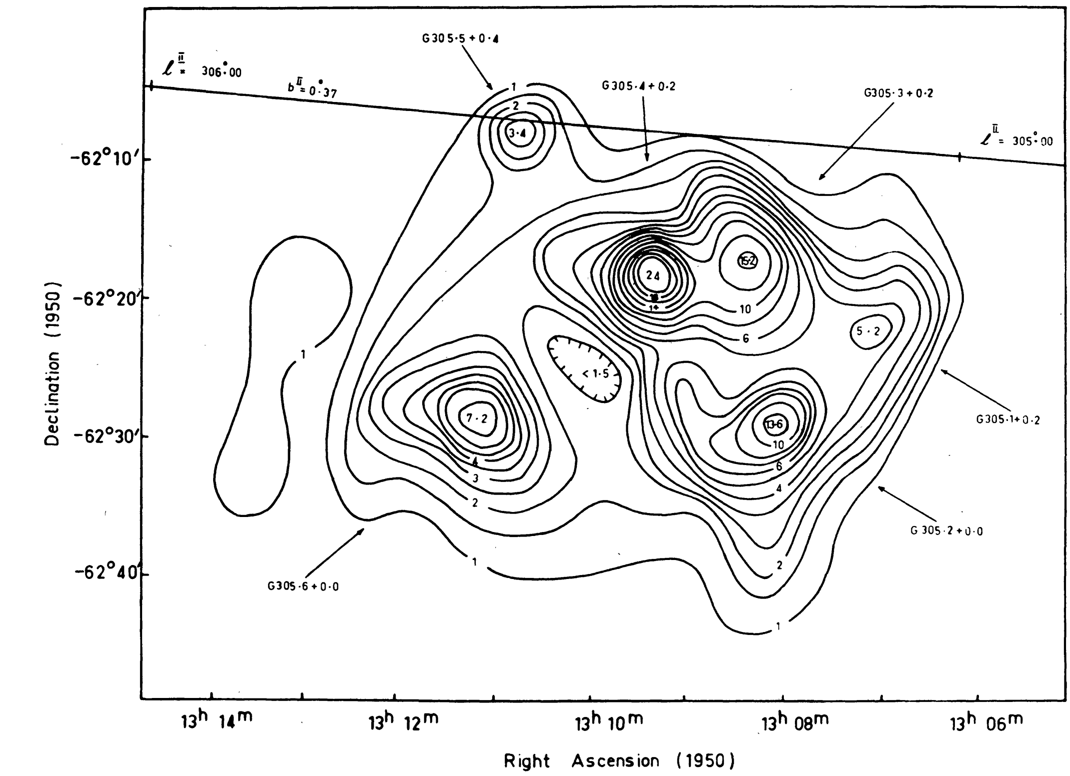

Fig. 15

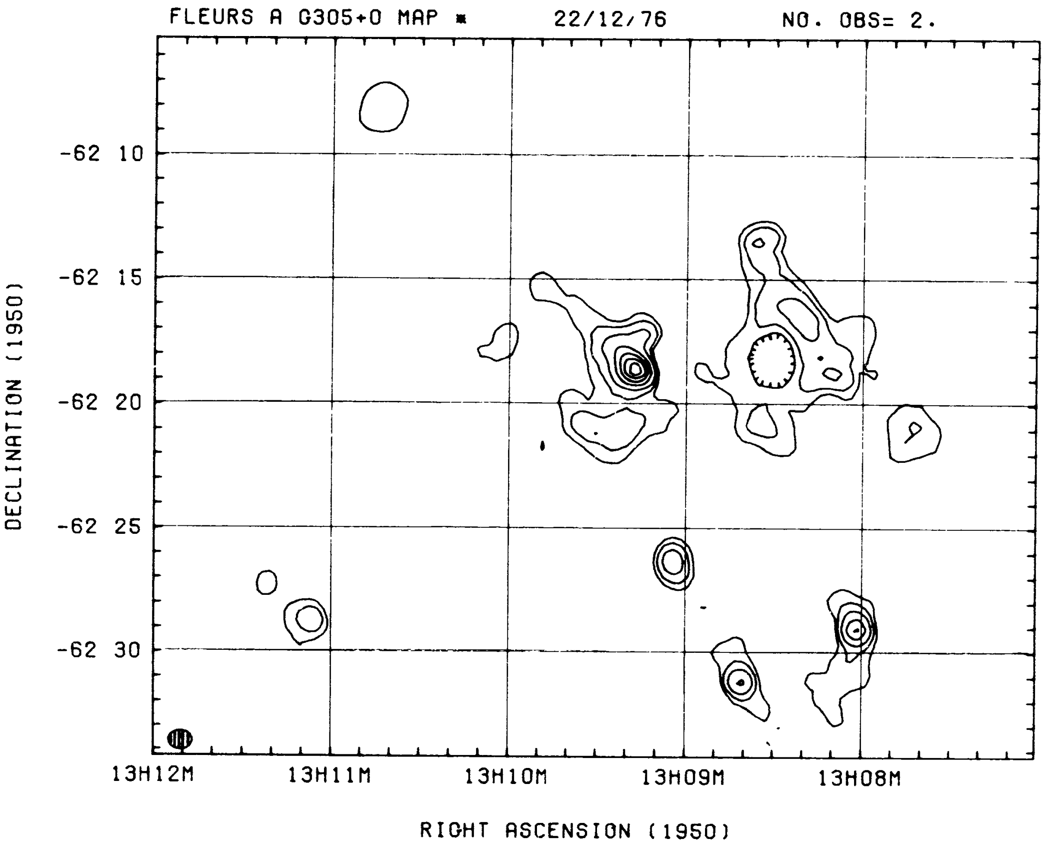

Figure 2.1: The radio structure of G305. Top: low-resolution observations of G305 at 5000 MHz (Goss & Shaver, 1970; Shaver & Goss, 1970). Bottom: higher resolution 1415 MHz observations (Retallack, 1979).

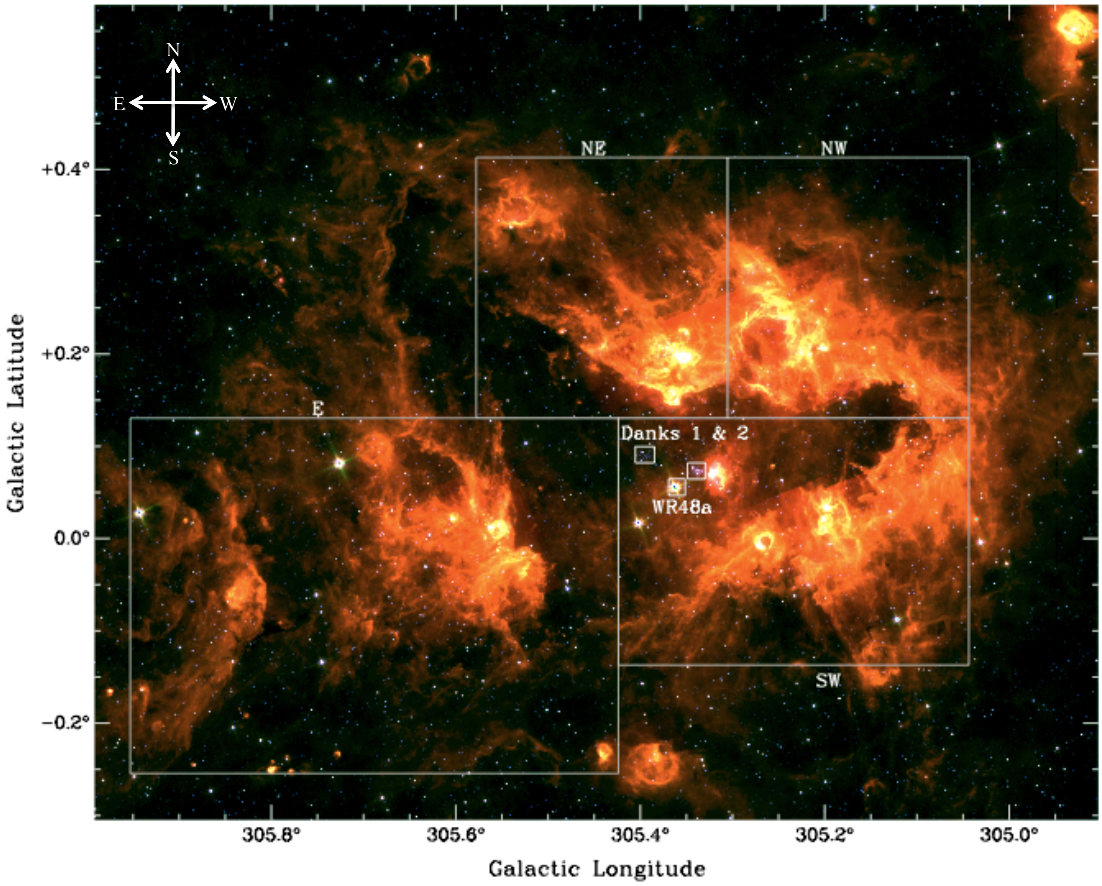

FIGURE 2.2: Three colour mid-infrared image of G305 produced by combining the 4.5, 5.8 and 8.0 μm bands from the GLIMPSE survey in blue, green and red respectively. White boxes highlight the central clusters Danks 1 and 2 and the Wolf-Rayet star WR 48A. The complex is split into four main sub-regions according to Galactic position relative to Danks 2 (see text for details).

and 8.0 μm. Emission within these bands occurs in different environments and so provides an excellent tool with which to study mid-infrared emission mechanisms (Section 2.7.1). Combining the 4.5, 5.8 and 8.0 μm band in a three colour image (blue, green and red respectively) reveals G305 to be a large tri-lobed nebula surrounding a non-spherical cavity roughly centred on the open clusters Danks 1 and 2 and the Wolf Rayet (WR) star WR 48A (Fig. 2.2). The powerful UV radiation and winds from these sources are prime candidates for the driving force behind the cavity. There is a great deal of complex structure visible in the mid-infrared such as filaments, bright and compact hot spots and shells suggestive of HII regions and embedded star formation activity. The central cavity is not bound on all sides by mid-infrared emission particularly to the (Galactic) South- and North- East where radiation and winds appears to be have blown a hole in the surrounding molecular envelope. This suggests that the distribution of molecular gas in G305 is not homogenous and the radiation powering the cavity is in the process of breaking out of the complex. The morphology and distribution of the radio and mid-infrared emission reveals G305 to be a highly dynamic region and is suggestive of strong interaction between the ionised and neutral environment.

2.3 Distance

The distance is often one of the most poorly constrained parameters in astronomical studies. Fortunately, several studies have reported the distance to G305 using a range of independent methods including spectroscopy and photometry (Danks et al., 1983, 1984; Leistra et al., 2005), colour magnitude diagrams (Bica et al., 2004) and kinematics (Georgelin et al., 1988; Russeil et al., 1998). Within the errors these studies agree that G305 is a single, coherent complex at a heliocentric distance between 3.3 and 4.6 kpc.

Work carried out as part of the G305 collaboration has recently refined both the kinematic and spectrophotometric distance to G305 (Davies et al., 2012). Using the Red MSX Source (RMS) survey (Hoare et al. 2005, see Section 2.7.2) 15 YSOs with known radial velocities (Urquhart et al., 2007b, 2009) are found to be associated with G305. With a mean radial velocity of $V_{\rm LSR} = -39.4 \pm 3.0\,{\rm km\,s^{-1}}$ application of the Galactic rotation curve of Brand & Blitz (1993) gives a kinematic distance to G305 of 4.2 ± 2.0 kpc. The spectrophotometric distance to individual members of Danks 1 and 2 (Davies et al., 2012) is found to be 4.16 ± 0.6 and 3.4 ± 0.2 kpc respectively consistent with the kinematic distance. Taking the weighted average of the spectrophotometric and kinematic distances results in a distance to G305 of 3.8 ± 0.6 kpc. This distance applies to the radio and CO studies (Chapter 3 and Chapter 4). Before Davies et al. (2012) the best estimate of the distance to G305 was 4 ± 0.5 kpc (Clark & Porter, 2004) this has been assumed in the NH_3 study (Chapter 3). The difference between these two distance estimates does not have any impact on the results of this study. It is important to note that the distance estimates presented above have been made towards stellar sources, Hα and molecular emission which suggest that the massive stars in G305 are associated with the wider complex.

With the distance defined it is possible to comment on the projected position and physical scale of features in the G305 complex as seen in Fig. 2.2. At a distance of 3.8 kpc G305 is located within the Scutum Crux arm of the Milky Way (Fig. 2.3) and extends over $\sim 100 \pm 15$ pc in size. The two central clusters (Danks 1 and 2) are separated by a projected distance of ~ 3 pc with WR 48A only ~ 2 pc from either cluster centre. The central cavity has an irregular geometry best expressed by an ellipse centred on Danks 2 with semi-major and minor distances of 15×6 pc ($0.21^\circ \times 0.08^\circ$).

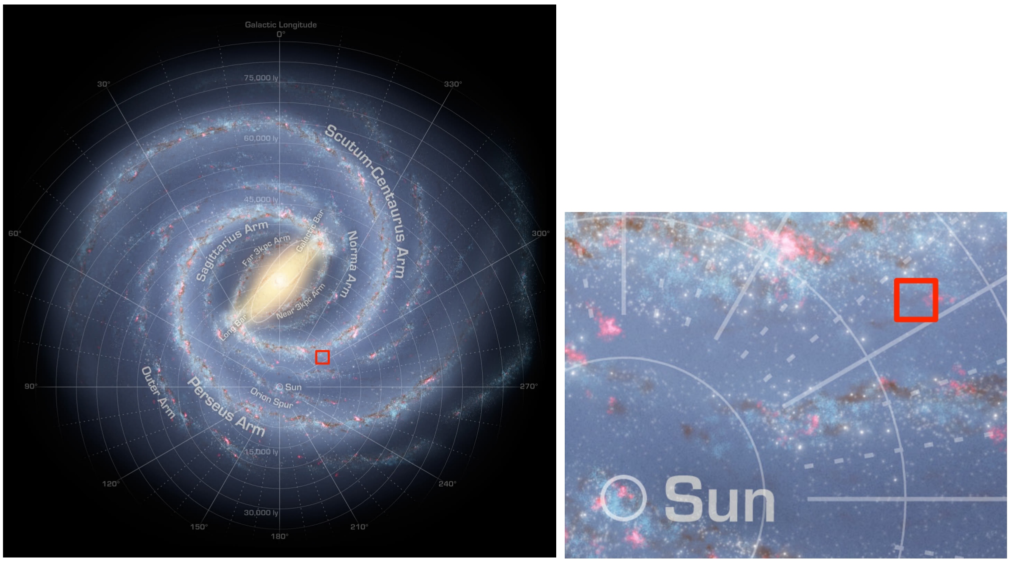

FIGURE 2.3: The location of G305 within the Milky Way is shown by a red box at l = 305° and a distance of 3.8 kpc from the sun.

2.4 Age

As has been demonstrated above Danks 1 and 2 are associated with the wider G305 complex and as the only optically visible clusters represent the most evolved state of stellar evolution in this region. Therefore, assuming star formation began soon after cloud formation, the age of these clusters represents the age of the complex as a whole.

An upper limit to the age of the complex can be inferred by the fact that there are no supernova remnants detected towards G305 and thus the age is expected to be less than 10 Myrs. In addition the lack of luminous red supergiants, which would have dominated the near-infrared output of Danks 1 and 2 if present (Davies et al., 2012), suggests an upper limit to the age of the cluster of ~ 4–5 Myr.

The age of the Danks 1 and 2 has been estimated by Davies et al. (2012) using three methods; analysis of their stellar populations, examining the MS turn-offs, and by studying the low-mass pre-MS population of each cluster. Accounting for the results of each of these methods the age of Danks 1 and 2 is found to be $1.5^{+1.5}_{-0.5}$ and $3.0^{+3.0}_{-1.0}$ Myr respectively. This suggests that Danks 1 may be younger than Danks 2, however the errors suggest that the two clusters may of formed at the same time.

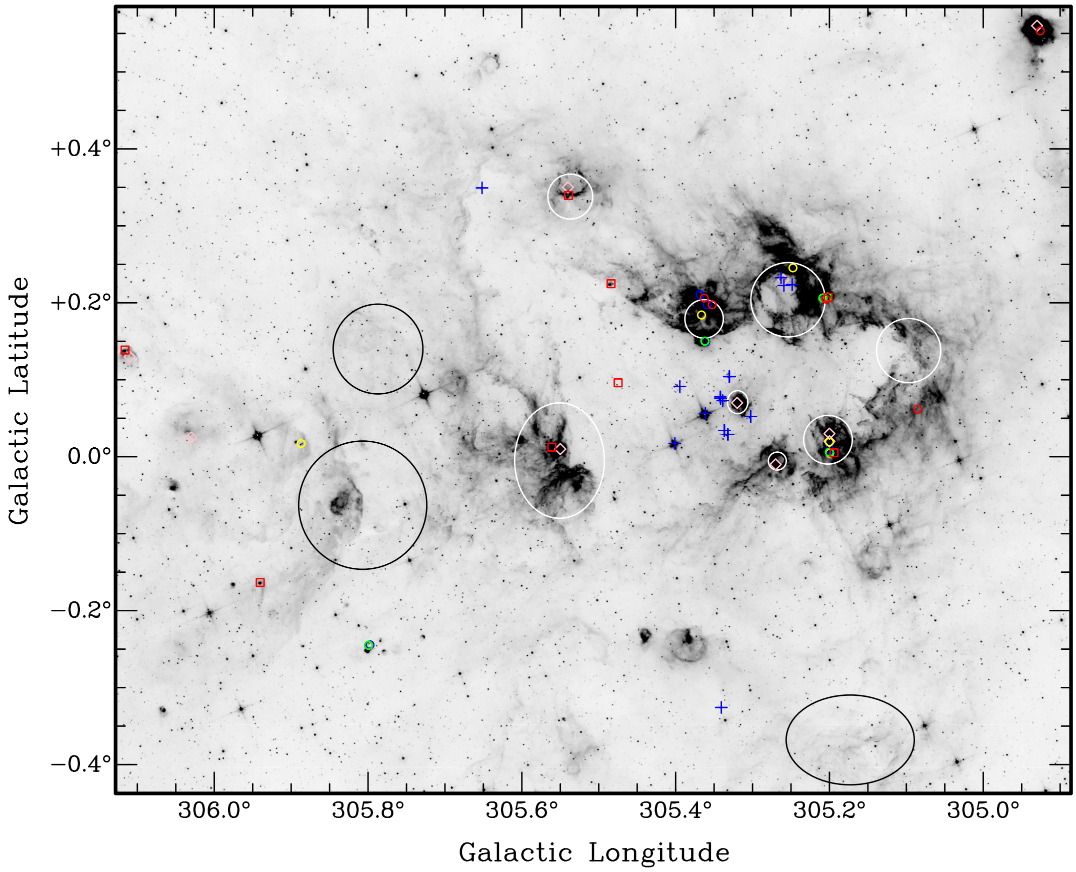

FIGURE 2.4: Current view of the massive stellar population and ongoing star formation towards G305 overlaid onto a Glimpse 5.8 μm image. Blue crosses highlight high-mass stars, masers are shown as circles; Methanol = yellow, H_2O = blue, OH = green. Thermal SiO emission is shown by red circles and pink diamonds indicate embedded infrared excess sources Dutra et al. (2003) and red boxes indicated RMS detected YSOs. Finally, for contrast black and white ellipses highlight the position and semi-schematic size of HII regions (Caswell & Haynes, 1987; Danks et al., 1984) detected towards G305.

2.5 Star formation in G305

In the following sub-sections an overview of the recent and ongoing star formation across the extent of G305 is given. To aid in the description a GLIMPSE 5.8 μm image of G305 is presented (Fig. 2.4) with known massive stars, HII regions and star formation tracers overlaid. The region is separated into four sub-regions (Fig. 2.2) using Danks 2 as a reference these are defined as (Galactic) North-East (NE), North-West (NW), South-West (SW) and East (E).

2.5.1 Recent star formation history

Massive star formation appears to have commenced in G305 within the last 6 Myr with the formation of Danks 2 and soon after Danks 1 towards the center of what was most likely the densest part of the molecular cloud at the time. Danks 1 and 2 contain a confirmed population of 20 massive stars (see Table 2 of Davies et al. 2012), however there exist at least two further populations of massive stars towards the region.

The first of these populations is found in the three massive stars discovered towards the centre of the HII region designated G305.254+0.204 (Table. A.1; L05-A1, A2 and A3) in the NW of the complex (Leistra et al., 2005). It has been postulated that these sources may be responsible for driving the expansion of the HII region. The second population is a diffuse group of at least eight WR stars (Table. A.1) found within the central cavity of G305 with projected distances from Danks 1 and 2 of $\sim$ 2–25 pc (MDM4 and MDM9). The origin of this diffuse population is unclear, they may have formed in-situ, however given their close proximity to Danks 1 and 2, apparent isolation from other stellar sources and the relatively young age of the clusters it is plausible that they are runaway stars (Mauerhan, Van Dyk & Morris, 2011; Baume, Carraro & Momany, 2009; Lundstrom & Stenholm, 1984). Studies of massive stars in the field (remote from any significant episode of star formation) show that $\sim$ 20–25% of O stars escape their natal star-forming regions via dynamical interactions (Moffat et al., 1998; Oey & Lamb, 2011). With an upper limit to ejection velocities of $\sim$ 10 km s^{-1} it would take $\sim$ 2.5 Myr for massive stars to reach a distance of 25 pc well within the age of the complex. Finally, early OB pre-MS stars are also suspected to be located in the ionised bubble designated PMN1308-6215 (G304.93+0.56) to the far NW of the region (Clark & Porter, 2004). These high-mass stars have been identified because they are optically visible, however there is also evidence of a considerable population of embedded high-mass stars.

HII regions in G305 betray the presence of a younger generation of massive stars. As shown in Fig. 2.1 there is a clumpy distribution of ionised gas that would suggest at least six HII regions are associated with G305. Systematic analysis of these HII regions is complicated by the low-resolution, differing beam sizes and wavelengths used in these prior studies. To give some idea of the distribution of HII regions and their relation to massive stars and ongoing star formation the sizes provided in the 6 cm survey of Caswell & Haynes (1987) and the 20 cm pointed observations of Danks et al. (1984) are utilised in Fig. 2.4. In addition to the central cavity G305 contains approximately eleven HII regions, six of which are located around the periphery of the central cavity. These HII regions indicate that there is a younger generation of massive stars that, unlike Danks 1 and 2, have not had sufficient time to completely clear their surroundings. Whilst the nature of the massive stars responsible for these HII regions remains unknown the integrated radio flux at 5 GHz is $\sim$ 200 Jy would require the presence of $>$ 30 "canonical" O7 V stars (Clark & Porter, 2004).

In total G305 contains a confirmed population of $\sim$ 30 massive stars the majority (20) of which lie within Danks 1 and 2. The ionising radiation and powerful winds of these massive stars has driven a cavity into the surrounding regions clearing away the natal molecular cloud in the vicinity of Danks 1 and 2 and potentially compressing gas and triggering a further generation of star formation at the cavity periphery. The distribution of massive stars suggests that star formation within G305 is multi-seeded, however the presence of star formation tracers around the periphery of the central cavity and the embedded HII regions would suggest that at least some of the star formation may have been triggered.

2.5.2 Ongoing star formation

In addition to the confirmed massive star population, G305 shows evidence of vigorous and ongoing star formation in the numerous H_2O, OH and methanol masers and embedded infrared sources found towards the region. Presented in the following section is the current view of ongoing star formation in G305.

As mentioned in Chapter 1 Section 1.5.3, certain masers have been found to preferentially form in the dense and heated environments that surround young forming stars. A literature search reveals 25 masers towards G305 (Table. A.2) including; five H_2O masers[1] (Caswell et al., 1989), nine methanol masers (Caswell, 2009), five OH masers (Caswell, 1998). We also note the location of highly excited shocked gas traced by five thermal SiO sources (Harju et al., 1998). The RMS survey (see Section 2.7.2) is used to identify sites of ongoing star formation. Searching the RMS database[2] reveals eight intermediate to high-mass YSOs towards G305 as well as sources confirming the HII regions reported in the previous section (Table. A.3). There are eight embedded infrared clusters (Dutra et al., 2003) distributed across G305. These clusters remain deeply embedded within a cocoon of dust and gas indicating that they are at an early stage of their evolution. In a study of the G305.2+0.2 region, Longmore et al. (2007b) identify 12 infrared excess sources and put forward the hypothesis that the G305.254+0.204 cluster may be responsible for triggering the formation of the infrared excess sources in this region.

The ongoing star formation indicated by these sources is occurring at a projected distance from the centre of the cavity of ∼ 2–42 pc. The closest of these is an embedded cluster (Dutra et al., 2003) to the east of Danks 2. However, since the three-dimensional geometry of the G305 complex is unknown this central "blob" could be at the near or far side of the complex. The furthest sign of ongoing star formation is in the apparently isolated bubble to the far NW (G304.93+0.56) at a projected distance from Danks 2 of 42 pc. The vast majority of ongoing star formation is located in the narrow (∼ 2 pc) photodissociation ring around the periphery of the central cavity at a projected distance between 7 and 17 pc. The star formation in this ring is concentrated towards the embedded HII regions and bright mid-infrared emission indicating that star formation is taking place in close proximity to massive stars still embedded in the molecular environment.

[1] The H_2O maser at 305.36 + 0.20 is at $-90\,\mathrm{km\,s^{-1}}$ and so not likely to be associated with the complex

[2] http://www.ast.leeds.ac.uk/RMS/

The oldest massive star population (Danks 1 and 2) is found towards the centre of the complex surrounded by a number of HII regions located on the borders of the central cavity. These embedded HII regions reveal a population of massive stars that are younger than Danks 1 and 2, and it is around these HII regions that we find ongoing star formation. The morphology of the region coupled with the nature and location of the ongoing star formation is highly suggestive of triggered star formation (Elmegreen & Lada, 1977; Elmegreen, 1998).

2.6 Motivation

G305 was chosen as the target of this multi-wavelength study for a number of reasons. Firstly, the ionising photon flux produced by high-mass stars in the Milky Way is concentrated within a small number of GMCs. In a study by Murray & Rahman (2010), the Wilkinson Microwave Anisotropy Probe (WMAP) was used to survey the Galaxy between 10 and 100 GHz and discovered that more than 50% of the ionising flux is contributed by only 18 star-forming regions. G305 is listed as the 15$^{\text{th}}$ brightest radio complex in the Milky Way (Murray & Rahman, 2010) and the ionising flux of the region is comparable to other well-known GMCs. The G305 complex is therefore representative of high-mass star-forming regions in the Galaxy. Secondly, previous observations reveal multiple epochs of star formation, which coupled with the mid-infrared and radio morphology is highly suggestive of triggering (Clark & Porter, 2004). For these reasons G305 is an excellent laboratory in which to study high-mass star formation and the impact of feedback on the evolution of GMCs.

There is a distinct lack of sensitive, high-resolution and uniform observations of the molecular and ionised environment of G305 and this hampers the investigation of the star-forming environment and the SFH. Previous observations of the molecular environment have been limited to the G305.2+0.2 region (Walsh & Burton, 2006; Walsh et al., 2007) whilst observations of the ionised environment are either global but low-resolution (Goss & Shaver, 1970) or high-resolution but low spatial sensitivity and limited to small areas (Walsh et al., 1998). As a result, we do not yet fully understand the relationship between the stars that have already formed in the central clusters and the ongoing (possibly triggered) star formation. The degree to which feedback from high-mass stars is inhibiting or enhancing star formation via destruction or compression of the molecular material is unknown but is a vital parameter required in models of galaxy formation and evolution (Hopkins, Quataert & Murray, 2011; Scannapieco et al., 2011).

2.7 Ancillary data

In recent years, a number of wide-area surveys at a range of wavelengths have become publicly available. Careful comparison between datasets can reveal a great deal about star formation and the environment of GMCs. The following section presents an overview of the ancillary data utilised in this study.

2.7.1 Galactic Legacy Infrared Mid-Plane Survey Extraordinaire

The GLIMPSE survey has used the InfraRed Array Camera (IRAC; Fazio & Hora 2004) on the *Spitzer* space telescope to survey the Galactic plane between $l = 65°$and $l = 295°$ and $b = \pm1°$ with an angular resolution of $\sim 2''$. The four IRAC bands at 3.6, 4.5, 5.8 and 8.0 µm trace different physical properties and so analysis of these provide a means to explore the nature of the mid-infrared emission processes in a wide variety of objects (Cohen et al., 2007). The 3.6 µm band is dominated by field stars, while an excess in the 4.5 µm band is thought to arise from shocked molecular hydrogen and CO band-heads, possibly indicating the presence of outflows (Cyganowski et al., 2008). The 5.8 and 8.0 µm IRAC bands are dominated by strong PAH features that are excited in the PDRs that lie in a thin shell of neutral gas located between an ionisation front and cold molecular gas (Leger & Puget, 1984). Figure. 2.2 presents a three-colour composite image utilising the 4.5, 5.8 and 8.0 µm IRAC bands, in blue, green and red respectively. The nature of the PAH emission mechanism identifies the main interaction layer between the ionised and molecular environment and therefore delineates the boundary between HII regions and the surrounding molecular gas. Throughout this thesis GLIMPSE images are used extensively primarily to define the overall structure of the region, provide a backdrop with which to compare the molecular and ionised environment and as a means of distinguishing the nature of radio continuum emission.

2.7.2 Red MSX Source Survey

The RMS survey[3] (Urquhart et al., 2008) aims to locate massive young stellar objects (MYSOs), and so highlight regions of ongoing intermediate to high-mass star formation. Objects with mid-infrared colours that match well-known MYSOs are identified through colour selection in the Midcourse Space Experiment (MSX) point source catalogue (PSC). The survey is limited by the resolution of MSX ($\sim 18''$) (Price et al., 2001) and contamination from many objects that have very similar colours to the very red MYSOs such as UC HII regions, compact planetary nebula,

[3]http://www.ast.leeds.ac.uk/RMS/

low-mass YSOs and evolved stars. However, the RMS team has carried out extensive multi-wavelength follow-up observations to determine the nature of these sources (Urquhart et al., 2007b,a, 2009, 2011) and therefore provides a reliable sample of young massive stars.

2.7.3 Methanol Multi Beam survey

The Methanol Multi Beam (MMB) survey is a Galactic wide survey sensitive enough (0.17 Jy) to detect all 6.7 GHz methanol masers in the Galaxy (Green et al., 2009, 2012; Caswell, 2009) with a positional accuracy of $0.1''$. The survey makes use of the Parkes 64 m radio telescope in the Southern hemisphere using a multibeam receiver system. All detected masers are later positioned to sub-arcsecond precision by interferometric observations. The MMB survey detects 17 methanol masers towards G305 (see Table 2 of Green et al. 2012) and will be presented and discussed later in this work.

Chapter 3

The Molecular Environment : low and high-density gas and H_2O masers

This chapter is based in part on the article, Hindson et al. (2010), published in "Monthly Notices of the Astronomical Society".

3.1 Motivation

Chapter 2 makes it clear that the G305 complex is undergoing vigorous star formation that is concentrated around the rim of the central cavity. The mid-infrared morphology of the complex (Fig. 2.2) suggests that this star formation is occurring in close proximity to PDRs, which indicates that star formation is embedded within, or on the borders of, molecular material (Clark & Porter, 2004). This leads to the following questions:

- What are the properties of the molecular environment in G305?
- What is the reservoir for future star formation?
- How does the ongoing and recent star formation relate to the molecular material?

Answering such questions is vital to our understanding of how massive stars form, affect the natal molecular environment and drive the evolution of GMCs. Addressing these questions requires wide-area observations of both the diffuse and dense molecular environment. We therefore set out to characterise the molecular environment of G305 with two observing programs at 3 and 12 mm (22 and 115 GHz respectively, Table 3.1) of CO and NH_3 molecular emission respectively using the Mopra radio telescope.

FIGURE 3.1: The Mopra telescope.

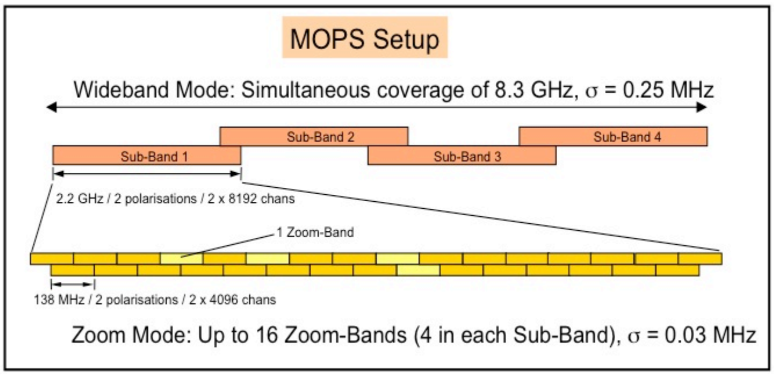

FIGURE 3.2: The arrangement of the four bands that make up the 8 GHz bandwidth of MOPS and available zoom windows.

Frequency Band	16–27 GHz (12 mm)	76–117 GHz (3 mm)
Central frequency	24 GHz	115 GHz
Beam width (FWHM)	$\sim 119''$	$\sim 34''$
Velocity resolution	0.4 km s^{-1}	0.1 km s^{-1}
Average T_{sys}	~ 70 K	~ 600 K
Antenna efficiency	~ 0.6	~ 0.4

TABLE 3.1: Properties of the two Mopra receivers used in this study.

3.2 Mopra telescope

The single-dish Mopra telescope[1] (Fig. 3.1) is a 22 m antenna located 26 km outside the town of Coonabarrabran in New South Wales at an elevation of 866 metres above sea level and at a latitude of 31 degrees South.

At the heart of Mopra is the University of New South Wales (UNSW) Mopra Spectrometer (MOPS), which consists of four 2.2 GHz wide bands that overlap slightly to provide 8 GHz of continuous bandwidth (Fig. 3.2). The narrow band or "zoom" mode of MOPS was used in these observations and provides four intermediate frequencies (IFs) with four zoom "windows"

[1]Mopra is operated by CSIROs Astronomy and Space Science division.

in each IF allowing 16 separate bands to be observed simultaneously. Each zoom window has a bandwidth of 137.5 MHz over 4096 channels resulting in a channel spacing of 34 kHz.

These observations took advantage of Mopra's on-the-fly (OTF) observing mode. In this mode the telescope beam is scanned along a line on the sky at a constant rate whilst recording spectra every few seconds. This results in a large number of scans that, when combined in a mosaic, effectively map a large area. In order to ensure Nyquist sampling the scans must be separated by less than half a beam width between each scan row and cycle. Two averaged scans in orthogonal directions are required to remove striping caused by the sensitivity varying within each scan row and also results in an improvement in the signal-to-noise (S/N).

The calibration of the telescope dependent antenna temperature scale ($T_{\rm A}^*$) is achieved by measuring the system temperature ($T_{\rm sys}$) at regular intervals. The system temperature is the contribution to the received signal from the microwave and Galactic background and atmospheric emission, spill over and scattering losses and noise introduced by the telescope feed and receiver. These factors are calibrated by observing an emission free reference position before each scan row and measuring the level of attenuation due to the atmosphere using the "chopper wheel" technique. This involves alternatively introducing and removing a blackbody emitter of known physical properties into the signal path. Comparison between the measured voltage induced by the blackbody and emission free reference position provides the necessary scaling of the measured flux to obtain $T_{\rm A}^*$.

The temperature measured by Mopra may vary due to a number of factors. Observations of standards such as Orion allow the stability of the Mopra system over time and through different observing conditions to be assessed. The H_2O Southern Galactic Plane Survey (HOPS; Walsh et al. 2011) found the integrated intensities of H69α and H62α observations suggest an upper limit to the absolute integrated intensity error for Mopra of $< 30\%$ (Walsh et al., 2011). However, the relative intensity scale of different spectral lines measured using simultaneous observations is likely to be no worse than 5% (Walsh et al., 2011). This suggests that the temperature scale introduces little error into the individual NH_3 and CO studies but care should be taken when comparing the two.

3.3 Observations

Presented below is the setup of the two observations that underpin this study of the global molecular environment of G305. The first of these observations was designed to probe the dense molecular environment traced by the NH_3 inversion transition in the rotational-inversion levels $(J, K) = (1, 1)$, (2,2) and (3,3) at $\sim$ 24 GHz and star formation traced by H_2O (6–5) masers at $\sim$ 22 GHz. The second set of observations is designed to study the lower density molecular

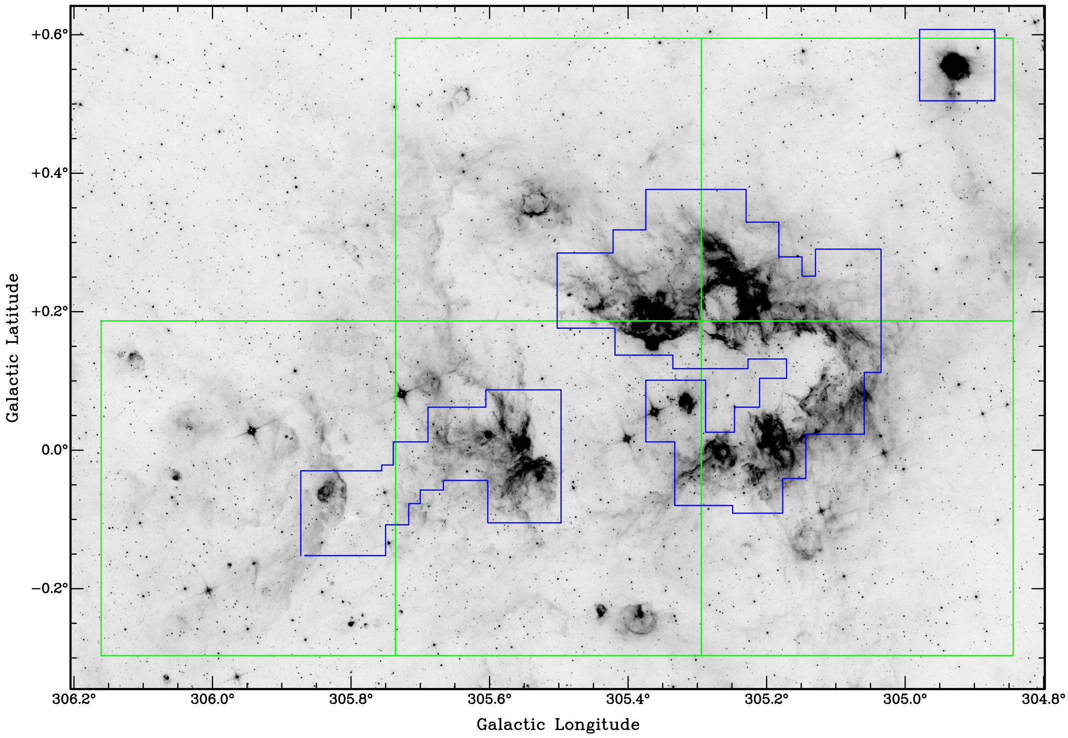

FIGURE 3.3: The area covered by the NH_3 and CO molecular observing programs in green and blue respectively.

environment and kinematics through the ^{12}CO, ^{13}CO and C^{18}O J = (1–0) rotational transition at a frequency of ~ 110–115 GHz.

3.3.1 NH_3 and H_2O maser observations

The NH_3 molecule is an excellent dense gas and temperature probe because it has a critical density of ~ 10^4 cm^{-3} (Stahler, S. W. & Palla, F., 2005) and the emission spectrum exhibits hyperfine structure. This allows the optical depth to be derived from a single transition (Ho & Townes, 1983) and comparison with higher J, K inversion transitions allows the rotational and kinetic temperature to be estimated leading to column densities and mass. NH_3 emission is most often associated with cool dense clouds and hot molecular cores with temperatures of < 10 to ~ 30 K (Molinari et al., 1996; Tieftrunk et al., 1998; Urquhart et al., 2011) and > 100 K (Cesaroni et al., 1994) respectively. In these cool dense clouds the temperature can be too low for more common gas tracers like CO to be released into the gas phase (Bergin et al., 2006; Aikawa et al., 2001).

The 16 available zoom windows in MOPS were selected to match those in HOPS[2]. The lines that were detected above three times the noise level (3σ) in these observations are summarised

[2]See Table 1 in Walsh et al. 2011 for the full list of targeted lines.

Line	Frequency (GHz)	FWHM ($''$)
H_2O (6–5)	22.235	144
NH_3 (1,1)	23.694	136
NH_3 (2,2)	23.722	136
NH_3 (3,3)	23.870	136
HC_3N (3,2)	27.294	120
H69α	19.951	164
CH_3OH (3_2 - 3_1)	24.928	131
CH_3OH (4_2 - 4_1)	24.933	131
CH_3OH (2_2 - 2_1)	24.934	131
CH_3OH (6_2 - 6_1)	24.959	131
CH_3OH (7_2 - 7_1)	25.018	131

Table 3.2: Molecular transitions, corresponding frequencies, and beam sizes of the positive detections in the NH_3 observations.

in Table 3.2. This work focuses on the analysis of the NH_3 and H_2O maser detections and postpones the analysis of the remaining detections (H69α, CH_3OH and HC_3N) to future work.

The NH_3 observations consisted of five sub-maps each covering an area of $28' \times 28'$ (Fig. 3.3) with a $3'$ overlap between adjacent sub-maps. The sub-maps were sampled in OTF mode with $51''$ spacing between each scan row to give Nyquist sampling at the highest frequency (27.4 GHz) and oversample at lower frequencies. The fastest scan rate of two seconds per point was used and an off source position was observed periodically to remove sky emission. A single map took approximately two hours to complete in one scan direction, and four hours with two orthogonal (Galactic latitude & longitude) co-added scans. In total five complete co-added scans were obtained in 50 hours of observing time during a number of nights in April and May of 2009. The weather conditions were changeable over this period with water vapour levels between 15 and 25 mm and system temperatures of $\sim$ 100 K with a variation in $T_{\rm sys}$ of no more than 20% during the course of any particular map. During times of dense cloud cover and rain observations were halted as these conditions caused system temperatures > 120 K, which introduced a large amount of noise into maps.

3.3.2 CO observations

As has been mentioned, CO is the next most abundant molecule after H_2 and has an effective critical density of $\sim 10^2\,\mathrm{cm}^{-3}$ (Evans, 1999) making it one of the best tracers of the global distribution of molecular gas. The higher frequency at which rotational emission from CO is generated results in an increased spatial and velocity resolution compared to NH_3 and allows the study of the kinematics and sub-structure of the molecular gas associated with G305.

Line (J = 1–0)	Frequency (GHz)	FWHW (″)
$C^{18}O$	109.738	36 ± 3
^{13}CO	110.221	36 ± 3
^{12}CO	115.258	33 ± 2

Table 3.3: Molecular transitions detected in the CO observations, central frequency and the size of the Mopra beam at the given frequency.

The MOPS zoom bands were selected to observe three CO isotopologues; ^{12}CO, ^{13}CO and $C^{18}O$ in the J = 1–0 rotational transition (Table 3.3). The remaining zoom windows were set to the rest frequency of lines of interest such as HC_3N (12-11), CH_3CN (6–5) and $C^{17}O$ (1–0) but no significant emission (> 3σ) was detected.

The mapping strategy was based upon wide-area, low sensitivity ^{12}CO (J =1–0) Mopra observations taken during the test phase of an increased OTF mapping speed (Fig. C.1; Urquhart priv. comm.). Using these observations as a pathfinder a number of sub-maps, ranging from 3′ to 7′ squares were centred on the prominent ^{12}CO emission (Fig. 3.3). Each of these sub-maps overlaps its neighbour by 56″ and each scan row is separated by 9″ to ensure Nyquist sampling at the highest frequency (115.258 GHz). Using the fastest scan rate available of two seconds per field and including calibration and other overheads resulted in two orthogonal maps taking between two and four hours. The observations were obtained during two separate observing runs in September 2010 and 2011. Changeable weather conditions resulted in water vapour between 15 and 25 mm and system temperatures (T_{sys}) between ∼ 250–350 K for ^{13}CO and $C^{18}O$ and ∼ 500–600 K for ^{12}CO. Antenna pointing checks performed every two hours showed that the average pointing accuracy was better than 10″ rms. During the 2011 observing run there were a number of high wind warnings and the telescope had to be stowed on several occasions for safety reasons. Poor weather and limited observing time meant that we were unable to observe the whole G305 region (Fig. 3.3).

3.4 Data reduction

The reduction of Mopra data is fairly straight forward, two packages are provided called LIVEDATA and GRIDZILLA, both are AIPS++ packages written by Mark Calabretta[3] for the Parkes radio telescope and adapted for Mopra. Raw data files are first processed in LIVEDATA, which applies user specified flagging to bad channels followed by a bandpass calibration for each scan row using the off-source reference position. This is followed by fitting a user specified polynomial to the spectral baseline using line-free channels and applying a position and time stamp

[3]http://www.atnf.csiro.au/computing/software/livedata.html

to each spectrum. The data is then passed to GRIDZILLA, which calculates the pixel value from the spectral values of multiple files using the weighted mean estimation. GRIDZILLA then resamples the data onto a common pixel scale (l, b and v) using the position and time stamp written by LIVEDATA and performs interpolation in velocity space to convert measured topocentric frequency channels into LSR velocity.

Data from Mopra is calibrated in temperature units (K) on the antenna temperature (T_A^*) scale, i.e. corrected for the system temperature. It is desirable to convert this onto a telescope-independent main beam brightness temperature scale ($T_{\rm mb}$), which is also corrected for forward scattering[4]. The appropriate frequency dependent scaling is determined through observations of planets and masers for which the properties are well-known. This allows the beam size, shape and efficiency ($\eta_{\rm mb}$) to be characterised. The corrected main beam brightness temperature is then given by $T_{\rm mb} = T_A^*/\eta_{\rm mb}$. The beam efficiency of Mopra between 17 and 49 GHz has been characterised by Urquhart et al. (2010), interpolation within Table 3 therein gives the NH_3 (1,1), (2,2) and (3,3) efficiency of $\eta_{\rm mb} = 0.57$. The antenna temperature may be converted into Jy using the Jy K^{-1} conversion factor, which for H_2O masers at 22.2 GHz is 12.49. The Mopra beam efficiency between 86–115 GHz was characterised by Ladd et al. (2005) and for CO (J =1–0) observations the main beam efficiency is $\eta_{\rm mb} = 0.42$.

The raw data files from the observations were first read into LIVEDATA where known radio frequency interference (RFI) and first and last hundred channels are removed and the bandpass and appropriate flux scaling is applied. The data files were then processed in GRIDZILLA where the data is resampled using a pixel size that samples the beam by three pixels. A Gaussian smoothing kernel equal to the beam size was then applied to produce maps with minimal smoothing. The sensitivity in the NH_3 and H_2O maps is $\sigma_{T_A^*} \approx 0.07$ K per 0.42 km s^{-1} channel approximately twice as sensitive as the HOPS survey (Walsh et al., 2011). The ^{12}CO, ^{13}CO, and C^{18}O maps have a sensitivity of approximately 0.27, 0.19 and 0.15 K per 0.09 km s^{-1} channel respectively. The RMS noise across these maps varies by $\sim$ 10% due to the different atmospheric conditions, elevations and receiver performance during observations.

3.5 NH_3 results and analysis

3.5.1 Clump identification

The molecular environment of GMCs is inherently complex and clumpy and so to decompose molecular emission into discrete clumps by eye would be both impractical and somewhat subjective. To address this problem a number of "clump finding" algorithms have been developed

[4]The measured $T_{\rm mb}$ of a source would equal to the true brightness temperature if the source just filled the main beam.

to automate the assigning of emission into discrete clumps based on user controlled inputs. This makes the clump finding process objective, repeatable and removes problems that arise when classifying by eye. Clump finding is performed using CUPID, available as part of the STARLINK project software[5], which is computationally efficient and provides a range of clump finding algorithms.

The output of clump finding is an image with dimensions identical to the input image but with the physical pixel values reassigned to either integer values corresponding to the identified clump or a blank value. This provides a mask with which to extract the properties of the emission assigned to clumps such as positions, sizes and brightness. It is important to realise that parameters extracted using clump finding techniques have been determined from emission that has been altered by user-defined criteria. Therefore, any analysis must take into account selection effects and bias that may be introduced (Schneider & Brooks, 2004; Curtis & Richer, 2010). Caution should be taken when deriving properties based on the results of clump finding and particularly when comparing catalogue results and trends based on physical properties where the data has been analysed with different techniques. Especially when the original data format is position-position (PP) data as opposed to position-position-velocity (PPV) (Smith, Clark & Bonnell, 2008), or when the comparison is between molecular line and continuum data (Pineda, Rosolowsky & Goodman, 2009).

3.5.2 NH_3 clump identification

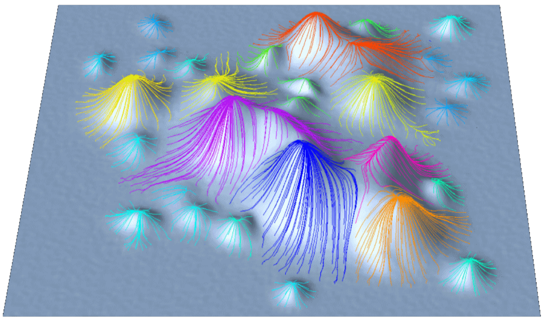

FIGURE 3.4: Representation of how the FELLWALKER algorithm assigns clumps (Berry et al., 2007).

The resolution of the NH_3 observations is $\sim 2'$, which corresponds to a physical radius at 3.8 kpc of ~ 1.3 pc. We are therefore limited to resolving only the general distribution of NH_3 emission on the scale of molecular clouds. In addition, the hyperfine nature of the NH_3 spectral profile results in emission from satellite components being detected at a wide range of velocities (v) and so the velocity information is of little practical use for three-dimensional source extraction.

[5] www.starlink.rl.ac.uk/star/docs/sun255.htx/sun255.html

These factors led to the decision to apply a two-dimensional clump finding algorithm to a NH_3 (1,1) cube that was collapsed between the velocity range of emission (-65 to -10 km s^{-1} see Section 3.5.3), using a peak intensity algorithm[6], producing a two-dimensional image with a noise of $\sigma = 0.06$ K (Fig. 3.5).

The FELLWALKER algorithm (Fig. 3.4), developed by David Berry (Berry et al., 2007), was chosen to automatically decompose emission in the peak intensity NH_3 (1,1) map into discrete clumps. FELLWALKER is a simple and robust algorithm that works by finding the paths of steepest gradient from each pixel in the image (called a "walk"). The main parameters[7] chosen are given in the following description. Starting with the first pixel in the image that is above $Noise = 2\sigma$ each of the surrounding pixels in l and b are inspected to locate the pixel with the highest ascending gradient. This process continues until a peak is located (i.e. a pixel surrounded by flat or descending gradients). An area of $MaxJump = 4$ pixels is then checked to ensure there are no other peaks in the area. Any initial section to a walk leading to a peak that has an average gradient (measured over 4 steps) less than $FlatSlope = \sigma$ will not be included in the clump. Pixels leading to a peak are assigned an arbitrary integer to represent their connection along a path. If at any point a walk reaches a pixel that has already been assigned to a clump all pixels on the walk are assigned the same clump value. Otherwise, the walk continues until there are no higher pixels in the local area (Fig. 3.4). If the gradient between any two nearby peaks is less $MinDip = 3\sigma$ they are merged.

The distribution of NH_3 emission in two dimensions is fairly simple, however FELLWALKER is not as widely used as other clump finding algorithms and so a number of tests were performed using well-known algorithms such as GAUSSCLUMPS and CLUMPFIND as well as manual aperture photometry to check for consistency. The FELLWALKER algorithm gives very similar results to GAUSSCLUMPS, CLUMPFIND and manual aperture photometry with a significantly higher robustness to varying input parameters (e.g. for a discussion of the effect of varying the step size in CLUMPFIND see Pineda, Rosolowsky & Goodman 2009).

3.5.3 NH_3 results

A total of 15 NH_3 (1,1) clumps are identified, 12 of which are associated with (2,2) emission and a further 6 exhibit (3,3) emission (Tables 3.4, 3.5, 3.6 and Fig. 3.5). NH_3 emission is found between -65.0 and -10.0 km s^{-1} with the peak emission occurring at -36.6 km s^{-1}. This broad velocity range is due to the hyperfine nature of the NH_3 spectral profile and so does not reflect the physical velocity range of the complex. At this point it is important to consider the beam filling factor, which is the fraction of the primary beam that is filled by emission and its impact on these observations. The beam filling factor is unknown but likely to be significantly less than

[6] Moment -2: the peak intensity using a three-point quadratic fit
[7] http://www.starlink.rl.ac.uk/docs/sun255.htx/node25.html

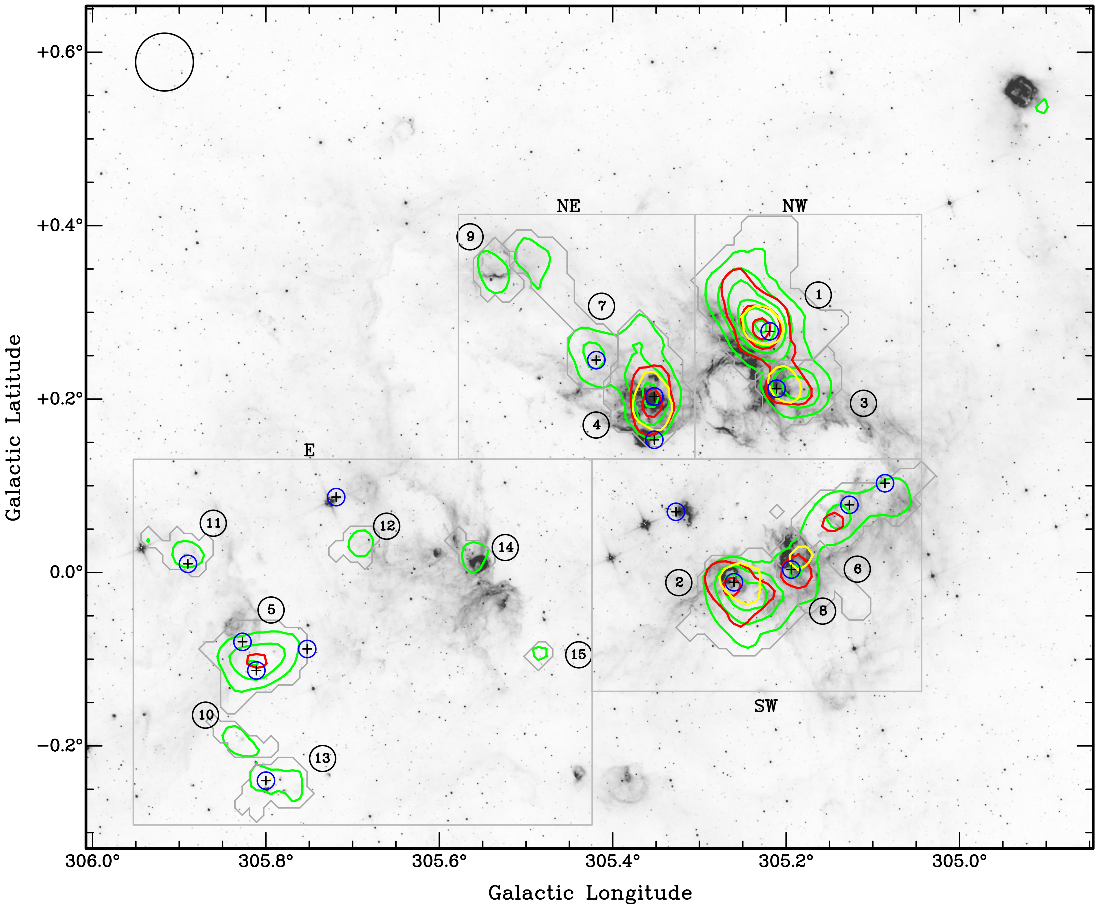

FIGURE 3.5: Contour map of the peak temperature NH_3 (1,1), (2,2) and (3,3) emission towards G305 in green, red and yellow contours respectively. Emission is over-plotted onto a GLIMPSE 5.8 µm (greyscale) image. Detected H_2O masers are shown by blue circles centered on black crosses. The boundaries defined by FELLWALKER are shown by a grey outline and numbered according to Table 3.4. All contours begin at 0.15 K and increment by 0.1 K, the noise in the map is 0.06 K. The Mopra beam at 23.694 GHz (136″) is presented in the top left. Following the nomenclature presented in Chapter 2 the complex is separated into four sub-regions with grey boxes.

one[8] in the NH_3 observations presented here due to the large Mopra primary beam at 23 GHz. For beam filling factors of less than one emission will be smeared out by the primary beam shape (beam smearing). This blends discrete emission features within the beam area together and can cause emission features to drop below our detection threshold. The beam filling factor is discussed further in Section 3.7.2.

[8]The beam filling factor is assumed to be unity in the detection equation (Eq. B.64).

Region	Clump Number	Peak Galactic (l)	Peak Galactic (b)	V_{LSR} (km s^{-1})	ΔV (km s^{-1})	R (pc)	Peak T_{mb}(1,1) (K)	Avg T_{mb}(1,1) (K)
NW	1	305.23	0.29	−40.4	3.8	5.1	1.21	0.33
	3	305.19	0.21	−42.1	4.6	2.6	0.56	0.22
NE	4	305.36	0.20	−38.8	5.6	3.8	0.55	0.22
	7	305.42	0.25	−39.8	3.1	3.7	0.46	0.19
	9	305.54	0.34	−36.4	4.8	1.7	0.32	0.17
SW	2	305.26	−0.02	−32.3	4.9	3.7	0.74	0.28
	8	305.19	0.01	−34.0	7.1	2.6	0.43	0.15
	6	305.14	0.06	−37.4	3.4	3.5	0.45	0.21
E	5	305.82	−0.11	−42.7	3.0	3.0	0.60	0.22
	10	305.83	−0.19	−34.7	3.5	1.6	0.28	0.12
	11	305.89	0.02	−35.1	3.2	2.0	0.27	0.16
	12	305.69	0.04	−37.4	1.7	1.5	0.34	0.18
	13	305.77	−0.25	−32.3	4.1	2.0	0.34	0.14
	14	305.56	0.02	−40.4	3.9	1.9	0.34	0.16
	15	305.48	−0.10	−39.3	2.6	1.5	0.31	0.19

TABLE 3.4: NH_3 (1,1) clump properties, showing central position, velocity, radius, peak main beam temperature and clump averaged main beam temperature. These values are taken from the spectra averaged over the NH_3 (1,1) clump region defined by FELLWALKER.

Region	Clump Number	Peak Galactic (l)	Peak Galactic (b)	V_{LSR} (km s^{-1})	ΔV (km s^{-1})	R (pc)	Peak T_{mb}(2,2) (K)	Avg T_{mb}(2,2) (K)
NW	1	305.23	0.28	−39.9	3.8	3.2	0.66	0.17
	3	305.20	0.21	−41.6	6.2	2.2	0.32	0.14
NE	4	305.36	0.19	−38.6	6.2	2.3	0.34	0.14
	7	305.42	0.25	−39.2	2.9	< 1.3	0.39	0.09
	9	305.49	0.35	−36.3	6.3	< 1.3	0.30	0.07
SW	2	305.26	−0.02	−32.1	5.0	2.6	0.46	0.14
	8	305.19	0.00	−33.5	6.3	1.5	0.31	0.10
	6	305.15	0.03	−37.1	3.7	< 1.3	0.45	0.10
E	5	305.84	−0.07	−41.7	2.5	< 1.3	0.33	0.08
	12	305.69	0.06	−37.7	3.2	< 1.3	0.23	0.07
	13	305.89	−0.25	−32.3	5.1	< 1.3	0.25	0.07
	14	305.57	0.03	−39.2	4.4	< 1.3	0.26	0.08

TABLE 3.5: NH_3 (2,2) clump properties, showing central position, velocity, radius, peak main beam temperature and clump averaged main beam temperature, these values are taken from the NH_3 (2,2) spectra averaged over the NH_3 (1,1) clump region defined by FELLWALKER.

Region	Clump Number	Peak Galactic (l)	Peak Galactic (b)	V_{LSR} (km s^{-1})	ΔV (km s^{-1})	R (pc)	Peak T_{mb}(3,3) (K)	Avg T_{mb}(3,3) (K)
NW	1	305.22	0.28	−40.2	6.3	2.9	0.42	0.20
	3	305.20	0.21	−42.0	8.0	1.9	0.36	0.20
NE	4	305.35	0.20	−38.6	7.5	2.2	0.36	0.20
SW	2	305.25	−0.02	−32.2	6.1	2.2	0.42	0.15
	8	305.19	0.00	−33.6	9.4	1.4	0.23	0.08
E	5	305.81	−0.1	−41.9	2.0	< 1.3	0.28	0.14

TABLE 3.6: NH_3 (3,3) clump properties, showing central position, velocity, radius, peak main beam temperature and clump averaged main beam temperature. Note that these NH_3 (3,3) clump values are averaged over the NH_3 (1,1) emission area as defined by FELLWALKER.

3.5.4 NH_3 clump spectra

The NH_3 (1,1), (2,2) and (3,3) spectra presented in Fig. 3.6 and 3.7 have been averaged over the clump area defined by FELLWALKER (Fig. 3.5) and Hanning smoothed to improve the S/N to ~ 0.01 K per ~ 0.8 km s^{-1} channel.

The NH_3 (1,1) hyperfine spectral profiles are clearly resolved and were fitted with multiple Gaussians using the Interactive Data Language (IDL) function CURVEFIT. The NH_3 (2,2) and (3,3) spectra have insufficient S/N to resolve the hyperfine profile and so single Gaussians were fitted using the IDL function GAUSSFIT. The fitting process is only performed if the peak emission is $> 3\sigma$, leaving only NH_3 Clumps 10, 11 and 15 with no associated (2,2) emission (Fig. 3.6). The GAUSSFIT function computes a non-linear least-squares fit to the data whilst the CURVEFIT function uses a gradient-expansion algorithm to compute a non-linear least squares fit to a user-supplied function with an arbitrary number of parameters. Iterations are performed until the χ^2 factor changes by a specified amount, or until a maximum number of iterations have been performed. To fit the NH_3 hyperfine profile it is assumed that all the hyperfine components have equal excitation temperatures and the line widths and separations are identical to laboratory values (Ho & Townes, 1983). The properties extracted from these fits to the clump averaged spectral profiles are presented in Tables 3.4, 3.5 and 3.6.

The NH_3 main line widths range from 1.7 km s^{-1} to 10.0 km s^{-1}. The thermal part of the line width (Eq. B.20) accounts for only 0.28 km s^{-1} (for $T_{\rm kin}$ = 30 K) so it is valid to assume the line widths are largely dominated by non-thermal turbulent motion. It can be clearly seen that several spectra exhibit blended main line and first satellite lines (e.g. Clumps 2, 4 and 8), this is most likely caused by emission from several unresolved clumps with differing velocities along the same line of sight. The NH_3 (3,3) line widths are found to be wider than the lower transitions for all clumps with the exception of NH_3 Clump 5, which may suggest they are within a more turbulent medium.

3.5.5 H_2O masers

Sixteen H_2O masers were detected towards G305 (Table 3.7, Fig. 3.5) and their peak spectra are presented in Fig. C.2. Six of these H_2O masers are new detections that have not been reported in the literature. It is important to note that due to the large size of the Mopra beam at 22 GHz (~ 2′) the positional accuracy is limited, however because the masers are so bright the positional accuracy is most likely between 20″ and 60″ (e.g. Walsh et al. 2011). high-resolution follow up observations are currently being obtained by the HOPS survey (Walsh et al., 2008) that will accurately determine the locations to within a few arc-seconds. It is interesting to note that Walsh et al. (2008) report the detection of thirteen H_2O masers towards G305, two of which at

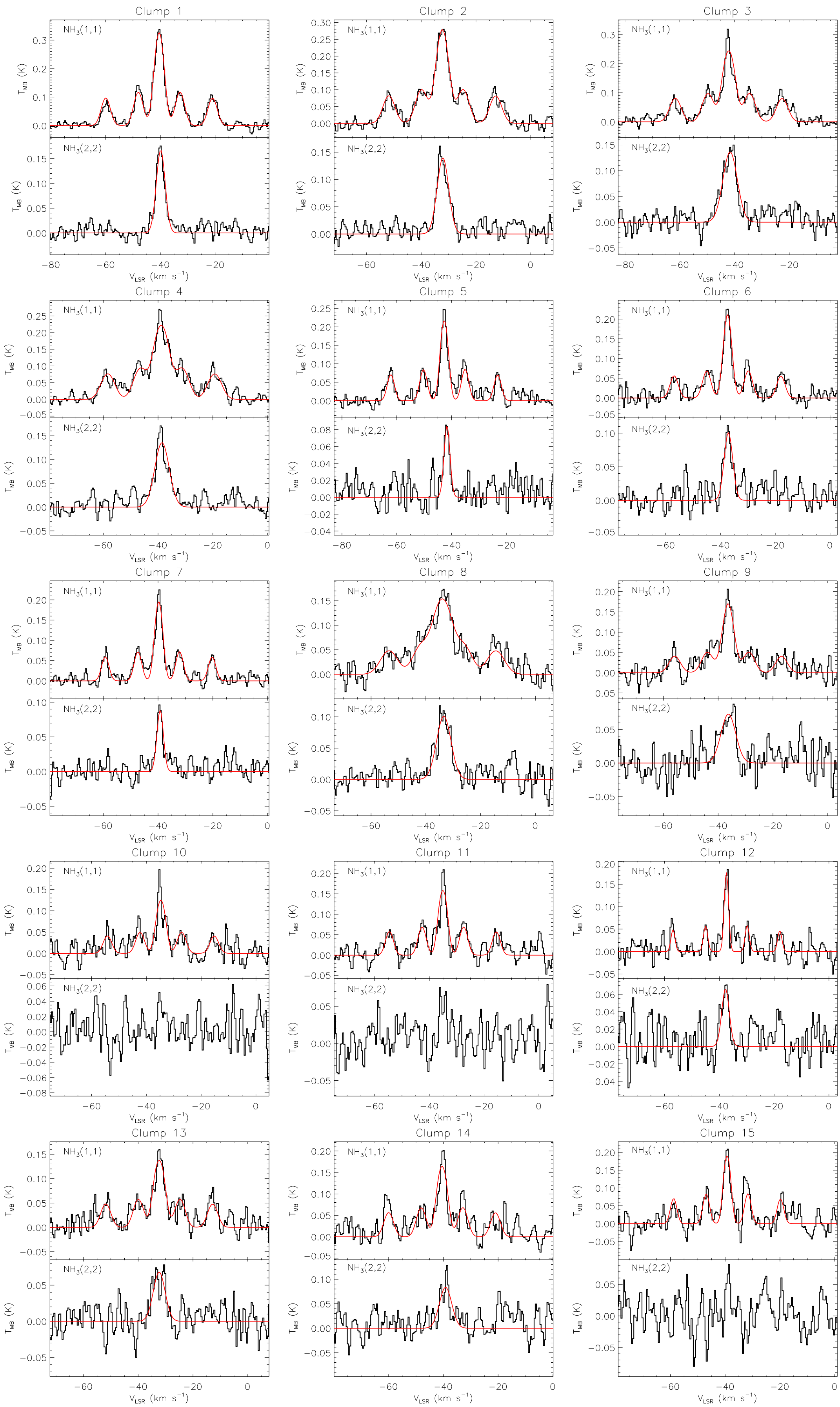

FIGURE 3.6: Clump averaged spectra of the 15 NH_3 clumps towards G305. Clump spectra have been averaged over the NH_3 (1,1) clump area defined by FELLWALKER and Hanning smoothed to provide a sensitivity of ~ 0.01 K per ~ 0.8 km s^{-1} channel. Hyperfine fitting is applied to the (1,1) emission and Gaussian fitting to the (2,2), shown as red over plots.

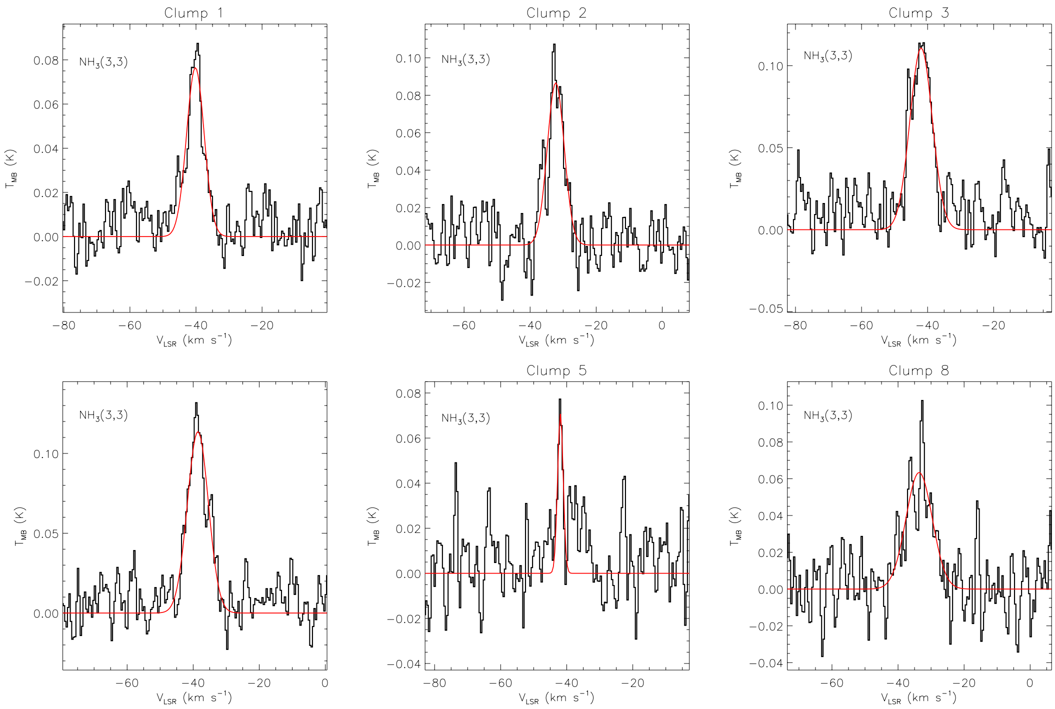

FIGURE 3.7: Source averaged spectra of the 6 NH_3 (3,3) clumps towards G305. Clump spectra have been averaged over the NH_3 (1,1) emission area defined by FELLWALKER, spectra have been Hanning smoothed to provide a sensitivity of ~ 0.01 K per ~ 0.8 km s^{-1} channel. Gaussian fitting is applied, shown as red over plots.

l = 305.55, b = −0.02 and l = 305.85, b = +0.07 are not detected in the observations presented here. In addition, the reported peak flux densities of H_2O masers detected in both studies do not match. This is a testament to the extreme variability of H_2O masers, e.g. Felli et al. (2007).

H_2O maser emission is detected across a broad velocity range between −120.8 and −10.4 km s^{-1} with the peak intensity varying between 2.4 and 1087.8 Jy, characteristic features of H_2O maser emission (Breen et al., 2007). The peak H_2O maser velocities match the velocity of the NH_3 emission, suggesting that they are associated with the molecular environment of G305, except for maser 12, which has a peak velocity of −97.6 km s^{-1}.

3.5.6 NH_3 analysis

The NH_3 clump-averaged spectra (Fig. 3.6) are used to derive the following average physical properties (Table 3.8). Before going further it is important to mention the beam filling factor, describes the fraction of the beam that contains emission, and the impact of beam dilution on the NH_3 analysis. The large Mopra beam at 23 GHz (2.3′) means that any emission that is smaller than the beam will be beam diluted that is smeared out over the area of the beam. This results in emission appearing

Region	Maser Number	Peak Galactic (l)	Peak Galactic (b)	V_{LSR} Peak (km s^{-1})	Velocity Range (km s^{-1})	Peak Flux (Jy)
NW	1*	305.22	0.28	−34.0	−37.7, −33.1	9.1
	4	305.21	0.21	−36.8	−44.5, −15.9	256.0
NE	2*	305.41	0.25	−32.1	−76.3, −32.2	6.6
	3	305.35	0.20	−30.9	−87.6, −18.1	65.8
	5	305.35	0.15	−32.7	−39.9, −20.4	303.6
SW	8	305.33	0.07	−42.7	−61.3, −26.8	225.2
	9*	305.09	0.10	−48.6	−50.1, −46.6	4.6
	10	305.13	0.08	−35.9	−34.9, −34.5	6.6
	11	305.20	0.00	−36.3	−36.8, −24.5	12.5
	16	305.26	−0.10	−23.1	−22.0, −22.5,	4.1
E	6	305.72	0.09	−39.9	−41.8, −38.6	8.8
	7	305.89	0.03	−24.5	−36.8, −22.2	44.8
	12*	305.83	−0.08	−97.6	−120.8, −85.4	13.5
	13*	305.75	−0.08	−45.8	−45.4, −43.6	6.9
	14*	305.81	−0.11	−37.7	−38.6, −35.8	12.9
	15	305.80	−0.24	−25.4	−44.5, −10.4	1123.2

Table 3.7: H_2O maser positions, peak velocity, velocity range and peak flux. Asterisks above the maser number show new detections over those identified by Walsh et al. (2008).

3.5.6.1 Size

The physical size of the clumps found in both CO and NH_3 observations are determined in the following way. First the area is determined by counting the number of pixels within the maximum extent in l and b of each discrete region of emission defined by clump finding. The angular size of each pixel ($9''$ and $30''$ for ^{13}CO and NH_3 respectively) and distance to G305 is known (3.8 kpc) so the physical area of each pixel can be derived (0.03 pc^2 and 0.3 pc^2 respectively). It is then a simple matter of multiplying the total number of pixels in a clump by the physical area of a single pixel to obtain the total physical area (A) of the clump. The three-dimensional geometry of the clumps is unknown, under the assumption that they are spherical the radius is given by:

$$R = \sqrt{\frac{A}{\pi}}\ \text{[pc]} \tag{3.1}$$

The error associated with the radius is dependent on the distance uncertainty. The distance to G305 is assumed to be 3.8 ± 0.6 kpc and so imparts an error of ~ 10% into the radius.

3.5.6.2 Optical depth

The hyperfine structure of the clump-averaged NH_3 spectral profile allows the average optical depth to be derived from the ratio of satellite to main line intensity, using Eq. B.89. An implicit assumption is that the beam filling factors are equal as are the excitation temperatures for the different hyperfine components. This is a reasonable assumption because of the very close energy separations and the small probability of special excitation mechanisms that differentiate between the hyperfine components (Ho & Townes, 1983). The NH_3 main line optical depth ($\tau_{(1,1,\mathrm{m})}$) ranges between 0.3 ± 0.1 and 1.5 ± 0.2 with a mean of 0.9 suggesting that most of the NH_3 emission is optically thin.

3.5.6.3 Temperature

Once the optical depth of the NH_3 line is known the excitation temperature (T_{ex}) can be derived (Eq. B.76). However, this approach yields very low excitation temperatures of $T_{\mathrm{ex}} \approx 3$ K because it assumes a beam filling factor of one. This assumption is almost certainly invalid because of the large $2'$ beam. These unfeasibly low values of T_{ex} introduce significant error due to being so close to the background temperature and leads to lower limits for the mass of the detected clumps. A more representative excitation temperature of $T_{\mathrm{ex}} = 10$ K is assumed for the rest of this analysis (Harju, Walmsley & Wouterloot, 1993) and is justified in Section 3.7.2.

Fortunately, the NH_3 metastable inversion transitions (i.e. $J = K$) give a reliable estimate of the rotational temperature (T_{rot}). Using the (1,1) and (2,2) transition the rotational temperature is given by Eq. B.81. There is no detection of NH_3 (2,2) in NH_3 Clumps 10, 11 and 15, therefore, the rotational temperature cannot be calculated for these clumps. However, a range of values may be estimated for each parameter of interest such as H_2 column, number densities and clump masses by using a range of rotational temperatures typical of similar clumps. Studies of NH_3 in GMCs report a range of rotational temperatures from 10–40 K (Wu et al., 2006; Tieftrunk et al., 1998). This range of rotational temperatures is assumed for NH_3 Clumps 10, 11 and 15, corresponds to at most a factor of two difference in column density and so will not affect results significantly.

The rotational temperature is a good indicator of the gas temperature kinetic temperature (T_{kin}) for temperatures less than 20 K, although T_{rot} underestimates T_{kin} for temperature over 20 K (see e.g. Walmsley & Ungerechts 1983; Danby et al. 1988) where there may be a significant population in the non-metastable state. The kinetic temperature may be estimated by solving Eq. B.86 and is found to range between 20.7 ± 1.8 and 30.6 ± 2.9 K with a mean of 24.8 K. The uncertainty associated with the kinetic temperature arises from the uncertainty in the temperature scale.

3.5.6.4 Column density

The column density (N_u) of the molecules in the upper state of the transition $u \rightarrow l$ can be expressed as a function of the integrated optical depth of the observed line using Equation B.97. By applying the Boltzmann equation with the assumption that $T_{ex} = 10\,K$ the total column density in the $N(1,1)$ transition may be derived assuming that both upper and lower levels are evenly populated via Equation B.98. The total column density of NH_3 in all rotational levels is estimated using Equation B.99.

The fractional abundance between NH_3 and H_2 is assumed to be 3×10^{-8} (e.g. Wu et al. 2006; Harju, Walmsley & Wouterloot 1993). Without knowledge of the variation of the abundance ratio across the complex, it is implicit that the NH_3 abundance ratio is constant across the entire region. The N_{H_2} column density traced by NH_3 ranges between $1.9 \pm 1.2 \times 10^{22}$ and $15.3 \pm 7.4 \times 10^{22}\,cm^{-2}$ with a mean of $8.2 \times 10^{22}\,cm^{-2}$. Errors associated with the column density originate from the uncertainty in the opacities, rotational temperature and abundance ratios (see Section 3.7.3), which may vary by up to an order of magnitude.

3.5.6.5 Mass

With the column density and physical area of the clump defined it is possible to obtain an appropriate estimate of the mass via:

$$M = AN_{NH_3}X\mu_m m_{H_2}\ [M_\odot] \tag{3.2}$$

where A is the area (cm^2) determined in Section 3.5.6.1, N_{NH_3} is the NH_3 column density (cm^{-2}), X is the abundance ratio, μ_m is the mean molecular weight of 2.72, which accounts for the presence of both H_2 and He (i.e. Roman-Duval et al. 2010) and m_{H_2} is the mass of H_2 (kg). The mass estimates, based on the assumption of LTE, range between $3 \pm 2 \times 10^3$ and $122 \pm 59 \times 10^3\,M_\odot$ with a mean of $49 \times 10^3\,M_\odot$. Sources of error in the mass estimate originate from the distance and abundance ratio uncertainty and are $< 50\%$.

3.5.6.6 Virial mass

The stability of these NH_3 clumps against collapse may be estimated by calculating the virial mass, which is derived using Equation B.101 (e.g. Evans 1999). The virial mass is found to range between $2 \pm 2 \times 10^3$ and $27 \pm 18 \times 10^3\,M_\odot$ with a mean of $12 \times 10^3\,M_\odot$. The virial parameter (Section B.9.5) α_{vir} is simply the ratio of virial to LTE mass (M_{vir}/M) and is found to range between 0.1 and 1.6 with a mean of 0.35.

The virial mass estimate depends on the FWHM line width of the emission and the radius of the clump. Due to the low velocity resolution and hyperfine nature of the NH_3 spectral profile we are unable to distinguish clumps along the line of sight. Therefore it is likely that the main line FWHM reported in Table 3.8 is the contribution of a number of individual clumps along the line of sight and so overestimated. In addition, the size of the clump will appear much larger than it physically is due to beam smearing. For these reasons the NH_3 virial mass should be considered an overestimate. Despite this the virial mass is significantly lower than the LTE mass, this is most likely due to a combination of factors including the low-resolution of the NH_3 observations and the unknown abundance ratio. This leads to a large error associated with the LTE derived mass.

Region	Clump Number	Clump Name	$\tau_{(1,1,m)}$	T_{rot} (K)	T_{kin} (K)	N_{H_2} $10^{22}(cm^{-2})$	n_{H_2} $10^3(cm^{-3})$	M $10^3(M_\odot)$	M_{vir} $10^3(M_\odot)$	α_{vir}
NW	1	G305.23+0.29	0.8 ± 0.2	21.3 ± 0.6	25.2 ± 0.9	6.4 ± 1.8	4 ± 1	88 ± 25	15 ± 4	0.2 ± 0.1
	3	G305.19+0.21	1.1 ± 0.3	22.3 ± 0.9	26.8 ± 1.5	11.0 ± 4.7	14 ± 6	53 ± 22	11 ± 5	0.2 ± 0.1
NE	4	G305.36+0.2	1.3 ± 0.3	23.5 ± 1.2	28.8 ± 2.1	15.4 ± 7.5	13 ± 7	122 ± 59	25 ± 13	0.2 ± 0.1
	7	G305.42+0.25	0.9 ± 0.2	20.1 ± 0.8	23.2 ± 1.2	5.7 ± 2.8	5 ± 2	43 ± 20	7 ± 4	0.2 ± 0.1
	9	G305.54+0.34	0.3 ± 0.1	2.0 ± 0.6	19.5 ± 1.1	22.4 ± 1.6	4 ± 2	5 ± 3	8 ± 4	1.7 ± 1.1
SW	2	G305.26−0.02	0.8 ± 0.2	21.1 ± 0.7	24.8 ± 1.2	8.2 ± 3.2	7 ± 0.3	71 ± 27	18 ± 7	0.3 ± 0.1
	8	G305.19+0.01	1.0 ± 0.3	24.4 ± 1.6	30.6 ± 2.9	14.6 ± 9.7	18 ± 12	69 ± 46	27 ± 18	0.4 ± 0.3
	6	G305.14+0.06	0.5 ± 0.1	20.6 ± 0.8	24.0 ± 1.3	3.5 ± 2.3	3 ± 2	25 ± 16	8 ± 4	0.3 ± 0.2
E	5	G305.82−0.11	1.1 ± 0.3	18.7 ± 0.9	21.2 ± 1.3	6.9 ± 3.8	8 ± 4	46 ± 25	5 ± 3	0.1 ± 0.1
	10	G305.83−0.19	1.1 ± 0.3	10 – 40	10 – 74	9 – 16	18 – 33	21 – 37	4 ± 2	-
	11	G305.89+0.02	1.5 ± 0.4	10 – 40	10 – 74	11 – 20	18 – 32	27 – 48	4 ± 2	-
	12	G305.69+0.04	0.4 ± 0.1	18.3 ± 1.2	20.7 ± 1.8	1.9 ± 1.5	4 ± 3	2 ± 2	2 ± 2	0.3 ± 0.3
	13	G305.77−0.25	1.3 ± 0.3	20.9 ± 1.2	24.6 ± 1.9	11.6 ± 7.3	19 ± 12	43 ± 27	6 ± 3	0.2 ± 0.1
	14	G305.56+0.02	1.2 ± 0.3	21.2 ± 1.3	25.1 ± 2.1	10.5 ± 7.2	18 ± 12	22 ± 15	6 ± 3	0.3 ± 0.2
	15	G305.48−0.1	1.5 ± 0.4	10 – 40	10 – 74	9 – 17	21 – 37	11 – 20	3 ± 2	-

TABLE 3.8: NH_3 emission physical properties derived by fitting the clump-averaged spectral profile.

3.6 CO results and analysis

3.6.1 CO clump identification

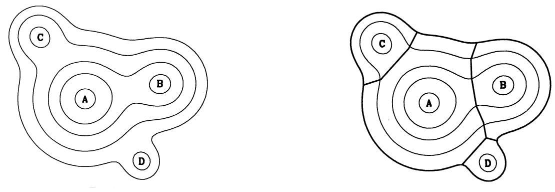

FIGURE 3.8: Representation of how the CLUMPFIND algorithm assigns emission into clumps using contours (Williams, de Geus & Blitz, 1994).

The higher angular and velocity resolution of the CO observations is able to resolve a physical size and velocity of $\sim$ 0.6 pc and 0.1 km s^{-1} respectively, making it a good tracer of the three-dimensional velocity structure. Therefore, the more widely used three-dimensional clump finding algorithm CLUMPFIND (Williams, de Geus & Blitz, 1994) was chosen to decompose the optically thin ^{13}CO emission into clumps and retain the velocity information. CLUMPFIND was chosen because it is more widely used and will better allow comparison between other surveys (e.g. Rathborne et al. 2009; Roman-Duval et al. 2010).

CLUMPFIND works in a "top-down" approach by finding peaks within the data and then contouring down to a user defined base level (Fig. 3.8) detecting new peaks along the way and assigning pixels associated with more than one peak to a specific clump using the "friends-of-friends" algorithm (Williams, de Geus & Blitz, 1994). To account for noise variations CLUMPFIND was applied to a ^{13}CO S/N cube with a uniform background noise of $\sigma_{\rm S/N}$ = 0.3 K.

Two parameters are responsible for the majority of control in CLUMPFIND, the minimum emission level to begin clump finding ($T_{\rm low}$) and the step width that defines the spacing of the contours (ΔT). The recommended parameters for CLUMPFIND is a level spacing of $\Delta T = 2\sigma$ and a lowest level of $T_{\rm low} = 2\sigma$ (Williams, de Geus & Blitz, 1994). However, these parameters resulted in emission being broken up into a large number of small clumps that did not appear to trace the true distribution of emission (e.g. Pineda, Rosolowsky & Goodman 2009; Rathborne et al. 2009). This is because the CO J =1–0 transition is easily excited and can be found in low-density diffuse regions which leads to confusion. To avoid this problem the minimum emission level chosen to begin clump finding was $T_{\rm low} = 9\sigma_{\rm S/N}$ and the step width that defines the spacing of the contours $\Delta T = 3\sigma_{\rm S/N}$. Additionally, clumps were rejected if they touched any edge of the data cube, contained fewer than nine (three-dimensional) pixels or were smaller than the beam size. The final catalogue was then checked by eye and using manual aperture photometry to ensure that only meaningful structures were included in the final catalogue.

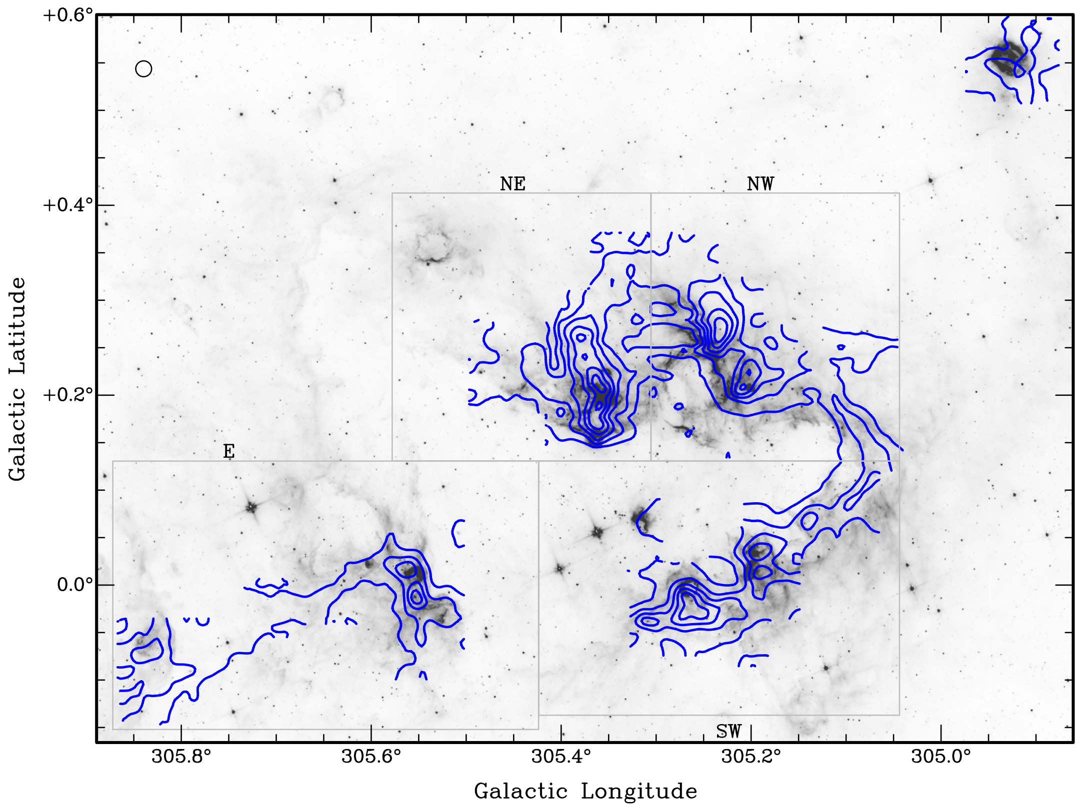

FIGURE 3.9: The integrated (Moment 0) ^{13}CO emission towards G305 in blue contours overplotted onto a GLIMPSE 5.8 µm (greyscale) image. Contours begin at 7 K km s^{-1} and increment by 5 K km s^{-1}. The Mopra beam at 110.221 GHz (30″) is presented in the top left. Following our nomenclature we separate the complex into four regions of emission with grey boxes.

3.6.2 CO results

A total of 57 clumps were identified by CLUMPFIND in the ^{13}CO PPV cube, all of which are associated with ^{12}CO and C^{18}O emission. The bulk of CO emission is found between −42.9 and −28.2 km s^{-1} and peaks at −37.5 km s^{-1} (Table 3.10 and Fig. 3.16). Faint emission is also detected in the isolated CO clump 56 at −17 km s^{-1} and an extended low brightness feature at −3 km s^{-1} (Fig. 3.13).

3.6.3 CO clump spectra

The output generated by the ^{13}CO clump finding is used as a mask to extract the ^{12}CO, ^{13}CO and C^{18}O spectra averaged over the extent of the clump in l and b and v. An issue is immediately apparent with spectra extracted using such a three-dimensional mask, the high cut-off level used in the clump finding step ($T_{\mathrm{low}} = 9\sigma_{\mathrm{S/N}}$) severely limits the spectral profiles in velocity space (Fig. 3.10).

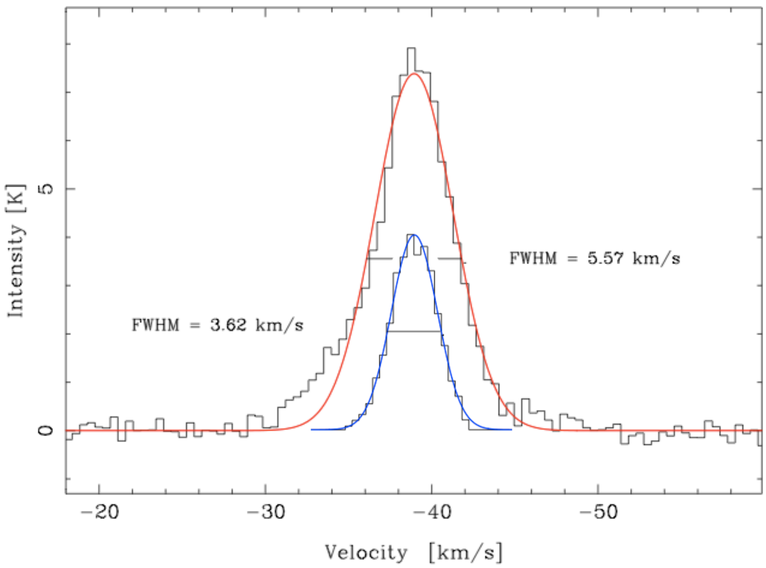

FIGURE 3.10: Comparison between the Gaussian fit to the clump averaged spectra defined by CLUMPFIND shown in blue and the Gaussian fit to the full velocity range performed in IDL shown in red. The effect of the $T_{\mathrm{low}} = 9\sigma$ is apparent in the lower FWHM of the CLUMPFIND spectra.

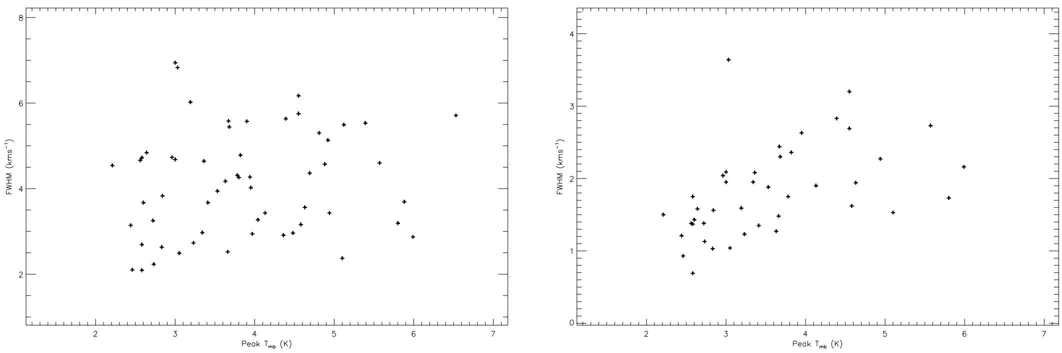

FIGURE 3.11: The peak main beam brightness (T_{mb}) of the CO clumps is plotted against the clump FWHM. Left: the peak and FWHM determined via a Gaussian fit to the clump averaged spectra that includes all v. Right: the FWHM derived using the l, b and v mask produced by CLUMPFIND. This clearly shows that the FWHM derived using the clump find mask in l, b and v determines a lower FWHM and peak temperature that scales with the peak temperature.

This high cut-off results in the clump averaged peak brightness and FWHM being systematically underestimated (Fig. 3.10, blue) dependent on the peak brightness of the source (Fig. 3.11, right panel). To solve this issue the clump averaged spectra are determined within the clump mask for the maximum extent in l and b along all v where the pixel values are $> 4\sigma$ (Fig. 3.10, red and Fig. 3.11, left panel). However, for several clumps this leads to blending along the line of sight as overlapping clumps in l and b contaminate the clump averaged spectra.

Producing clump-averaged spectra without taking blending into account leads to an overestimate of the FWHM and in many cases makes it difficult to fit the spectral profile. In an effort to reduce

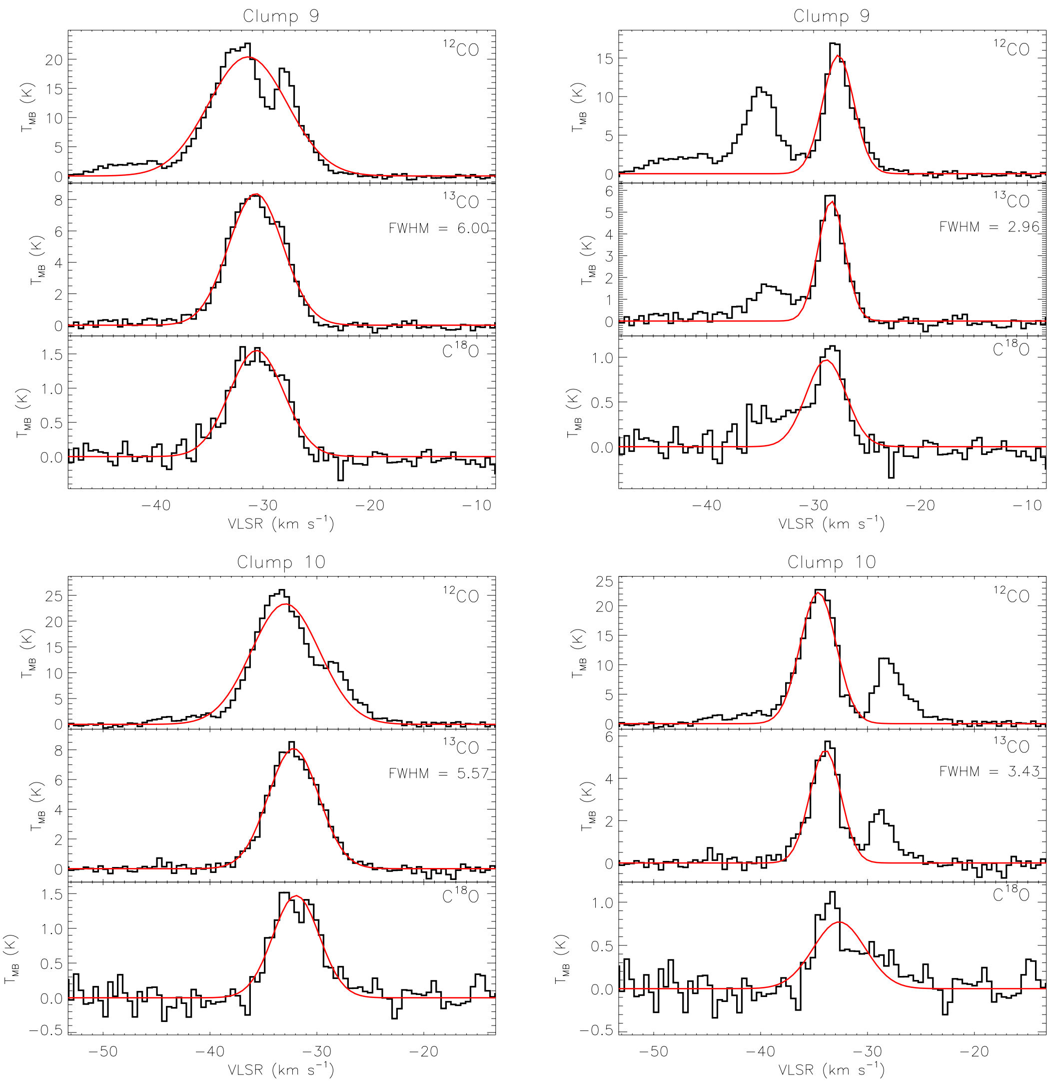

FIGURE 3.12: Left panel: clump-averaged spectra for Clump 9 and 10, the two peaks are visible in the ^{12}CO spectra but merge in the ^{13}CO. Right panel: the same spectra with the pixels that overlap in l, b and v set to the 3σ, which clearly separates the emission into two distinct peaks.

blending and improve FWHM estimates a clipping process is applied when constructing the averaged spectra. For a given clump region any pixel that has been assigned to a different clump that overlaps in l and b is set to three times the noise level (Fig. 3.12). As well as outputting clipped CO spectra a clipped PPV cube is written for the purposes of analysis.

These clipped, clump-averaged spectral profiles were fitted with a Gaussian using the IDL function GAUSSFIT (Fig. 3.14). Despite clipping, a number of spectra remain difficult to fit using this method. The properties of the ^{13}CO spectra are used in the analysis of the CO emission and so for ^{13}CO spectra with poorly fitted Gaussians the XS data reduction software[9] tool is used to

[9]http://www.chalmers.se/rss/oso-en/observations/data-reduction-software

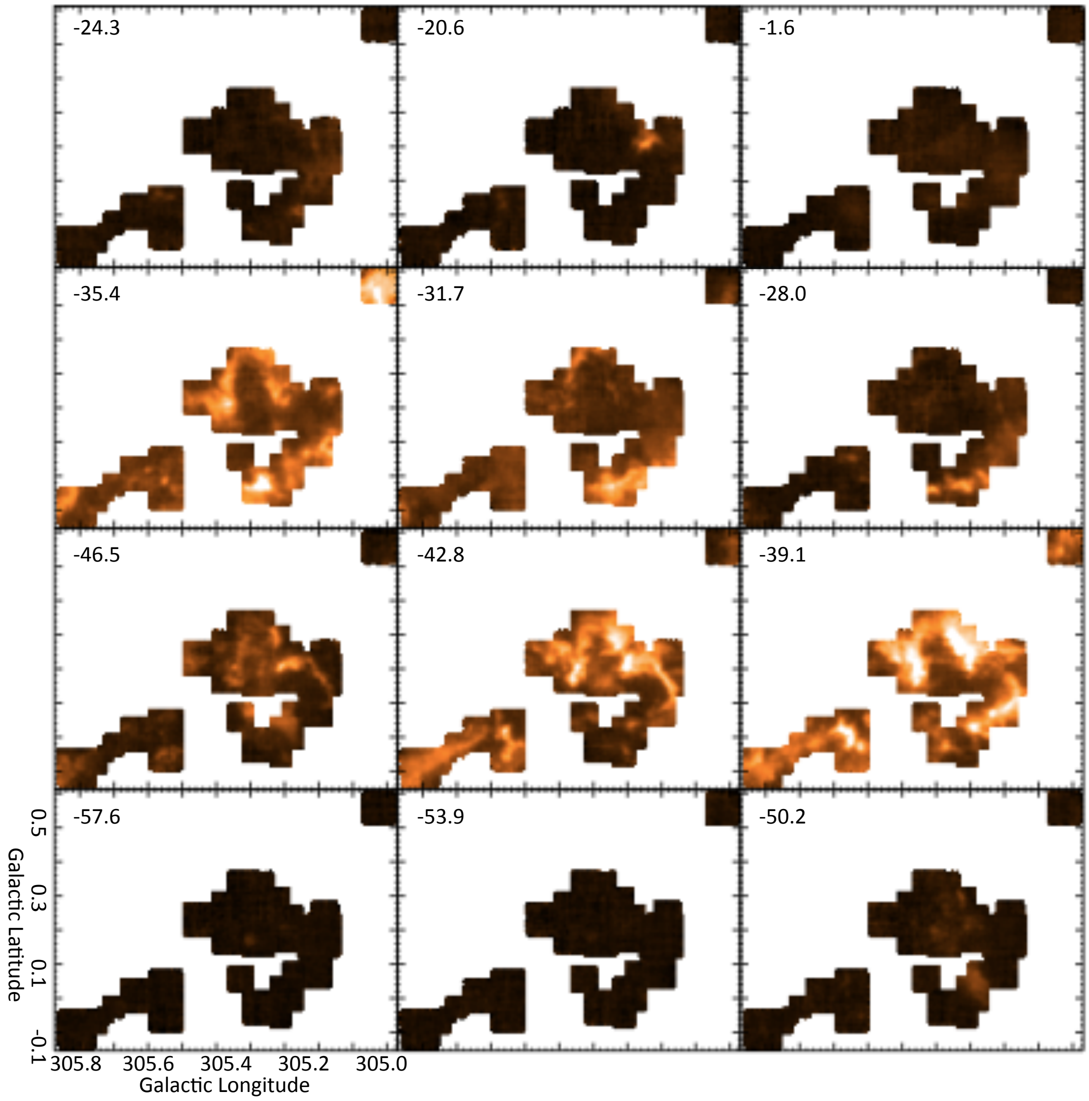

FIGURE 3.13: Channel map of the ^{12}CO data cube beginning at $-57.6\,\mathrm{km\ s^{-1}}$ in the bottom left and proceeding to the right and returning to the left at the end of each row. The emission is integrated over $3.7\,\mathrm{km\ s^{-1}}$ channels per image up to $-1.6\,\mathrm{km\ s^{-1}}$ in the top right. The corresponding velocity channels can be found in the top left of each channel map image.

fit Gaussians by hand (see Fig. 3.14, Clump 7 blue fit). The CO spectral profiles can be found in Fig. C.3 and the extracted parameters are presented in Table 3.9.

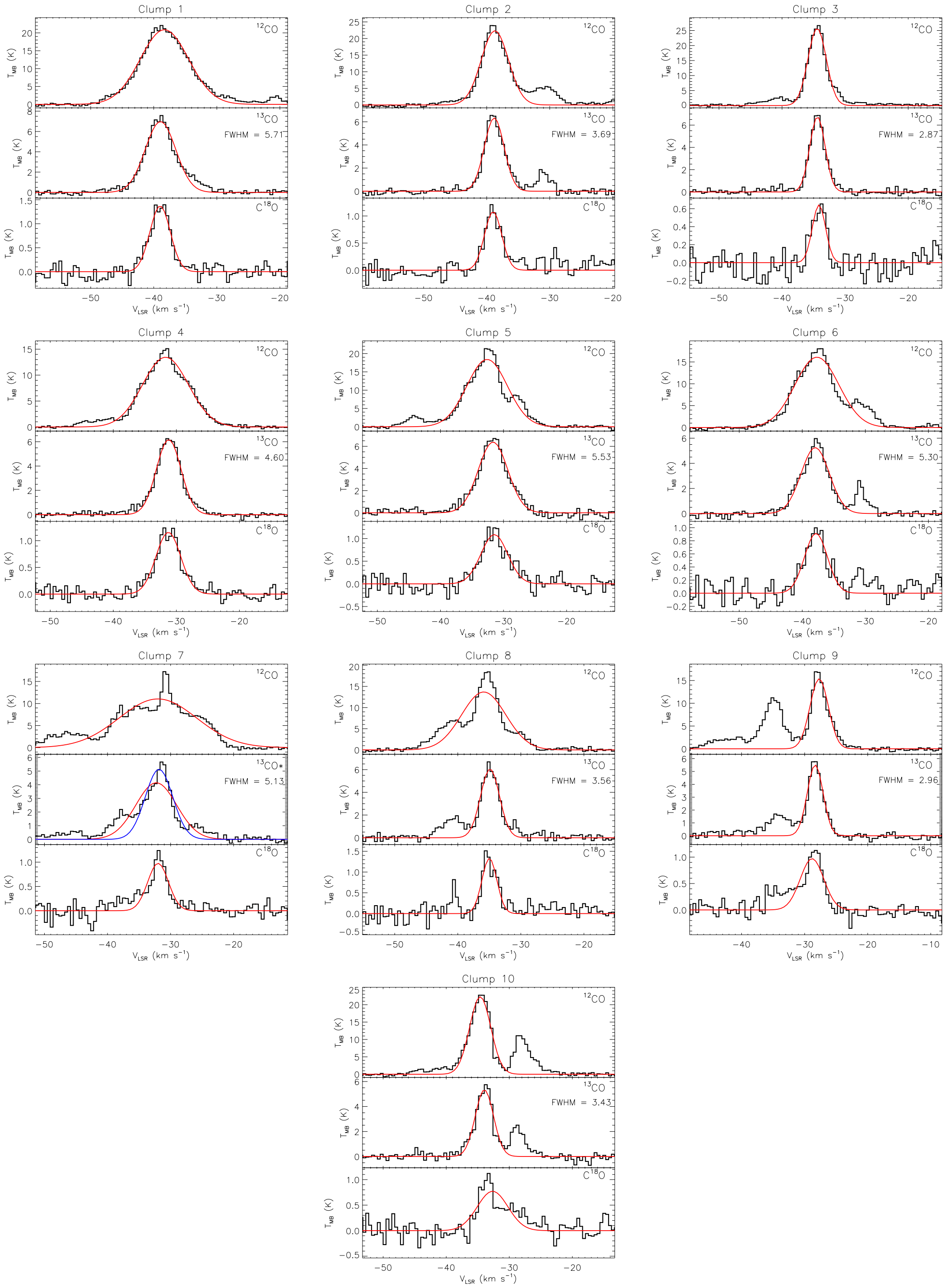

FIGURE 3.14: Clump-averaged spectra of the first 10 of 57 CO clumps towards G305. Spectra have been averaged over the clump area defined by CLUMPFIND. Gaussian fitting is applied to the spectral profiles emission shown as red over plots in the case of poor fits due to blending the ^{13}CO Gaussian profile is fitted manually using XS and presented in blue. A complete set of images can be found in Fig. C.3.

Clump	Clump	Peak			Dimension				Peak
Number	Name	Galactic		V_{LSR}	Δl	Δb	R	Δv	T_{mb}
		(l)	(b)	(km s^{-1})	($''$)	($''$)	(pc)	(km s^{-1})	(K)
1	G305.24+0.26	305.24	0.26	−38.8	295.34	324.52	2.42	5.71	15.55
2	G305.56+0.02	305.56	0.02	−39.7	222.51	156.10	1.50	3.69	14.00
3	G304.94+0.55	304.94	0.55	−34.6	385.20	261.13	2.46	2.87	14.26
4	G305.26−0.03	305.26	−0.03	−32.4	410.77	332.67	2.77	4.60	13.26
5	G305.27−0.02	305.27	−0.02	−32.4	169.69	140.30	1.23	5.53	12.83
6	G305.55−0.01	305.55	−0.01	−37.9	156.76	202.59	1.47	5.30	11.45
7	G305.19+0.01	305.19	0.01	−31.4	265.25	128.08	1.47	5.13	11.71
8	G305.82−0.05	305.82	−0.05	−35.1	138.68	244.36	1.42	3.56	11.02
9	G305.24−0.03	305.24	−0.03	−28.2	196.72	157.68	1.35	2.96	10.67
10	G305.27−0.04	305.27	−0.04	−33.3	172.82	163.42	1.36	3.43	11.76

TABLE 3.9: The first 10 identifiers and observed properties of the 57 detected ^{13}CO clumps reported by CLUMPFIND. This table can be found in its entirety in Table C.2.

3.6.4 CO analysis

3.6.4.1 Excitation temperature

Assuming the ^{12}CO emission is in LTE and optically thick, the observed brightness temperature ($T_{\rm mb}$) and excitation temperature ($T_{\rm ex}$) are linked (Eq. B.67). The excitation temperature is calculated for each voxel in the clipped PPV cubes (i.e. (l, b, v) position) defined by clump finding and globally for pixels above 4σ using:

$$T_{\rm ex}(l, b, v) = 5.53 \frac{1}{\ln\left(1 + \frac{5.53}{T_{\rm mb}(l,b,v)+0.837}\right)} \text{ [K]} \tag{3.3}$$

The average ^{12}CO excitation temperature ranges from 12.54 ± 0.30 to 23.8 ± 0.29 K with a mean of 17.05 K. The CO excitation temperature was assumed to be identical for ^{13}CO and ^{12}CO. Since CO is usually thermalised within molecular clouds due to its low dipole moment this is a reasonable assumption. However, this assumption may break down in the more diffuse envelopes of molecular clouds, where the optically thick ^{12}CO can remain thermalised due to radiative trapping, while the optically thin ^{13}CO is radiatively excited. In this case, the ^{13}CO excitation temperature would be lower than the ^{12}CO excitation temperature. This effect is most likely not important in the above analysis due to the high CO clump finding cut-off. In addition, the emission may not completely fill the beam in which case the excitation temperature will also be underestimated.

3.6.4.2 Optical depth

The ^{13}CO optical depth (Eq. B.87) is derived by using the ^{12}CO excitation temperature as a proxy for the ^{13}CO excitation temperature. The optical depth was evaluated at each voxel (l, b, v) where a ^{12}CO excitation temperature is available:

$$\tau_{13}(l, b, v) = -\ln\left(1 - \frac{0.189 T_{13}(l, b, v)}{\left(e^{\frac{5.3}{T_{\rm ex}(l,b,v)}} - 1\right)^{-1} - 0.16}\right) \tag{3.4}$$

The line center optical depth was computed at each pixel (l, b) by taking the peak optical depth along the line of sight. The average of the line center optical depths over the clump was then determined and is presented in Table 3.10. All ^{13}CO emission is found to be optically thin with a range of 0.31 ± 0.02 to 0.9 ± 0.08 and average of 0.47. The error associated with the optical depth is dependent on the excitation temperature and the temperature scale.

3.6.4.3 Column densities

From the optical depths and excitation temperature the ^{13}CO column density may be derived at each pixel (l, b) by applying Equation B.95:

$$N_{^{13}\mathrm{CO}}(l,b) = 2.6\times 10^{14}\int \frac{T_{\mathrm{ex}}\,(l,b,v)\,\tau_{13}(l,b,v)}{1-e^{\frac{-5.3}{T_{\mathrm{ex}}(l,b,v)}}}\,dv\ [\mathrm{cm}^{-2}] \tag{3.5}$$

where the integration is performed over the velocity in km s^{-1}. The abundance ratio between ^{13}CO and ^{12}CO exhibits a gradient with distance from the Galactic center that follows the relationship ^{12}CO : ^{13}CO = $6.21D_{\mathrm{GC}} + 18.71$ (Milam et al., 2005) where D_{GC} = 6.5 kpc is the distance of G305 from the Galactic center. The abundance ratio between ^{12}CO and ^{13}CO is then ^{12}CO : ^{13}CO = 59. The abundance ratio between ^{12}CO and H_2 is then ^{12}CO : H_2 = 8×10^{-5} (Langer & Penzias, 1990; Blake et al., 1987). Therefore, assuming an abundance ratio between ^{13}CO and H_2 of 1.356×10^{-6} results in clump averaged column densities ranging from $1.94\pm0.19\times10^{22}$ to $7.73\pm0.40\times10^{22}$ cm^{-2} with a mean of 3.73×10^{22} cm^{-2}. The error associated with the column density originates from the uncertainty in opacity and the abundance ratio which is discussed further in Section 3.9.

3.6.4.4 Mass

In the case of CO the mass is derived in essentially the same way as Eq. 3.2, however in this case the integrations are performed analytically. Substituting for physical constants and conversion factors the mass Eq. 3.2 may be expressed as:

$$M = 0.35\,D^2\int_{l,b,v}\frac{T_{\mathrm{ex}}(l,b,v)\tau_{13}(l,b,v)}{1-e^{\frac{-5.3}{T_{\mathrm{ex}}(l,b,v)}}}\,dv\,dl\,db\ [\mathrm{M}_\odot] \tag{3.6}$$

where D is the distance to G305 in kpc and the integral is performed over the velocity in km s^{-1} and extent in l and b in arc-minutes. This results in clump averaged masses ranging from $0.4\pm0.1\times10^3$ to $22.0\pm1.8\times10^3$ M$_\odot$ with a mean of 4.4×10^3 M$_\odot$. Once again, the error associated with the mass is dependent on the distance uncertainty and abundance ratio.

3.6.4.5 Virial mass

The virial mass (M_{vir}) and virial mass parameter (α_{vir}) for CO clumps is determined in the same way as Section 3.5.6.6 and is found to range between 0.55 and 4.11 with a mean value of 1.69. This interpretation of the virial mass is expected to be more representative than that derived for NH_3 because of the improved spatial and velocity resolution and three-dimensional decomposition of clumps.

3.6.4.6 Number and surface density

The mean number density of particles (H_2 and He) in the molecular clumps is estimated assuming spherical symmetry via:

$$n(\mathrm{H_2} + \mathrm{He}) = 15.1 \times M \times \left(\frac{4}{3}\pi R^3\right)^{-1} \ [\mathrm{cm^{-3}}] \tag{3.7}$$

Where R is the physical radius in pc, M is the mass in solar mass units. In this way the number density is found to be between $2.7 \pm 1.3 \times 10^3$–$8.9 \pm 4.5 \times 10^3$ cm^{-3} with a mean of 5.4×10^3 cm^{-3}. The surface mass density $\sum_c$ of the molecular clouds is calculated by simply dividing the mass by the area:

$$\Sigma_c = MA^{-1}[\mathrm{M_\odot\,pc^{-2}}] \tag{3.8}$$

We find surface densities ranging from $3.3 \pm 1.1 \times 10^2$ to $12.0 \pm 3.9 \times 10^2$ M$_\odot$ pc^{-2} with a mean of 6.1×10^2 M$_\odot$ pc^{-2}.

Clump No.	Clump Name	τ (^{13}CO)	T_{ex} (K)	N_{H_2} 10^{22}(cm^{-2})	n_{H_2} 10^{3}(cm^{-3})	$\sum_c$ 10^{2}(M$_\odot$ pc^{-2})	M 10^{3}(M$_\odot$)	M_{vir} 10^{3}(M$_\odot$)	α_{vir}
1	G305.24+0.26	0.46 ± 0.03	21.34 ± 0.21	5.27 ± 0.43	5.5 ± 2.7	12.0 ± 3.9	22.0 ± 1.8	12.0 ± 2.0	0.58 ± 0.10
2	G305.56+0.02	0.34 ± 0.02	21.56 ± 0.20	3.18 ± 0.27	5.4 ± 2.6	7.1 ± 2.3	5.0 ± 0.4	5.0 ± 0.8	0.99 ± 0.18
3	G304.94+0.55	0.41 ± 0.02	23.80 ± 0.29	2.74 ± 0.21	2.8 ± 1.4	6.1 ± 2.0	12.0 ± 0.9	6.4 ± 1.0	0.55 ± 0.10
4	G305.26−0.03	0.67 ± 0.06	17.01 ± 0.29	3.33 ± 0.30	3.1 ± 1.5	7.5 ± 2.5	18.0 ± 1.7	12.0 ± 1.8	0.64 ± 0.12
5	G305.27−0.02	0.45 ± 0.03	18.76 ± 0.22	4.25 ± 0.37	8.8 ± 4.2	9.5 ± 3.1	4.5 ± 0.4	6.1 ± 1.0	1.36 ± 0.25
6	G305.55−0.01*	0.44 ± 0.03	17.73 ± 0.23	3.24 ± 0.33	5.6 ± 2.7	7.3 ± 2.4	4.9 ± 0.5	7.0 ± 1.1	1.43 ± 0.28
7	G305.19+0.01*	0.60 ± 0.05	15.11 ± 0.26	3.06 ± 0.35	5.3 ± 2.6	6.9 ± 2.3	4.7 ± 0.6	6.8 ± 1.6	1.46 ± 0.38
8	G305.82−0.05	0.55 ± 0.04	15.56 ± 0.33	2.73 ± 0.29	4.9 ± 2.4	6.1 ± 2.0	3.9 ± 0.4	4.6 ± 0.8	1.18 ± 0.23
9	G305.24−0.03	0.57 ± 0.04	17.92 ± 0.21	2.24 ± 0.21	4.2 ± 2.0	5.0 ± 1.7	2.9 ± 0.3	3.6 ± 0.6	1.25 ± 0.24
10	G305.27−0.04	0.35 ± 0.02	21.76 ± 0.19	2.76 ± 0.25	5.2 ± 2.5	6.2 ± 2.0	3.6 ± 0.3	4.2 ± 0.7	1.17 ± 0.22

TABLE 3.10: Physical properties of the first 10 of 57 ^{13}CO clumps. Asterisks above the clump name highlights clumps that have been fitted by hand using XS due to blended spectra.

3.7 Properties of the molecular environment

The previous sections present the observations and results of the molecular environment towards G305 traced by NH_3 and CO. In this section we discuss the physical properties of the molecular environment revealed by these two molecular tracers.

3.7.1 Morphology

The global distribution and morphology of the molecular environment towards G305, traced by ^{13}CO and NH_3 clumps and clouds respectively, is presented in Figs. 3.5 and 3.9 and a comparison can be found in Fig. 3.15 where we show images of the four sub-regions. The low-resolution NH_3 observations (green contours) preferentially trace dense gas on the scale of clouds whilst higher resolution ^{13}CO emission (blue contours) traces smaller, less dense emission on the scale of clumps. These observations reveal a complex and clumpy molecular environment with multiple scales of both interconnected and isolated molecular gas typical of GMCs. The vast majority of molecular gas is in three large and dense clouds, highlighted by NH_3, to the North and South of the central cavity. These three dense clouds are embedded within, and connected by, low-density gas traced by CO. The dense cores traced by both CO and NH_3 emission appears to be in approximately the same position with the higher resolution CO observations revealing substructure within the dense NH_3 clouds.

Comparison to the GLIMPSE 5.8 μm mid-infrared background reveals that the molecular material is coincident with the PDR surrounding the central cavity of G305. The central cavity is bound to the North by two large NH_3 clouds (NE and NW), to the South by a fragmented lobe of dense gas (SW) and to the West by a tenuous strip of gas only detected in CO. The cores of the molecular emission within these clouds lie behind the leading edge of the PDR facing the cavity indicating that the molecular material is being effectively shielded. A gradient in the molecular emission is clearly visible in a number of regions, particularly in CO, sloping away from the PDR and ionising sources. This suggests that the molecular material close to the cavity has been swept up and compressed into a dense layer. Conversely there are a number of regions in which the molecular material appears to be being dispersed or destroyed such as between the NE and NW clouds, several sites along the SW lobe and most noticeably toward the East. To the East the powerful radiation and winds of massive stars found towards the centre of G305 appear to have completely blown out of the cavity and into the wider ISM, leaving only a small pocket of over-dense gas (NH_3 Clump 14) near to the PDR and a number of small dense clumps scattered further to the East. This implies two things, first that in the past the molecular material in G305 was not homogenous, secondly some fraction of the high energy radiation originating from massive stars in the central cavity is free to escape the complex. In some cases, such as towards the NW, the CO emission peaks closer to the PDR than NH_3 this may be for a number of reasons: the CO molecules may be freezing onto dust grains in the cold environments, the density may not be high enough to form NH_3 close to the PDR or it may simply be a projection affect. Alternatively, the NH_3 clouds may predate the arrival of the ionisation front, where as the CO has been compressed as the ionisation front has expanded.

In addition to the main complex, there are a number of isolated sources of molecular emission. This includes the isolated mid-infrared core in the far North-West (G304.93+0.55), which is associated with CO and faint ($T_{\mathrm{mb}} \approx 0.15$ K) NH_3 (1,1) emission. Towards the centre of the cavity, faint ^{12}CO and ^{13}CO emission ($T_{\mathrm{mb}} = 7.4$ and 2.8 K respectively) is associated with the "blob" but is below the clump finding threshold. There is no NH_3 emission detected towards this region but there appears to be ongoing star formation as evidenced by the presence of the H_2O maser 8.

A striking filamentary structure is detected in ^{12}CO and ^{13}CO to the far East that appears to connect the dense boundary (NH_3 Clump 14) with emission further to the East (NH_3 Clump 5). This filament extends over $\sim 0.3°$ in angular scale or ~ 20 pc in length and $\sim 0.04°$ or ~ 2.5 pc in width. The filament has a coherent velocity with a slight gradient of ~ 0.05 km s^{-1} pc leading away from the cavity boundary (Figs. 3.16 and 3.17). The central velocity of the filament is ~ -37.5 km s^{-1} suggesting it is associated with the G305 complex. This provides strong supporting evidence that the filament is a single coherent structure and not the chance alignment of a number of separate clumps along the line of sight. Similar large cohesive filaments are being discovered in the Galaxy (Hill et al., 2011; Arzoumanian et al., 2011) such as the "Nessie" nebula (Jackson et al., 2010) an IRDC ~ 80 pc in length and 0.5 pc in width. Exactly how such large features form is a topic of debate but they seem to be associated with a large number of star-forming regions, this example in G305 is an excellent candidate for future study.

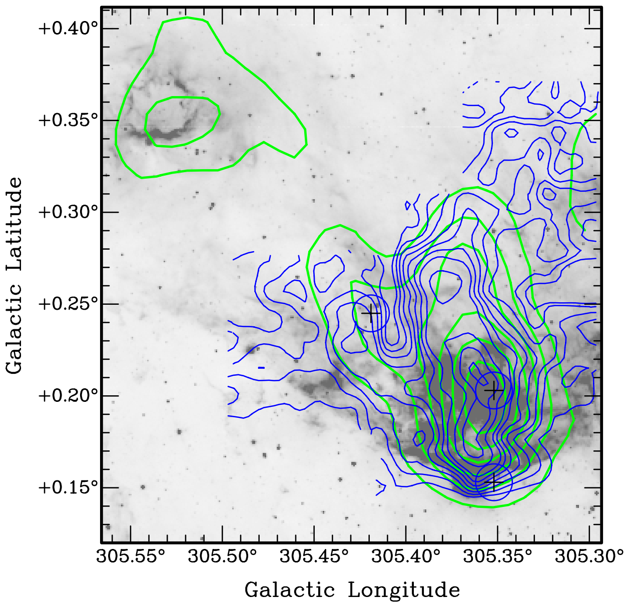

(a) North-East

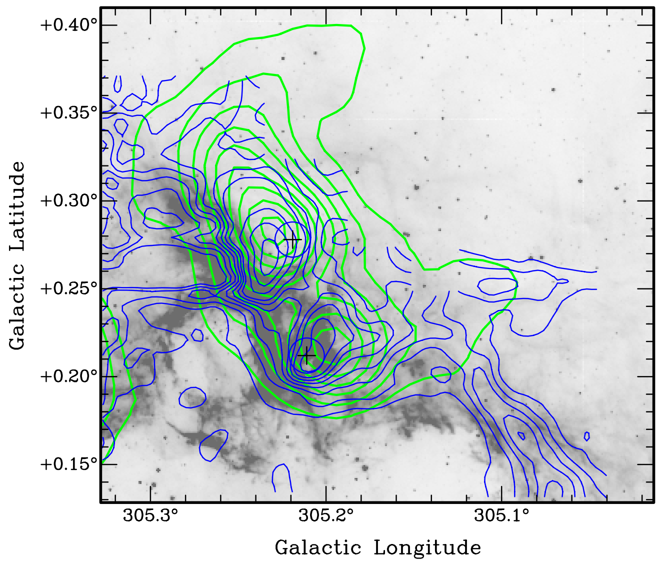

(b) North-West

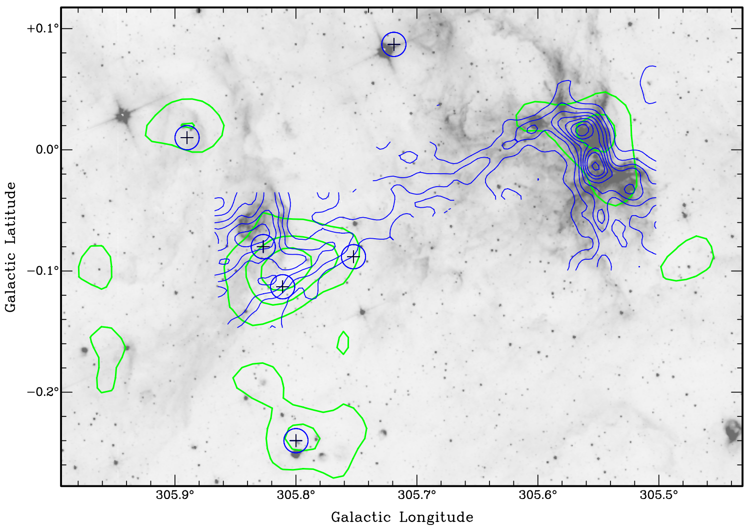

(c) East

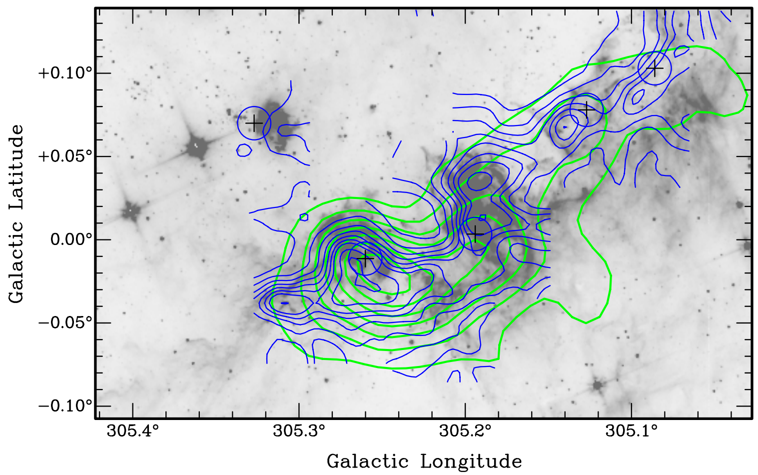

(d) South-West

FIGURE 3.15: NH_3 (1,1) and ^{13}CO integrated emission contoured over greyscale GLIMPSE 5.8 μm image in green and blue respectively. NH_3 contours begin at 0.9 K km s^{-1} (3σ) and increment by 0.6 K km s^{-1} and ^{13}CO contours begin at 6.6 K km s^{-1} and increment by 2.2 K km s^{-1}. Detected H_2O masers are shown by blue circles with black crosses for contrast.

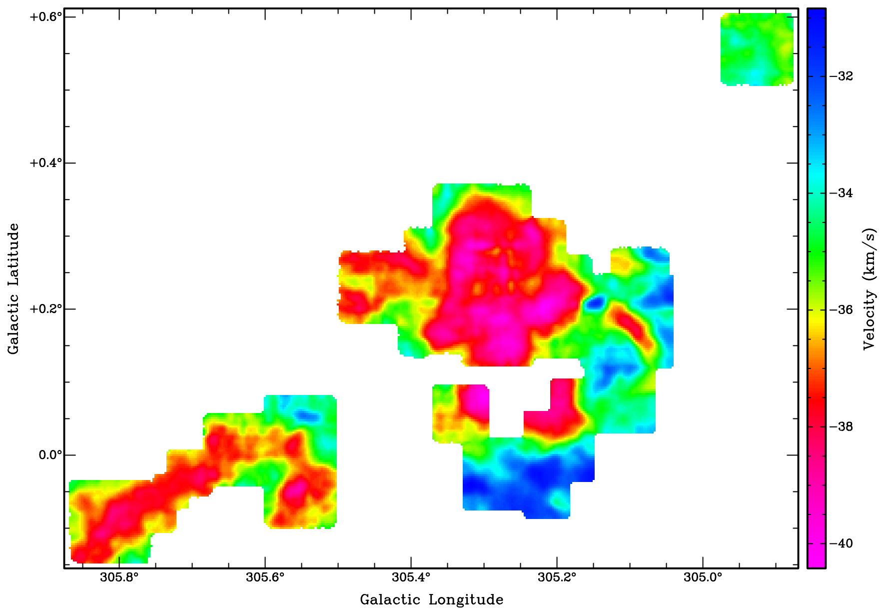

FIGURE 3.16: The intensity weighted ^{12}CO velocity centroid (1st moment).

The spatial and velocity resolution of the CO observations allow the kinematics of the molecular gas to be studied. In particular, the optically thick ^{12}CO line is able to provide information concerning the velocity structure at unit optical depth of the molecular material whilst the optically thin ^{13}CO and C^{18}O emission is able to probe through the column of gas.

The mean central velocity of the CO and NH_3 emission is in good agreement at −36.6 and −37.5 km s^{-1} respectively (Table 3.10 and 3.13) suggesting they trace the same material. However, the CO observations resolve multiple clumps not only in l and b but also along the line of sight v. The intensity weighted central velocity[10] of ^{12}CO emission towards G305 (Fig. 3.16 and 3.17) reveals that the lobes of molecular gas to the North and South of the central cavity are at approximately −41 and −30 km s^{-1} respectively. The Northern lobe of gas is approaching $>$ 10 km s^{-1} faster than the Southern lobe. This velocity gradient across the complex could be driven by expansion or shearing motion and indicates that G305 is not being viewed straight on but projected at an angle. To explore the three-dimensional morphology further we may consider the PAH morphology indicated by the 5.8 µm emission, which highlights the boundary between the ionised and molecular gas. If we were viewing the complex face on we would expect to see a clear boundary between the PAH and molecular emission whilst if the orientation is side on we would expect the PAH and molecular emission to be superimposed upon each other. We find both instances within G305, with the NE region appearing to have PAH emission projected onto the face of the molecular emission whilst the NW appears to show a clear boundary and the

[10]Moment 1: $\Sigma(I * v)/\Sigma(I)$, (velocity centroid, km s^{-1}), where v is the velocity and I is the intensity

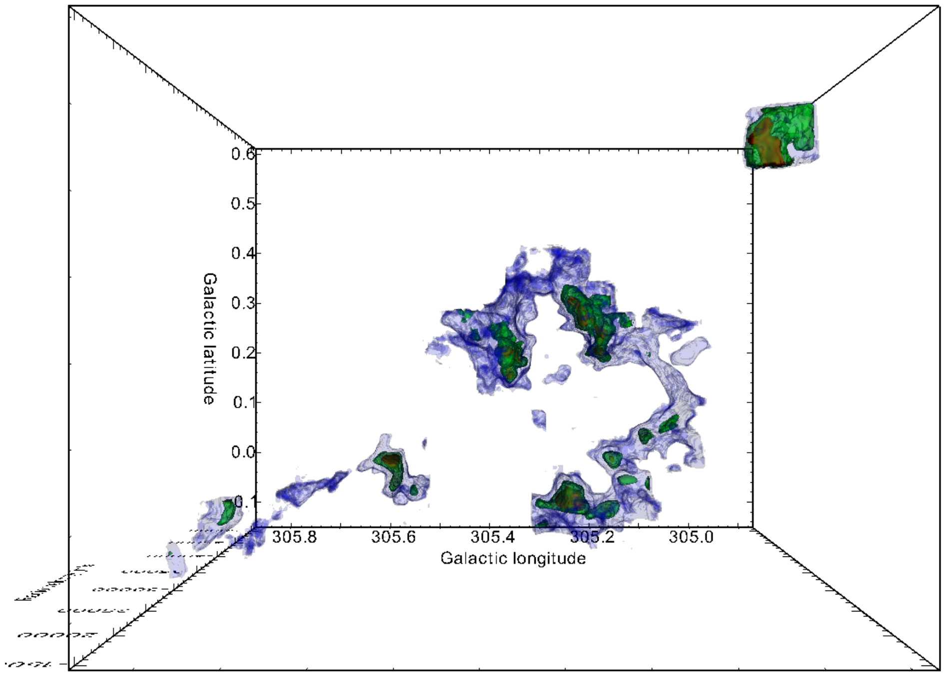

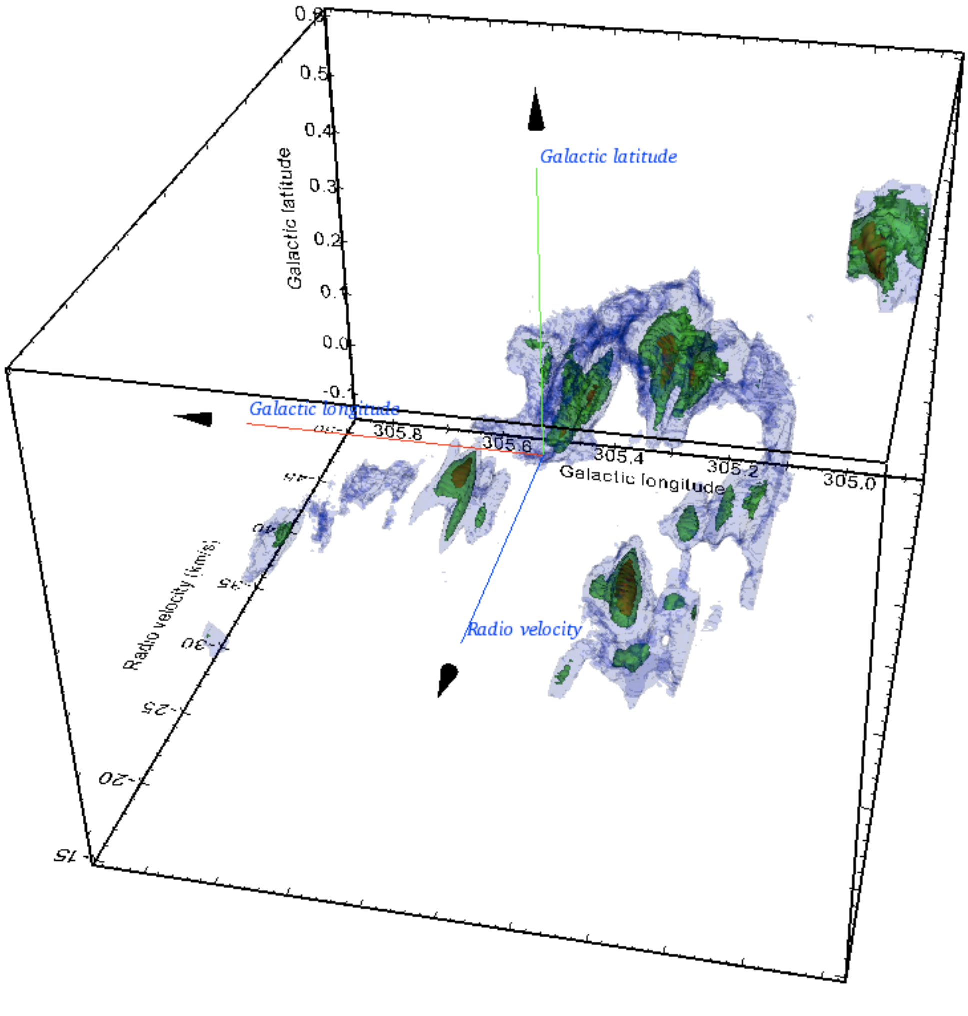

FIGURE 3.17: Three-dimensional render of the PPV ^{12}CO cube. Top panel shows a face on orientation with red, blue and green surface contours are at 6, 9 and 12 K. The bottom hand panel shows the same render from a rotated viewing angle.

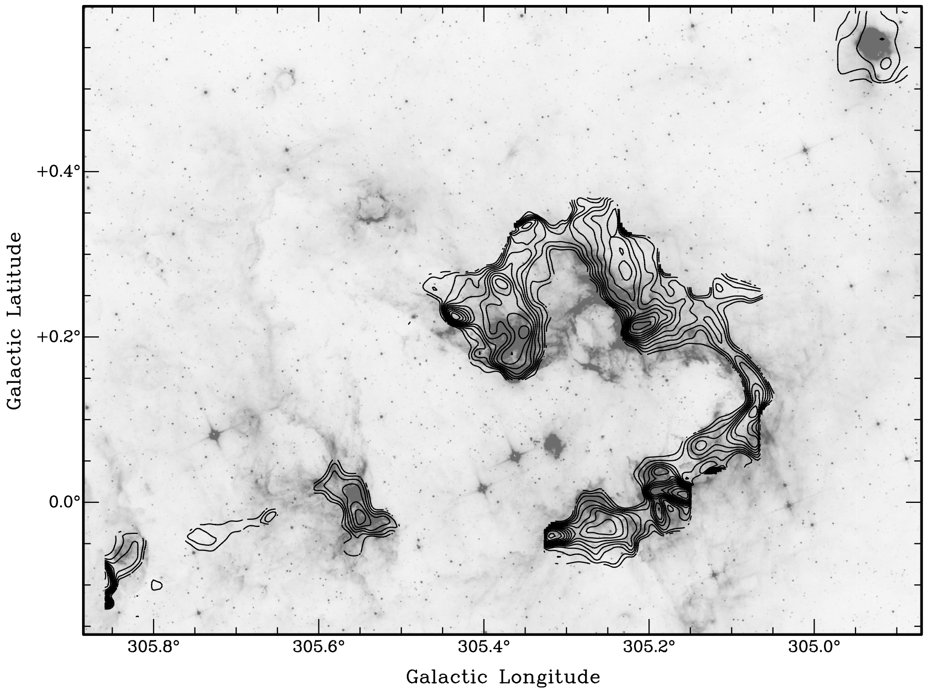

(a) ^{12}CO velocity dispersion

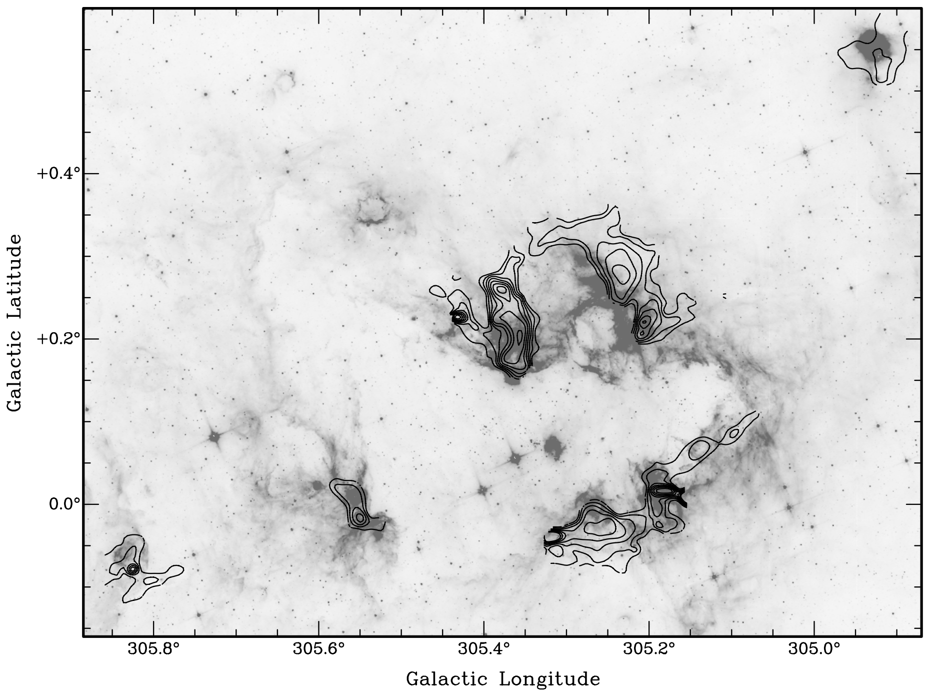

(b) ^{13}CO velocity dispersion

FIGURE 3.18: Top: the ^{12}CO velocity dispersion (moment 2) map generated for pixels $T_A^* > 1$ K. Bottom: the ^{13}CO velocity dispersion contours overlaid onto a GLIMPSE 5.8 μm image. In both cases the contours begin at 0.5 km s^{-1} and increase by steps of 0.25 km s^{-1}

SW a mixture of the two. This suggests that there is complex three-dimensional structure and non-uniform orientation in the G305 complex that must be considered.

The CO lines allow the investigation of the distribution of turbulent velocities[11] within G305 (Fig. 3.18). The velocity dispersion ranges from 0.2–4.2 km s^{-1} with the ^{12}CO showing localised peaks of up to 6.1 km s^{-1}. The distribution of turbulent velocities is subtly different for the optically thick ^{12}CO and the optically thin ^{13}CO. Each lobe of molecular gas contains several prominent peaks and steep velocity gradients are clearly visible leading away from the central cavity at the interface between the PDR and molecular gas. These velocity gradients are particularly prominent in the ^{12}CO velocity dispersion map indicating possible interaction with external pressure forces such as HII regions (see Chapter 5).

3.7.2 Beam filling factor

The beam filling factor is assumed to be of order unity in the detection equation (Eq. B.64) and analysis presented in Section 3.5.6 and 3.6.4. This assumption can be tested using the calculated excitation and rotation temperatures derived from the NH_3 emission. A scatter plot compares the derived NH_3 excitation and rotation temperatures (Fig. 3.19), where the dashed line indicates the line of equality ($T_{ex} = T_{rot}$). For comparison the ^{12}CO excitation temperature corresponding to each NH_3 clump is presented by averaging the ^{12}CO derived excitation temperature map (Fig. 3.21) within the NH_3 boundaries defined by clump finding. This plot clearly shows that NH_3 rotation temperatures are systematically ~ 6 times higher than the NH_3 excitation temperatures whilst the ^{12}CO derived excitation temperatures are lower by less than a factor of two. Since the rotation temperature is derived from the line intensity ratio of the NH_3 (1,1) and (2,2) transitions the beam filling factor is effectively divided out and thus provides a more reliable estimate of the gas temperature.

The assumption of LTE implies that T_{ex} should be equal to T_{rot}. Hence, the derived values of T_{ex} are actually $\simeq T_{rot} \times \eta_{ff}$ and so the beam filling factor can be estimated from the ratio of the excitation and rotation temperatures, i.e. $\eta_{ff} = T_{ex}/T_{rot}$. Note the non-linear nature of the detection equation (Eq. B.64), however given that $J(T) \sim T$ in Eq. B.62 for $T \gg h\nu/k_B$, which corresponds to a temperature of 1.1 K at $\nu = 23$ GHz and so Eq. B.64 is approximately linear in T. Therefore the beam filling factor of the NH_3 observations has a mean value of $\eta_{ff} \approx 0.3$; this compares well to the values reported in the literature (cf. Urquhart et al. 2011; $\eta_{ff} \sim 0.3$–0.5). Accounting for a beam filling factor of 0.3 in the detection equation raises the average NH_3 excitation temperature from ~ 3 K to ~ 10 K in good agreement with the assumption made in Section 3.5.6.3. Assuming LTE and that they trace the same gas, the NH_3 rotational temperature is equal to the CO excitation temperature and so we arrive at a beam filling factor for the CO

[11]Moment 2: $\sqrt{\left(\Sigma\left(I \times (v - M1)^2\right)/\Sigma(I)\right)}$, where M1 is the first moment, v is the velocity and I is the intensity.

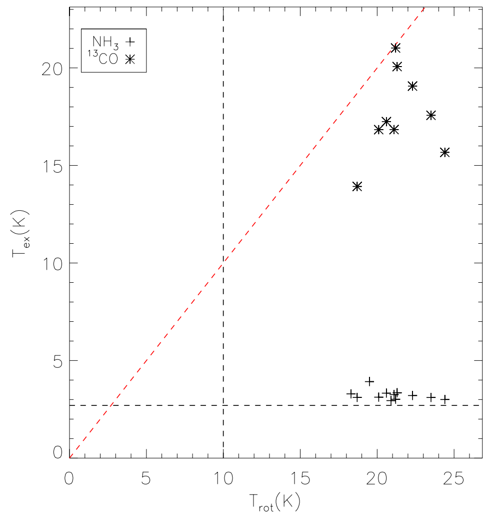

FIGURE 3.19: Plot comparing the derived excitation and rotation temperatures derived for NH_3 (crosses) and also the average ^{13}CO excitation temperature (stars, see text). The red dashed line indicates the line of equality. The black vertical line indicates the minimum cloud temperatures expected due to heating by cosmic rays and the UV radiation field ($\sim$ 10 K; Evans 1999), whilst the black horizontal line indicates the temperature of the cosmic microwave background radiation.

observations of $\eta_{ff} \approx 0.8$. It is unlikely that the NH_3 inversion transitions would be sub-thermally excited, whilst the CO rotation transitions are thermalised and so the low beam filling factors coupled with CO substructure confirms that high-contrast substructure exists within the NH_3 clouds.

3.7.3 Abundance ratios

The abundance ratio between the observed molecular gas tracers and H_2 (NH_3:H_2 and CO:H_2) is assumed to be constant across the complex. This assumption is implicit but almost certainly invalid as many processes affect the molecular abundance ratios (van Dishoeck & Blake, 1998) such as: photodissociation, fractionation and when the density is $> 10^4\,\mathrm{cm}^{-3}$ CO is likely to freeze-out onto dust grains (Bacmann et al., 2002). Therefore, the abundance ratio represents one of the largest sources of error in this study and warrants further investigation.

The abundance ratio of NH_3:H_2 has been found to vary from $\sim 1 \times 10^{-6}$, towards hot regions such as UC HII regions (Cesaroni et al., 1994), to $\sim 1 \times 10^{-8}$ in cold, low-mass, dark cores (Myers & Benson, 1983). These environments almost certainly exist within G305 and may even exist within a single $2'$ beam, therefore the measurements of the H_2 column density based on NH_3 could be up to two orders of magnitude higher than those presented in Table 3.8. This two order of magnitude difference is not due to NH_3 depleting on to dust grains as the derived kinetic temperatures are in excess of 20 K but may be due to NH_3 evaporating off the dust grain

NH_3 Clump	$N_{^{13}CO}$ $10^{16}(cm^{-2})$	N_{NH_3} $10^{16}(cm^{-2})$	$\chi(NH_3)$ 10^{-8}
1	8.61	0.19	3.01
2	5.93	0.26	5.63
3	5.62	0.33	7.99
4	6.08	0.46	10.28
5	5.17	0.21	5.47
6	4.44	0.10	3.17
7	4.95	0.17	4.71
8	5.51	0.44	10.77
14	6.36	0.32	6.73

TABLE 3.11: The NH_3 to H_2 abundance ratio derived for NH_3 based on the CO and NH_3 column density using Eq. 3.9.

ice mantles as they evolve and heat up. Compared to NH_3 the CO abundance ratio varies little in GMCs with reported variations of ~ 3 (Lacy et al., 1994). The average temperatures within the bounds of the NH_3 emission is > 20 K, which suggests that CO will not suffer significant freeze out onto dust grains and there should be minimal photodissociation towards the dense NH_3 clouds (Collings et al., 2003; Bergin & Tafalla, 2007).

We demonstrated that for observations of CO the beam filling factor is much nearer unity (Section 3.7.2) and assume that the CO:H_2 abundance ratio varies little compared to NH_3. We are therefore in a position to test the assumption that the NH_3 abundance ratio is constant across the G305 complex by comparing the CO and NH_3 column densities. The NH_3 abundance may be expressed as:

$$\chi(\mathrm{NH_3}) = \frac{N_{^{13}\mathrm{CO}}}{N_{\mathrm{NH_3}}}\chi(^{13}\mathrm{CO}) \tag{3.9}$$

where $N_{^{13}CO}$ is the ^{13}CO column density (Fig. 3.21) averaged over each NH_3 cloud, N_{NH_3} is the NH_3 column density and $\chi(^{13}CO)$ is the $^{13}CO:H_2$ abundance ratio assumed to be $^{13}CO : H_2 = 1.4\times10^{-6}$. For the NH_3 clouds with CO coverage the abundance ratio ranges between 1.0×10^{-7} to 8.0×10^{-8} with an average of 6.4×10^{-8} (Table 3.11). This suggests that the assumed NH_3 abundance of $\chi(NH_3) = 3 \times 10^{-8}$ may overestimate the NH_3 mass by a factor of two or three. The NH_3:H_2 abundance ratio is highest towards NH_3 Clouds 4 and 8, these clouds display the highest kinetic temperatures (28.8 ± 2.1 and 30.6 ± 2.9 K respectively) and may represent two of the most intense sites of star formation within G305. It is likely that towards these regions the internal heating provided by star formation is releasing complex molecules, including NH_3, from dust grains and is responsible for the increased abundance ratio (Viti et al., 2004).

^{13}CO Property	Min	Max	Mean	Median
T_{ex} (K)	12.54	23.8	17.05	17.01
$\tau_{^{13}CO}$	0.31	0.90	0.47	0.44
R (pc)	0.58	2.77	1.36	1.31
ΔV (km s^{-1})	2.09	6.94	4.12	4.17
V_{LSR} (km s^{-1})	−42.90	−17.70	−36.58	−37.90
$N_{H_2}10^{22}$(cm^{-2})	1.94	7.73	3.73	3.61
Mass 10^3(M$_\odot$)	0.4	22.0	4.4	3.6
$\sum_c$ 10^2(M$_\odot$ pc^{-2})	3.3	12.0	6.1	5.8
$M_{vir}10^3$(M$_\odot$)	1.1	12.0	5.3	4.6
α_{vir}	0.55	4.11	1.69	1.43
$n_{H_2}10^3$(cm^{-3})	2.7	8.9	5.4	5.4

TABLE 3.12: The global physical properties of the ^{13}CO clumps in G305.

NH_3 Property	Min	Max	Mean	Median
T_{kin} (K)	20.7	30.6	24.8	24.8
τ_{NH^3}	0.3	1.3	0.9	1.0
R (pc)	1.5	5.1	2.7	2.6
ΔV (km s^{-1})	1.7	7.1	4.0	3.8
V_{LSR} (km s^{-1})	−42.5	−32.2	−37.5	−37.3
$N_{H_2}10^{22}$ (cm^{-2})	1.9	15.3	8.2	8.2
Mass 10^3 (M$_\odot$)	3	122	49	46
$M_{vir}10^3$(M$_\odot$)	2	27	12	8
α_{vir}	0.1	1.6	0.35	0.26
$n_{H_2}10^3$(cm^{-3})	3	37	14	13

TABLE 3.13: The global physical properties of the NH_3 (1,1) clouds in G305.

3.7.4 General physical properties of the molecular material

A summary of the general physical properties derived following the analysis method described in Sections 3.5.6 and 3.6.4 is presented in Tables 3.12 and 3.13 and histograms of the CO clump physical properties can be found in Fig. 4.6.

The physical radius of the molecular emission ranges from 0.58–2.77 and 1.5–5.1 pc for ^{13}CO (1–0) (Fig. 3.20(c)) and NH_3 (1,1) respectively. The size of the NH_3 emission is significantly greater than the CO and similar surveys of NH_3 towards star-forming regions (e.g. Wu et al. 2006; 0.4–3.1 pc, Harju, Walmsley & Wouterloot 1993; ⟨0.3⟩ pc). This is due to the NH_3 emission in G305 being smoothed by the large Mopra beam (2′) at 22 GHz, which limits the NH_3 observations to resolving radii > 1.3 pc on the scale of molecular clouds (Table 1.1). On the other hand, the higher resolution provided by CO (30″) at 115 GHz resolves structure on the scale of molecular clumps (> 0.6 pc) and reveals significant substructure within the bounds of the NH_3 emission.

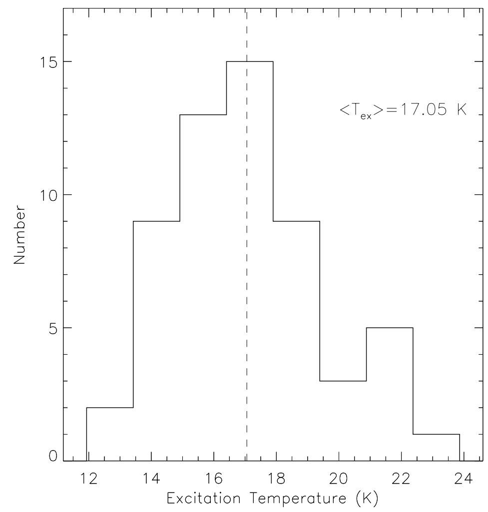

(a) Excitation Temperature

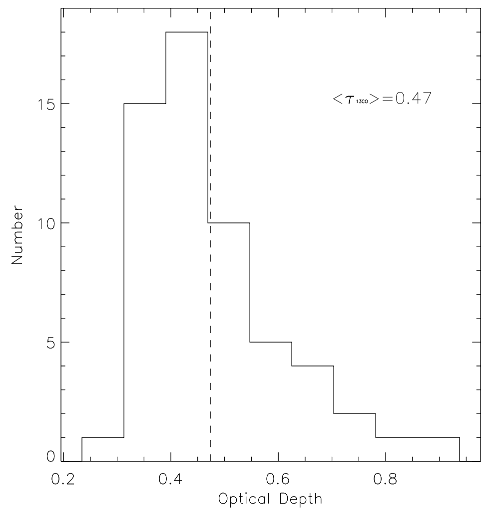

(b) Optical Depth

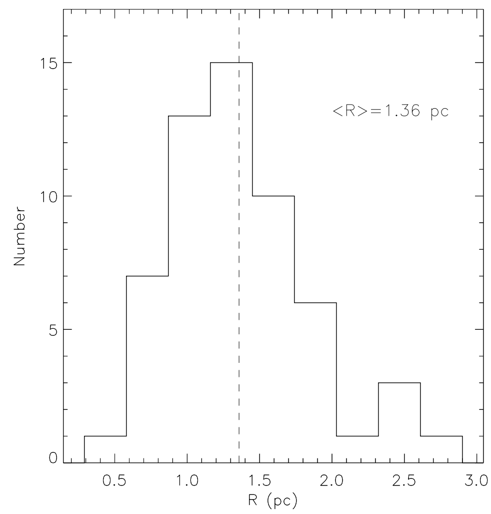

(c) Radius

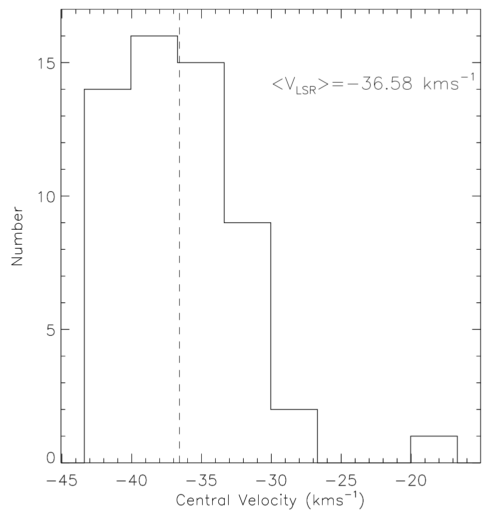

(d) Central Velocity

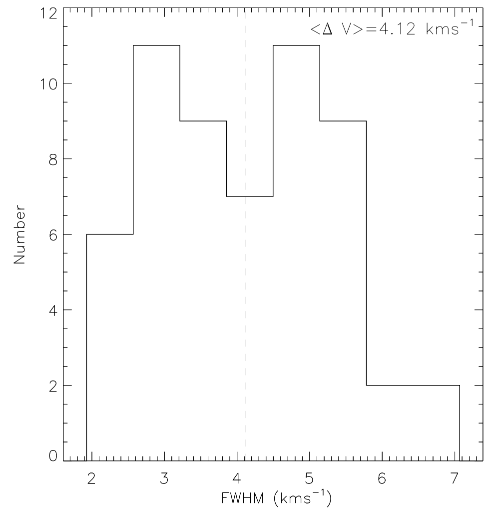

(e) FWHM

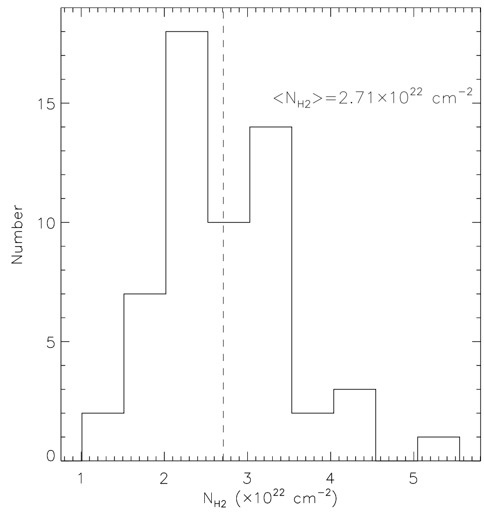

(f) Column Density

FIGURE 3.20: Histogram of the various physical properties derived for the 57 ^{13}CO clumps. A dashed line represents the mean that is presented in the top right of each plot.

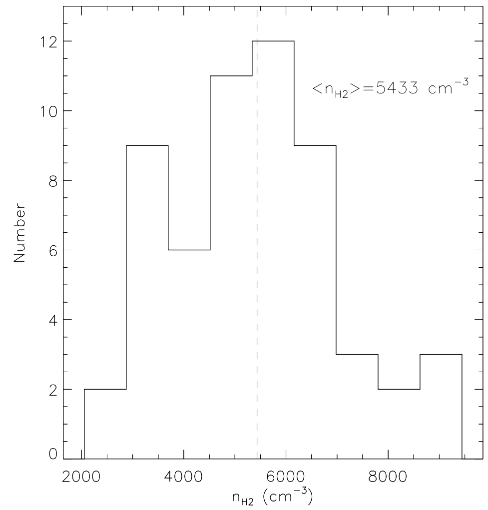

(g) Number Density

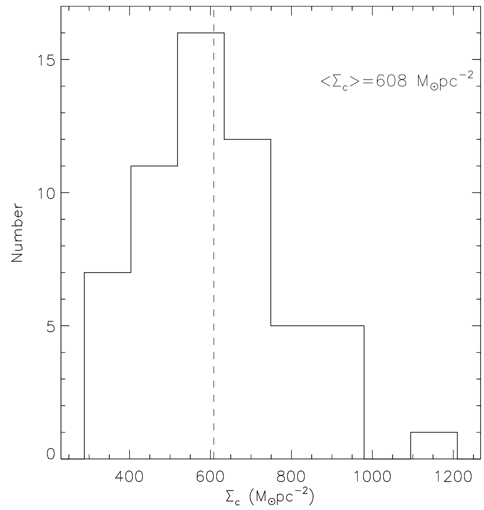

(h) Surface Mass

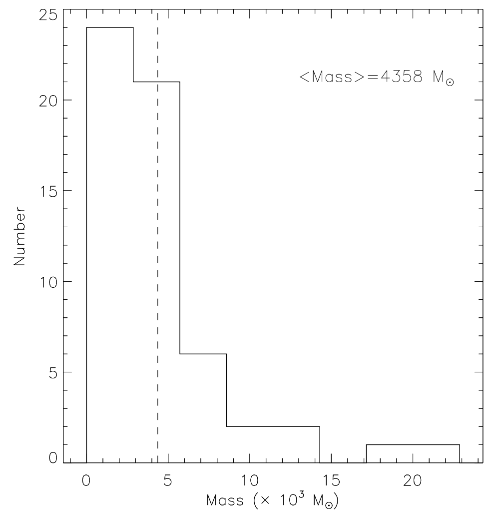

(i) Mass

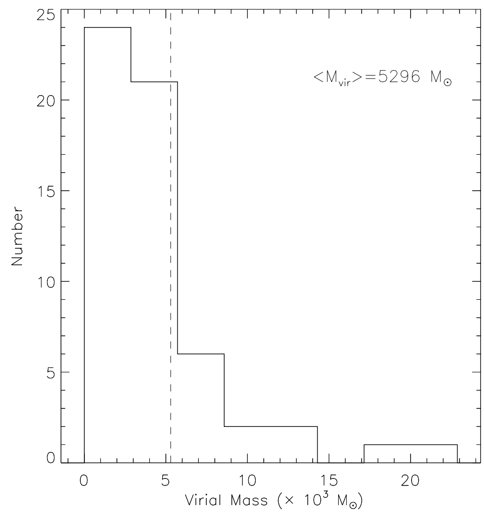

(j) Virial Mass

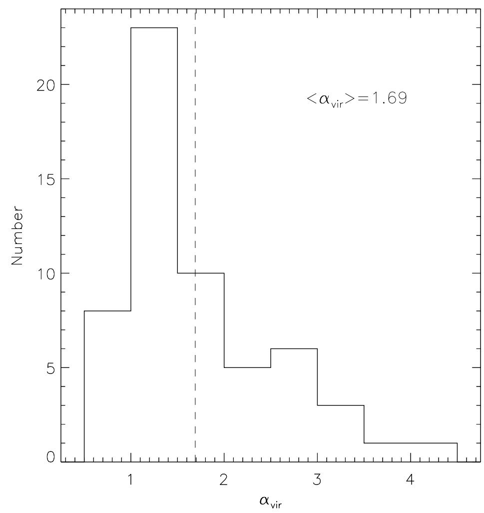

(k) Virial Parameter

FIGURE 3.20: continued.

The Galactic Ring Survey (GRS; Jackson et al. 2006; Rathborne et al. 2009; Roman-Duval et al. 2010) provides an excellent sample with which to compare the global properties of the molecular gas in G305. The GRS has sampled ^{12}CO and ^{13}CO in the Galactic plane with a spatial and velocity resolution of $\sim$ 46″ and 0.2 km s^{-1} respectively and a sensitivity of 4 K. The survey coverage is −5 to 135 km s^{-1} for Galactic longitudes $l \leqslant 40°$ and −5 to 85 km s^{-1} for Galactic longitudes $l > 40°$. The emission present in the GRS is smoothed to a resolution of 6′ and by using an altered form of the CLUMPFIND algorithm is decomposed into 829 large-scale clouds. Within the bounds of these clouds clump finding, using the standard CLUMPFIND algorithm, is performed on a full resolution image using identical input parameters to those presented in Section 3.6.1 and identifies 6135 clumps. Unfortunately, the GRS molecular clump analysis has not been published and so we are limited to comparing to the physical properties and analysis of the clouds identified in the GRS (Roman-Duval et al., 2010). On average the size of emission features presented here are lower than those presented in GRS ($\sim$ 8.3 pc).

The kinetic temperature of the NH_3 clouds range between 20.7–30.6 K with an average of 24.8 K. These values are more than twice what would be expected due to heating from the interstellar radiation field alone ($\sim$ 10 K; Evans 1999, Fig. 3.19). These temperatures would require the presence of either an internal or external heating source, both are possible as we know these clouds are associated with ongoing star formation and in close proximity to HII regions and massive stellar clusters. This observed range of NH_3 kinetic temperature is comparable to the values found in similar surveys of NH_3 emission (e.g. Harju, Walmsley & Wouterloot 1993; Purcell et al. 2009; Urquhart et al. 2011, i.e. 12.7–32.8 K, 15–47 K and 13.76–25.0 K respectively). The CO clump averaged excitation temperatures are lower than the NH_3 derived temperatures, ranging from 11.95 to 20.47 K with a mean value of 15.57 K for the entire complex (Fig. 3.20(a)). This may be due to the difference in resolution or may suggest a temperature gradient in the molecular material.

The CO excitation temperature is within the range expected for massive star-forming molecular gas (e.g. Guan, Wu & Ju 2008) but considerably higher than the average of 6.32 K found in the GRS. This may be a result of the high-density of star formation towards G305, the high clump finding cut off applied or the propensity of the GRS to trace cloud scale emission or the inclusion of low surface brightness diffuse emission in the GRS survey (Rathborne et al., 2009). The presence of even hotter gas is indicated by NH_3 (3,3) emission and so Clouds 1–5 and 8 are likely to be more evolved than other, cooler clumps. The clumps that exhibit (3,3) emission correlate well with PAH emission, with the strongest and therefore hottest clumps found close to the central cavity boundary. We will investigate the correlation of these clumps with star formation in Chapter 5.

The average column density ($N_{\mathrm{H_2}}$) of the molecular gas traced by CO (Fig. 3.20(f)) and NH_3 is 3.73 and 8.2×10^{22} cm^{-2} respectively and the highest values are found closest to the PDR boundary Fig. 3.22. The corresponding average H_2 density derived for the largest NH_3 clouds in the NE, NW and SW regions is $\sim 1 \times 10^3\,cm^{-3}$. This is an order of magnitude lower than the NH_3 critical density (10^4–$10^5\,cm^{-3}$ Stahler, S. W. & Palla, F. 2005). Conversely, the smallest NH_3 clouds have the highest H_2 number densities of $\sim 10^4\,cm^{-3}$. This appears to be a result of the large clouds in the NE, NW and SW regions being comprised of unresolved clumps, as seen in the CO morphology and Section 3.7.2, that have been smoothed into single clouds by the large Mopra beam. This drives down the estimated density for the largest NH_3 clouds but has less of an affect on the smaller clumps. The average H_2 density traced by CO ranges from 2.7–$8.9\times10^3\,cm^{-3}$ peaking towards the dense NH_3 cloud cores. The average surface density in G305 is $608\,M_\odot\,pc^{-2}$, this is a factor of four higher than the average in the GRS survey ($144\,M_\odot\,pc^{-2}$; Roman-Duval et al. 2010).

The mass of the NH_3 molecular clouds is in excess of a thousand solar masses, whilst CO traces clumps with mass down to $\sim 400M_\odot$. The total molecular mass of G305 indicated by CO clumps and NH_3 clouds is $\sim 2.5 \pm 0.8$ and $6.5 \pm 3 \times 10^5\,M_\odot$ respectively. The total CO mass is lower by a factor of 2.6, the reason for this may lie in the variation of the abundance ratio, high clump finding cut off level and the incomplete sampling of the CO emission towards G305. To investigate the mass of molecular gas in diffuse envelopes that may have been missed due to the high CO clump finding cut off the ^{13}CO mass has been derived using the global column density for emission above 4σ. Using this method the total molecular mass traced by ^{13}CO increases by approximately 20% to $\sim 3.0 \pm 1.0 \times 10^5\,M_\odot$. Therefore, the majority (> 80%) of the molecular gas traced by ^{13}CO in these incomplete maps of G305 is found within dense clumps.

The FWHM of the CO clumps (Fig. 3.20(e)) ranges between 2.09 and 6.94 km s^{-1} and shows a bimodal distribution with eleven clumps in each bin at 2.8 and 4.8 km s^{-1} either side of the mean (4.12 km s^{-1}). This suggests there are two separate populations of sources, one with low velocity dispersion and one with high velocity dispersion. We will discuss the correlation of these populations with star formation in Chapter 5.

The virial mass suggests that the majority (86%) of CO clumps are not gravitationally bound (i.e. $M_{\rm LTE} > M$, $\alpha_{\rm vir} > 1$) leaving only eight clumps that are bound ($M_{\rm LTE} < M$, $\alpha_{\rm vir} < 1$), (Fig. 3.20(k)) and may go on to collapse. In contrast 14 of the 15 NH_3 clouds are gravitationally bound $\alpha_{\rm vir} < 1$. Observation of the molecular clouds in the GRS found that 70% of the molecular clouds are gravitationally bound (Roman-Duval et al., 2010), which would agree with the derived NH_3 virial balance. Conversely, molecular material is most often found to be unbound on smaller clump scales and it has been suggested that this may be due to the transient nature of molecular clouds (Dobbs, Burkert & Pringle, 2011). This result suggests that the complex is bound on large-scales and mostly unbound on small scales. However, caution should be taken with this interpretation because this feature may simply be a result of different resolutions.

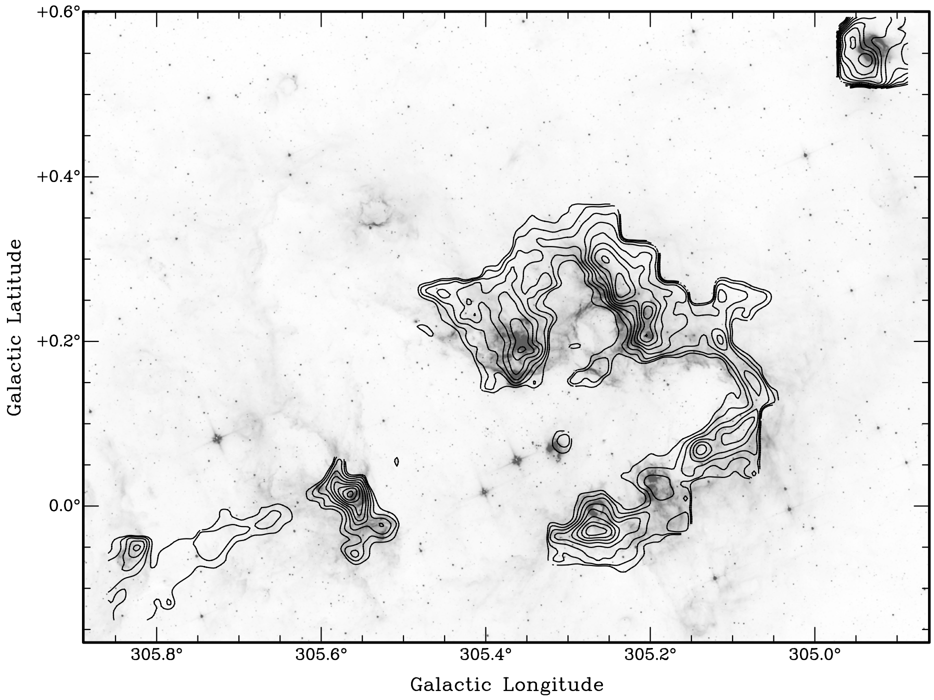

FIGURE 3.21: The spatial distribution of the ^{13}CO excitation temperature in the G305 complex overlaid onto a GLIMPSE 5.8 μm background. ^{13}CO excitation contours begin at 12 and increment by 2 K.

The physical properties and morphology give the impression that G305 is significantly more massive, dense and hot than many molecular clouds but appears to be representative of the general population of massive star-forming regions found in the Galaxy. The molecular material shows significant evidence of interaction with the ionised environment, appearing to be sculpted by powerful winds and ionising radiation.

3.8 The reservoir for future star formation

It is clear that there is sufficient molecular gas within the G305 complex to form multiple massive stars. The distribution of the dense molecular gas and mid-infrared emission suggests that this future star formation will occur around the central cavity and in close proximity to recent and ongoing star formation. There is approximately 6×10^5 $M_\odot$ of dense gas available to form stars in G305, however star formation is a highly inefficient process and so we might expect only between 2–17% (Williams & McKee, 1997) of this molecular gas to form stars. In addition not all of this molecular material is found in clumps that are likely to collapse, by considering the virial parameter we can examine how much of this material is in gravitationally unstable clumps that may collapse. As mentioned in Section 3.7.4 only 14% of the CO clumps are gravitationally unstable. By assuming G305 has a similar range of SFE only $\sim 8 \times 10^3$ $M_\odot$ is likely to form stars.

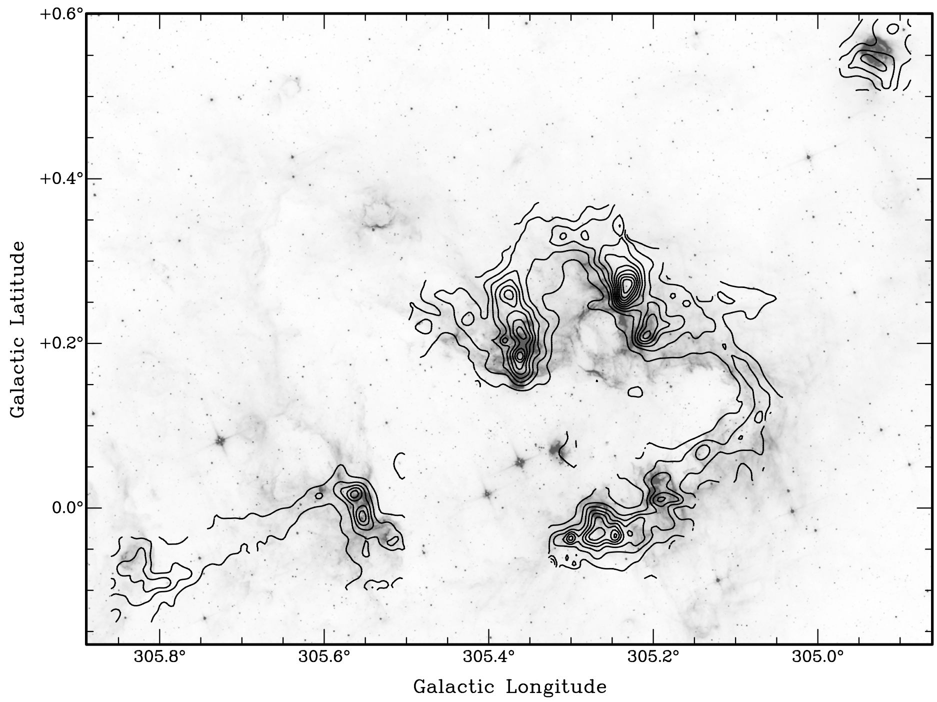

FIGURE 3.22: The spatial distribution of the ^{13}CO column density overlaid onto a GLIMPSE 5.8 μm background. ^{13}CO column density contours begin at 1×10^{16} and increment by 2.5×10^{16} cm^{-2}.

Examining the position of the eight bound CO clumps with $\alpha_{\mathrm{vir}} < 1$ reveals that six are associated with the most massive CO clumps on the periphery of the central cavity and two with the G304.93+0.55 region to the far North-West. All eight bound clumps are associated with bright mid-infrared emission, HII regions and the most excited and dense regions of the complex. These bound clumps have masses, surface densities, column densities, excitation temperatures and sizes well above the mean values and will be discussed in more detail in relation to the future star formation of G305 in Chapter 5.

The clump formation efficiency (CFE) is a measure of the fraction of molecular gas that has been converted into dense clumps. This quantity is analogous (or a precursor) to the star formation efficiency and provides an upper limit. The CFE is a time-integrated quantity expressed as:

$$CFE = \frac{M_{\mathrm{dense}}}{M_{\mathrm{dense}} + M_{\mathrm{diffuse}}} = \frac{1}{M_{\mathrm{diffuse}}} \int_0^t \frac{dM}{dt}\, dt \tag{3.10}$$

where dM/dt is the rate of dense clump formation from the available gas. Therefore, a high value for the CFE can indicate either a high clump formation rate or a long formation timescale.

The CFE may be determined for G305 by cross matching the mass of dense and diffuse gas derived in the NH_3 and CO analysis respectively. This is achieved by deriving the mass of the ^{13}CO clumps within the bounds of the NH_3 clouds along the line of sight using the ^{13}CO column

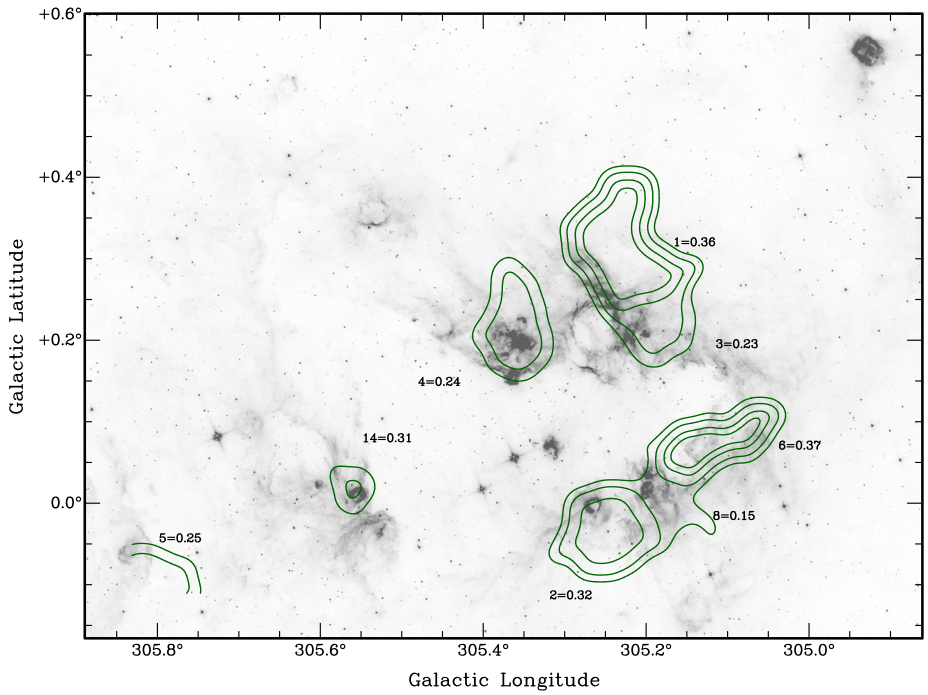

FIGURE 3.23: The derived CFE of the molecular clouds in G305 is presented by green contours at the 0.1, 0.2 0.3 and 0.35 levels. The NH_3 clump numbers, for which the CFE can be calculated are presented with the corresponding CFE.

density (Fig. 3.22). The various uncertainties associated with the NH_3 and CO derived mass and complications with the comparison of the two studies leads to uncertainties in the CFE on the order of 50%. However, the relative CFE should be comparable because any variations ought to be constant across the complex.

The CFE within G305 varies from 15% to 37% with an average of 28%. These values are similar to the CFEs estimated in a number of similar regions such as 20% for the entire W43 star-forming complex (Nguyen Luong et al., 2011), ~ 1–2% in quiescent gas and ~ 20–40% toward regions of star formation in the W3 GMC (Polychroni, Moore & Allsopp, 2012; Moore et al., 2007). Finally, the CFE towards W43 shows a significant increase in the CFE towards HII regions from 3.6 up to 55% (Eden et al., 2012). The Global CFE of G305 may be derived from the CO mass derived for the whole complex. This gives a CFE of 68%, however this is an upper limit due to the incomplete mapping in CO and the only way to address this would be to obtain a complete map of the complex. As has been shown, the majority of the molecular gas is unbound and only 14% of the CO molecular clumps are gravitationally bound. It is therefore more informative to report the clump formation efficiency of bound clumps (BCFE), as this is more likely to reflect how the star formation efficiency will evolve over time. We estimate the BCFE using:

$$BCFE = \frac{M_{\alpha<1}}{M_{\rm dense} + M_{\rm diffuse}} \tag{3.11}$$

where the total mass in bound CO clumps is $M_{\alpha<1} = 8.6 \times 10^4\,{\rm M}_\odot$. We find that for the G305 complex the BCFE is $\sim 10 \pm 5\%$. The BCFE is comparable to the CFE reported for the regions described above and comparable to the SFE of molecular clouds within the Milky Way ($\sim$ 2–17% Williams & McKee 1997). Next we examine the relationship between star formation and the surface density of molecular gas.

The turbulent core model proposed by Krumholz & McKee (2008) predicts that the surface density threshold necessary for the formation of massive stars of 10–200 $\rm M_\odot$ is 1 g cm^{-2}. Below this threshold the molecular gas is thought to fragment into much lower masses. By converting the range of CO derived surface densities presented in Table 3.10 to units of g cm^{-2} we are able to test this model and determine if molecular gas in G305 is suitable for massive star formation as proposed by Krumholz & McKee (2008). We find that the CO surface density lies between 0.07 and 0.25 g cm^{-2} with a mean of 0.12 g cm^{-2}. Based on the 1 g cm^{-2} threshold none of the CO clumps in G305 are capable of forming massive stars. This is clearly not the case, in Chapter 2 we presented a number of methanol masers that are a clear indication of ongoing massive star formation. It is possible that on scales smaller than the resolution of the CO and NH_3 observations the surface density exceeds this critical threshold but we are unable to resolve such dense gas due to beam dilution. Higher resolution observations of the dense gas and dust are required to probe the substructure and determine if the environment is conducive to massive star formation based on the surface density threshold presented by Krumholz & McKee (2008).

This trend of surface densities below the 1 g cm^{-2} threshold has been reported in a number of studies and we present three of these for comparison. The Balloon-Borne Large Aperture Submillimeter Telescope (BLAST; Pascale et al. 2008) recently surveyed the star-forming region Cygnus X (Roy et al., 2011) in search of thermal emission from dust at a resolution of 30–60″. Roy et al. (2011) report on the surface density and find that only approximately eight out of 183 cold dust cores exceed the 1 g cm^{-2} surface density threshold. high-resolution *Herschel* observations (5–35″ for 70–500 µm; Pilbratt et al. 2010) of compact dust condensations as part of the Hi-GAL survey (Molinari et al., 2010b) between $l, b = 30°, 0°$ and $l, b = 59°, 0°$ (Elia et al., 2010) reveal that of a sample of 528 and 444 cores only 10 are above the 1 g cm^{-2} threshold. Finally a recent study by Parsons, Thompson & Chrysostomou (2012) studied the molecular gas associated with the W51 complex using observations of ^{13}CO J = 3–2 and found surface densities ranging from 0.002–0.19 g cm^{-2} with a median of 0.02 g cm^{-2}, well below the critical surface density. Whilst the low-resolution observations presented in this chapter are likely to underestimate the surface density due to beam dilution it appears that observationally this threshold does not apply in many cases. One possible explanation put forward by Roy et al. (2011) is that these sub 1 g cm^{-2} surface density regions represent the precursor of clumps that will evolve over time and increase in mass until this threshold is reached and massive star formation commences.

This situation regarding the reservoir for future star formation is somewhat of a paradox, whilst the CFE of G305 is comparable to other well-known massive star-forming regions the virial parameter and surface density suggests that the molecular gas is mostly unbound and unable to form massive stars. This is clearly not the case as there are numerous signs of ongoing star formation (e.g. methanol masers, YSOs) in G305 as will be demonstrated in the next Chapter and explored further in Chapter 5.

3.9 Relationship between molecular gas and star formation

Discussion of the relationship between star formation tracers presented in Chapter 2 and the molecular material is deferred to Chapter 5 where we present a full discussion of the distribution, rate and history of star formation in the G305 complex. In this section the discussion is limited to star formation that is revealed by the two molecular line studies. This includes H_2O masers and the search for outflow motions within G305.

The identification of 16 H_2O masers suggests there is ongoing star formation in G305. Fourteen of these masers are associated with NH_3 emission and in 12 instances these masers are found towards the dense NH_3 cores (Fig. 3.15). These tracers of ongoing star formation are not limited to the periphery of the central cavity but extend out into the Eastern region with NH_3 Clump 5 showing the highest density of H_2O maser emission. The lack of bright 5.8 μm emission towards these Eastern H_2O masers suggests that they are most likely tracing low-mass star formation. We note that H_2O maser 8 is projected against the centre of the cavity less than 2 pc from Danks 2 and is associated with bright mid-infrared emission referred to as the “blob” in Chapter 2 Section 2.5.2. This may be a projection effect, where we are seeing the star formation occurring at the front or back of the complex. In a study of the GMC RCW106 Breen et al. (2007) report on the detection of nine H_2O masers and draw comparisons with ^{13}CO data. This study reveals that H_2O masers are found to be associated with bigger, brighter, more massive and dense ^{13}CO clumps. This appears to be the case in G305, with H_2O masers being found embedded within the bright ^{13}CO clumps (Fig. 3.15). The H_2O masers towards G305 reveal that star formation is not confined to the periphery of the central cavity but extends out to the East of the complex.

3.9.1 Outflow candidates in G305

We made use of the ^{12}CO emission map to search for outflows associated with molecular material in G305. Unfortunately, the ^{12}CO $J = 1$–0 transition is not ideal for outflow detection

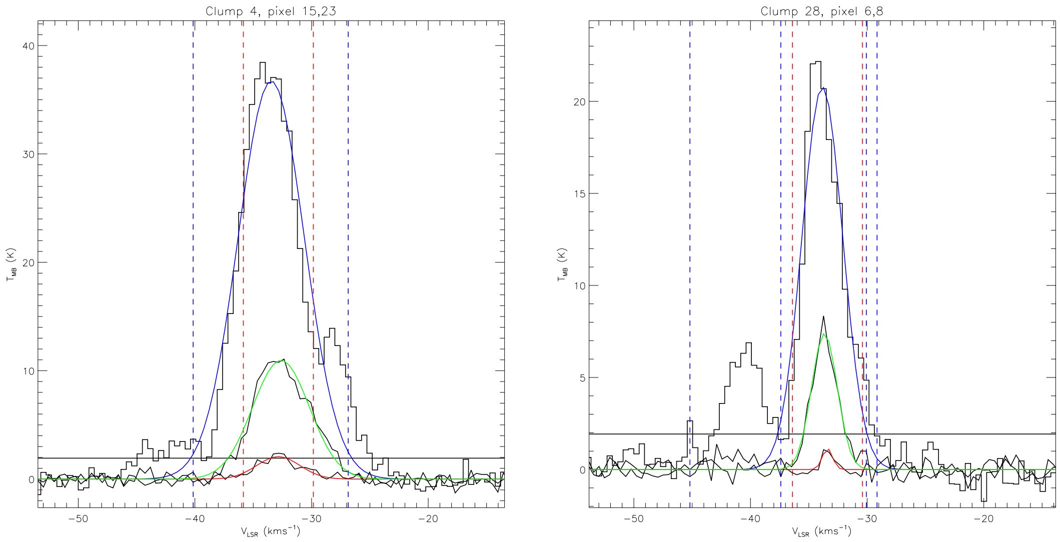

FIGURE 3.24: An example of the spectral search for outflows following the criteria of Hatchell, Fuller & Richer (2007). The ^{12}CO, ^{13}CO and C^{18}O spectra are presented with fitted Gaussians in blue, green and red respectively. Red vertical dashed lines show $\pm 3\,\mathrm{km\ s^{-1}}$ from the C^{18}O central velocity. In the left panel the blue horizontal dashed line shows the point at which the ^{12}CO Gaussian falls below $3\sigma_{^{12}\mathrm{CO}}$. In the right panel this criterion is relaxed and the dashed blue line shows the point at which the ^{12}CO emission is above $3\sigma_{^{12}\mathrm{CO}}$. Line wing emission is searched for between the red and blue dashed lines.

because it is easily excited in diffuse regions that obscure outflow velocity structure making it difficult to separate outflows from the surrounding low-density gas. Nevertheless, ^{12}CO $J = 1$–0 emission is still a useful outflow tracer when performing wide-field observations of nearby emission (e.g. Shepherd & Churchwell 1996b,a; Arce et al. 2010) where it may be used to lay the foundation for future follow-up observations in higher J transitions. To make the detection of outflows in G305 both efficient and robust requires a combination of the methods described in Section 1.5.4.1. The automated identification of line wing emission is objective and simple to code, however the chance of false-positive identification in G305 is high due to the complex velocity structure along the line of sight.

First, we search the spectral profile of each pixel (l, b) for ling wing emission using the criterion of Hatchell, Fuller & Richer (2007) in the following way: first the pixel is checked for C^{18}O emission above $3\sigma_{\mathrm{C}^{18}\mathrm{O}}$ to determine the systematic velocity of the clump. If the pixel meets this criterion Gaussian fitting is then applied to the CO spectral profiles. Line-wing emission is confirmed if the ^{12}CO spectral profile is $> 3\sigma_{^{12}\mathrm{CO}}$ above the fitted ^{12}CO Gaussian (where the Gaussian profile is $> 3\sigma_{^{12}\mathrm{CO}}$) at velocities greater than $\pm 3\,\mathrm{km\ s^{-1}}$ from the systematic velocity (Fig. 3.24, left). If a pixel satisfies these conditions, it is assigned to a positive detection mask (Fig. 3.25, green).

Complications arise when analysing spectra that have complex line profiles that are not well fit by a single Gaussian. Such spectra may represent outflows or multiple clumps along the line

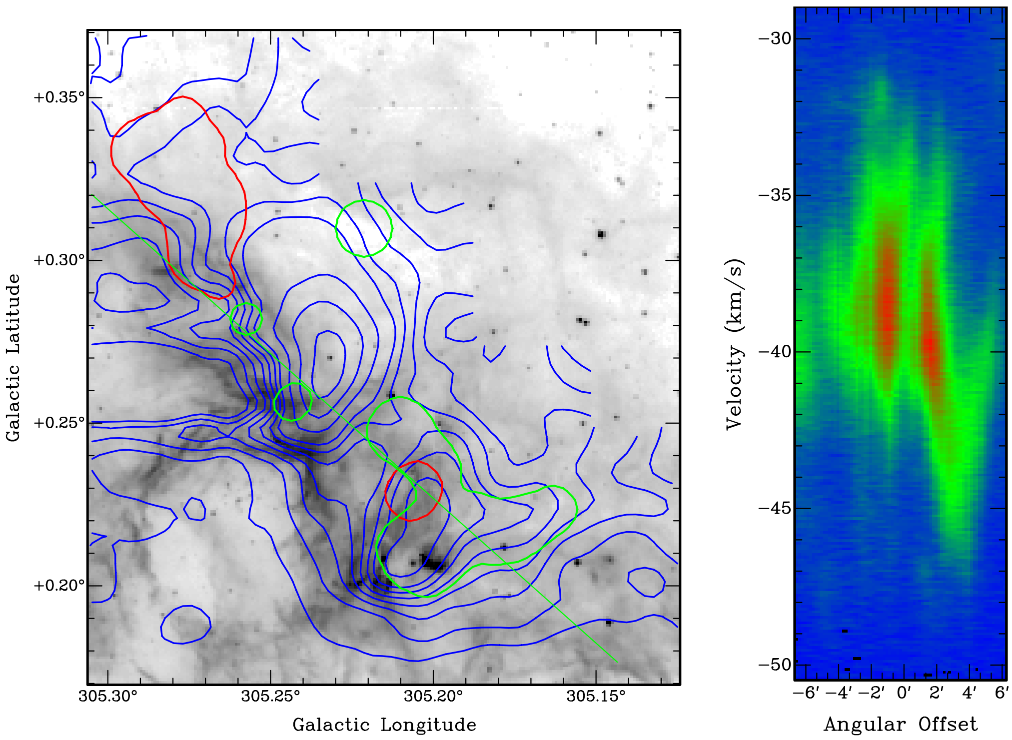

(a) North West

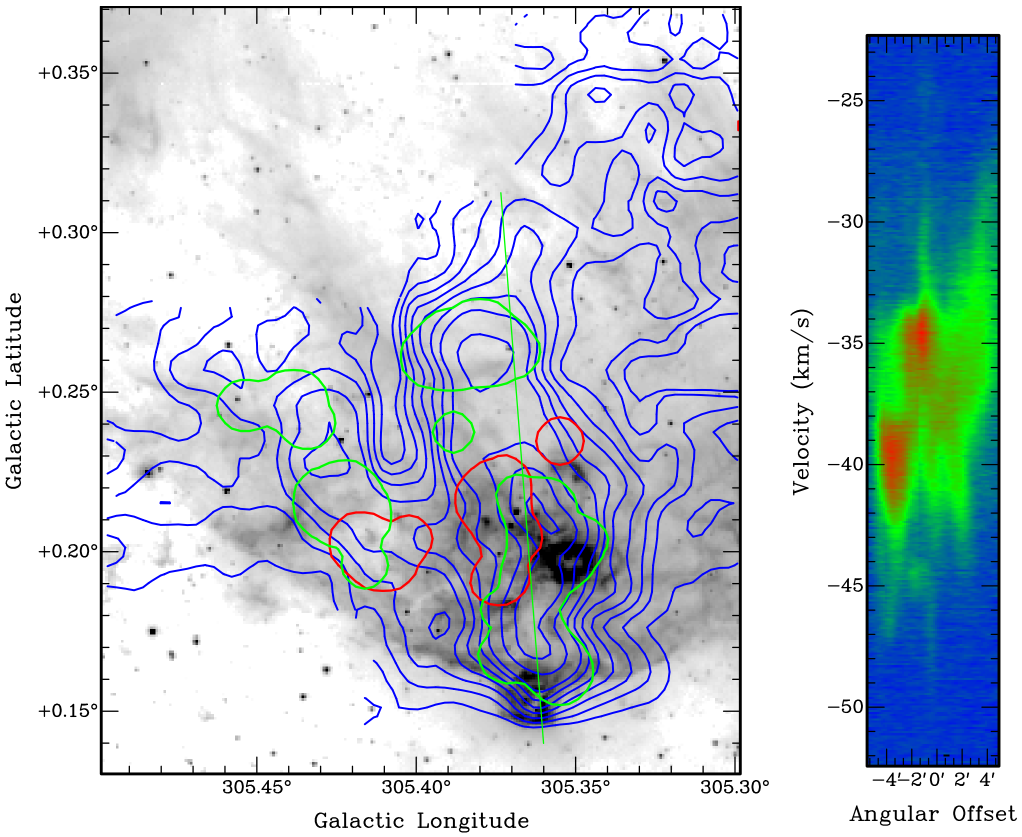

(b) North East

FIGURE 3.25: The results of searching the CO clumps for velocity structure indicative of outflows via the objective criteria of Hatchell, Fuller & Richer (2007). Green contours highlight regions of pixels that match the criteria whilst red contours have had the Gaussian $3\sigma_{^{12}\mathrm{CO}}$ limit relaxed. Blue contours correspond to the integrated ^{13}CO emission and these are overlaid onto a 5.8 μm GLIMPSE image. PV diagrams corresponding to the green straight lines have been constructed.

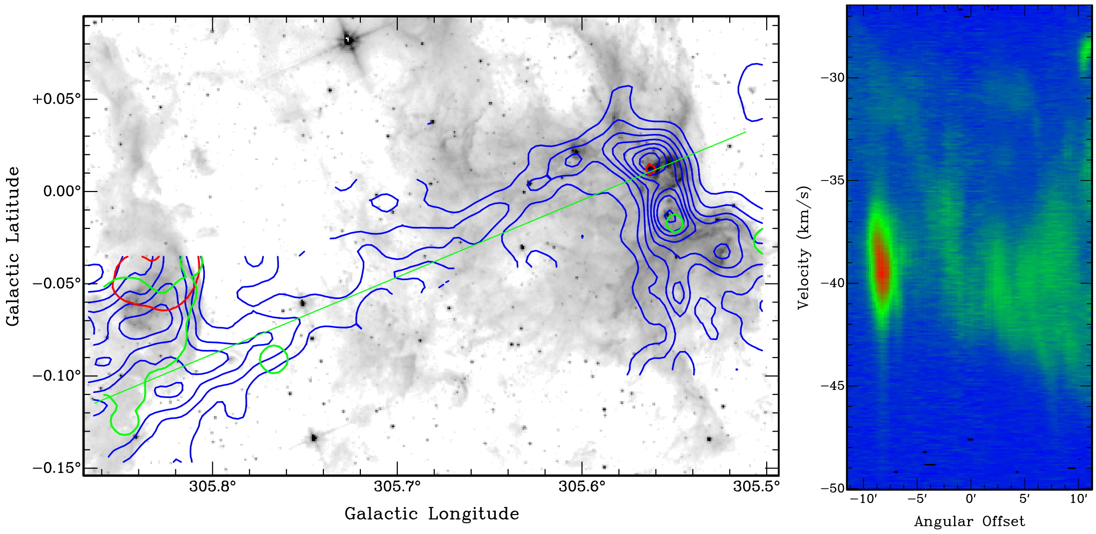

(c) East

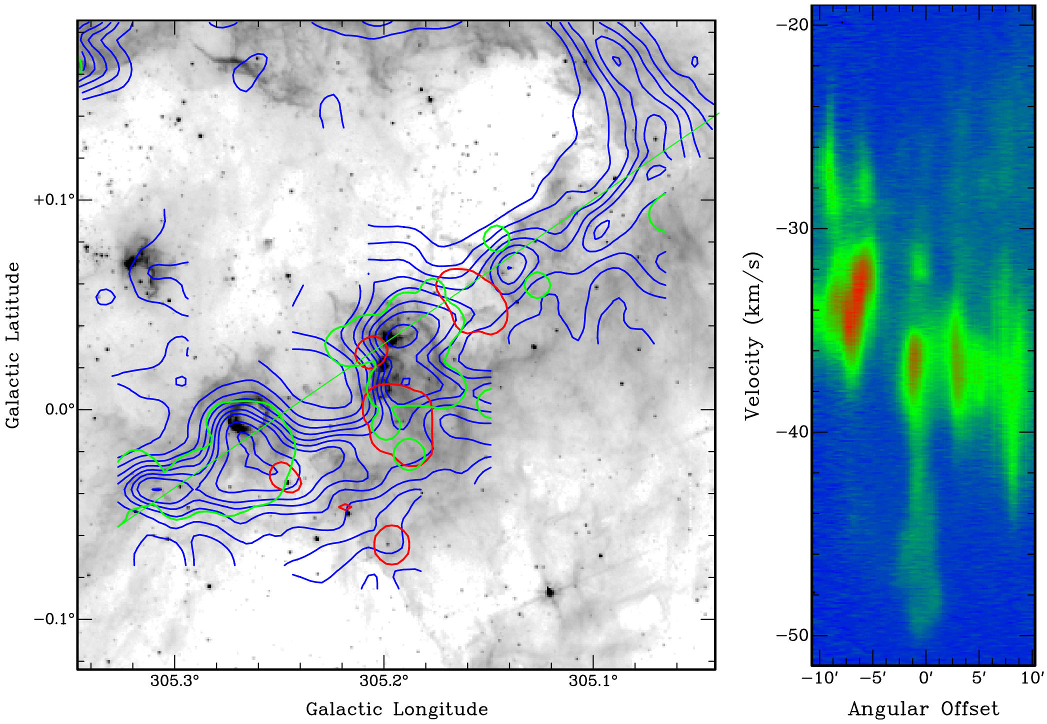

(d) South West

Figure 3.25: continued.

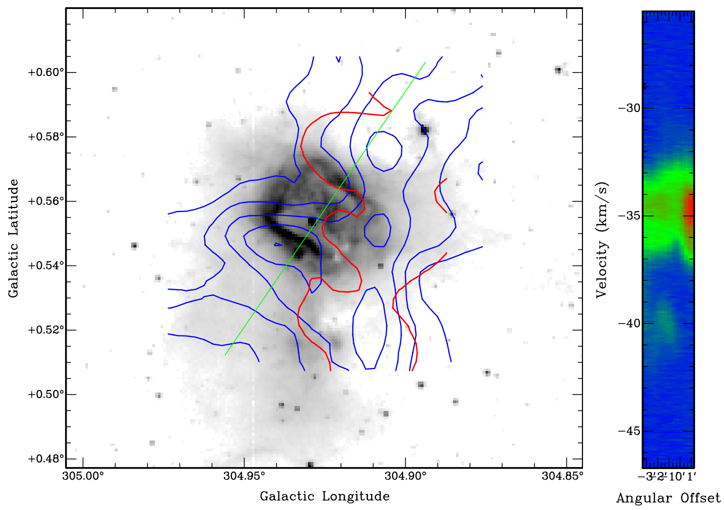

(e) Far North West

FIGURE 3.25: continued.

of sight and so are flagged for further consideration. These pixels are excluded in the method described above but are accounted for by relaxing the requirement that the line wing emission be above the fitted Gaussian by $3\sigma_{^{12}CO}$ (Fig. 3.24, right). These sources are included in the positive detection mask as possible outflow sources (Fig. 3.25, red).

This method reveals $>$ 1000 spectral profiles with outflow motions within 35 clumps and a further 458 possible pixels in eight clumps (Fig. 3.24). Caution should be taken as there is likely to be a number of false positive detections due to multiple velocity components along the line of sight or other unusual velocity structures in the ambient cloud.

To explore the nature of these outflow candidates further, PV diagrams are constructed that bisect the outflow candidate positions (Fig. 3.25). In all regions velocity dispersions from the quiescent cloud velocity of $\sim$ 5–10 km s^{-1} can be seen in the ^{12}CO profiles this is highly suggestive of outflow motions, large envelopes of diffuse gas or multiple sources along the line of sight. Finally candidate outflow regions are examined in three-dimensions using the ^{12}CO map and GAIA3D[12]. Identification via this method highlights the difficulties faced due to the low excitation energy and large distance, making it difficult to pick out outflows from the surrounding diffuse emission. Nevertheless, prominent deviations from the systematic clump velocity can be seen in a number of regions Fig. 3.17.

It is difficult to resolve individual outflows with a beam of 30$''$ at a distance of 3.8 kpc using ^{12}CO J =1–0 because outflow motions blend with the low surface brightness emission. Nevertheless, 35 strong detections of outflow regions have been identified with an additional 8 possible detections. In combination with PV and three-dimensional diagrams, this provides evidence of

[12]http://star-www.dur.ac.uk/ pdraper/gaia/gaia3dvis/index.html

outflows around the rim of the central cavity. Higher resolution and excitation transition observations such as ^{12}CO J=2–1 or 3–2 are required in order to reduce the impact of diffuse, low excitation temperature emission and resolve outflow structure.

3.10 Summary

This chapter presents observations, analysis and interpretation of the molecular gas traced by CO and NH_3 in the G305 complex. The global physical properties and morphology is discussed in some detail and compared to other studies. The reservoir for future star formation and its potential for ongoing star formation are explored. The relationship between the star formation indicated by the molecular line observations is then presented. The relationship of the molecular and ionised gas with recent and ongoing star formation will be discussed in more detail in Chapter 5. The following are the main conclusions of this chapter:

- The distribution and morphology of the molecular material is suggestive of interaction between the ionised and molecular environments. The Northern and Southern lobes of molecular gas in G305 are separated by $\sim$ 10 km s^{-1} suggesting that the complex may be expanding and is not being viewed face on.
- We have estimated the physical properties of the molecular gas in G305 and present a summary in Tables 3.10 and 3.13.
- G305 contains a large reservoir of dense gas for future star formation ($\sim$ 6 $\times$ 10^5 M$_\odot$). Only 14% of the CO clumps are gravitationally bound but these clumps represent more than 30% of the total, CO derived, mass. The location of these clumps suggests that future star formation will occur around the periphery of the central cavity within the most massive molecular clumps.
- G305 has a clump formation efficiency of $\sim$ 27% with local variations from 15 to 37% whilst the bound clump forming efficiency is $\sim$ 10%. These values reflects an upper limit to the star formation efficiency and are comparable to other well-known massive star-forming regions.
- There are 16 H_2O masers distributed throughout the complex. These are concentrated around the central cavity and extend out to the East demonstrating that there is significant ongoing star formation within G305.
- Potential outflow motions are detected towards 35 clumps with a further eight weaker detections. This demonstrates there is significant turbulent motion within the molecular material and provides an excellent pathfinder for future follow-up.

Chapter 4

The Ionised Environment: small- and large-scale radio continuum

This chapter is in part based on the article, Hindson et al. (2012), published in "Monthly Notices of the Astronomical Society".

4.1 Motivation

Observations presented in Chapter 3 reveal that the molecular gas in G305 is concentrated around the central cavity coincident with the PDR. The morphology and velocity distribution of this molecular gas suggests that there is interaction between the ionised and molecular environment. In addition, the detection of H_2O masers reveals embedded star formation within the dense molecular gas. However, H_2O masers are known to form in both low- and high-mass star-forming regions. In order to understand the formation and impact of massive stars in G305 requires that we identify the youngest examples of massive star formation and the energy input of massive stars into the region. One of the best tracers of massive star formation is the HII region they generate. By obtaining high-resolution and sensitive radio continuum observations the evolutionary sequence of HII regions from $< 10^5$ up to $> 10^6$ yrs can be uncovered to reveal the distribution of massive star formation.

Previous radio continuum observations of G305 have had insufficient resolution to resolve the radio continuum substructure of G305 (Goss & Shaver, 1970; Retallack, 1979) at the level required to detect UC and compact HII regions or have been at high-resolution but limited in spatial sensitivity and observing area (Walsh et al., 1998). We are therefore unable to resolve the relationship between the ionised and molecular environment or recent and ongoing star formation. For this reason we set out to obtain multi-scale, high-resolution and sensitive observations of the radio continuum towards G305 that are sensitive enough to detect the faint ($< 20\,\mathrm{mJy\,beam^{-1}}$) and compact ($< 0.1$ pc) ionised gas associated with UC HII regions and yet retain sufficient dynamic range and spatial sensitivity to detect compact and classical HII regions.

4.2 Australia Telescope Compact Array

FIGURE 4.1: The ATCA in a compact hybrid array configuration.

The radio observations presented in this chapter were obtained using the Australia Telescope Compact Array (ATCA) located at the Paul Wild Observatory, Narrabri, New South Wales, Australia [1]. The ATCA consists of 6×22 m antennas, five of which lie on a 3 km East-West (E-W) railway track with the sixth antenna located 3 km further West. The array also has a 214 m North spur that allows the antenna to be positioned in compact "hybrid" array configurations where the extra North-South baseline orientation allows denser sampling of the *u*-*v* plane in a shorter time interval. The antennas can be positioned in several configurations with maximum and minimum baselines of 6 km and 30 m respectively.

4.2.1 Compact Array Broadband Backend

These observations were made possible by the upgraded Compact Array Broadband Backend (CABB) installed on the ATCA between March and April 2009 (Wilson et al., 2011). The CABB upgrade provides a wide-bandwidth correlator for the ATCA, significantly more versatile and powerful than the original correlator. The CABB improves the maximum bandwidth of the ATCA from 128 MHz to 2 GHz, a 16-fold increase, in two independently tuneable IFs. CABB provides a number of improvements particularly relevant to this study such as reducing

[1]The Australia Telescope Compact Array is part of the Australia Telescope National Facility, which is funded by the Commonwealth of Australia for operation as a National Facility managed by CSIRO.

the time required to reach any particular continuum sensitivity and increased sampling depth allowing higher dynamic range imaging and lower T_{sys}. The increased bandwidth also results in improved multi-frequency synthesis (MFS; see Taylor, Carilli & Perley 1999; Sault & Wieringa 1994) allowing the spectral behaviour of continuum sources to be studied without resorting to frequency switching. The CABB has made OTF mapping of large areas at high sensitivity and resolution with the ATCA practical for the first time and the observations presented below were the first wide-area mosaic observations attempted with the CABB (see Wilson et al. 2011 Section 6.1).

4.3 Observations

Wide-area observations of the radio continuum emission associated with GMCs using interferometric methods are challenging because GMCs consist of complex emission on a wide range of spatial and brightness scales. Therefore, observations must take into consideration a number of limiting factors and be planned accordingly (Taylor, Carilli & Perley, 1999). Interferometers act as spatial filters and to obtain sensitivity to a wide range of spatial scales requires uniform *u*-*v* coverage from short ($\sim$ 30 m) to long ($>$ 5 km) baselines. No matter how short the baseline, interferometric observations will suffer from a lack of *u*-*v* coverage at short spacing, the so called “zero spacing” problem that leads to a loss of information regarding large-scale extended emission and can severely impact observations. Finally, imaging wide-areas requires “snapshot” observations, in this observing mode individual fields are sampled using short integration times at multiple hour angles during an observing track, this allows wide-areas to be mapped but results in sparse *u*-*v* sampling of individual *u*-*v* fields.

To map the G305 complex at 8.8 GHz with a primary beam of $5.3'$ a hexagonal grid of 357 individual fields is required (Fig. 4.2) leading to over sampling at 5.5 GHz where the beam is $8.5'$. As a hexagonal pattern can increase the drive time between points, the mapping strategy was optimised to decrease the drive time between points and increase the dwell time on any one mosaic position.

To ensure sensitivity to both small- and large-scale emission (high and low spatial frequencies respectively) the observations were carried out using six array configurations. These were the predominantly long baseline E-W arrays 6A, 1.5A and 750B and the short baseline hybrid arrays H214, H168 and H75 (Table 4.1). Observations were made simultaneously at two IF bands centred at 5.5 and 8.8 GHz utilising the wide-band continuum mode of CABB. This resulted in a bandwidth of 2 GHz with 2048×1 MHz channels in each IF. At the longest baseline of 6 km we obtain a maximum resolution of $1.5 \times 1.4''$ and at the shortest baseline of 30 m we are sensitive to emission on a scale of $\sim$ 5 and $\sim$ $3'$ at 5.5 and 8.8 GHz respectively.

Array Config	Date dd/mm/yy	Synthesised Beam (″)	Baseline Range (m)
750B	26/02/10	9.3 × 10.5	168 – 4500
1.5A	28/07/09	4.8 × 5.4	153 – 4469
H75	10/07/09	87.0 × 87.0	31 – 82(4408)
6A	06/06/09	1.5 × 1.4	628 – 5939
H214	23/05/09	33.6 × 33.6	92 – 247(4500)
H168	10/05/09	40.8 × 40.8	61 – 192(4469)

TABLE 4.1: Observational parameters for ATCA radio observations. Bracketed baseline ranges for the hybrid arrays represent the maximum baseline including the sixth antenna.

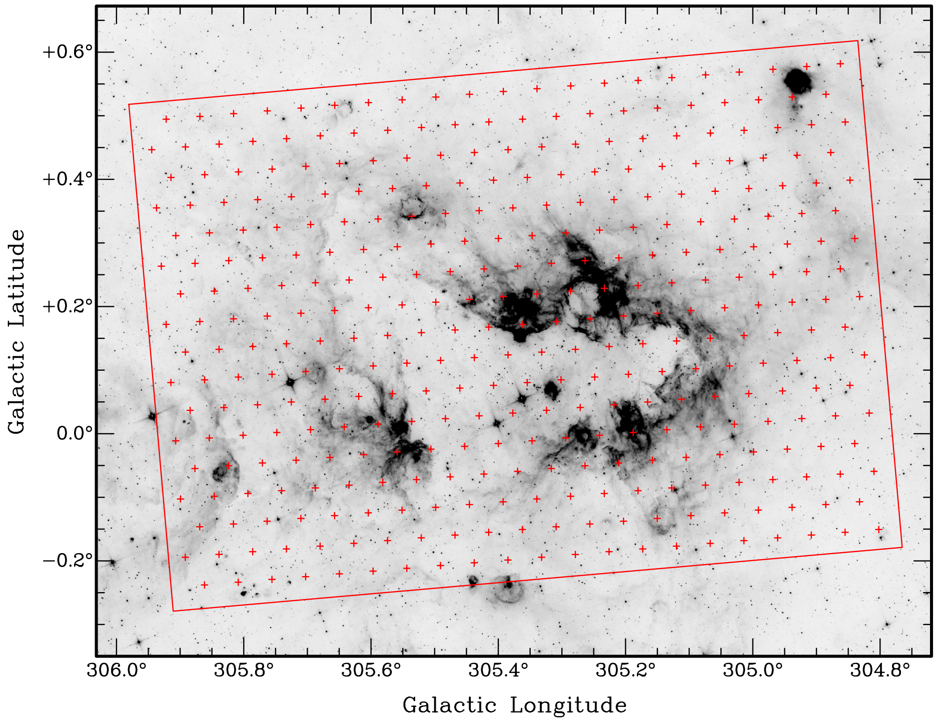

FIGURE 4.2: The ATCA radio continuum observations consisted of 357 individual fields distributed across G305 in an overlapping hexagonal pattern at 8.8 GHz with a primary beam field of view of 5.4′ to ensure Nyquist sampling.

The E-W and hybrid array snap-shot observations were made over a twelve- and six-hour period respectively to provide good hour angle coverage. To correct for fluctuations in the phase and amplitude, caused by atmospheric and instrumental effects, the total scan time is split into blocks of 15 minutes of on source integration sandwiched between 2-minute observations of the phase calibrator 1352-63. For absolute calibration of the flux density the standard flux calibrator 1934-638 was observed once during the observation for approximately 10 minutes. To calibrate the bandpass the bright point source 1253-055 was also observed during the observations. With a dwell time of 2s per point, spaced over a range of hour angles, to improve *u*-*v* coverage, a complete map took approximately one hour and in total each pointing centre was observed ∼ 7 and 11 (Fig. 4.3) times for each hybrid and E-W configurations respectively. The *u*-*v* coverage

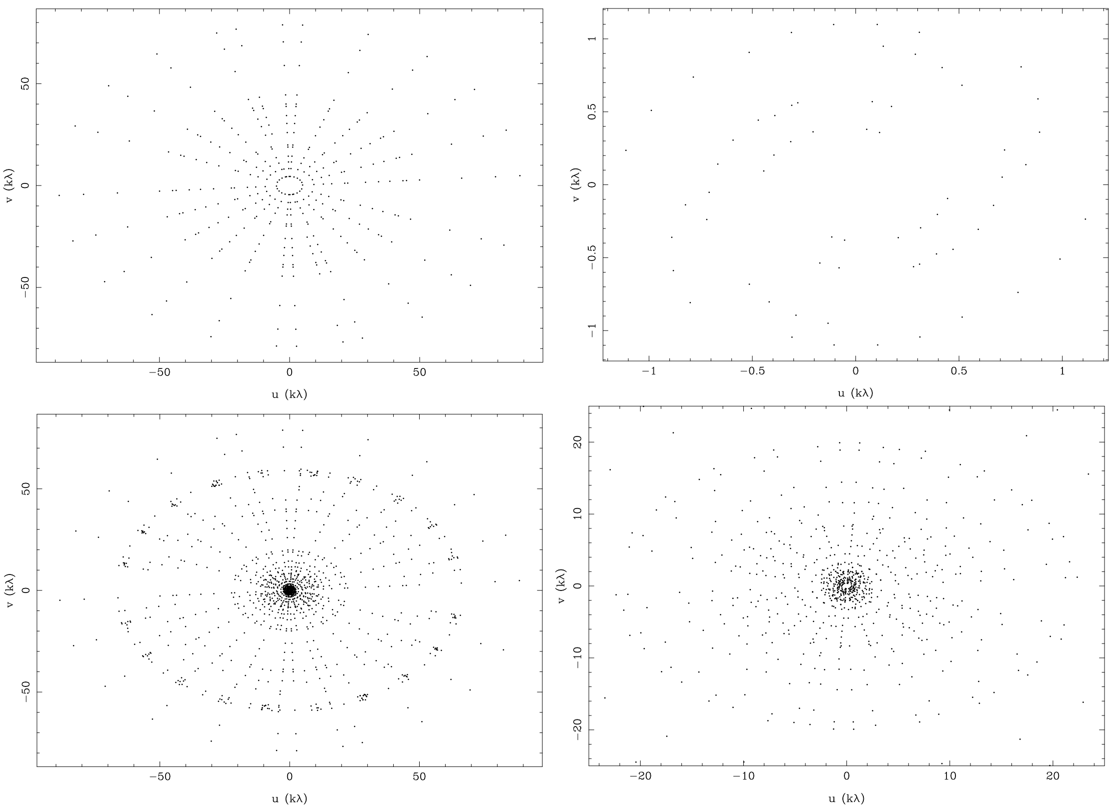

FIGURE 4.3: Top left: *u*-*v* coverage of a single field in the most extended 6A configuration. Top right: *u*-*v* coverage corresponding to a single field in the most compact H75 configuration with the 6th antenna removed. Bottom left: The combined *u*-*v* coverage from all configurations for a single field. Bottom right: A zoom in from −25–25 $k\lambda$ of the combined configurations for a single field. Note that the *u*-*v* points are averaged over the 2 GHz bandwidth and do not show the effect of MFS.

is improved by combining the observations carried out with each array (Fig. 4.4) to give a total on source integration time on each field of ∼ 1 minute.

4.4 Data reduction

The calibration of the data were performed using the MIRIAD[2] reduction package (Sault, Teuben & Wright, 1995) following standard ATCA continuum procedures.

Each array configuration was examined for bad data that may be present for a number of reasons such as problems with the antenna, RFI and shadowing of the antennas. Calibration of the bandpass was performed using the standard 1253-055, the phase was then calibrated using the regular observation of 1352-63 to account for variability in the atmosphere. Finally, the flux was calibrated using 1934-638 and the combined complex gains describing the phase, flux and baseline calibration is applied to science source.

[2]http://www.atnf.csiro.au/computing/software/miriad/

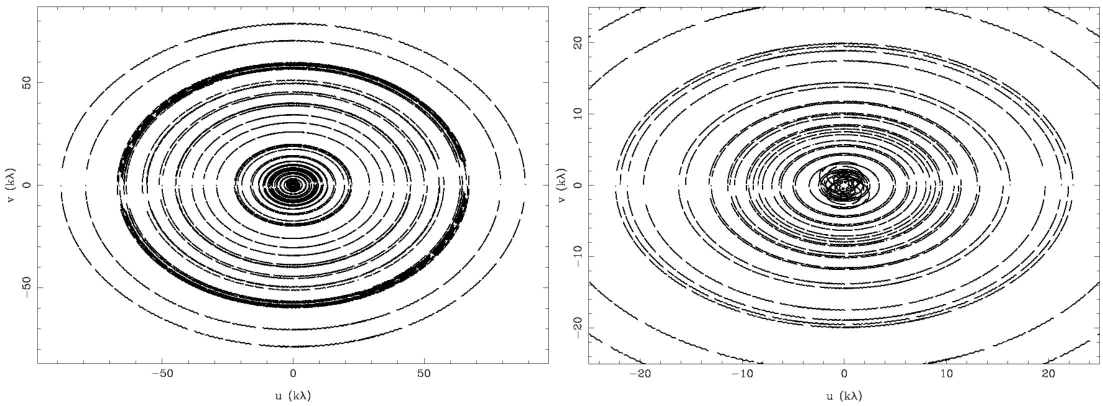

FIGURE 4.4: Combination of all six array configurations and all 357 fields yields the above *u*-*v* coverage. The right panel presents the inner 25 $k\lambda$.

With the bad data flagged and calibration checked, the data reduction diverges into two separate imaging strategies. The science goals described in Section 4.1 requires imaging of both the small-scale emission ($< 5''$) to detect UC HII regions and the extended emission on a large-scale ($> 30''$) to study emission associated with compact and classical HII regions. Therefore, two distinct imaging methods were applied to reduce this mosaic experiment and study the large- and small-scale radio emission called the "joint" and "individual" approach respectively.

4.5 Imaging large-scale emission: the joint approach

The steps taken to image the large-scale radio emission follows the standard joint deconvolution approach, with the inclusion of single-dish data, described in the MIRIAD user manual. In this case, all fields are handled simultaneously by the imaging and deconvolution software. This results in a simplified and faster imaging process that is particularly beneficial for low signal-to-noise ratio mosaics and extended emission (Cornwell, 1988).

The entire calibrated *u*-*v* data set was first Fourier transformed into the image plane using the task INVERT with super-uniform weighting applied to reduce side-lobes caused by gaps in the *u*-*v* coverage and the over density of *u*-*v* points near the centre of the *u*-*v* plane. A $5 \times 5''$ Gaussian tapering function is applied in the *u*-*v* plane to down-weight the data at the outer edge of the *u*-*v* plane and suppress small-scale side-lobes. A pixel size was chosen to ensure the synthesised beam is sampled by three pixels and fields were imaged to twice the primary beam main-lobe to account for bright emission outside of the primary beam. To take advantage of the available 2 GHz bandwidth MFS was applied to improve the *u*-*v* coverage and account for possible spectral variation within the band.

It is well-known that interferometers suffer from a lack of *u*-*v* coverage at short and zero spacing, which results in imaging artefacts such as corrugations and dark bowls in fields containing large-scale emission (Taylor, Carilli & Perley, 1999). Total power (zero spacing) data is provided by the Parkes-MIT-NRAO survey (PMN) (Condon, Griffith & Wright, 1993) at 4.85 GHz with a resolution of 4.92′. Fortunately, the maximum entropy MEM algorithm (MOSMEM) is particularly well suited to including single dish data when performing deconvolution and automatically determines the appropriate flux scaling between the single dish and interferometric observations by comparing the *u*-*v* space in which both the single and array observations overlap. This provides the distribution of flux and total integrated flux that is consistent with the single-dish image. Unfortunately, no single dish data exists at 8.8 GHz and so total flux estimates had to be scaled assuming an optically thin SED (Eq. B.43). This assumption is valid for thermal Bremsstrahlung emission associated with HII regions, where the SED turns over from optically thick to thin above 5 GHz for UC HII regions and progressively lower frequencies with increasing emission size (Fig. B.11).

The final 5.5 and 8.8 GHz maps have a resolution of $10.2 \times 8.2''$ and $8.7 \times 7.6''$ and sensitivity of 0.30 and 0.35 mJy beam^{-1} respectively (Fig. 4.5). This is lower by a factor of 10 than the expected theoretical thermal noise of 0.03 mJy beam^{-1}. The brightest source in the 5.5 GHz map is $\sim$ 1500 mJy beam^{-1} and so the dynamic range is $\sim$ 5000. An integrated flux of 180 and 170 Jy is estimated for the 5.5 and 8.8 GHz maps respectively in good agreement with previous estimates (190 Jy (Table A.4) at 5 GHz; Clark & Porter 2004) suggesting that the flux distribution has been reliably recovered.

The snap-shot nature of these observations results in large gaps in the *u*-*v* plane that introduce significant artefacts (Fig. 4.5) (Taylor, Carilli & Perley, 1999). The emission associated with these artefacts is up to 30 mJy beam^{-1} and so analysis of emission in the direct vicinity of these sources will be correspondingly limited. This is in stark contrast to sources of lower brightness and simpler morphology that are located away from bright sources such as the ring and cometary structures seen at 305.53 + 0.35 and 305.55 + 0.01 and low surface brightness extended emission around 305.07 + 0.16 that are well imaged (Fig. 4.5). A number of methods were applied in an attempt to remove the artefacts associated with the brightest sources such as "peeling" (Intema et al., 2009), multi-scale clean (Rich et al., 2008) and various weighting schemes but these were either very difficult to implement or provided only minor improvements. In principle this image could be improved via self-calibration, however this is both difficult and time consuming especially given the limited number of ATCA antenna (Taylor, Carilli & Perley, 1999), limitations of Miriad and poor *u*-*v* coverage. At a more fundamental level the mosaic requires additional observations to improve the density and coverage of the *u*-*v* plane towards the three brightest sources 305.352 + 0.193 in the NW and 305.195 + 0.033 and 305.270 − 0.007 in the SE. Due to the scope of this thesis, there was unfortunately not enough time to acquire these data.

4.6 The classification of large-scale emission

Within the 5.5 GHz large-scale map the resolution of $10.2 \times 8.2''$ is able to resolve structures with a physical radius of > 0.1 pc corresponding to classical and compact HII regions. The radio emission associated with G305 ranges from extended low surface brightness features to compact bright emission (Fig. 4.5). To characterise the different scales of emission in the large-scale radio mosaic we first apply the two dimensional clump finding algorithm FELLWALKER to a 5.5 GHz image that has been smoothed using a $30 \times 30''$ Gaussian (Fig. 4.5; Bottom). This smooths out artefacts associated with the bright radio sources and results in the large-scale emission being separated into 16 broad but distinct features presented in Fig. 4.5 and Table 4.2. Comparison of these 16 radio emission features with the HII regions reported by Caswell & Haynes (1987) (Fig. 4.5; black ellipses) reveals that all the radio emission, with exception of large-scale sources 13, 15 and 16, is associated with previously detected HII regions. However, we clearly resolve these HII regions and identify multiple emission features and substructure.

The next step is to characterise the substructure within these 16 broad radio features. This is achieved by searching for obviously isolated compact radio features by eye in the full resolution large-scale 5.5 GHz mosaic. The substructure (Fig. 4.5; white outline) is defined by carefully fitting apertures around the emission for pixels that are 3σ above the average flux of the associated large-scale emission. In this way we identify five compact sources apparently embedded or projected against the large-scale radio emission. The positions, peak and integrated flux, spectral index, Lyman continuum photon rate and corresponding spectral type of the sources identified in this way can be found in Table 4.2. The Lyman continuum flux is derived using Equation B.107 and the corresponding spectral type is derived following the outline presented in Section B.10.5. The estimated spectral type should be considered with caution due to possible underestimation of the Lyman flux due to absorption from dust and the difficulty in separating compact and extended emission. Assuming that a single high-mass star is responsible for the Lyman continuum leads to an uncertainty of approximately half a spectral type whilst ignoring the absorption due to dust leads to an underestimate of the spectral class (see Section B.10.5). The ATCA is not a scaled array and so the *u*-*v* plane will be sampled differently at 5.5 and 8.8 GHz leading to uncertainty when comparing the 5.5 and 8.8 GHz flux and the spectral index.

Using a simple model described by (Dyson & Williams, 1997; Hosokawa & Inutsuka, 2005) the dynamical age of an HII region is given by:

$$t_{\rm dyn}(R) = \frac{4R_{\rm s}}{7c_{\rm s}}\left[\left(\frac{R}{R_{\rm s}}\right)^{7/4} - 1\right]\ [{\rm s}] \tag{4.1}$$

where $R_{\rm s}$ is the radius of a Stromgren sphere (Eq. B.42), R is the physical radius of the HII region, $c_{\rm s}$ is the sound velocity in the ionised gas ($c_{\rm s} = 10\,{\rm km\ s^{-1}}$) and $N_{\rm Ly}$ is the number of

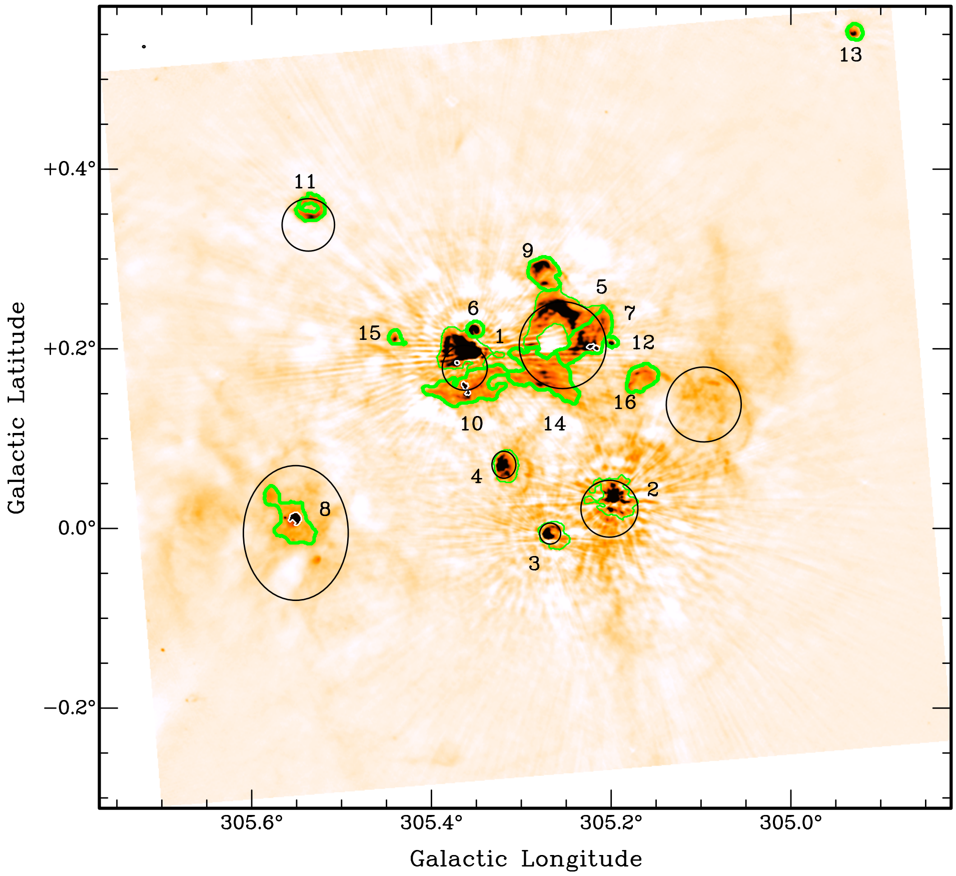

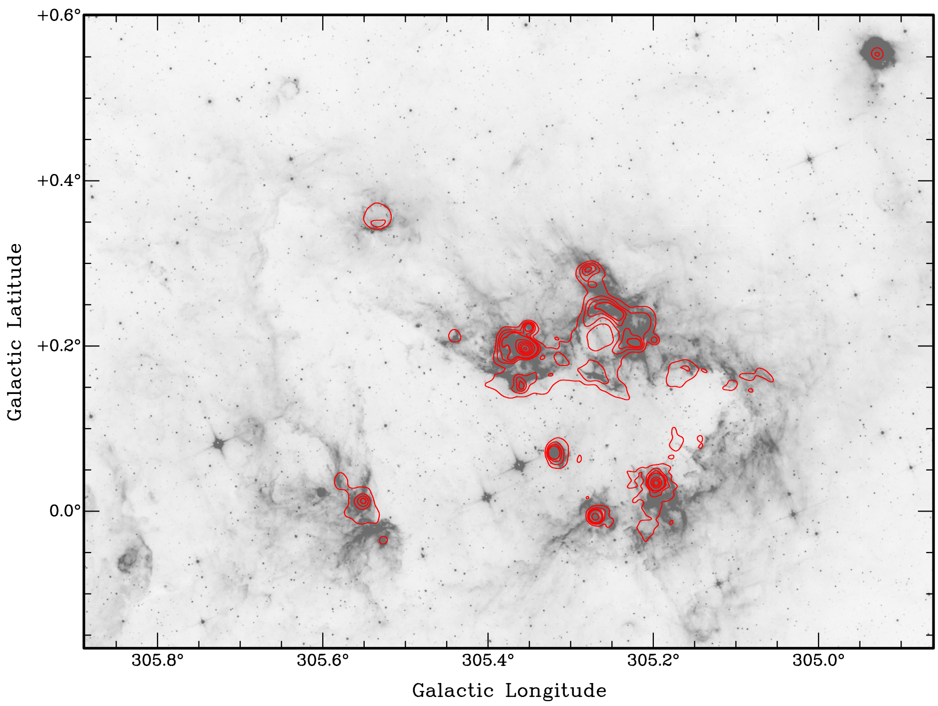

FIGURE 4.5: Top: The 5.5 GHz large-scale radio continuum map with the sources identified by FELLWALKER outlined in green and the compact sources identified by eye outlined in white. The corresponding source numbers are presented as well as ellipses indicating previously identified HII regions (Caswell & Haynes, 1987). Bottom: The 5.5 GHz radio emission contours that have been smoothed by a $30 \times 30''$ Gaussian are presented over a 5.8 μm GLIMPSE image. Contours begin and increment by 0.15 Jy beam^{-1} up to 0.75 Jy beam^{-1} and then proceed in steps of 1 Jy beam^{-1} up to 5.75 Jy beam^{-1}.

ionising photons per unit time (s^{-1}). In order to derive the Stromgren radius we must assume an initial density of the ambient medium. The density of gas that surrounds UC HII regions has been reported as $\sim 1{\times}10^5$ cm^{-3} (Wood & Churchwell, 1989a) but may be as high as $1{\times}10^7$ cm^{-3} (de Pree, Rodriguez & Goss, 1995) although this is likely to be a strong upper limit (Xie et al., 1996). Without prior knowledge of the ambient density we assume a representative density of $1{\times}10^5$ cm^{-3}. Uncertainty in the dynamical age estimate also stems from the difficulty in defining the physical radius of the radio emission because of its association with extended emission. For these reasons the dynamical age presented in Table 4.2 should be considered a lower limit.

Source Index	Source Name	Dimensions Observed maj (")	min (")	R (pc)	Observed flux density Peak (mJy beam^{-1}) $f_{5.5}$	$f_{8.8}$	Integrated (Jy) $f_{5.5}$	$f_{8.8}$	Spectral Index (α)	N_{Ly} Log (s^{-1})	Spectral Type	Dynamical Age (Myr)
1^{HII}	G305.353+0.193	270.6	181.5	2.04	1136.7	923.2	35.2	28.5	-0.5 ± 0.2	49.67	O5	1.8
$1\text{-}1^{\mathrm{C}}$	G305.370+0.185	13.2	9.9	0.10	146.0	110.9	0.3	0.3	-0.3 ± 0.1	47.61	B0	
2^{HII}	G305.195+0.033	211.2	178.2	1.79	1526.5	1286.3	15.0	12.6	-0.4 ± 0.2	49.30	O6	1.7
3^{HII}	G305.270−0.007	118.8	108.9	1.05	729.6	592.7	6.5	6.3	-0.1 ± 0.1	48.93	O6.5	0.8
4^{HII}	G305.320+0.070	92.4	128.7	1.00	251.5	188.9	5.9	5.3	-0.2 ± 0.1	48.89	O6.5	0.8
5^{HII}	G305.244+0.240	330.0	240.9	2.30*	148.7	107.3	17.7	11.3	-1.0 ± 0.5	49.37	O5.5	2.4*
6^{HII}	G305.348+0.223	69.3	62.7	0.61	215.5	146.0	2.4	1.6	-0.9 ± 0.4	48.50	O8	0.4
7^{HII}	G305.215+0.200	237.6	231.0	2.30*	168.1	117.2	12.1	6.6	-1.3 ± 0.7	49.20	O6	2.4*
$7\text{-}1^{\mathrm{C}}$	G305.223+0.202	26.4	13.2	0.14	132.1	91.3	0.6	0.5	-0.4 ± 0.2	47.87	O9.5	< 0.1
$7\text{-}2^{\mathrm{C}}$	G305.215+0.200	19.8	16.5	0.13	168.1	117.2	0.5	0.4	-0.7 ± 0.3	47.84	O9.5	< 0.1
8^{E}	G305.551+0.014	194.7	240.9	2.00	90.9	71.0	6.7	4.1	-1.0 ± 0.5	48.94	O6.5	-
$8\text{-}1^{\mathrm{HII}}$	G305.551+0.014	46.2	46.2	0.43	90.9	71.0	1.5	1.3	-0.3 ± 0.1	48.28	O8.5	0.3
9^{U}	G305.278+0.295	125.4	132.0	1.12	98.0	72.2	5.2	4.4	-0.4 ± 0.2	48.84	O6.5	-
10^{E}	G305.358+0.152	343.2	148.5	2.08	195.4	156.5	10.1	5.8	-1.2 ± 0.6	49.13	O6	-
$10\text{-}1^{\mathrm{C}}$	G305.358+0.152	16.5	16.5	0.13	195.4	156.5	0.5	0.4	-0.2 ± 0.1	47.80	B0	< 0.1
$10\text{-}2^{\mathrm{C}}$	G305.361+0.158	19.8	26.4	0.16	120.0	82.9	0.5	0.4	-0.5 ± 0.3	47.84	O9.5	< 0.1
11^{HII}	G305.532+0.348	115.5	105.6	1.02	51.2	42.9	3.0	3.1	0.1 ± 0.1	48.59	O7.5	1.0
12^{C}	G305.197+0.206	49.5	36.3	0.39	194.5	142.3	0.7	0.5	-1.0 ± 0.5	47.98	O9.5	0.2
13^{HII}	G304.929+0.552	59.4	59.4	0.55	62.4	60.1	0.8	1.1	0.6 ± 0.3	48.05	O9.5	0.5
14^{E}	G305.277+0.161	277.2	237.6	2.36	56.7	38.6	12.0	7.1	-1.1 ± -0.6	49.20	O6	-
15^{U}	G305.439+0.211	62.7	56.1	0.55	52.3	31.7	0.7	0.4	-1.2 ± -0.6	47.98	O9.5	-
16^{E}	G305.169+0.174	128.7	108.9	1.09	45.6	30.9	3.2	2.9	-0.2 ± -0.1	48.63	O7	-

TABLE 4.2: Identifiers and observed properties of the 16 detected large-scale radio sources. The classification of the source (see Section 4.6 for details) is presented as a superscript above the source index. HII - HII region, C - Compact HII region, E - Extended and U - Unknown. Source 5 and 7 appear to be part of the same HII region (G305.254+0.204) see text for details.

To aid in the classification of the large-scale radio emission we extract images from the GLIMPSE survey (Benjamin et al., 2003; Churchwell et al., 2009). To take advantage of the sensitivity to different physical phenomena traced by the GLIMPSE bands (see Section 2.7.1) we have created three-colour images centered on the radio features (Fig. 4.6) using the 4.5, 5.8 and 8.0 μm IRAC bands in blue, green and red, respectively (cf. Cohen et al. 2007; Urquhart et al. 2009) and overlay the 5.5 GHz large-scale radio contours.

Due to the varied and complex nature of the large-scale radio emission we consider each source individually and classify the source based on features such as the morphology, coincidence with mid-infrared emission, size and age (Deharveng et al., 2010). We classify radio emission as an HII region if it shows a bubble, or spherical morphology (50% of HII regions have such a morphology Anderson et al. 2011) that is associated with mid-infrared emission, strong in the 4.5 and 5.8 μm bands, indicative of heated dust and the feature has a radius of > 0.5 pc. Compact HII regions are much younger (< 0.4 Myr), smaller (< 0.5 pc) and compact but are also associated with bright compact mid-infrared emission indicating heated dust. Extended radio emission is classified by its association with the border of the PDR with no obvious core or spherical morphology. Finally, sources that do not fall into any of these categories are classified as unknown sources and discussed further below. These sources are all described in more detail in Section 4.6.1 and following these criteria we label the source index in Table 4.2 accordingly.

We identify five compact HII regions, ten HII regions and four extended emission features. Large-scales sources 9 and 15 do not fall into the HII region or extended classification but appear to be associated with some kind of ionisation front or shock. This method of classification is subjective, further classification would require improved *u*-*v* coverage to reduce artefacts and improve physical property estimates and/or follow-up observations of radio recombination line emission (Anderson et al., 2011) to obtain turbulent and thermal energies in the HII regions and derive electron temperatures.

4.6.1 Distribution and morphology of the large-scale radio emission

There is a significant diffuse, low surface brightness radio component associated with G305 (Fig. 4.5). This extended emission is seen predominantly in the West of the complex and accounts for approximately 40% of the total integrated flux at 5.5 GHz. This kind of extended emission is often missed in high-resolution interferometric observations due to a combination of spatial-filtering, poor surface brightness sensitivity and primary beam attenuation (Kurtz et al., 1999; Longmore et al., 2009). Almost all of the bright compact radio emission is associated with an envelope of extended, low surface brightness radio emission, however it is unclear whether these compact sources are embedded within or superposed upon the extended emission. The importance of the extended radio continuum within GMCs is unclear but has been studied in

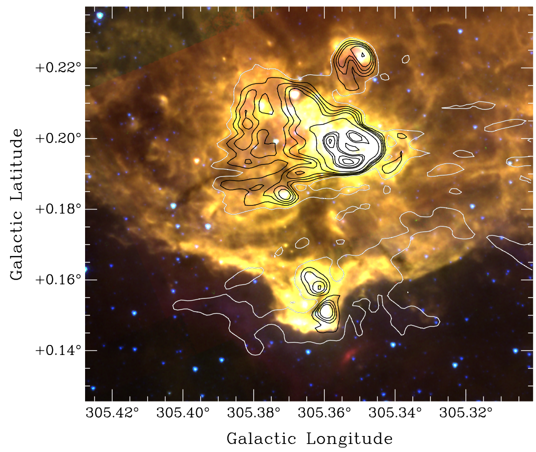

(a) Sources 1, 1-1, 6, 10, 10-1 and 10-2*

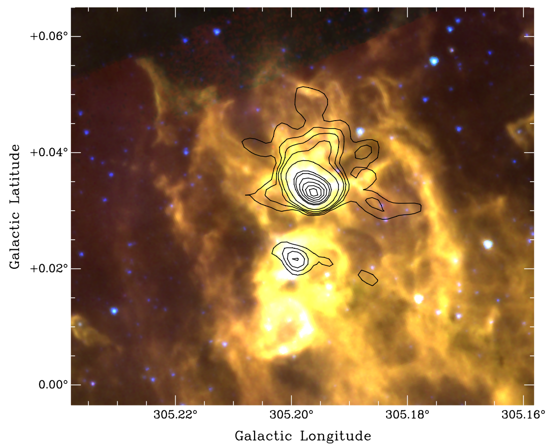

(b) Source 2*

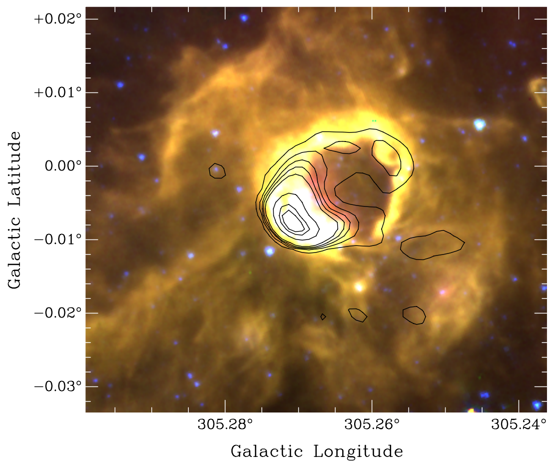

(c) Source 3*

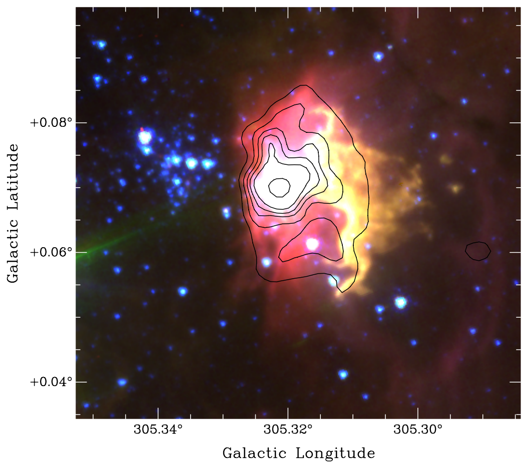

(d) Source 4

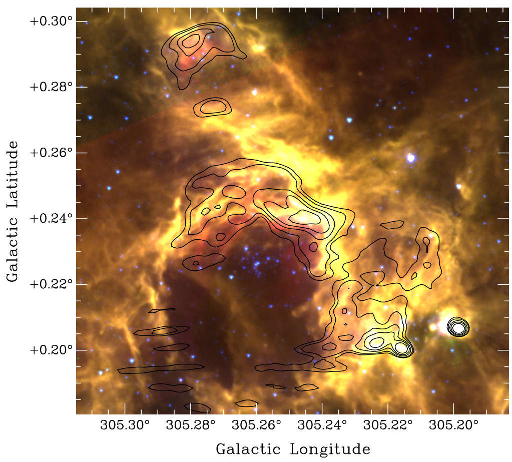

(e) Sources 5, 7, 7-1, 7-2, 9 and 12

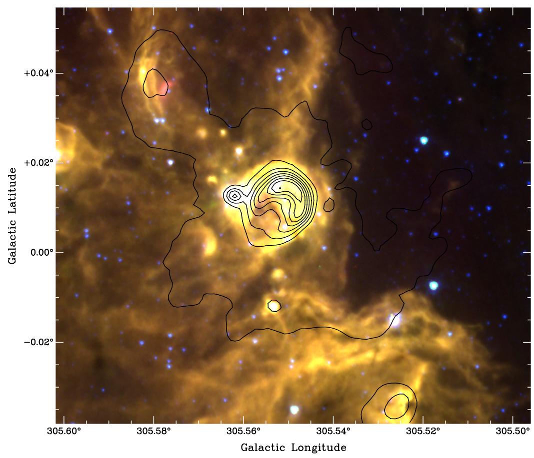

(f) Source 8 and 8-1

FIGURE 4.6: The large-scale 5.5 GHz radio contours are presented over a three-colour images GLIMPSE image using the 4.5, 5.8 and 8.0 μm bands (red, blue and green respectively). Contour levels vary between maps due to artefacts, for images marked with an asterisk contours begin at 0.04 and increment by 0.02 Jy beam^{-1} sources without an asterisk begin at 0.01 and increment by 0.01 Jy beam^{-1}.

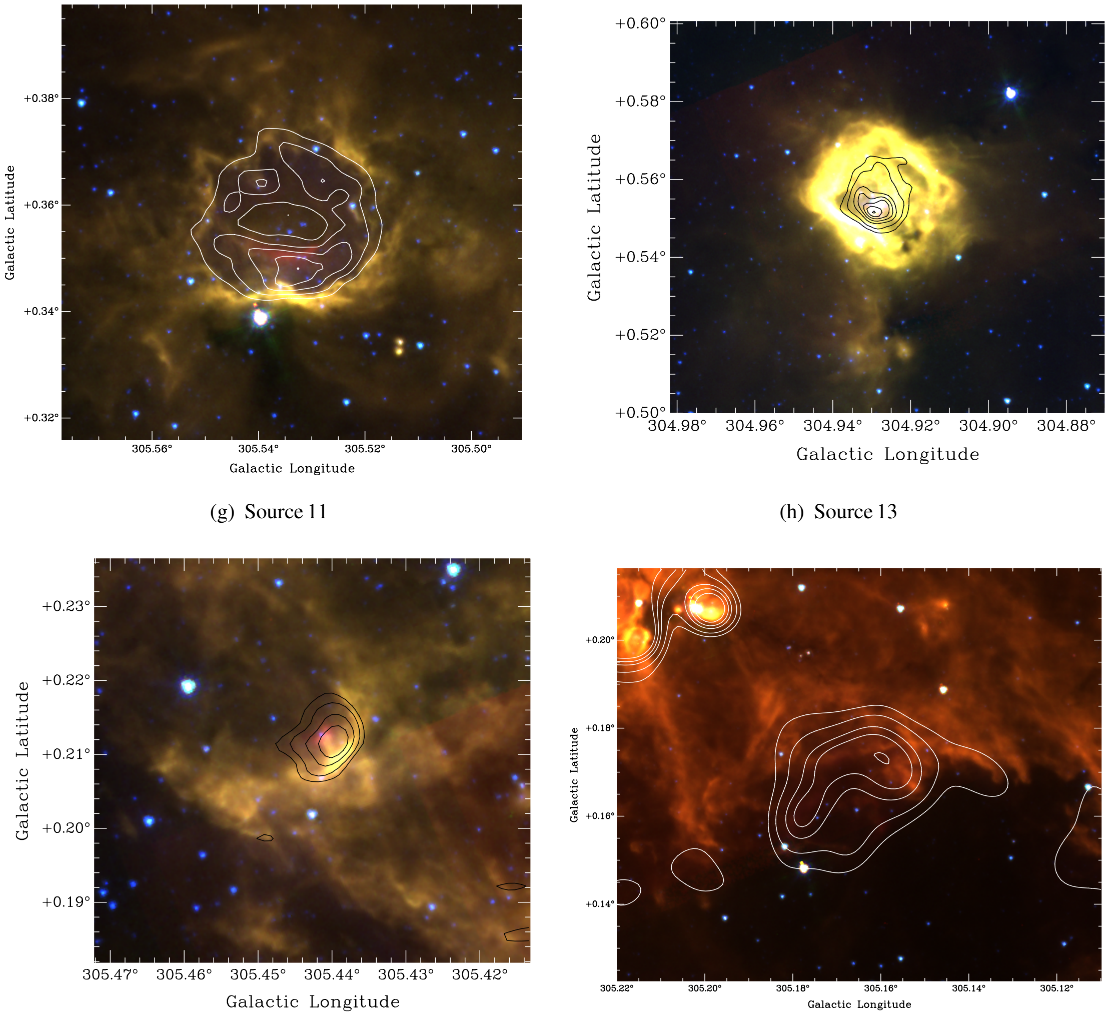

(g) Source 11

(h) Source 13

(i) Source 15

(j) Source 16

FIGURE 4.6: continued.

some detail (e.g. de Pree, Rodriguez & Goss 1995; Kurtz et al. 1999; Longmore et al. 2009). If the extended radio continuum is associated with compact emission then it will have fundamental implications to the theory and models of HII regions (cf. Kurtz et al. 1999; Franco et al. 2000). One method to determine if the two are associated is to compare a near-infrared recombination line image to a radio continuum image to search for variation in the extinction. The extended radio emission within G305 appears to be concentrated to the West and shows a porous structure. To the North and South of the large-scale source 8 in the East we find very little radio emission that suggests the radiation is free to escape in this region. A diffuse extended radio feature (Sources 10 and 14) connects the two Northern lobes of radio emission and appears to merge with a classical HII region in the NW (large-scale sources 5 and 7) G305.254+0.204. Within these broad features we find a great deal of compact and bright sub-structure. We briefly describe each of these large-scale radio sources below.

Large-scale source 1 (Fig. 4.6(a)) has the highest integrated flux in the region and has been identified as an HII region by Caswell & Haynes (1987). The radio emission has a complex multi-peaked morphology, a radius > 1 pc and is associated with bright mid-infrared emission. We therefore classify this source as an HII region. To the South of large-scale source 1 we identify the compact radio **large-scale source 1-2** a dense knot of radio emission suggestive of a compact HII region. Further to the South the extended ionised boundary layer **large-scale source 10** can be seen (white contours) and is associated with two compact HII regions (**large-scale sources 10-1 and 10-2**). Unfortunately due to the limited *u*-*v* coverage large-scale source 1 introduce significant artefacts to this region that limits the identification of further compact emission. To the North of large-scale source 1 we identify a dense knot of ionised gas that is classified as an HII region.

Large-scale source 2 (Fig. 4.6(b)) is classified as an HII region and has the highest peak radio flux in the complex. This source has cometary morphology with the head pointing South and is associated with a bright mid-infrared core. Unfortunately, this source suffers from considerable artefacts that hamper the description of the morphology and surrounding radio sources. However, to the South of large-scale source 2 there appears to be a small radio source that may be a compact HII region.

Large-scale source 3 is easily identified as an HII region by its cometary and shell like structure in the radio and mid-infrared. The head of this HII region is oriented to the South-East and a cavity is clearly visible towards the centre.

Large-scale source 4 is projected towards the centre of the cavity in G305 and at a projected distance of < 2 pc Danks 2 is visible as a bright cluster of blue point sources to the left in Fig. 4.6(d). This radio emission is associated with the "blob" detected in molecular emission in the previous chapter.

The radio emission associated with **large-scale source 5 and 7** (Fig. 4.6(e)) clearly traces the PDR that surrounds a cavity in the molecular gas suggesting these sources are part of a single classical HII region defined as G305.254+0.204 and previously identified by (Caswell & Haynes, 1987). Three compact HII regions (**large-scale source 12, 7-1 and 7-2**) are projected against the Southern lobe of ionised gas, these are associated with the G305.2+0.2 regions a region of intense star formation (Walsh & Burton, 2006; Walsh et al., 2007).

Large-scale source 8 (Fig. 4.6(f)) is an extended emission feature that is associated with an HII region (**large-scale source 8-1**) which itself appears to be associated with a compact unresolved radio source to the East. The nature of this compact source will be explored in Section 4.8. The HII region 8-1 shows distinct cometary morphology orientated with the head towards the PDR boundary.

Large-scale source 11 is a ring of radio emission previously identified as an HII region by Caswell & Haynes (1987) and located 23 pc from Danks 2. The radio emission is surrounded by a diffuse halo of mid-infrared emission. The low mid-infrared brightness towards the centre of the ring suggests that the HII region has created a cavity that is almost devoid of dust. The HII region appears to be sweeping up material to the south where a bright ridge can be seen in both the radio and mid-infrared.

Large-scale source 13 is an HII region (G304.93+0.56) located at a projected distance of 42 pc from Danks 2, isolated to the far North-West of G305. The radio emission associated with this HII region is surrounded by bright mid-infrared emission that shows a complex porous morphology.

Large-scale sources 9, 15 and 16 do not appear to be HII regions but rather some kind of extended ionised boundary layer. They show cometary morphology but are not particularly bright. Source 16 appears to be the brightest section of large low brightness extended radio emission towards the West. This region has been identified as an HII region by Caswell & Haynes (1987) but we suggest that it is extended radio emission associated with the ionised boundary layer.

4.6.2 The total ionising flux of G305

Single dish observations of G305 reveal the total integrated radio flux at 5 GHz to be ~ 200 Jy (Goss & Shaver, 1970; Caswell & Haynes, 1987; Clark & Porter, 2004). This is in good agreement with the total integrated flux found in Section 4.5, which suggests that the joint deconvolution approach in combination with single dish data has accurately reproduced the total flux of the complex. It has been suggested that to power this observed radio flux requires the presence of ~ 30 "canonical" O 7V stars (Clark & Porter, 2004).

The morphology and integrated 5.5 GHz radio flux of the sources presented in Table D.1 suggests that approximately 110 Jy of the total 5.5 GHz flux (180 Jy) is associated with HII regions embedded around the rim of the central cavity and not the massive stars within the central cavity. This would suggest that in addition to the ~ 30 massive stars already detected in G305 (Davies et al., 2012) there is an embedded population of > 15 massive stars (Table D.1) bringing the total number of massive stars within G305 to > 45. However, just because no diffuse radio emission appears to be associated with Danks 1 and 2 does not mean they are not significant sources of ionising radiation. What this result suggests is that there is little gas left within the central cavity for Danks 1 and 2 to ionise.

The ionising flux produced by Danks 1 and 2 and the massive stars within G305 is difficult to determine accurately without modelling each star individually. This is far beyond the scope of this thesis but we may estimate the ionising flux of Danks 1 and 2 by realising that in practice the ionising flux of a cluster is dominated by the most massive stars. In the case of G305 this is given by the ionising flux of the three WNLh stars, D1-1, D1-2 and D1-3 (see Table 2 in Davies et al. 2012). The ionising flux associated with these massive stars may be estimated by utilising the Lyman flux estimates for similar WNLh stars in the Arches cluster scaled to the luminosities of these objects (Martins et al., 2008). The amount of ionising radiation emitted by the three WNLh stars in Danks 1 alone appears comparable to the total ionising flux within the entire G305 region estimated here (Davies et al., 2012; Mauerhan, Van Dyk & Morris, 2011).

This suggests that G305 suffers a significant leakage of UV photons to its surroundings. Hence, estimating the stellar contents and star formation rates of G305 and similar regions using radio fluxes alone will almost certainly result in significant underestimates for all but the youngest complexes, where feedback has yet to disrupt the molecular material. It is difficult to estimate the level of photon leakage without knowing the three-dimensional geometry of the region and the ionising flux of the stellar population. However, considering that three stars in Danks 1 alone have sufficient energy to account for the total observed flux density at 5.5 GHz, whilst not appearing to be responsible for the observed large-scale radio emission (Fig. 4.5) suggests that the ionising output of the G305 complex could be underestimated by $> 50\%$.

4.7 Imaging small-scale emission: the individual approach

The imaging strategy described below is designed to emphasise the faint and compact radio emission (radii $< 5''$) associated with UC HII regions. The joint approach is not practical in this case, due to the much higher resolution and resultant data sizes, Miriad is not yet capable of reducing such large data sets at full resolution[3]. The individual approach where each field is imaged individually has to be applied, however the large number of fields and high-resolution posed a number of difficulties described below.

The reduction strategy described here follows the individual approach detailed in the Miriad user manual and is as follows. Single fields were first Fourier transformed using MFS mode to improve *u*-*v* coverage and image fidelity. These individual "dirty" fields were imaged out to twice the primary beam ($\sim 5'$ at 8.8 GHz and $\sim 8'$ at 5.5 GHz) to account for emission from bright sources outside of the primary beam main lobe. These maps were produced with a pixel size that samples the synthesised beam by three pixels and a robust weighting of 0.5, as opposed to natural or uniform, in order to reduce side lobe levels and produce a uniform synthesised beam shape at the sacrifice of some sensitivity.

The artefacts present in these fields can be easily confused with real compact emission and results in the localised noise being up to three times higher towards bright large-scale emission. We are interested in detecting the compact radio emission associated with UC HII regions and

[3]Miriad user manual Section 2.15.

these artefacts as well as the bright extended emission hamper this goal. Therefore, to emphasise small-scale structure and remove artefacts all baselines $< 15\,\mathrm{k}\lambda$ were cut (cf. Kurtz, Churchwell & Wood 1994; Mücke et al. 2002) from the *u*-*v* data set, which results in the removal of all flux associated with the large-scale emission corresponding to scales $> 0.2'$. An inverse tapering function would have been preferable however, Miriad does not have such functionality. As a result, the integrated flux of resolved sources in this *u*-*v* truncated map may be underestimated by as much as 50% and should be considered as a lower limit. This removal of extended flux does not significantly affect the identification of UC HII regions and is deemed an acceptable consequence of the improved data reduction and compact source detection.

A CLEAN cut off level of 3σ was selected resulting in a few hundred to few thousand clean components depending on the emission in the image. Finally, the 357 individual fields were stitched together using the linear mosaic task LINMOS. In this compact emission mosaic we obtain a sensitivity of 0.07 and 0.15 mJy beam^{-1} for the 5.5 and 8.8 GHz maps respectively and a dynamic range of $\sim$ 1000.

The final compact emission radio mosaic was analysed in the following way. First, the source extracting algorithm DUCHAMP (Whiting, 2012) was applied to automatically extract the small-scale sources. These sources were then confirmed by eye by spatially filtering the 5.5 GHz map using the CUPID function FINDBACK to remove any remaining large-scale emission and artefacts. Peak flux densities and coordinates of sources were then determined using the task MAXFIT in MIRIAD. For unresolved and spherical sources the integrated flux density and size was determined by fitting a Gaussian using the task IMFIT. In the case of sources that are resolved and not well fit by a Gaussian, the integrated flux densities and sizes are determined by carefully fitting irregular-shaped apertures around the sources and extracting the flux.

4.8 Compact source classification

Radio emission detected at 5.5 and 8.8 GHz is not only generated by the thermal free-free emission associated with HII regions but may also originate from a number of astronomical sources such as; thermal emission from stellar winds (Kenny & Taylor, 2007), bright-rimmed clouds (BRCs; Thompson, Urquhart & White 2004; Urquhart et al. 2007b) and non-thermal emission from colliding wind binaries (Dougherty et al., 2003), pulsars (Lazaridis et al., 2008), supernova remnants (Gaensler et al., 1997) and active galactic nuclei (Soria et al., 2010). In the following section, we describe how we separate candidate UC HII regions from these contaminating sources by using ancillary mid-infrared data.

In Fig. 4.7 we present a mid-infrared image of the G305 region that shows the distribution of the detected compact radio sources. These are randomly distributed across the field, which would suggest many are background sources, rather than being associated with G305. In Table. D.1 we present the positions and extracted properties of the 71 compact radio sources identified from our small-scale radio mosaic. Several sources are not detected in the lower sensitivity 8.8 GHz maps and for these sources we present the upper limit 3σ flux level. We find the majority of radio sources detected are unresolved (59) and given that the majority of UC HII regions presented in the literature are resolved at similar distances and resolutions (e.g. Wood & Churchwell 1989b; Kurtz et al. 1999; Urquhart et al. 2007b, 2009) it is likely that most of these unresolved sources are extragalactic in origin.

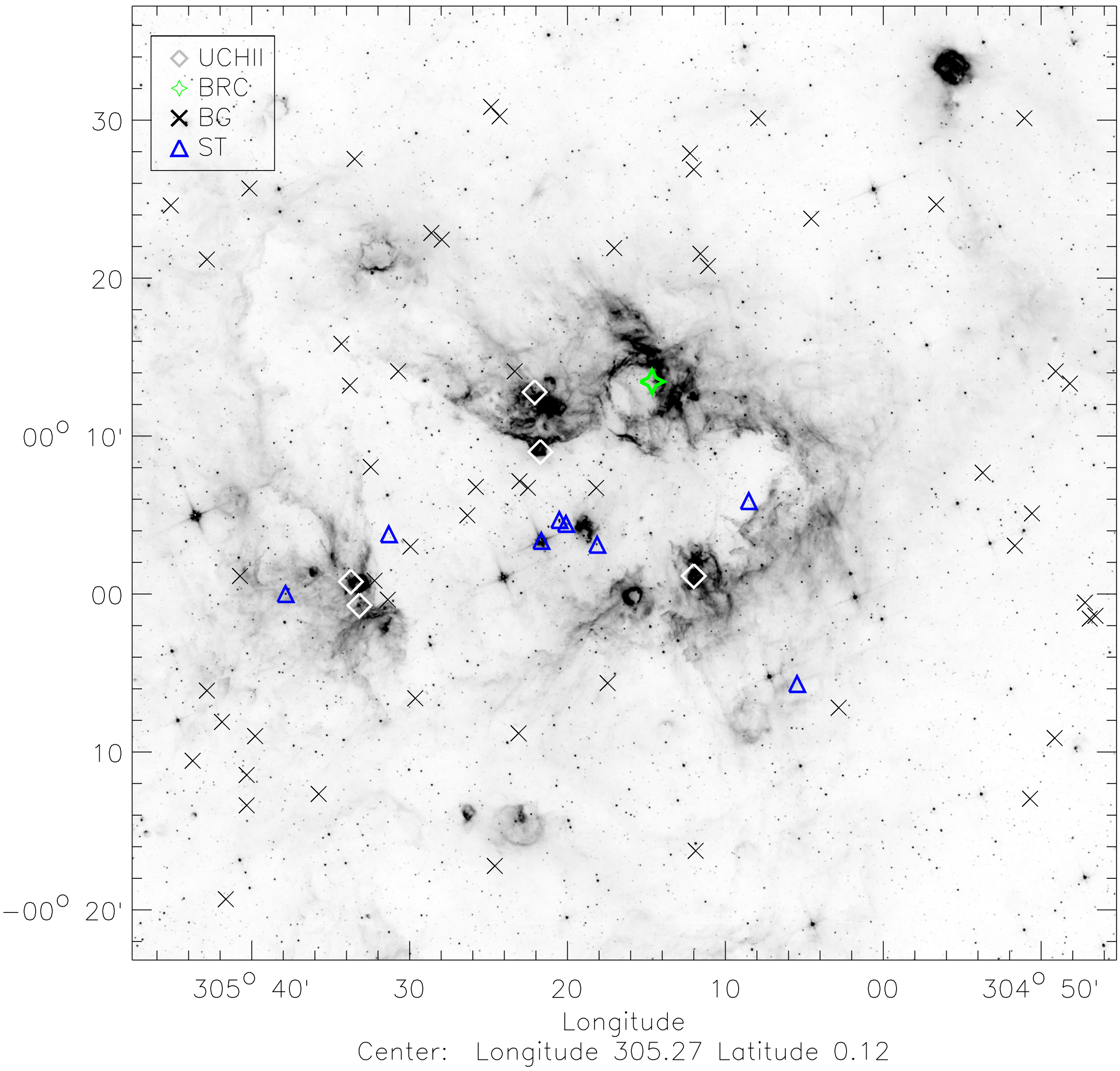

FIGURE 4.7: The 71 compact radio sources are overlaid onto a 5.8 µm GLIMPSE image. White diamonds indicate candidate UC HII regions, blue triangles are stellar sources, black crosses show background sources and a green star highlights the BRC.

We have created three-colour images, in the same manner as Section 4.6, centred on the compact emission 5.5 GHz peak, using the 4.5, 5.8 and 8.0 µm IRAC bands in blue, green and red, respectively (cf. Cohen et al. 2007; Urquhart et al. 2009). From a visual examination of these images, we find that the radio sources can be separated into four distinct categories. In Fig. 4.8 we present an example of each of these and describe the main features of each category below:

- Radio emission is coincident with strong compact mid-infrared emission, which is itself associated with extended PAH emission and/or extinction, which are commonly associated with star formation regions. These are considered UC HII candidates (Fig. 4.8 top-left).
- Radio and mid-infrared emission are both unresolved and correlated and the mid-infrared emission is dominated by the shorter (blue) wavelengths. We consider that the radio emission seen towards these sources arises from a stellar source. Additionally, these radio and mid-infrared sources are often isolated which suggests they are not associated with star formation. (Fig. 4.8 top-right).
- We classify a source as a bright-rimmed cloud (BRC) if the radio and mid-infrared emission have a similar cometary morphology with no obvious core and the radio emission is offset from the mid-infrared emission (Fig. 4.8 bottom-left).
- Radio sources that are devoid of any mid-infrared emission are assumed extragalactic radio sources. A large proportion of the unresolved radio sources fall into this category (Fig. 4.8 bottom-right).

We derive the spectral index (α) of sources by taking the logarithm and fitting a straight line to the relation $S_{\rm int} \propto \nu^{\alpha}$, where $S_{\rm int}$ is the integrated flux and ν is the frequency. To search for non-linear variation of flux with frequency we split the full 2 GHz bandwidth into 1 GHz wide bands centred at 5.0, 6.0, 8.3 and 9.3 GHz and generate images following the steps outlined in Section 4.7. We find no convincing evidence of non-linear SEDs, within the errors. As mentioned in Section 4.7 the integrated flux for resolved sources is a lower limit and cannot be reliably estimated; in addition, the *u*-*v* plane has been sampled differently at the two frequencies, as the ATCA is not a scaled array, and so the flux cannot be reliably compared. For these reasons the spectral index cannot be determined reliably for resolved sources and is presented for only the unresolved and isolated sources.

We will further consider the UC HII region candidates in the next section. For the remainder of this section we briefly discuss the other classes of object discovered.

We find eight of the 71 radio sources (Fig. 4.8) are associated with more evolved stars (isolated, unresolved and possessing blue colours). Approximately half of these stellar sources are found towards the centre of G305 and are associated with well-known massive stars. Two sources, 2 and 59, are associated with the most massive members of Danks 1 (D1-1 and D1-2), whilst Source 3 is associated with the WR star WR 48A and Source 56 with the massive star MDM3

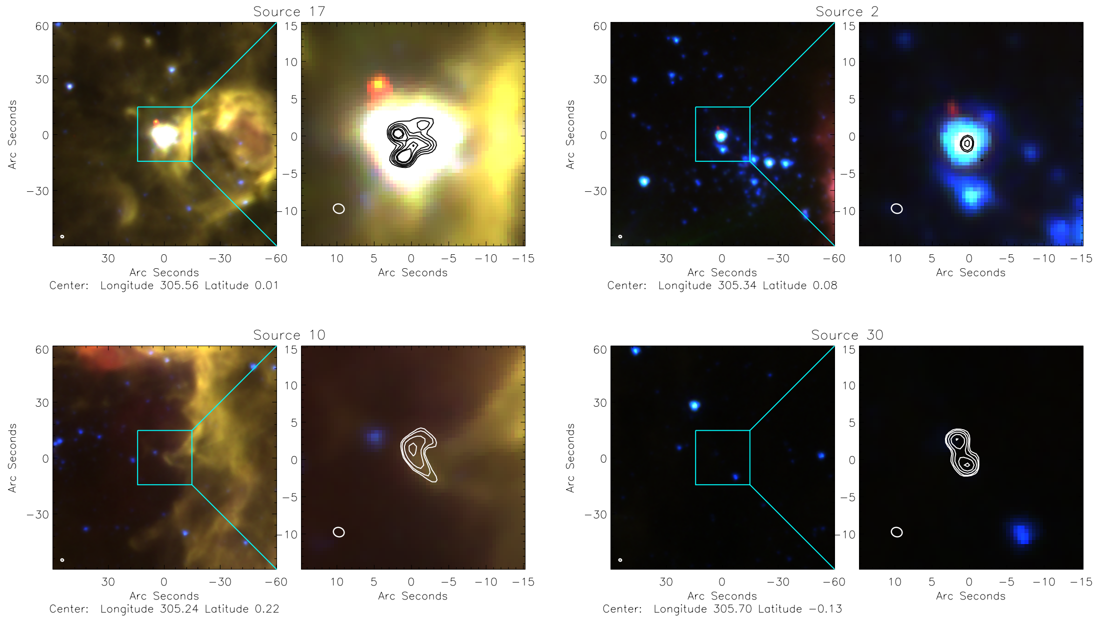

FIGURE 4.8: Three-colour 4.5, 5.8 and 8.0 µm composite GLIMPSE (b, g, r respectively) cut-out images centred on the peak 5.5 GHz radio emission with contours beginning and incrementing by 3σ. An example of an UC HII region (top left), stellar (top right), BRC (bottom left) and background galaxy (bottom right) are shown. These are classified following the criteria outlined in Section 4.8. The beam is presented in the lower left corner of each image.

(Davies et al., 2012). Examination of the spectral index reveals the radio emission associated with six stellar sources is positive (2, 3, 56, 59, 63 67) and only two are negative (11, 60). Sources with a positive spectral index are most likely generating thermal emission associated with an ionised stellar wind, whilst negative spectral index sources are most likely generating non-thermal emission via wind shocks or colliding winds from binary stars (Dougherty et al., 2003). As we are principally interested in the star formation within G305 further analysis of these stellar sources is beyond the scope of this study.

BRCs are found on the edge of evolved HII regions where the ionising radiation emitted from an OB star(s) ionises the surface of a molecular cloud (Sugitani, Fukui & Ogura, 1991; Thompson, Urquhart & White, 2004). This molecular material is often swept into cometary morphology by the radiation pressure and results in a dense core at the head that shields the remaining cloud material resulting in a finger or column. Comparison with mid-infrared data reveals Source 10 has this characteristic morphology and is found on the inner borders of a shell of diffuse 5.8 µm emission that has been identified as an evolved HII region (Caswell & Haynes, 1987; Clark & Porter, 2004). The cometary morphology of the radio and mid-infrared emission points to an ionising source to the east of the BRC towards the centre of the evolved HII region. Compelling candidates for the source of ionisation are found within the HII region in the massive star L05-A2 (Davies et al. 2012; Table A.1) and a deeply embedded IR excess cluster (Longmore et al., 2007b).

As previously mentioned, we failed to associate the majority of radio sources with any mid-infrared emission and these are assumed to be extragalactic background sources. To test this assumption it is useful to compare the number in this category with the estimated number of background radio sources ($\langle N \rangle$) one would expect given the size of the observed region and the frequency at which the observations were performed. We can estimate this number empirically from extragalactic source counts using the following equation from Anglada et al. (1998):

$$\langle N \rangle \simeq \left(\frac{\theta_{\rm f}}{\theta_{\rm A}} \right) 1.1 S_0^{-0.75} \tag{4.2}$$

where $\theta_{\rm f}$ is the diameter of the observed field, $\theta_{\rm A}$ is the FWHM of the primary beam in arcminutes and S_0 is the sensitivity at 5.5 GHz. Using this equation we estimate that $\sim 60 \pm 8$ background sources should be detected in the $\sim 1.0 \times 1.0^{\circ}$ field. From our comparison with the mid-infrared we find 56 compact radio sources that fit the criteria of extragalactic sources, which is in good agreement with the result obtained above from Equation 4.2. These background sources are mainly unresolved point sources but there are a number of resolved sources that exhibit lobes of emission similar to the radio lobes seen in active radio galaxies (Fig. 4.8 bottom-right). We expect to find a negative or flat spectral index for background radio galaxies associated with non-thermal radiation and we find this is the case for the majority. Only nine of these background sources have $\alpha > -0.1$ consistent with optically thick thermal free-free emission while 42 have $\alpha < -0.1$ indicating a non-thermal emission mechanism.

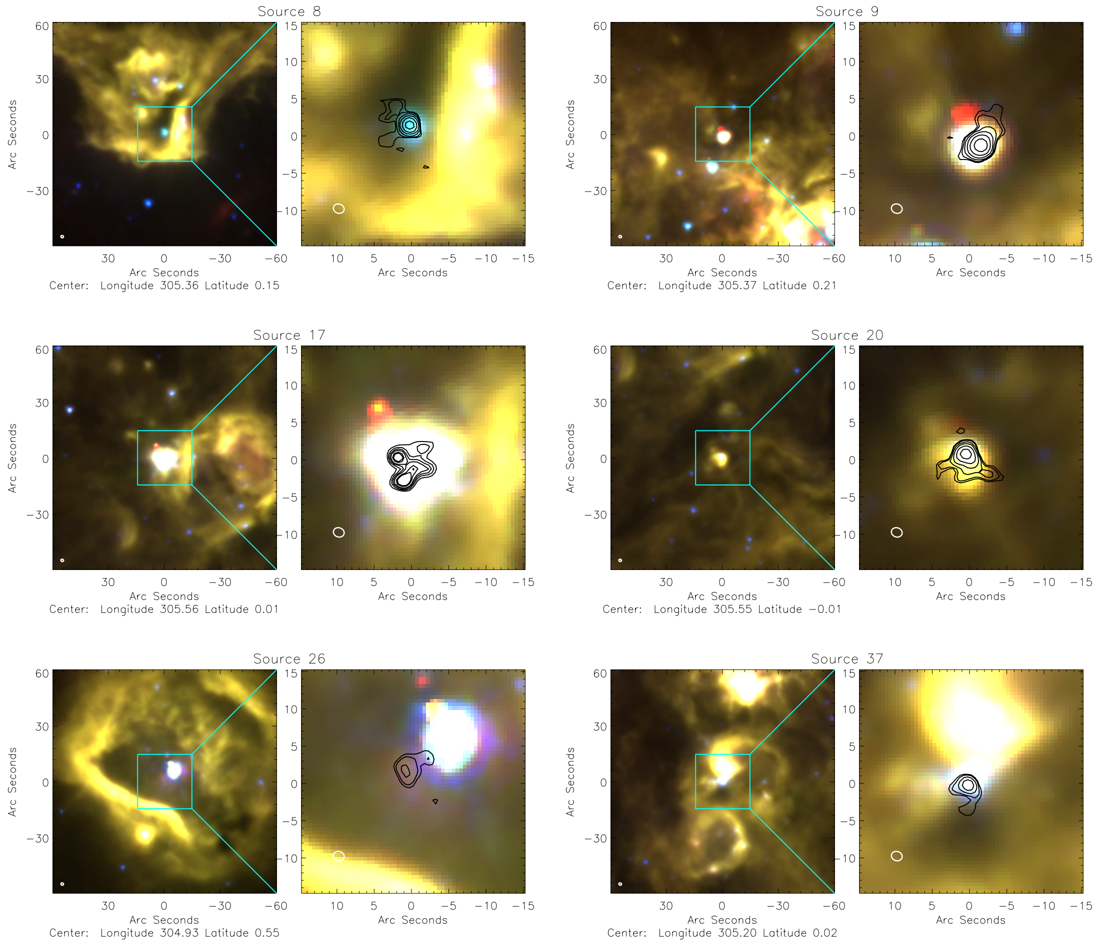

FIGURE 4.9: Three-colour 4.5, 5.8 and 8.0 µm composite GLIMPSE (b, g, r respectively) cut-out images centred on the peak 5.5 GHz radio emission of the six candidate UC HII regions. First panel shows a wide field of view image with a cyan box centred on the peak of the radio emission. Second panel shows the outlined field of view the cyan box. Black contours are of the 5.5 GHz radio emission with contours beginning and incrementing by 3σ. Sources are coincident with mid-infrared emission indicative of an embedded stellar source (see criteria in Section 4.8). The beam is presented in the lower left corner of each image.

Source Index	Source Name	Dimensions Observed maj (”)	min (”)	Observed flux density Peak (mJy beam^{-1}) $f_{5.5}$	$f_{8.8}$	Integrated (mJy) $f_{5.5}$	$f_{8.8}$	Spectral Index (α)
0	G305.375+00.112	unresolved		2.9 ± 0.3	2.2 ± 0.3	3.3	2.6	−0.2
1	G305.384+00.119	unresolved		1.2 ± 0.3	1.5 ± 0.3	1.5	1.9	0.7
2^{st}	G305.342+00.078	unresolved		0.9 ± 0.1	1.6 ± 0.2	1.0	1.9	1.7
3^{st}	G305.361+00.056	unresolved		1.8 ± 0.3	2.5 ± 0.3	2.4	2.9	0.6
4	G305.303+00.112	unresolved		7.4 ± 0.3	6.7 ± 0.2	9.3	7.9	−0.4
5	G305.439+00.083	unresolved		3.1 ± 0.3	4.4 ± 0.1	3.8	5.7	0.8
6	G305.430+00.113	unresolved		0.9 ± 0.1	1.0 ± 0.1	0.9	1.0	0.4
7	G305.541+00.134	unresolved		0.7 ± 0.3	0.6 ± 0.1	1.0	0.6	−1.4
8^{uc}	G305.362+00.150	2.40 ± 0.05	3.0 ± 0.05	24.0 ± 0.8	26.0 ± 0.9	29.0	34.0	-
9^{uc}	G305.368+00.213	4.20 ± 0.09	4.2 ± 0.08	28.0 ± 1.1	15.0 ± 1.0	62.0	54.0	-
10^{brc}	G305.244+00.224	3.60 ± 0.66	4.8 ± 0.36	1.7 ± 0.2	0.9 ± 0.1	5.5	1.7	-

TABLE 4.3: Identifiers and observed properties of the first 10 of 71 detected compact radio sources (Table D.1). For sources that fall below the detection limit at 8.8 GHz we present the upper limit $3 \times \sigma$ value where σ is the rms noise. Superscript above the source index indicates the nature of the source as derived in Section 4.8, *st* corresponds to stellar, *uc* to UC HII candidate and *brc* to BRC sources with no superscript are background. The spectral index is derived from the 1 GHz split dataset and presented for unresolved sources only.

4.8.1 Derived physical properties of the candidate UC HII regions

In the previous section, we described how mid-infrared data were used to separate the compact radio sources into four distinct categories. We identified six sources that appear to be good candidates for classification as UC HII regions (see Fig. 4.9 for mid-infrared three-colour images of these). In this section, we will determine the physical properties of these candidate UC HII for comparison with bona fide UC HII regions reported in the literature.

In the following analysis, we assume the origin of the radio emission is free-free (Bremsstrahlung), optically thin and thermal arising in an ionised circumstellar environment. This assumption must be treated with some caution as the opacity of a typical UC HII region with emission measure $> 10^7$ pc cm^{-6}, diameter of ~ 0.1 pc and electron density $> 10^4$ cm^{-3} is found to turn over from optically thin to optically thick below 5 GHz (Kurtz, 2005). To test the validity of this assumption we derive the physical properties using both the 5.5 and 8.8 GHz data and find they agree to within a factor of two, which, would suggest that the assumption of optically thin emission at 5.5 GHz is valid. We therefore only report the properties derived from the higher signal to noise 5.5 GHz data.

As mentioned in Section 4.7 the integrated flux of resolved compact radio sources in the small-scale maps is underestimated due to the removal of short baselines used to emphasise small-scale structure. The peak emission of sources is unaffected by the removal of short baselines and so we derive the peak (mJy beam^{-1}) properties, averaged over the area of the synthesised beam, following the method of Wood & Churchwell (1989a). The main beam brightness temperature is estimated from:

$$T_{\rm b} = \frac{S_\nu 10^{-29} c^2}{2\nu^2 k_{\rm B} \Omega_{\rm b}} \text{ [K]} \tag{4.3}$$

where S_ν is the peak flux density (mJy beam^{-1}), ν is the frequency (Hz), c is the speed of light (m s^{-1}) and $\Omega_{\rm b}$ is the beam solid angle (3.36×10^{-11} sr at 5.5 GHz). The peak optical depth τ is estimated using $T_{\rm b} = T_{\rm e}(1 - {\rm e}^{-\tau})$ assuming the beam is uniformly filled with ionised gas. The electron temperature of the ionised gas within HII regions has been shown to vary between 6800-13000 K (Spitzer & Savedoff, 1950; Caswell & Haynes, 1987). The electron temperature towards regions in G305 is unknown and so we assume a value of $T_{\rm e} = 10^4$ K throughout the rest of this analysis. This assumption results in an uncertainty of $\sim 20\%$ in the derived optical depth and $< 10\%$ in the physical properties derived below. The optical depth τ is derived using Eq. B.102.

We calculate the peak emission measure (EM) from the expression of the optical depth (τ) for free-free radiation using Equation B.104 and the electron density using Equation B.105. We estimate the peak ionised gas mass ($M_{\rm HII}$) by multiplying the peak electron density by the proton mass and volume of the emitting region assuming spherical morphology.

The remaining physical properties ($N_{\rm Ly}$, M_* and spectral type) have been derived using the integrated flux and it is important to reiterate that since the integrated flux is underestimated these properties should be considered lower limits. The total ionising photon flux of the Lyman continuum ($N_{\rm Ly}$) is independent of source geometry and is determined using the modified Equation B.107. This value of the ionising flux should be considered a lower limit due to dust absorption of the UV flux and the underestimated integrated flux.

We are able to estimate the mass of the ionising source (M_*) responsible for the observed Lyman flux by interpolating between the calculated values of mass and Lyman flux presented in Table 1 of Davies et al. (2011). The values in this table were computed by combining the results from stellar atmosphere models by various authors, see Davies et al. (2011) for more details. The resultant masses are presented in Col. 10 of Table 4.4 and should be treated as a lower limit with errors of $\sim$ 30–50% caused by the calibration of Lyman flux to ionising source mass (Davies et al., 2011).

We estimate the spectral type of the ionising star by comparing the estimated Lyman continuum flux to the derived value of the total number of ionising photons generated by massive stars tabulated by Panagia (1973). We assume the radio emission observed is caused by a single zero-age main-sequence (ZAMS) star, that no UV flux is absorbed by dust and that the HII region is ionisation bounded. The most massive star will dominate the Lyman flux, if there are multiple stars that make a significant contribution to the ionising flux the spectral type will be later than we have estimated. Conversely, if there is significant absorption by dust and/or the nebular is not ionisation bounded the spectral type may be earlier than our estimate.

Source Index	Source Name	Radius (pc)	T_b (K)	τ 10^{-3}	n_e $10^4(\mathrm{cm}^{-3})$	EM $10^6(\mathrm{pc\ cm}^{-6})$	M_{HII} $10^{-3}(\mathrm{M}_\odot)$	Log N_{Ly} (s^{-1})	M_* $(\mathrm{M}_\odot)$	Spectral Type
8	G305.362+00.150	0.04	770.0	80.03	1.03	8.76	74.0	46.62	13.8	B0.5
9	G305.368+00.213	0.08	900.0	94.02	0.79	10.3	440.0	46.95	14.8	B0.5
17	G305.562+00.013	0.11	240.0	23.80	0.34	2.60	480.0	46.65	13.9	B0.5
20	G305.553−00.012	0.08	270.0	27.29	0.44	2.99	200.0	46.36	13.0	B0.5
26	G304.930+00.552	0.07	77.0	7.72	0.25	0.84	84.0	46.02	12.0	B1
37	G305.200+00.019	0.04	230.0	23.34	0.58	2.56	32.0	46.12	12.3	B1

TABLE 4.4: Derived source properties for candidate UC HII regions.

The physical properties determined for all but one of the candidate UC HII regions in Table 4.4 are typical of UC HII regions described in the literature e.g. small diameter (< 0.1 pc), high electron density ($> 10^4\,\mathrm{cm}^{-3}$) and high emission measure ($> 10^7\,\mathrm{pc\,cm}^{-6}$). We find that the derived physical properties for Source 26 associated with G304.93+0.56 are significantly lower than the other candidate UC HII regions. Moreover, comparison with the NH_3 and CO emission maps (Chapter 3, Figs. 3.5 and 3.9) reveal a lack of dense gas towards Source 26 that would indicate that the region either is a more evolved HII region having already dissipated its natal cloud or has another origin. Finally, visual comparison with the large-scale and mid-infrared image of this source, presented in Fig. 4.9 reveals that the radio emission is actually offset from the bright mid-infrared source that dominates the image and associated with the peak of the large-scale radio source 13 (Fig. 4.6(h)). This source highlights the care that must be taken when analysing spatially filtered interferometer images, this source is clearly the compact peak of spatially filtered large-scale emission so Source 26 is removed from the list of UC HII regions.

For the five remaining sources we find radii ranging from 0.04 to 0.11 pc, electron densities in the range of 0.34–1.03 $\times\ 10^4\,\mathrm{cm}^{-3}$ and emission measures at 2.56–10.3 $\times\ 10^6\,\mathrm{pc\,cm}^{-6}$ (see Table 4.4). These values correspond to UC HII regions in the classification scheme of Kurtz (2002) and Wood & Churchwell (1989a,b). Based on the correlation with mid-infrared emission and derived physical properties we classify the compact radio sources 8, 9, 17, 20 and 37 as UC HII regions.

4.8.2 Distribution of UC HII regions

All five UC HII regions are located around the inner rim of the central cavity, within the PDR, towards areas where the mid-infrared emission is bright and compact (Fig. 4.9) and towards HII regions projected against large-scale ionised gas (Fig. 4.5). There is no evidence of UC HII regions within the central cavity, outside the bounds of the PDR or towards the G305.2+0.2 (NW) region. Although all five UC HII regions are resolved we find four possess a simple morphology, primarily consisting of a compact core which is associated with some low surface brightness diffuse emission and one source with an irregular distribution. The lack of structure seen toward the majority of these radio sources may suggest that they are still at an early stage of their evolution. We will discuss the relationship between the embedded massive star formation indicated by UC HII regions, large-scale ionised and molecular gas and star formation in Chapter 5.

4.9 The star formation rate

In (Davies et al., 2012) we determined the mass and age of the two central stellar clusters Danks 1 and 2, which are 8000±1500, 3000±800 $M_\odot$ and $1.5^{+1.5}_{-0.5}$ and 3^{+3}_{-1} Myr respectively. If we make the assumption that the star formation within these clusters has proceeded constantly over their lifetimes then these masses and ages imply star formation rates of $\sim$ 0.003–0.005 $M_{\odot}\,yr^{-1}$, i.e. at a similar rate to the Carina complex (Povich et al., 2011). In this section, we use our UC HII, compact and classical HII region detections to estimate the star formation rate in G305 so that we may compare the star formation rate of these apparently temporally isolated episodes of star formation to that of Danks 1 and 2.

Before doing so we will briefly dwell upon the caveats involved in this calculation. Firstly, the stars powering the HII regions are by definition massive and thus we are forced to extrapolate the number of lower mass stars by integrating over the initial mass function (IMF). Secondly, the timescale for this star formation is not well-known and will vary across the IMF from high-mass to low-mass. Low-mass stars take ~0.5 Myr to reach the pre-main sequence (PMS) phase (i.e. the stage at which most of their stellar mass is assembled, Evans et al. 2009; McKee & Offner 2010; Offner & McKee 2011) whereas the higher mass stars that are the source of the ionising photons powering the UC HII regions reach the MS while still accreting. Both of these errors likely dominate over the error in determining the radio luminosity of the HII regions due to the uncertain distance of G305 (3.8±0.6 kpc; Davies et al. 2012).

However, obtaining even an order of magnitude estimate for the current star formation rate is instructive to compare with that determined for Danks 1 and 2. Large differences in the star formation rate may indicate that the influence of Danks 1 and 2 is either enhancing or suppressing star formation in the surrounding cloud. Our estimated star formation rate can also be compared with other star-forming complexes, such as Carina, to place G305 in context with the rest of the Milky Way.

To derive the current star formation rate over the past 0.5 Myr we assume that for each of our five UC HII regions, the most massive star present (shown in Table 4.4) produces the majority of the ionising photon flux and is accompanied by a cluster of lower mass stars or YSOs. We then determine the total mass of stars and YSOs that may be present by extrapolating over a Salpeter IMF (Salpeter, 1955) fixed to the mass of the most massive star in each UC HII region. We assume an upper and lower mass limit of 50 and 0.1 $M_{\odot}$ (Robitaille & Whitney, 2010).

This extrapolation yields a total number of $\sim 1 \times 10^3$ stars or YSOs, which corresponds to a total stellar mass of $1.5 \times 10^3\,M_{\odot}$. This is of the same order of magnitude as the mass in each of the Danks clusters and similar to the number of YSOs detected in a recent study of the Carina complex (Preibisch et al., 2011). As a consistency check we compared the number of the massive YSOs (i.e. $L > 10^3\,L_{\odot}$) predicted by our IMF to the number of massive YSOs observed in the complex by the RMS and MMB surveys and found an agreement to within a factor of 2.

Assuming that the stars or YSOs have formed constantly over the last 0.5 Myr this implies an average star formation rate based on UC HII regions of 0.002–0.004 $M_{\odot}\,yr^{-1}$. We consider this rate to be a lower limit due to the likely incompleteness of our survey for UC HII regions located near to the bright and extended classical HII regions within G305. We find that this estimate of the star formation rate in G305 is consistent with similar estimates made of the star formation rate in Carina (Povich et al., 2011) and M17 (Chomiuk & Povich, 2011).

We may perform these steps to derive the SFR based upon the older population of massive stars indicated by compact and classical HII regions presented in Table 4.2. Extrapolation of the IMF reveals 4.8×10^4 stars or YSOs which corresponds to a total stellar mass of 1.6×10^4 $M_\odot$ comparable to the combined mass of Danks 1 and 2. Assuming these stars formed within 0.5 Myr yields a SFR based on compact and classical HII regions of $\sim$ 0.02–0.04 $M_\odot$ yr^{-1}.

Above we derive the SFR for Danks 1 and 2 assuming a constant SFR during their lifetime. In order to compare the SFR of these clusters with the SFR derived from HII regions requires that we estimate the SFR assuming a formation timescale of 0.5 Myr. This results in the SFR for Danks 1 and 2 being 0.02–0.04 $M_\odot$ yr^{-1}. This agrees remarkably well with the SFR derived for compact and classical HII regions and is approximately an order of magnitude greater than the SFR implied by UC HII regions. Even given caveats and errors this large difference in SFR between Danks 1 and 2 and HII regions compared to UC HII regions implies that the SFR may have decreased rapidly in the last 1–2 Myrs. The SFR averaged over the age of the entire complex may be derived by combining the mass determined for Danks 1 and 2 and by fitting the IMF to each epoch of massive star formation and dividing by the total life time of the cloud ($\sim$ 5 Myr). This gives a total mass in stars of $\sim 2.8 \times 10^4$ $M_\odot$ and an average SFR, assuming constant star formation over the past 3^{+3}_{-1} Myr, of 0.005–0.014 $M_\odot$ yr^{-1}.

We find that our derived SFR for G305 is comparable to other well-known massive star-forming complex in the Galaxy, namely the Carina complex (Povich et al., 2011), and M17 (Chomiuk & Povich, 2011). We stress that the derived SFR value is based on a small sample of high-mass stars, and has been extrapolated over a large range of stellar masses; when considering the lower mass stars present, their lifetimes may well be 1–2 orders of magnitude longer. For completeness, the Galactic SFR is found to be ≈ 2 $M_\odot$ yr^{-1} (Chomiuk & Povich, 2011; Davies et al., 2011), suggesting that a few tens to hundreds of G305 complexes are analogous to the entire star formation rate of the Milky Way, and suggests that just as the IMF is dominated by the more massive stars present, the Galactic SFR is probably dominated by the few rigorous star-forming regions present.

Star formation within the G305 complex appears to have proceeded in a punctuated fashion, with bursts of star formation at different epochs over the history of the complex. The morphology of G305 also suggests a multi-seeded star-forming nature, with several distinct HII regions surrounding the main body of the complex that appear to be unrelated to the intense star formation happening at the rim of the central cavity. We will discuss these results in more detail in the following chapter in relation to recent and ongoing star formation and the molecular gas.

4.10 Summary

We have surveyed the G305 complex in search of radio emission at 5.5 and 8.8 GHz associated with the small- and large-scale ionised environment. We resolve the large-scale radio structure of G305 and identify significant extended low surface brightness emission associated with complex and compact emission around the periphery of the central cavity. We identify 18 broad emission features and within these we identify six compact sources. By considering the large-scale radio emission morphology, size, dynamical age and association with GLIMPSE mid-infrared data we classify the large-scale radio emission into eleven classical HII regions, five compact HII regions, four extended features and we are unable to positively classify two sources.

We find that approximately 40% of the large-scale 5.5 GHz radio integrated flux is associated with low surface brightness extended features. The morphology of the large-scale 5.5 GHz emission suggests that 60% of the total integrated flux is associated with HII regions around the periphery of the central cavity. Previous observations by Davies et al. (2012) reveal that Danks 1 contains massive stars with sufficient ionising flux to power the observed emission at 5.5 GHz however they do not appear to be responsible for the observed emission. It is therefore likely that there is significant (> 50%) photon leakage as suggested by Clark & Porter (2004).

By spatially filtering the interferometric data, we are able to image the small-scale radio environment towards G305 and identify 71 compact radio sources randomly distributed across the observed field (Fig. 4.7). Cross matching these 71 compact radio sources to GLIMPSE mid-infrared data reveals 15 sources that are associated with G305, six of which we identify as candidate UC HII regions, one as a BRC, eight as stellar radio sources leaving 56 background radio sources. Analysis of the six candidate UC HII regions reveals radio sources with physical properties consistent with known UC HII regions in five cases. We find typical UC HII properties for these sources, with source radii ranging from 0.04–0.1 pc, emission measures $\sim$ 2.56–10.3 $\times 10^6$ pc cm^{-6} and electron densities $\sim$ 0.34–1.03 $\times 10^4$ cm^{-3}.

By assuming that the observed Lyman continuum photon rate of the detected HII regions are powered by a single massive star we derive the corresponding spectral type and mass. By extrapolating the IMF based on the mass of this star we are able to estimate the total mass of stars associated with each HII region and by dividing by the formation timescale of a YSO determine the SFR. In this way we estimate a SFR based on UC HII regions of 0.002–0.004 $M_\odot$ yr^{-1} and based on compact and classical HII regions $\sim$ 0.02–0.04 $M_\odot$ yr^{-1}. In addition to the 30 massive stars detected by Davies et al. (2012) we identify at least 15 in the large-scale radio emission and a further five indicated by UC HII regions bringing the total number of massive stars in G305 to more than 50.

Chapter 5

Dissecting the environment and star formation within G305

5.1 Introduction

The overall view of the G305 complex is that of a large star-forming region comprised of at least two populations of massive stars and ongoing star formation (Clark & Porter, 2004). The feedback from massive stars in the centre of the complex is responsible for creating a large cavity in the surrounding molecular gas within which we see numerous HII regions and signs of ongoing star formation. A number of authors (e.g. Clark & Porter 2004; Longmore et al. 2007b; Davies et al. 2012) have suggested that the distribution of massive stars and star formation in G305 indicates that the ionised environment, generated by 45 or more massive stars, is interacting with the molecular environment potentially triggering new episodes of star formation. In the two previous chapters we present observations, analysis and discussion of the molecular and ionised environment towards G305. In this chapter we aim to bring together the findings from these two studies and in combination with recent and ongoing tracers of star formation explore the SFH and impact of massive stars on the evolution of the G305 complex.

In Section 5.2 we present a panoramic view of the ionised and molecular environment of G305 and star formation indicators. We then go on to discuss and compare several methods for deriving the star formation rate in G305 in Section 5.3. In Section 5.4 we present evidence for triggering in G305. To put G305 in context we compare the complex to other well-known star-forming regions in Section 5.5. We end this chapter with Section 5.6, a discussion of the SFH and possible future evolution of the G305 complex.

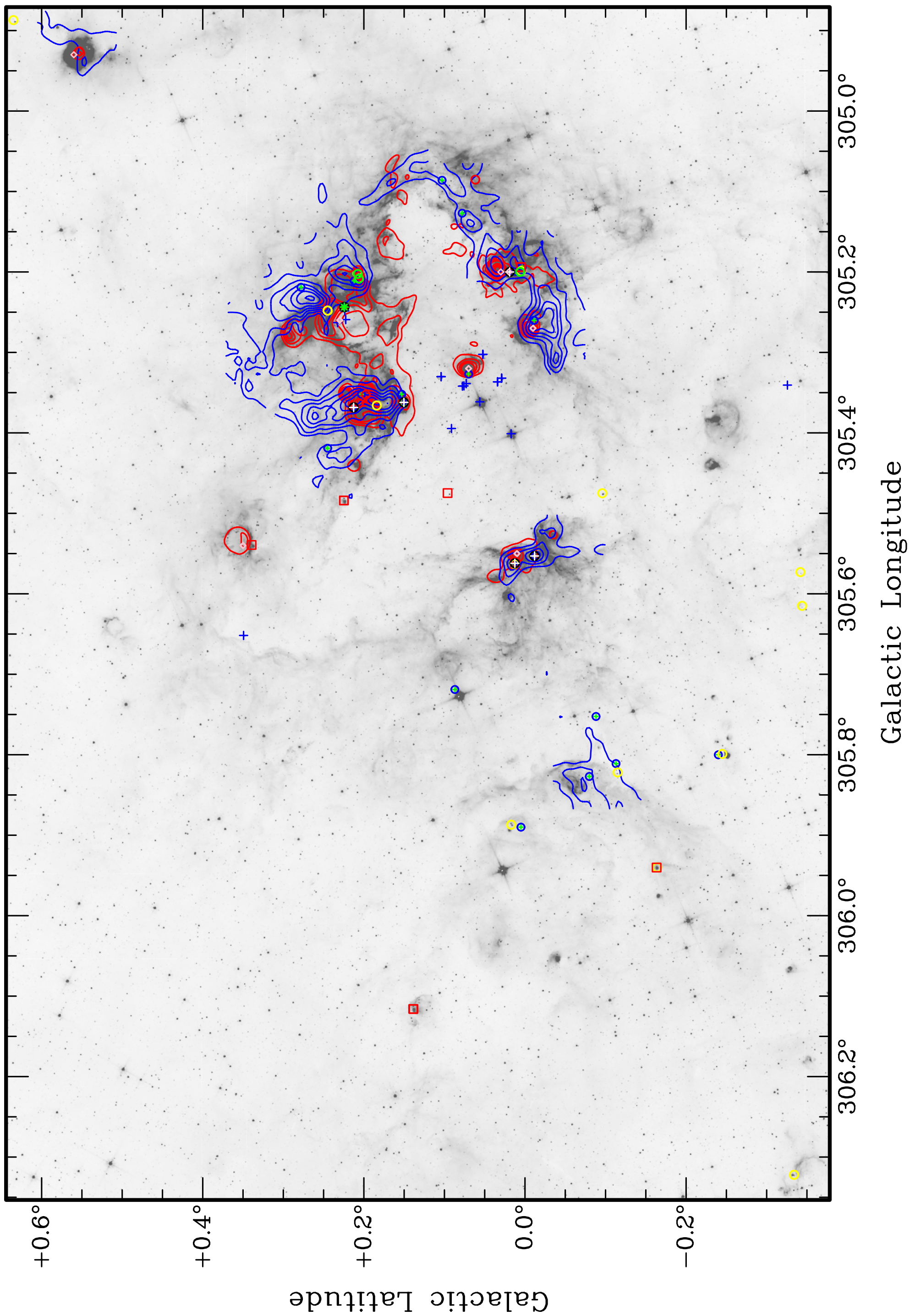

Figure 5.1: The 5.5 GHz radio emission, smoothed by a $30 \times 30''$ Gaussian and ^{13}CO contours in red and blue respectively (same levels as Figs. 4.5 and 3.9) are presented over a greyscale 5.8 μm GLIMPSE background. Identified massive stars are shown by blue crosses whilst black circles with white crosses indicate UC HII regions. Masers are shown as circles; Methanol = yellow, H_2O = blue (centred on green crosses), OH = green. Thermal SiO emission is shown by red circles and pink diamonds indicate embedded infrared clusters and red boxes indicate YSOs detected in the RMS survey.

5.2 A panoramic view of the environment and star formation towards G305

A key goal of this thesis is to explore the distribution of recent and ongoing star formation in relation to the ionised and molecular environment of G305. To briefly summarise, in Chapter 2, Section 2.5.1 we located recent star formation by identifying massive stars reported by Davies et al. (2012), Mauerhan, Van Dyk & Morris (2011) and (Leistra et al., 2005) and embedded infrared clusters in Dutra et al. (2003) (Table A.1). Ongoing star formation in G305 is identified by utilising YSOs discovered in the RMS survey (Urquhart et al., 2008), 6.7 GHz methanol masers drawn from Caswell (2009) and the MMB survey (Green et al., 2009), OH masers from Caswell (1998) and shocked gas traced by thermal SiO emission (Harju et al., 1998). To this view of recent and ongoing star formation we add six new H_2O masers (Section 3.5.5, Table 3.7) and five UC HII regions (Section 4.8.2, Table 4.4). In Fig. 5.1 we present these recent and ongoing star formation tracers overlaid onto a GLIMPSE 5.8 μm image of G305 to give the most detailed view of the distribution of star formation to date.

To explore the global distribution of star formation and the molecular and ionised environment of G305 we overlay ^{13}CO molecular line emission (blue contours) and 5.5 GHz radio continuum emission (red contours) in Fig. 5.1. This figure clearly shows that the ionised and molecular environment of G305 and ongoing star formation is concentrated around the periphery of the central cavity whilst towards the centre of the cavity we find the majority of the visible massive stars. The powerful winds and radiation from these massive stars appears to have completely destroyed or displaced the molecular gas directly to the North- and South- East of Danks 2 leaving only a compact over-dense pocket of molecular gas to the East. This feedback from the massive stars also appears to be in the process of breaking through the thin lobe of molecular gas that makes up the Western wall of the cavity. To explore the relationship between the ionised and molecular environment and star formation in more detail we present sub-figures of the North-East, North-West, South-West and East regions (Fig. 5.2) of G305 and describe each below.

NE Region: In this region (Fig. 5.2(a)) we identify two RMS sources (YSOs), two SiO sources, three H_2O masers, one OH maser, two methanol masers, an infrared cluster and two UC HII regions. The ionised and molecular emission are superimposed upon each other in this region, which suggests we are observing this part of the complex at a different projected angle compared to the other regions. Starting at the bottom-right of Fig. 5.2(a) we can see low surface brightness and extended 5.5 GHz emission indicating the boundary between the central cavity and the molecular gas. At this interface we identify an OH maser superimposed upon a methanol maser and UC HII region on the borders of an compact HII region and in close proximity to an H_2O maser. Directly to the North of the cavity boundary a bright HII region can be seen that is associated with complex multi-peaked ^{13}CO emission and a bright mid-infrared hotspot. Within

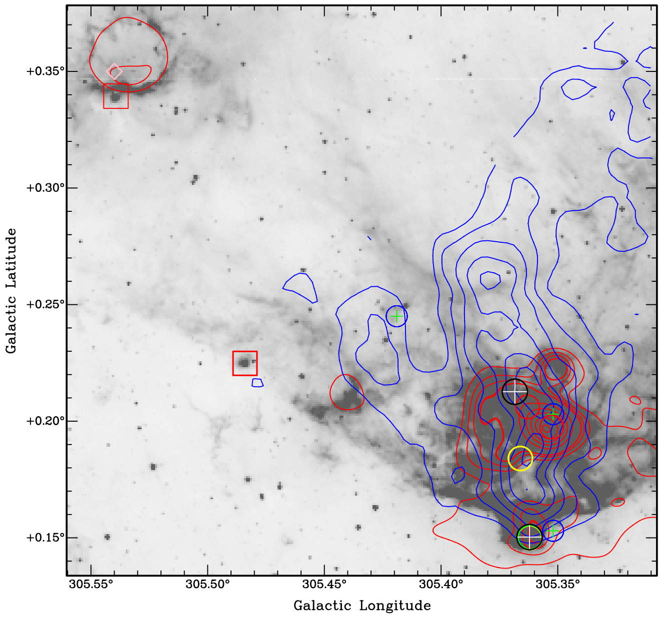

(a) North-East

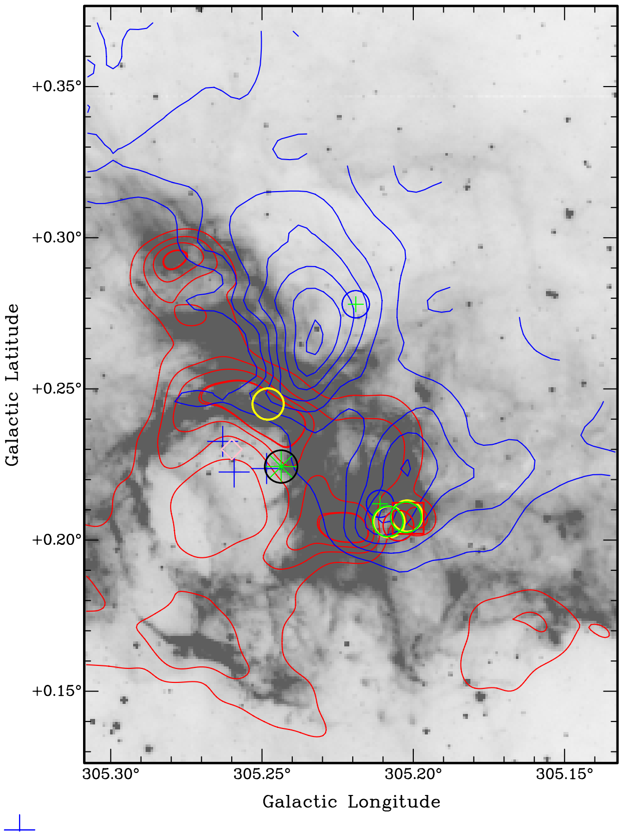

(b) North-West

FIGURE 5.2: GLIMPSE 5.8 µm grey scale background with 5.5 GHz radio continuum and molecular gas traced by ^{13}CO presented as red and blue contours. Identified massive stars are shown by blue crosses whilst black circles with white crosses indicate UC HII regions. Masers are shown as circles; Methanol = yellow, H_2O = blue (centred on green crosses), OH = green. Thermal SiO emission is shown by red circles and pink diamonds indicate embedded infrared clusters and red boxes indicate YSOs detected in the RMS survey.

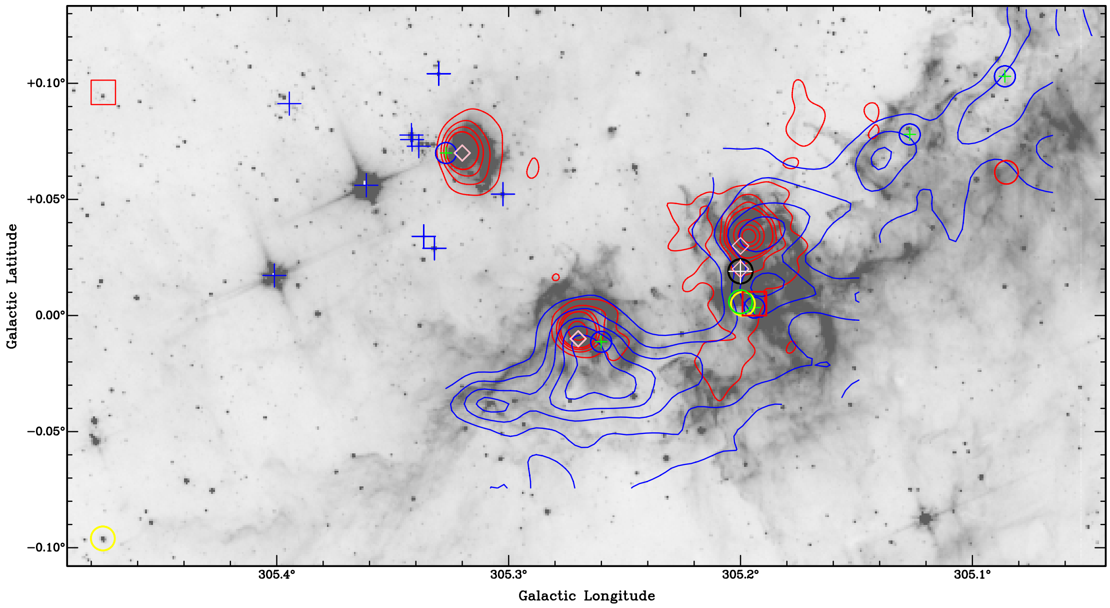

(c) South-West

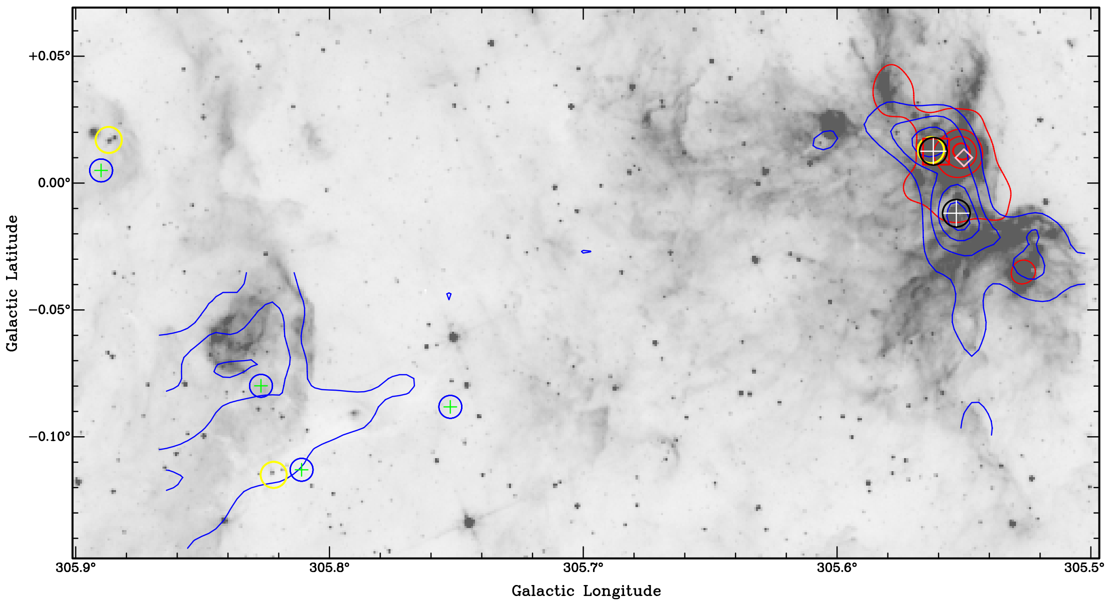

(d) East

FIGURE 5.2: Identified massive stars are shown by blue crosses whilst black circles with white crosses indicate UC HII regions. Masers are shown as circles; Methanol = yellow, H_2O = blue (centred on green crosses), OH = green. Thermal SiO emission is shown by red circles and pink diamonds indicate embedded infrared clusters and red boxes indicate YSOs detected in the RMS survey.

the bounds of the HII regions we identify two SiO sources, an H_2O and methanol maser and UC HII region. This region is host to intense ongoing star formation, however the orientation complicates the interpretation of the relationship between the molecular and ionised gas and star formation. The RMS source and infrared cluster to the North-West are associated with an isolated shell of radio emission (Source 11, G305.532+0.348, Fig. 4.6(g)) that is typical of an HII region. The RMS source is located on the outer rim of this ring whilst the infrared cluster is projected within the bounds of the ring. The morphology of this HII region coupled with the position of the YSO and infrared cluster is highly suggestive of triggering induced by the expansion of the HII region (Zavagno et al., 2007; Thompson et al., 2012).

NW Region: This region is dominated by the classical HII region G305.254+0.204 (Fig. 5.2(b)). Within this HII region we find three massive stars (Table A.1; L05-A1, A2 and A3) and an embedded infrared cluster. The winds and radiation associated with these massive stars is the most likely candidate for the driving force behind the observed HII region. The G305.254+0.204 HII region appears to have destroyed or swept up the molecular gas in the direct vicinity and is in the process of breaking through the low-density material between the two main molecular clumps to the North-West. There is a distinct lack of ^{13}CO emission to the South of the HII region. As mentioned in Chapter 2 both Longmore et al. (2007b) and Leistra et al. (2005) suggest that the HII region is responsible for triggering star formation in this region. We find evidence of such interaction in the BRC (compact radio source 10, Fig. 4.9). All star formation in this region is restricted to the West of the HII region within the molecular gas. Within the bounds of the molecular gas we find one YSO, three methanol masers, two of which are associated with OH masers and a single SiO source. One methanol maser is associated with the HII region and molecular cloud interface in the North of the region and one H_2O maser is found set back away from the interface in the Northern clump of gas. By far the most intense site of star formation in this region is in the Southern molecular clump where we identify two methanol masers also known as G305A (G305.21+0.21) and G305B (G305.21+0.20) (Walsh & Burton, 2006; Walsh et al., 2007). Both methanol masers are associated with OH masers and between these sites of massive star formation we see an SiO. G305A is associated with the peak ^{13}CO emission whilst G305B borders a compact HII region (large-scale Source 12, G305.197+0.206) and YSO. The presence of a YSO associated with G305B but not G305A supports the theory that G305B is more evolved than G305A (Walsh et al., 2007).

SW Region: Fig. 5.2(c) presents the ionised and molecular environment and star formation towards the SW region. We identify five H_2O masers, two methanol masers, a single SiO source and OH maser and YSO. The molecular gas runs in an unbroken strip from the North-West to South-East where it terminates. Two bright HII regions (large-scale sources 2 and 3, G305.195+0.033 and G305.270−0.007) are located along this strip and there is a significant component of low surface brightness radio emission. The molecular emission shows signs of being swept up and dispersed along its length with the two most prominent peaks associated with the two bright HII regions. Between these two HII regions the molecular gas appears to be significantly reduced. Star formation is concentrated around these HII regions particularly the HII regions Source 2 (G305.195+0.033) where we identify an UC HII region, methanol maser and infrared cluster. H_2O masers are distributed along the length of the molecular material suggesting there is ongoing star formation along its length. The centre of the G305 complex can be seen in the top-left of Fig. 5.2(c). Within the central cavity we find the highest density of identified massive stars, which surround Danks 1 and 2. The "blob" can be clearly seen projected within the cavity as a bright compact radio source associated with 5.8 μm emission and a H_2O maser and infrared cluster but no ^{13}CO emission.

E Region: This region is shown in its entirety in Fig. 5.1. Our CO and 5.5 GHz maps are limited to the periphery of the cavity and shown in Fig. 5.2(d). This region is distinctly different from the other regions we have discussed, star formation is dispersed across a distance of up to ~ 40 pc from the cavity boundary identified by bright mid-infrared emission. We find a total of four RMS sources, six MMB sources, six H_2O masers, two UC HII regions and an embedded cluster. This region has considerably less 5.8 μm and molecular emission (see Fig. 3.5) than those discussed above, with only a dense lobe of emission coincident with the boundary of the central cavity. This region is associated with two UC HII regions, one of which is on the borders of a bright mid-infrared cometary structure and associated with an RMS YSO and methanol maser.

5.2.1 Star formation and the molecular material

To assess the level of star formation associated with the molecular clumps in G305 and search for possible relations between the molecular clump properties we perform cross matching between star formation tracers (Appendix A.1) and CO clumps (Table C.2) in position (l, b) and when it is known velocity (v). Star formation tracers with unknown velocity are assigned to all clumps along the line of sight. Coupled with the derived physical properties this provides a tool with which to study the relationship between molecular gas and ongoing star formation. This method assumes that star formation sources and molecular gas coincident in velocity are associated spatially. Without knowledge of the true three-dimensional structure of the region this is implicit and may result in multiple or false positive associations of stars with molecular clumps along the line of sight. In this way we identify star formation associated with 15 CO clumps around the periphery of the central cavity. From Fig. 5.1 and 5.3 we can clearly see that these star-forming clumps are concentrated within the photodissociation ring around the periphery of the

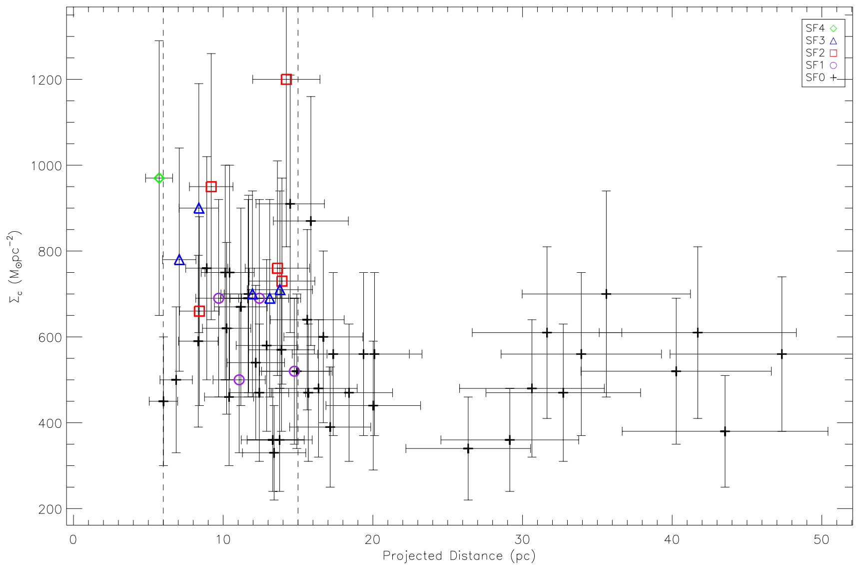

FIGURE 5.3: Plot showing the projected distance of the CO clumps from Danks 2 against the surface density. The number of star formation tracers coincident with each clump is indicated by the symbols described in the legend. Dashed vertical lines highlight the extent of the central cavity of G305 between 7 and 17 pc from Danks 2.

central cavity at a projected distance between 7 and 17 pc. We also note in this plot and Fig. 5.4 that star-forming clumps on the borders of the central cavity have a higher FWHM and surface density than quiescent clumps a trend that will be explored further in the following section (Lada et al., 2012).

The FWHM histogram of CO clumps presented in Section 3.7.4 Fig. 3.20(e) shows a bimodal population distribution that peaks with eleven clumps in the FWHM bins at 2.8 and 4.8 km s^{-1} either side of the mean (4.12 km s^{-1}). We searched for any intrinsic difference in the molecular properties and number of star formation tracers associated with the molecular clumps either side of the mean FWHM. We find that the 28 CO clumps with a FWHM less than 4.12 km s^{-1} are associated with 10 star formation tracers whilst the 29 CO clumps with FWHM greater than 4.12 km s^{-1} are associated with 23 star formation tracers (Fig. 5.4). This suggests that the FWHM increases towards regions of star formation in agreement with the turbulent core model of McKee & Tan (2003).

This raises the question, is the observed turbulence generated by star formation or is high turbulence a prerequisite for star formation? One way to test this is to look at the turbulent velocity of the gravitationally bound CO clumps in G305, which have yet to form stars (Fig. 5.5). We find that the FWHM of the eight bound CO clumps range from 2.37 to 5.71 km s^{-1} with a mean of 4.04 km s^{-1}. This is only slightly lower than the mean FWHM of the CO catalogue of 4.12 km s^{-1} and so does not suggest any intrinsic difference between the turbulent velocities of quiescent gravitationally bound clumps and star-forming clumps.

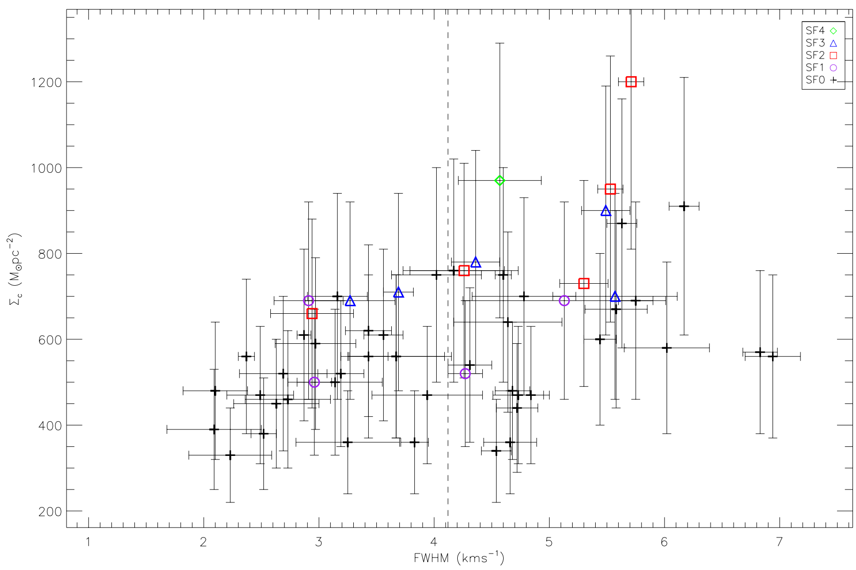

FIGURE 5.4: Plot showing the FWHM vs. surface mass density of the CO clump catalogue. The number of star formation tracers coincident with the source is indicated by the legend in the top right and the dashed vertical line indicates the mean FWHM of the CO catalogue.

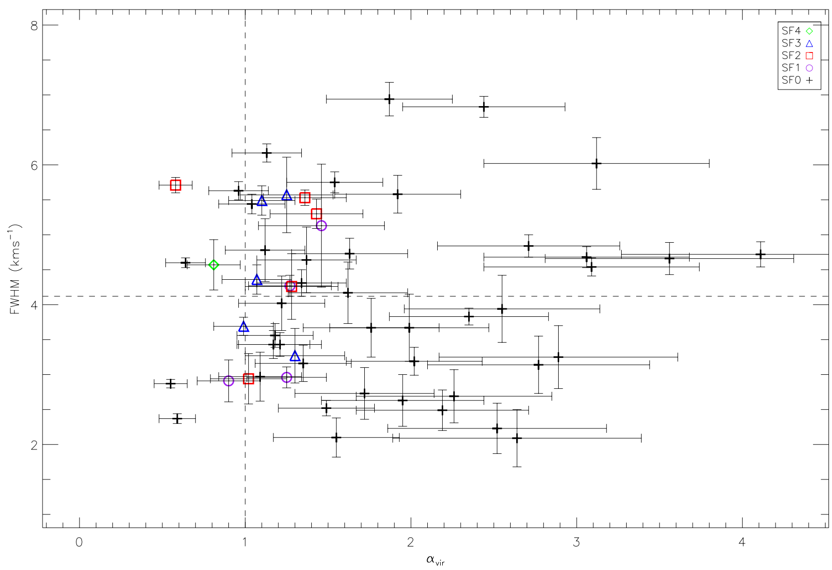

FIGURE 5.5: Plot showing the virial parameter of the CO clumps against the FWHM. The number of star formation tracers coincident with the source is indicated by the legend in the top right. The dashed vertical line indicates the point at which the virial mass is one below this clouds are gravitationally bound. The horizontal vertical line indicates the mean FWHM of the CO clump catalogue.

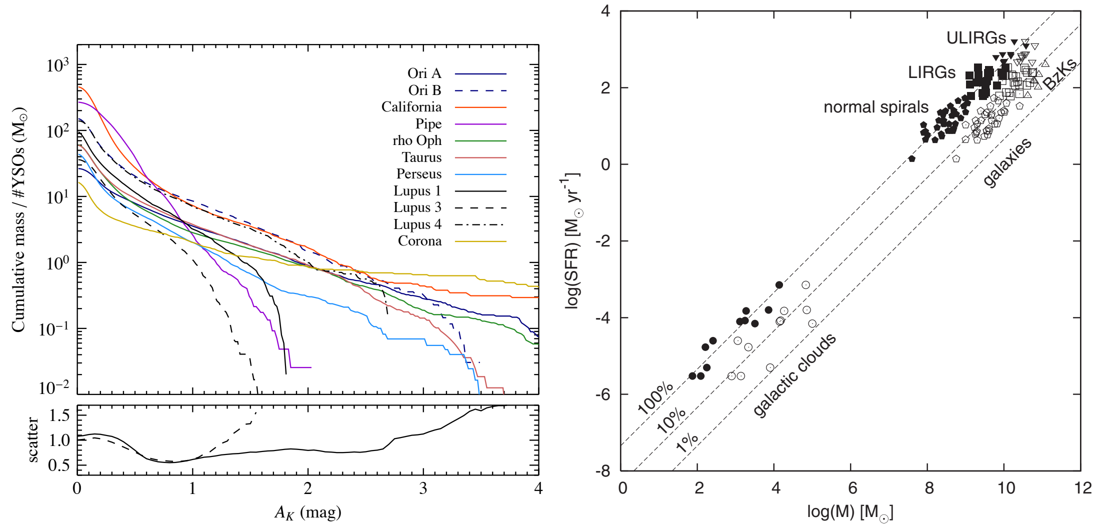

FIGURE 5.6: Left: Plot of the ratio of cumulative mass to YSO content vs. extinction for the local sample of star-forming molecular clouds in Lada, Lombardi & Alves (2010). The dispersion in the logarithms of these ratios (dashed trace) and the normalised dispersion (solid trace) are also plotted as a function of extinction. Right: SFR molecular-mass diagram for local molecular clouds and galaxies from Lada, Lombardi & Alves (2010). The solid symbols correspond to measurements of dense cloud masses either from extinction observations of the Galactic clouds or HCN observations of the galaxies. The open symbols correspond to measurements of total cloud masses of the same clouds and galaxies, either from extinction measurements for the Galactic clouds or CO observations for the galaxies. For the galaxies, pentagons represent the locations of normal spirals, while the positions of starburst galaxies are represented by squares (LIRGs) and inverted triangles (ULIRGs). Triangles represent high-z BzK galaxies. The parallel dashed lines are linear relations that indicate constant fractions of dense (i.e. $A_{\rm K} \geqslant 0.8$ mag; $n_{\rm H2} \geqslant 10^4\,{\rm cm}^3$) gas. The top line is the best linear fit to the solid symbols and represents the case where all the gas measured is dense star-forming material.

5.3 Star formation rate

The SFR describes the rate at which mass is converted into stars and provides a fundamental physical parameter for characterising the evolution of star-forming regions and galaxies (see, e.g. Kennicutt 1998; Calzetti et al. 2009; Kennicutt & Evans 2012 for reviews of SFR indicators). We have estimated the star formation rate of G305 from what appears to be three separate epochs of high-mass star formation, based on the mass of the central clusters Danks 1 and 2 and extrapolation of the IMF based on the most massive stars associated with compact, classical and UC HII regions (Section 4.9). A number of other methods exist for determining the SFR, which we discuss and apply below.

The star formation rate of molecular clouds within 0.5 kpc of the sun has been found to scale linearly with the molecular cloud mass (Heiderman et al., 2010; Lada, Lombardi & Alves, 2010) above an extinction threshold of $A_{\rm K} \approx 0.8$ mag. This conclusion is drawn from the relationship between the cumulative mass of YSOs within a molecular cloud as a function of extinction (Fig. 5.6; left), where a marked minimum dispersion of the cumulative YSO mass is seen at $A_V = 7.3 \pm 1.8$ mag. This extinction corresponds to a surface density of $\sum_c \approx 116\,M_\odot\,pc^{-2}$ and Lada, Lombardi & Alves (2010) argue that this equates to a gas volume density of $n_{H_2} \approx 10^4\,cm^{-3}$. In extragalactic studies the luminosity of dense gas tracers such as HCN, which has approximately the same critical density as NH_3 ($10^4\,cm^{-3}$), also shows a tight correlation with the total infrared luminosity, a proxy for the SFR (Gao & Solomon, 2004). The SFR and dense gas correlation holds on both a Galactic and extragalactic scales, over more than nine orders of magnitude in cloud mass (Fig. 5.6; right). This suggests that the close relationship between the SFRs and the dense gas masses of molecular clouds could be the underlying physical relation that connects star formation activity with interstellar gas over vast spatial scales from the immediate vicinity of the Sun to the most distant galaxies. The SFR based on dense molecular gas (Lada, Lombardi & Alves, 2010) is defined as:

$$SFR_{mol} = 4.6 \pm 2.6 \times 10^{-8} M_{0.8}\ [M_\odot\,yr^{-1}] \tag{5.1}$$

where $M_{0.8}$ corresponds to the cloud mass that is above the extinction threshold of $A_K \approx 0.8$. We may apply Equation 5.1 to derive the SFR for G305 based on the dense gas component in two ways. First, we apply the surface density threshold ($\sum_c \approx 116\,M_\odot\,pc^{-2}$) to the CO clump catalogue and find that all the detected CO clumps exceed the minimum surface density. With a total CO derived mass of $M_{0.8} = 2.5 \pm 0.8 \times 10^5\,M_\odot$ the SFR is $SFR_{CO} = 0.003$–$0.02\,M_\odot\,yr^{-1}$. Second, assuming that the relationship applies to densities of $n_{H_2} \approx 10^4\,cm^{-3}$ means that all NH_3 emission, which has a critical density of approximately $\sim 10^4\,cm^{-3}$, should apply. Therefore the SFR based on NH_3, where $M_{0.8} = 6.5 \pm 3 \times 10^5\,M_\odot$, is $SFR_{NH^3} = 0.007$–$0.07\,M_\odot\,yr^{-1}$. For the SFR based on the molecular material we take the range of these two values to arrive at a molecular gas based SFR of $SFR_{mol} = 0.003$–$0.07\,M_\odot\,yr^{-1}$. It should be stressed that this SFR relationship is averaged over a timescale of 2 ± 1 Myr, the age spread of low-mass YSOs ($0.5\,M_\odot$) in the local cloud sample of Lada, Lombardi & Alves (2010).

The SFR may also be independently estimated using the Lyman continuum photon rate. According to Kennicutt, Tamblyn & Congdon (1994) and Kennicutt (1998), a SFR of $1\,M_\odot\,yr^{-1}$ produces a Lyman continuum photon rate of $N_{Ly} = 9.26 \times 10^{52}$ photons s^{-1} for the Salpeter IMF (assuming a mass range of 0.1–100 $M_\odot$). It then follows that the SFR based on the Lyman continuum photon rate is:

$$SFR_{ion} = 1.08 \times 10^{-53} N_{Ly}\ [M_\odot\,yr^{-1}] \tag{5.2}$$

The integrated flux density of G305 at 5 GHz, based on single dish measurements, is approximately 200 Jy (Clark & Porter, 2004), therefore the corresponding total Lyman continuum rate given by Equation B.107 is $N_{Ly} = 2.61 \times 10^{50}$ photons s^{-1}. Applying this Lyman continuum rate

SFR Tracer	SFR ($M_\odot\,yr^{-1}$)
Danks 1 and 2	0.02–0.04
Compact and classical HII	0.02–0.04
UC HII regions	$\geqslant$ 0.002–0.004
Molecular gas	0.003–0.07
Lyman continuum	$\geqslant$ 0.002–0.005

TABLE 5.1: Calculated SFR for G305 using multiple SFR tracers (see text for details).

in Equation 5.2 yields a SFR based on the ionised gas of $SFR_{\rm ion} \approx 0.002$–$0.005\,M_\odot\,yr^{-1}$ similar to the SFR derived in the same way for M17 (Chomiuk & Povich, 2011). The SFR derived in this way should be interpreted as the continuous SFR required to maintain a steady state population (i.e. number of ionising stars born equals deaths) of ionising stars that produce the ionising flux rate. This means that the timescale assumed in Eq. 5.2 is in excess of the lifetime of the ionising stars. For a late O star this implies a time scale of $\sim$ 8 Myrs whilst for an early O star the time scale is $\sim$ 5 Myrs (Bertelli et al., 1994; Martins, Schaerer & Hillier, 2005). For G305 this steady state clearly does not apply, the oldest cluster Danks 2 is only 3^{+3}_{-1} Myrs old and the complex shows no signs of supernova remnants, indicating the death of massive stars, and so the SFR derived by Eq. 5.2 is an underestimate. In addition there is expected to be a high level of photon leakage towards G305 (see Section 4.6.2) and dust absorption that implies the Lyman continuum derived SFR may be underestimated by as much as 50%.

We find that the SFR derived using UC HII regions and the Lyman continuum are an order of magnitude lower than the SFR derived by other methods (Table 5.1). As discussed in Section 4.9, the SFR derived by extrapolating from the UC HII regions is a lower limit due to incompleteness in the UC HII sample. However, this may indicate that the SFR of G305 has lowered in the last 1–2 Myrs. Evans et al. (2009) have estimated values of SFR in giant molecular clouds and within some dense cloud cores. They find values of $SFR = 0.03$ to 0.06 for GMCs with mean densities distributed around a mean value of $\langle n \rangle = 390\,cm^{-3}$, and SFR = 0.05 to $0.25\,M_\odot\,yr^{-1}$ for dense cores with mean densities 50–200 times those of the GMCs. These values are computed by assuming that all the stars detected (by their infrared excess) have been formed in the last 2 Myr. The authors report a best estimate of 2 ± 1 Myr for the lifetime of the Class II YSO phase, so the SFR could be 50% lower, or 100% higher than the values given above. Accounting for this uncertainty, one gets $SFR = 0.02$ to $0.12\,M_\odot\,yr^{-1}$ for GMCs, and $SFR = 0.03$ to $0.5\,M_\odot\,yr^{-1}$ for dense cores, suggesting a characteristic value of order 0.1. We find that the results listed in Table 5.1 and the average SFR over the lifetime of G305 (Section 4.9; 0.005–0.014 $M_\odot\,yr^{-1}$) is consistent with these findings.

The average star formation rate for the entire Milky Way is estimated at $\sim 2\,M_\odot\,yr^{-1}$ (Chomiuk & Povich, 2011; Davies et al., 2011). With a star formation rate over its lifetime of between 0.005–0.014 $M_\odot\,yr^{-1}$ only a few tens to hundreds of complexes like G305, Carina and M17 could make up the bulk of the star formation in the Milky Way. The pinnacle is likely to be dominated by a few much larger complexes, for example the giant HII complexes identified by observations of the Galactic plane with the Wilkinson Microwave Anisotropy Probe (WMAP) that make up half the total Galactic ionising flux (Murray & Rahman, 2010). Just as the few most massive stars at the top of the IMF dominate the luminosity function, a few massive star-forming complexes likely dominate Galactic star formation.

5.4 Evidence for triggered star formation

When studying GMCs, HII regions and ongoing star formation, the question of triggered star formation often arises. Massive star(s) are thought to be able to promote further star formation in nearby molecular material by driving winds and shocks, which both sweep up material and overrun and compress pre-existing condensations (Section 1.6). Subsequent gravitational instability and/or radiatively driven implosion of the overrun condensations collectively lead to triggered star formation (Elmegreen, 1998; Zinnecker & Yorke, 2007). The result of triggered star formation should be a spatial ordering of sequentially younger generations of stars from the central massive star(s) that instigated the triggering cascade. Proving this conclusively is problematic at best. Typical methods involve “not disproving” the hypothesis, often by assembling a consistent time line for the different phases of star formation. In this section we discuss the evidence for triggered star formation in G305.

The morphology of the ionised and molecular gas and the location of star formation tracers within G305 is highly suggestive of triggered star formation as proposed by Elmegreen & Lada (1977). We find evidence of at least three generations of massive stars towards G305. The oldest generation (3–6 Myr) is found in Danks 1 and 2 and a co-spatial distribution of visible massive stars that have cleared the surrounding molecular gas. The second generation is indicated by classical and compact HII regions (0.1–2.4 Myr) surrounding the central cavity and in close proximity to molecular gas (Fig. 5.1). The third generation is found around these HII regions in the form of UC HII regions and methanol masers ($<$ 0.1 Myr). These epochs of massive star formation are separated both spatially and temporally, which suggests that massive star formation may have taken place in a number of distinct bursts rather than constantly over the lifetime of the complex. We note that there are two HII regions (G305.254+0.204 and G304.93+0.56) that are isolated away from the main cavity that suggests massive stars have also formed spontaneously within the complex. A number of star-forming regions show similar distributions of star formation and HII regions to G305 such as NGC3603 (Nürnberger et al., 2002), 30Dor (Walborn & Blades, 1997; Walborn, Maíz-Apellániz & Barbá, 2002) and to a lesser extent Carina (Brooks, Storey & Whiteoak, 2001). In all these cases the authors suggest that the distribution of star formation reflects the propagation of triggered star formation through the molecular cloud.

However, the morphology and distribution of stars is not considered sufficient evidence to confirm triggering. The central problem of triggered star formation is the difficulty in identifying the origin of the discovered star formation. When attempting to identify star formation that has been triggered one must first exclude the possibility that the star(s) would have formed spontaneously without the influence of a trigger. Star formation located around an HII region for instance may have formed spontaneously and simply been uncovered by the expansion of the HII region. Additional evidence is required to support the morphological evidence that a stars formation was induced and not spontaneous.

The best model for triggered star formation in G305, given its age and morphology, is the collect and collapse model, where an expanding HII region compresses the surrounding material and sweeps up a shell of dense gas. At some point, the dense shell becomes unstable, fragments, and collapses to form stars (Elmegreen & Lada, 1977). To explore the timescales involved in triggered star formation (Section 1.6.1.1) via the collect and collapse process we follow the approach of Dale, Bonnell & Whitworth (2007) and Whitworth et al. (1994) and calculate the time it would take for a swept up shell of molecular gas to gain sufficient mass to become gravitationally unstable and fragment called the "fragmentation timescale". In order for a region to be consistent with a triggered star formation scenario, the time from the formation of the ionising star and turning on of the associated HII region to the gravitational instability and fragmentation of the swept up shell, plus the age of the putatively triggered star formation population must be comparable to the total age of the triggering source. The fragmentation timescale is calculated by assuming a simple model of the gravitational stability of a uniform shocked shell driven by an HII region expanding in a medium of uniform density composed of pure hydrogen as:

$$t_{\mathrm{frag}} \sim 1.6 \frac{a^{7/11}}{0.2} \frac{N_{\mathrm{Ly}}^{-1/11}}{10^{49}} \frac{n_3^{-5/11}}{10^3} \text{ [Myr]} \tag{5.3}$$

where a is the sound speed inside of the shocked layer in units of 0.2 km s^{-1}, N_{Ly} is the Lyman continuum photon rate in s^{-1} and n_3 is the initial gas atomic number density in units of 10^3 cm^{-3}. The fragmentation timescale relies on the knowledge of the natal ambient density and the Lyman continuum photon rate, unfortunately neither of these values are easily derived for G305 and Danks 1 and 2. As with the dynamical age derived in Section 4.6, the natal ambient density is unknown and must be assumed. The atomic number density assumed in Dale, Bonnell & Whitworth (2007) is 200 cm^{-3} but in Chapter 3 we determine an average current molecular density of 5400 cm^{-3} implying that the assumed atomic density may be low by a factor of more than 50. In addition the assumption of a uniform medium certainly is not valid for G305 and the average temperature of molecular gas in G305 is $\sim$ 20 K giving an isothermal sound speed of 0.4 km s^{-1}. Finally, As we demonstrated in Section 4.6.2 the contribution to the Lyman continuum rate from Danks 1 and 2 and massive stars within the central cavity is difficult to reliably estimate. To obtain a rough estimate of the fragmentation timescale of Danks 1 and 2 we note that in Danks 1 the three WNLh stars have a Lyman continuum output proportional to the total Lyman continuum flux of the whole complex and so assume $N_{\rm Ly} =\sim 3.2 \times 10^{50}$ (Davies et al., 2012; Clark & Porter, 2004). Therefore, assuming the simple model of Dale, Bonnell & Whitworth (2007) $a = 0.2\,{\rm km\ s^{-1}}$ and $n_3 = 200\,{\rm cm^{-3}}$ the fragmentation timescale required for star formation to be triggered by Danks 1 and 2 is ~ 2.4 Myr. Comparing this to the dynamical age of the HII regions around the periphery of the central cavity (0.1–2.4 Myr; Table D.1) it is plausible that these HII regions formed within the fragmentation timescale and so could have been triggered by Danks 1 and 2.

One of the strongest cases for triggering in G305 is towards the HII region G305.254+0.204 (Fig. 5.2(b)). The radio and mid-infrared morphology of this HII region suggests that it is almost completely bound and has a Lyman continuum rate of approximately $3.9 \times 10^{49}\,{\rm s^{-1}}$. Under the same assumptions as the previous calculation ($n_3 = 200\,{\rm cm^{-3}}$ and $a_3 = 0.2$ kms) this give a fragmentation time scale of $t_{\rm frag} = 2.9$ Myr. However, we note that the current atomic density in this region is $\sim 11000\,{\rm cm^{-3}}$, and the temperature is $\sim 20\,K$. If we apply these values to Eq. 5.3 we derive a lower limit fragmentation timescale of $t_{\rm frag} = 0.7$ Myr. Considering the dynamical age of the G305.254+0.204 HII region is 2.4 Myr and the uncertainty inherent in the calculation of the dynamic age and fragmentation timescale and the star formation tracers detected along the periphery are < 0.5 Myr suggests that it is plausible that the expanding HII region could be responsible for triggering star formation.

More detailed modelling of G305 would be problematic due to the non-static large-scale structure. The HII region has formed and evolved in an expanding, increasingly more massive giant shell of molecular material. This type of dynamically changing environment in the surrounding ISM and its interaction with an evolving HII region is beyond the scope of current models. Given the inherent uncertainty in the calculation of the dynamical age and fragmentation timescale we suggest that these results are at most an indication that some star formation may have been triggered within G305. Without prior knowledge of the ambient density and more accurate estimates of the ages and timescales involved it is difficult to link the expansion of the central cavity or HII regions to triggered star formation.

Realising that if an HII region is expanding and driving shocks into the molecular environment we ought to see a clear signature in the velocity structure of the molecular gas may provide an alternative form of evidence. Ideally the orientation should be such that we view a clear boundary between the ionised and molecular gas, only the G305.254+0.204 HII region in the NW region meets this requirement. We generate PV diagrams (Fig. 5.7) by taking a velocity slice through the points at which the optically thick ^{12}CO emission shows the highest gradient, the ionised emission is brightest and star formation is concentrated. This reveals the velocity dispersion at unit optical depth in the ^{12}CO emission (Figs. 5.7(b) and Figs. 5.7(c)) revealing

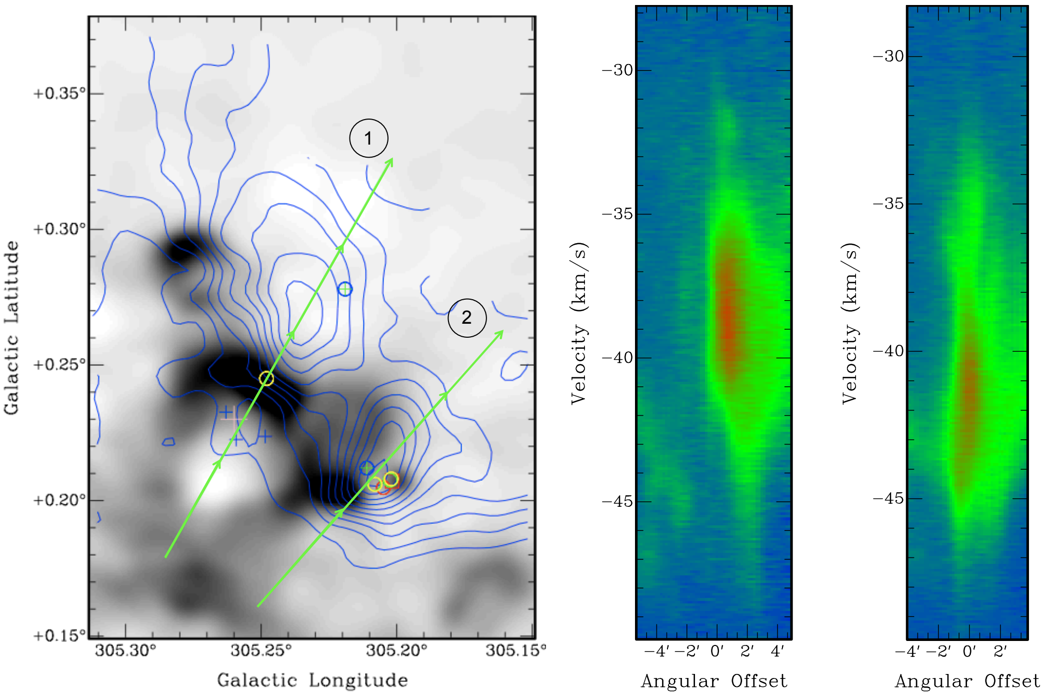

(a) G305.254+0.204 (b) PV slice 1 (c) PV slice 2

FIGURE 5.7: PV diagrams of the G305.254+0.204 HII region in search of velocity structure indicative of expansion motions of the HII region into the molecular gas. Blue contours are ^{12}CO emission and star formation tracers are overlaid (Section 5.2). Green lines with arrows indicate the direction of the PV slice through the ^{12}CO emission and the corresponding PV diagrams are presented to the right.

the velocity structure near the surface of the molecular gas. A large velocity dispersion can be clearly seen at the interface between the ionised and molecular gas through the PV cuts 1 and 2 in Fig. 5.7. This suggests that the molecular material at the boundary between the ionised and molecular gas is being forced towards and away from the observer at between 5 and 10 km s^{-1}. Whilst not conclusive evidence of triggering this does reveal that the HII region is compressing the molecular gas at the boundary, which may lead to triggered star formation.

To summarise, there is compelling morphological evidence for triggering within G305, however this is not sufficient to confirm that triggering is responsible for the observed star formation. We find that it is difficult to imply causality by comparing the fragmentation and dynamical timescales of HII regions in G305 due to the large uncertainties inherent in the assumptions and calculations. The HII region G305.254+0.204 seems to be the most compelling candidate for ongoing triggered star formation due to the morphology, distribution of star formation, velocity signature and association with a BRC.

TABLE 5.2: G305 Comparison, column 3 is molecular mass and column 5 shows the number of identified massive OB stars. Parameters have been taken from a literature search; numbers in brackets correspond to the following papers.

Region	Distance (kpc)	Mass ($M_\odot$)	N_{Ly} 10^{49} (s^{-1})	Stars OB
G305	3.2 – 4.4	10^5	> 31.6	> 45
W49A	10.2 – 12.6 (4)	10^6 (3)	162.2 (15)	> 40 (4)
NGC3603	5 – 8 (5)	10^5 (5)	316.2 (15)	20 (6)
M17	1.3 – 1.9 (9)	10^4 (9)	170.0 (15)	16 (9)
W3 main	1.9 – 2.1 (10)	10^4 (10)	17.8 (15)	12 (10)
Rosette Nebula	1.4 – 1.6 (11)	10^5 (11)	9.8 (14)	30 (11)
Westerlund 2	5 – 7 (12)	10^5 (12)	95.9 (2)	> 12 (12)
Carina	2.3 (13)	10^5 (13)	12.8 (15)	65 (13)

(1) Clark & Porter (2004) (2) Smith, Biermann & Mezger (1978) (3) Smith et al. (2009) (4) de Pree, Mehringer & Goss (1997) (5) Nürnberger et al. (2002) (6) Moffat (1983) (7) Dougherty et al. (2010) (8) Luna et al. (2009) (9) Povich et al. (2009) (10) Tieftrunk et al. (1998) (11) Wang et al. (2008) (12) Dame (2007) (13) Smith & Brooks (2008) (14) Churchwell (1975) (15) Conti & Crowther (2004)

5.5 Comparison to other star-forming regions

To put G305 into context it is useful to compare the region to other well-known GMCs and HII regions in the Galaxy. We have performed a literature search and present the molecular mass, total Lyman continuum photon rate and identified number of massive stars for a number of well-known massive star-forming regions in Table 5.2. It is apparent that G305 is one of the closest and most massive GMCs in the Galaxy, with a molecular mass approximately equal to or exceeding that of other well studied regions. G305 is significantly closer than star-forming complexes with similar masses detailed in Table 5.2. With its numerous HII regions, the integrated Lyman continuum photon count of G305 is on par with the most luminous HII regions in the Galaxy. However, whereas many of these regions comprise single HII regions, G305 is host to a number of individual HII regions surrounding a central cavity. We have confirmed the hypothesis presented by Clark & Porter (2004) that there is substantial photon leakage in Section 4.6 and so the massive stellar population of G305 is likely to be an underestimate. Comparison with the compilation of the mid-infrared and radio properties of giant HII regions presented by Conti & Crowther (2004) and Murray & Rahman (2010) suggests that G305 is amongst the most massive and vigorous star-forming regions in the Galaxy. Considering that the massive stars in G305 have dispersed a great deal of the natal molecular cloud, thus substantially reducing the radio and mid-infrared luminosity, only enhances such a conclusion.

5.6 Star formation history

By considering the distribution of high-mass stars, ongoing star formation, ionised and molecular gas, we can draw a broad-brush picture of the SFH of the G305 complex. In the initial stages the dense central region of the natal GMC collapsed to first form Danks 2 $\sim 3^{+3}_{-1}$ Myr ago and then shortly after Danks 1 $\sim 1.5^{+1.5}_{-0.5}$ Myr ago (Davies et al., 2012). We find a diffuse field of massive stars surrounding Danks 1 and 2 (Fig. 5.1), which may have formed in-situ but the lack of companions suggests that these massive stars are runaway stars ejected from Danks 1 and 2. For the last ~3–6 Myr the powerful UV radiation and winds from these massive stars have swept up and dispersed the surrounding molecular material into the morphology we see today in Fig. 5.1. The molecular material has been dispersed more rapidly in the East and to some extent the West of the complex, which suggests that the natal molecular density of gas was lower in these regions than in the North and South of the complex. We see little recent and no ongoing star formation within the bounds of the central cavity (assuming the blob is projected against the centre) and so feedback appears to have cut-off star formation within the direct vicinity of Danks 1 and 2. Shortly after the formation of Danks 1 a second generation of massive stars has formed, apparent by the presence of compact and classical HII regions (Clark & Porter, 2004) around the cavity. The evidence suggests that this generation of massive stars could have been triggered by the first generation. However, massive star formation has also taken place away from the main complex at projected from 23 to 42 pc from Danks 2 (G305.532+0.348 and G304.929+0.552). Star formation occurring at this distance from Danks 1 and 2 is outside of the central cavity boundary and could not of been affected by the winds and radiation of the massive clusters suggesting that at least some of the massive stars in G305 formed spontaneously. It is around the HII regions generated by this second generation of massive stars that we find evidence of the most recent episodes of massive star formation traced by UC HII regions $< 10^5$ yrs old. Maser emission towards the cores of dense molecular gas indicates that still younger epochs of high-mass star formation is taking place deeply embedded within the dense molecular material further still from the central cavity. Thus, it appears that the star formation in G305 is multi-generational and has at least partly occurred in spatially and temporally isolated bursts that may have been triggered.

We now briefly consider the possible future evolution of G305. Observations of the molecular and ionised gas suggest that the energy input into the region by Danks 1 and 2 is no longer the sole or dominant driving force behind the evolution of G305. This is because the massive stars in the central cavity have already destroyed or swept up the material in their direct vicinity. Instead, the compact and classical HII regions surrounding the central cavity now dominate the observable Lyman continuum photon flux affecting the molecular gas and are the principal source of feedback. Despite this strong feedback from numerous massive stars over the last 3–6 Myr there is still more than $10^5\,M_\odot$ of cool (~ 20 K) molecular material within which star formation is taking place (Fig. 5.1).

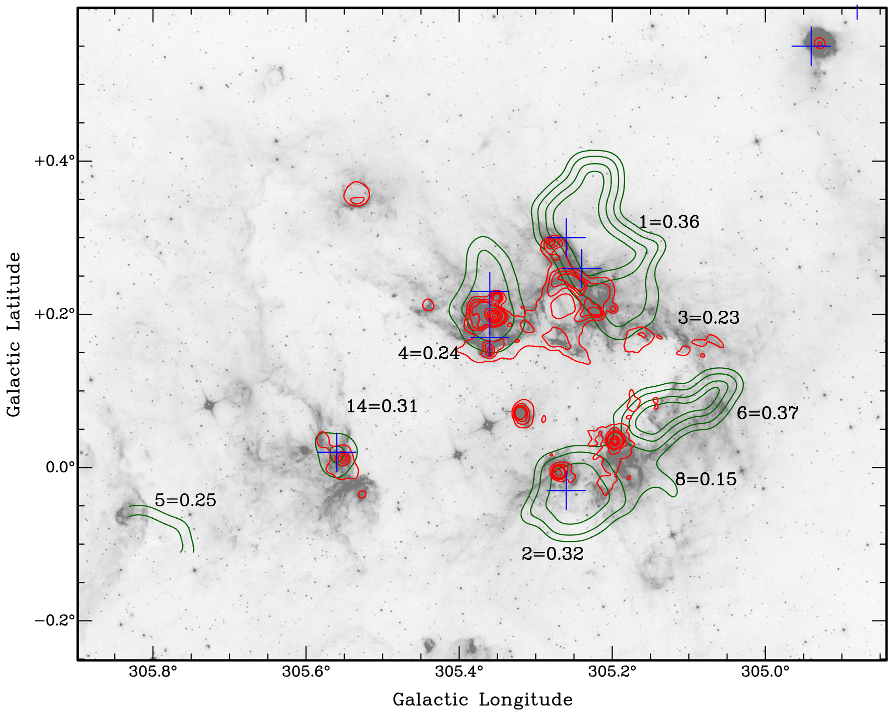

FIGURE 5.8: The 5.5 GHz radio emission and the CFE are shown by red and green contours with gravitationally bound CO clumps (Section 3.7.4) indicated by blue crosses. The NH_3 cloud numbers are presented as well as the corresponding value of the CFE.

Observations of CO presented in Chapter 2 show that approximately 14% of the molecular clumps detected in the G305 complex are gravitationally unstable and therefore likely to collapse (Fig. 5.8). These clumps make up 35% of the total CO mass (0.8×10^5 M$_\odot$). The location of these bound clumps can be seen in Fig. 5.8 as blue crosses and are found to reside on the borders of HII regions. If star formation takes place in these clumps, be it spontaneous or triggered, G305 will be host to a fourth generation of star formation that is morphologically suggestive of triggered star formation. Given that star formation is an inherently inefficient process, 2–17% (Williams & McKee, 1997; Tachihara et al., 2002) of the mass within these bound clumps is expected to form stars. Therefore, approximately 1.6–13.6$\times 10^3$ M$_\odot$ of material can be expected to go on to form stars in the future. Given that the mass in Danks 1 and 2 alone is $\sim 1.1 \times 10^4$ M$_\odot$ the end product of star formation in G305 may be similar to a loosely bound OB association (Zinnecker & Yorke, 2007) with a mass of 0.2–2.0 $\times 10^5$ M$_\odot$. In Chapter 2 we also derive the CFE of the large molecular clouds in G305 (Fig. 5.8). One might expect that if expanding HII regions are sweeping up molecular material the CFE would increase but we see no clear evidence of this being the case in G305. We do note that the NH_3 Cloud 6 is in close proximity to the Western wall of the central cavity, has the highest CFE and yet shows little sign of ongoing star formation or bound clumps.

G305 appears to be in an advanced stage of evolution and may be going through the final episodes of star formation before the molecular cloud is destroyed or rendered unrecognisable by feedback from massive stars. HII regions that surround the central cavity are clearly blowing away what remains of the molecular material in G305, leaving only the densest molecular clumps. This destruction of the molecular gas is apparent in a number of regions such as the Southern lobe where the HII region G305.195+0.033 appears to be destroying the molecular gas associated with NH_3 Cloud 8 lowering the CFE to 0.15 (Fig. 5.8) and punching a hole through the Southern lobe. Given the intense ongoing massive star formation and the unbound nature of the majority of the molecular gas it appears that star formation in G305 may cease in the next 1–3 Myr when massive stars in Danks 2 end their lives as supernova.

5.7 Summary

In this Chapter we combine the results of the molecular and ionised gas towards G305 presented in Chapters 3 and 4 and ongoing and recent star formation presented in Chapter 2. We reveal that the ionised and molecular gas is closely linked, concentrated around the periphery of the central cavity and peaks in approximately the same location. We also confirm that the massive clusters Danks 1 and 2 and surrounding visible massive stars are almost devoid of molecular and ionised gas whilst ongoing star formation is concentrated in a small number of sites in close proximity to the ionised gas and embedded within the densest molecular gas. We find that star formation extends out to the East of the complex beyond the cavity borders where there is little mid-infrared emission.

The morphology of the molecular and ionised gas and position of ongoing and recent star formation is highly suggestive of triggering via the collect and collapse process. Comparison of the fragmentation timescale and dynamical age of the surrounding HII regions suggests that within the errors star formation around the periphery of the central cavity is consistent with the collect and collapse model of triggered star formation. The most recent and compelling case for triggered star formation in G305 is found around the G305.254+0.204 HII region where we identify a BRC and velocity dispersions in the ^{12}CO emission indicative of interaction between the HII region and molecular material. We compare the SFR derived by extrapolating the IMF in Section 4.9 to the dense gas and Lyman continuum derived SFR and find that only a few tens to hundreds of complexes similar to G305 would be required to account for the total SFR of the Milky Way.

We close this chapter by considering the SFH and future evolution of G305. We suggest that star formation has taken place in a number of temporally and spatially isolated bursts that may have been triggered by the feedback of the massive stars in G305. Despite this powerful feedback, star formation is ongoing and appears set to continue on the borders of HII regions that surround the central cavity. We suggest that star formation will continue until the most massive stars in Danks 1 and 2 end their lives as supernova.

Chapter 6

Conclusion & future work

The main aim of this thesis was to investigate the relationship between the ionised and molecular environment, recent and ongoing star formation within the G305 complex. This is in an effort to shed light on the massive star formation process and investigate the impact of the feedback from massive stars on the evolution of G305. The approach used in this thesis, was to perform wide-field observations of the entire G305 complex to reveal the global distribution of the molecular and ionised gas and then compare this to the recent and ongoing star formation. In the following sections we present a brief summary of the main results from each chapter followed by the main conclusions and future work.

6.1 Summary and main results

This investigation began with Chapter 3 where we present observations of the dense and diffuse molecular gas and ongoing star formation towards G305 traced by NH_3, CO and H_2O masers respectively. The G305 complex was chosen because of previous studies that suggest there are multiple epochs of massive stars and ongoing star formation positioned in such a way as to suggest triggering (Chapter 2). Past studies of the molecular and ionised environment have been hampered by either a lack of resolution and sensitivity or incompleteness. The observations presented in Chapter 3 reveal a complex clumpy molecular environment that surrounds the central cavity of G305. By applying clump finding we identify 15 NH_3 clouds and 57 CO clumps towards G305 and we also detect 16 H_2O masers towards G305, 15 of which are likely to be associated with complex and suggests that there is ongoing star formation deeply embedded within the molecular gas. Analysis of the NH_3 and CO emission within these clouds and clumps, following the method outlined in Appendix B, reveals the physical properties of the dense and diffuse molecular gas (Tables 3.12 and 3.13). We find that the total mass of G305 traced by

CO and NH_3 is between 2.5–6.5 $\times 10^5$ $M_\odot$. The G305 complex exhibits complex velocity structure with a 10 km s^{-1} difference between the Northern and Southern lobes. We identify 35 CO clumps that have velocity motions suggestive of outflow motions but stress that confirmation requires follow-up observations. Comparison between the CO and NH_3 observations allows the derivation of the CFE towards G305, which is found to be between 15 and 37% similar to other well-known GMCs.

In Chapter 4 high-resolution and sensitive observations of the 5.5 and 8.8 GHz radio continuum towards G305 are presented. By applying two separate imaging strategies we are able to resolve both the large- and small-scale radio emission towards G305. We identify 16 large-scale radio features, six compact and low surface brightness extended emission. By considering the size and age of these features and comparing to previously identified HII regions and mid-infrared emission we identify eleven classical HII regions, five compact HII regions and four extended features. By resolving the large-scale radio emission we discover that more than 40% of the integrated flux at 5.5 GHz is associated with low surface density extended emission suggesting it is an important component in the radio environment of G305. We also find that 60% of the ionising flux in the region is associated with HII regions around the periphery of the central cavity suggesting that Danks 1 and 2 are no longer the dominant source of ionising photons in the region. The small-scale ionised emission towards G305 reveals 71 very compact radio sources. By matching these sources to GLIMPSE mid-infrared data we find that 15 sources are associated with G305, six of these are identified as UC HII candidates, one BRC, eight stellar radio sources and 56 background sources. The physical properties of the six UC HII candidates reveal five to have properties consistent with known UC HII regions. Using these five UC HII regions we extrapolate the IMF to infer a lower limit to the star formation rate of $\sim 0.003\,M_\odot\,yr^{-1}$.

In Chapter 5 we bring together the results and analysis of the molecular and ionised gas presented in Chapters 3 and 4 and recent and ongoing star formation. This reveals approximately three generations of massive stars, Danks 1 and 2 and visible massive stars, embedded HII regions and UC HII regions and methanol masers. The ongoing star formation in G305 is concentrated towards the peaks of the molecular gas around HII regions that surround the central cavity. We suggest that this morphology is suggestive of triggered star formation in the collect and collapse model (Elmegreen & Lada, 1977). Further investigation of the fragmentation timescale in the collect and collapse model yields inconclusive results due to the inherent simplicity of the model and large uncertainty in the derived timescales. We do however find that the HII region G305.254+0.204 in the NW of the complex has velocity structure indicative of strong interaction between the expanding HII region and molecular gas. We then go on to derive the SFR of G305 based on the dense molecular gas (Lada, Lombardi & Alves, 2010) and the Lyman continuum photon rate. We find that with a SFR of 0.005–0.014 $M_\odot\,yr^{-1}$ only a few tens to hundreds of complexes similar to G305 would be required to account for the SFR of the

Milky Way. We then go on to discuss the SFH of G305 and the possible future evolution of the complex.

6.2 Conclusions

Before this study the G305 complex was known to harbour at least two generations of massive stars as well as ongoing star formation (Clark & Porter, 2004) the distribution of which is suggestive of triggered star formation. However, the relationship between the molecular and ionised gas, massive stars and ongoing star formation was largely unknown. Our main conclusion has been to reveal these environments and find that G305 is amongst the most massive star-forming regions in the Galaxy with evidence of approximately three generations of massive stars, ongoing star formation and clear evidence of interaction between the molecular and ionised gas. We find compelling evidence that this interaction has resulted in at least some of the star formation in G305 being triggered. We also find that despite the clearly destructive actions of massive stars in G305, stars continue to form and star formation appears set to continue in a small number of the most massive gravitationally bound molecular clumps that are located on the borders of HII regions.

For the first time we have revealed both the high and low-density molecular gas across the entire G305 complex. We find that the molecular material borders the PDR seen in the mid-infrared as might be expected. The distribution of the molecular gas confirms that the central cavity of G305 is almost completely devoid of molecular material, having been swept up or destroyed by the actions of massive stars within and surrounding Danks 1 and 2. We find that the molecular environment of G305 shares similar properties to some of the most massive star-forming complexes in the Galaxy. There is between 2.5–6.5 $\times$ $10^5\,M_\odot$ of molecular material in G305 and approximately 35% of this is found in gravitationally unstable molecular clumps that are likely to collapse and contribute to future star formation. The surface density of the molecular gas was found to be below the theoretical surface density threshold ($1\,\mathrm{g\,cm^2}$) for forming massive stars suggested by Krumholz & McKee (2008). This result is consistent with findings by Elia et al. (2010), Roy et al. (2011) and Parsons, Thompson & Chrysostomou (2012) indicating that this result is independent of method, with low surface density values perhaps reflecting the time-dependent threshold for future massive star formation. Alternatively, this result may be a resolution issue with high surface densities lying below the detection limit due to beam dilution, further observations at high-resolution may reveal localised regions that exceed the $1\,\mathrm{g\,cm^2}$ threshold. In either case this demonstrates a clear contradiction between theory and observation that should be addressed. We demonstrated that Mopra observations of the CO J =1–0 transition are unable to identify individual molecular outflows at the distance of G305 due to confusion. However, we do identify a number of regions in which outflows may be contributing to broadened spectral profiles for future follow-up observations. These highly perturbed regions also pose the question of whether star formation occurs in turbulent regions or is turbulence the product of star formation? In this study we also identify H_2O maser emission indicating that star formation is taking place deeply embedded within the molecular material. Future developments in maser studies may allow the age of the star formation traced by masers to be determined which would provide a valuable tool for constraining the recent SFH in GMCs.

high-resolution and sensitive interferometric observations of radio continuum emission have allowed the complex radio substructure towards G305 to be resolved in unprecedented detail. We find that the HII regions reported by Caswell & Haynes (1987) consist of a number of features and that approximately 40% of the emission at 5.5 GHz is associated with low surface brightness extended emission. By considering the distribution of radio emission we suggest that the HII regions around the periphery of the central cavity and not Danks 1 and 2 are responsible for the majority of the observable ionising flux. We therefore confirm the hypothesis of Clark & Porter (2004) that there is significant photon leakage leading to an underestimation of the total ionising photon rate by as much as 50%. This important result clearly shows estimates of the SFR based on radio continuum observations will drastically underestimate the number of massive stars in GMCs where there is photon leakage and so provide an unreliable estimate of the SFR. We identify five UC HII regions that reveal very young ($< 10^5$ yr) massive stars that are located on the borders of evolved HII regions. The discovery of these UC HII regions along with methanol masers in close proximity to compact and classical HII regions and optically visible massive stars suggests that there are at least three epochs of massive stars towards G305. In light of these results we update the estimation of > 30 massive stars suggested by Clark & Porter (2004) by accounting for the 30 massive stars identified by Davies et al. (2012), 15 HII regions and five UC HII regions reported in this study to > 50 massive stars. Whilst the association of UC HII regions with the large-scale radio emission is unknown (i.e. embedded or projected), the fact that all UC HII regions in G305 are associated with large-scale radio emission suggests that they are likely to be embedded within diffuse radio emission as suggested by Kurtz et al. (1999). This is important to models of HII region formation and evolution, which assume that HII regions expand into a purely molecular medium. Finally, we determine the SFR of G305, by a number of methods, to be between 0.005–0.014 $M_\odot$ yr^{-1} and so only a few tens to hundreds of complexes similar to G305 are necessary to account for the total SFR in the Milky Way. This is an important result, suggesting that to understand star formation in the Milky Way we may need to observe a relatively small sample of the most massive star forming regions, many of which have already been identified (e.g Murray & Rahman 2010).

Comparison between the molecular and ionised gas, ongoing and recent star formation reveals that star formation in G305 is concentrated around the periphery of the central cavity as suggested by Clark & Porter (2004). This star formation is concentrated towards the dense molecular clumps on the borders or coincident with HII regions. This work provides an excellent case study for the combination of wavelengths that will be provided by current and soon to be available Galactic plane surveys discussed in the following section. In addition computational models of star-forming regions are beginning to incorporate more of the physical processes and feedback mechanisms in GMCs (e.g. Dale & Bonnell 2012). Studies such as the one presented in this thesis provide an excellent data set with which to compare theoretical models.

One of the main conclusions of this work is the construction of a plausible SFH of the G305 complex presented in Section 5.6. We find that star formation in G305 has occurred in a number of temporally and spatially isolated bursts that occurred in two modes; spontaneously and triggered by the feedback from massive stars. The current observations do not allow the mode of high-mass star formation, be it spontaneous or triggered, in G305 to be determined. However, by comparing to the collect and collapse model we find that triggering is a plausible explanation for the majority of the observed star formation in G305. In addition the velocity structure of molecular gas surrounding HII regions clearly shows signs of expansion and interaction. However, the situation is complicated as there is almost certainly a co-spatial population of high-mass stars that formed spontaneously.

The age of Danks 1 and 2 suggests that supernovae have played no role in the evolution of G305. We suggest that when they do occur in the next few Myrs they are likely to destroy the region. It is clear that the dominant form of feedback in G305 is ionising radiation, outflows and stellar winds from massive stars. Further study is required to determine if this is a common feature among GMCs, if it is then the importance of supernovae in the evolution of galaxies can be addressed. It has been suggested that the feedback from high-mass stars is the primary driving force that controls the age of GMCs. Authors such as Krumholz, Matzner & McKee (2006) suggest that the turbulence injected by high-mass sets up a state of quasi-equilibrium between gravitational collapse and turbulent support leading to long lifetimes. Alternatively, it has been suggested that the feedback from high-mass stars quickly destroys the molecular gas (Elmegreen, 2007) leading to short (< 10 Myr) lifetimes. In the case of G305 it appears that given the youth of the complex 3–6 Myr, and distribution of star formation that the high-mass stars tend to destroy the complex whilst simultaneously triggering stars rather than supporting the cloud against collapse.

6.3 Future work

Below I outline a number of ideas for future work in continuation of the G305 project.

6.3.1 Expanding the sample

One of the limitations of this study is low number statistics. What is needed is a large sample that is representative of the range of star-forming environments and epochs within the Milky Way. Such a sample is required if we wish to search for statistically significant trends and correlations and understand the underlying physics that is responsible for the difference we see in star-forming regions.

A first step would be to compare such a vigorous star-forming region as G305 to a more quiescent complex such as around the young massive cluster Havlen Moffat 1 (henceforth the HM1 complex (Vázquez & Baume, 2001)) for which we have obtained matching NH_3 and H_2O maser data. This would allow comparisons between the environment and star formation to look for trends that may suggest a reason as to why the star formation histories of HM1 and G305 are so different. In addition to expanding the sample there is also the opportunity to expand the multi-wavelength dataset. We have obtained LABOCA 870 μm maps and Hi-GAL fields of G305. These will allow us to probe different physical environments such as cold dust and embedded infrared objects to better constrain the SFH of G305.

Future Galactic plane surveys will soon provide similar multi-wavelength data-sets that encompass much of the Galactic plane. These surveys include: HOPS (Walsh et al., 2008), CORNISH (Purcell, Hoare & Diamond, 2008), MALT90 (Fig. 6.1) (Foster et al., 2011) and Hi-GAL (Molinari et al., 2010b). Using these large samples and wide range of wavelengths will allow rigorous statistical studies and resolve some of the long outstanding questions of massive star formation and evolution. The key here will be to develop a method for comparing data from these different surveys in a consistent manner.

6.3.2 high-resolution NH_3

The NH_3 observations presented in Chapter 3 have revealed the general distribution and properties of the dense molecular gas within G305. The fundamental limitations of these observations are the low-resolution, which limits the interpretation of the dense molecular gas. Observations of CO at higher resolution provides clear evidence of underlying substructure in these dense NH_3 clouds and higher J, K transitions hint at much hotter gas embedded within. These low-resolution NH_3 observations provide an excellent pathfinder for high-resolution follow-up ideally with the ATCA to obtain arc-second resolution and allow our Mopra observations to

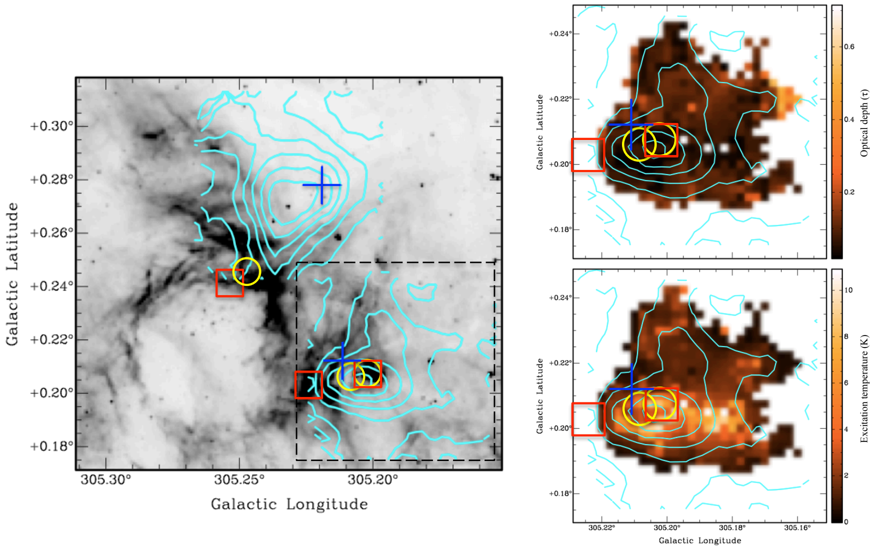

FIGURE 6.1: An example showing N_2H^+ emission detected by the MALT90 survey towards the G305.2+0.2 region. N_2H^+ is resistant to freeze-out and so is an excellent tracer of very cold dense gas.

provide total power information. This would reveal the substructure of the dense gas and uncover hot molecular cores, one of the key observable stages in massive star formation (Cesaroni, Walmsley & Churchwell, 1992) that would add to the SFH of G305.

6.3.3 Molecular outflows

Chapter 3 presented a search for outflows within the molecular gas associated with G305. The distance and complexity of the region coupled with the limitations of the ^{12}CO (J = 1–0) has prevented an in-depth study and the identification of individual outflows. Nevertheless, several promising regions of outflow activity have been identified and these provide an excellent target list for higher resolution observations with higher J CO transitions. Once the outflow material has been identified, it will be possible to obtain an estimate of the momentum and energy input from outflows within G305.

Appendix A

Appendix A

A.1 Massive stars in G305

Id	Galactic Position		Spectral
	(l)	(b)	Type
MDM 3	305.30	0.05	WN8-9
S09 845-34 (MDM 4)	305.33	0.10	WC8
MDM 5	305.33	0.03	WN9
S09 845-35 (MDM 6)	305.33	0.03	WC7
WR48A	305.36	0.06	WC6
S09 847-8	305.34	-0.33	WC6
L05-A1	305.26	0.23	O5-6
L05-A2	305.25	0.22	B0-1
L05-A3	305.26	0.22	B2-3
MSX305.4013+00.017	305.40	0.02	WCL
MDM9	305.65	0.35	WN8

Table A.1: Location and spectral type of the confirmed massive stars towards G305 (Mauerhan, Van Dyk & Morris, 2011; Leistra et al., 2005).

A.2 Star formation tracers in G305

Maser	Peak Galactic (l) ($^\circ$)	Peak Galactic (b) ($^\circ$)	$V_{\rm LSR}$ Peak (km s^{-1})	Peak Flux (Jy)
H_2O	305.20	0.01	−33	13.6
	305.21	0.21	−41	150
	305.36	0.15	−37	40
	305.37	0.21	−37	60
	305.36	0.20	−90	> 25
	305.80	−0.24	−34	2000
CH_3OH	305.200	0.019	−33.1	44
	305.199	0.005	−42.8	2.3
	305.202	0.207	−43.9	20
	305.208	0.206	−38.3	320
	305.247	0.245	−32.0	4
	305.362	0.150	−36.5	3
	305.366	0.184	−33.8	2.5
	305.475	-0.096	−39.0	2.6
	305.563	0.013	−37.3	4.6
	305.573	-0.342	−51.0	0.6
	305.615	-0.344	−34.9	2.8
	305.799	−0.245	−39.5	0.7
	305.822	−0.115	−42.2	2.9
	305.887	0.017	−34	5.5
OH	305.200	0.019	−31.5	1.33
	305.202	0.208	−42.5	0.4
	305.208	0.206	−38	7.5
	305.362	0.150	−39.5	56
	305.799	−0.245	−36.7	0.23
SiO	305.20	0.20	−40	0.37 (K)
	305.35	0.20	−41	0.12 (K)
	305.36	0.21	−37	0.13 (K)
	305.09	0.06	-	0.02 (K)
	304.93	0.55	-	0.02 (K)

TABLE A.2: maser positions, peak velocity and peak flux. SiO maser peak flux are reported in units of K on the T_A^* scale

RMS Id	MSX Name	Source Type	V_{LSR} (km s^{-1})	Bol.Lum $10^4(L_\odot)$
912	G305.2017 + 00.2072	YSO	−41.0	4.9
970	G305.4399 + 00.2103	Diffuse HII region	−40.9	0.9
930	G305.2535 + 00.2412	Diffuse HII region	−40.9	4.4
981	G305.5610 + 00.0124A	HII/YSO	−40.5	3.4
981	G305.5610 + 00.0124B	NULL	-40.5	NULL
960	G305.3611 + 00.1494	Diffuse HII region	−39.7	2.5
963	G305.3719 + 00.1837	HII region	−39.6	0.8
972	G305.4748 − 00.0961	YSO	−39.4	0.5
954	G305.3500 + 00.2240	HII region	−39.0	1.5
983	G305.5803 + 00.0381	Diffuse HII region	−38.2	0.5
980	G305.5528 − 00.0109	HII region	−38.2	1.1
917	G305.1997 + 00.0216	HII region	−37.2	5.4
975	G305.5393 + 00.3394	YSO	−35.8	0.4
990	G305.9402 − 00.1634	YSO	−35.6	0.7
915	G305.1967 + 00.0335	HII region	−35.6	< 20
992	G306.1160 + 00.1386	YSO	−33.6	0.4
916	G305.1940 − 00.0051	YSO	−33.0	0.2
939	G305.2694 − 00.0072	HII region	−32.3	4.3

TABLE A.3: Identifiers, positions, source classification, velocity and bolemetric luminosity. All sources are assumed to be at a distance of 3.6 kpc.

Radio Source	Flux (Jy)	$\log N_{Ly}$ (s^{-1})	No. O7 V	Associated Source(s)
[CH87] 305.097+0.138	15.3	49.37	2	-
[CH87] 305.173-0.368	10.0	49.20	2	-
[CH87] 305.202+0.022	26.0	49.60	4	[DBS2003] 83 and 84
[CH87] 305.254+0.204	51.0	49.90	8	DBS2003] 131
[CH87] 305.363+0.179	37.3	49.76	6	Anonymous IR cluster
[CH87] 305.537+0.338	5.4	48.92	1	[DBS2003] 133
[CH87] 305.551-0.005	35.4	49.74	6	DBS2003] 134
[CH87] 305.787+0.140	5.7	48.94	1	-
[CH87] 305.807-0.063	6.5	49.00	1	-
PMN J1308-6215	0.5	47.90	O9 V	[DBS2003] 82
Complex Total (6 cm)	193.1	50.50	31	
Danks84 G305.27-0.01 (20 cm)	8.4	49.02	1	[DBS2003] 130
Danks84 G305.32+0.07 (20 cm)	6.3	48.90	1	[DBS2003] 132

TABLE A.4: HII regions towards G305

Summary of HII regions towards G305 star forming complex from (Caswell & Haynes 1987; λ = 6 cm, upper panel) and (Danks et al. 1984; λ = 20 cm, lower panel). Radio fluxes, requisite LyC ionising fluxes and the corresponding number of canonical O7 V stars are listed. Finally, associated infrared clusters and cluster candidates from Dutra et al. 2003 are listed, as well as the anonymous infrared cluster associated with [CH87] 305.363+0.179 (Conti & Crowther, 2004).

Appendix B

Appendix B

B.1 Introduction

Our only tool with which to study the varied processes and environments within the ISM is through observations of emitted, absorbed or scattered radiation. Many physical phenomena give rise to such radiative processes and with the right tools and physical understanding of the process of emission and transmission of such radiation we are able to infer a great deal about the physical properties of the ISM.

At the heart of this thesis is an observational study of the radiation generated at millimetre and centimetre (radio) wavelengths by the molecular and ionised environment of the star-forming region G305. This chapter aims to provide a theoretical background to the physical processes of emission, transmission and detection of spectral line and maser emission at millimetre wavelengths and radio continuum emission at centimetre wavelengths.

B.2 Observing giant molecular clouds

When performing observations of GMCs from the ground, consideration must be given to the limitations imposed by the composition of the earth's atmosphere, dust present in the ISM and the type of emission that is to be observed.

The composition of the atmosphere, in particular H_2O vapor and O_2, is responsible for absorbing a large swathe of the electromagnetic spectrum (Fig. B.1) at high frequencies, leaving a transparent window from $\sim$ 15 MHz to $\sim$ 1.5 THz. There is a window at optical frequencies however, dust that is present in the ISM and is particularly dense towards star-forming regions absorbs and scatters a great deal of optical light. Due to these limitations and the fact that

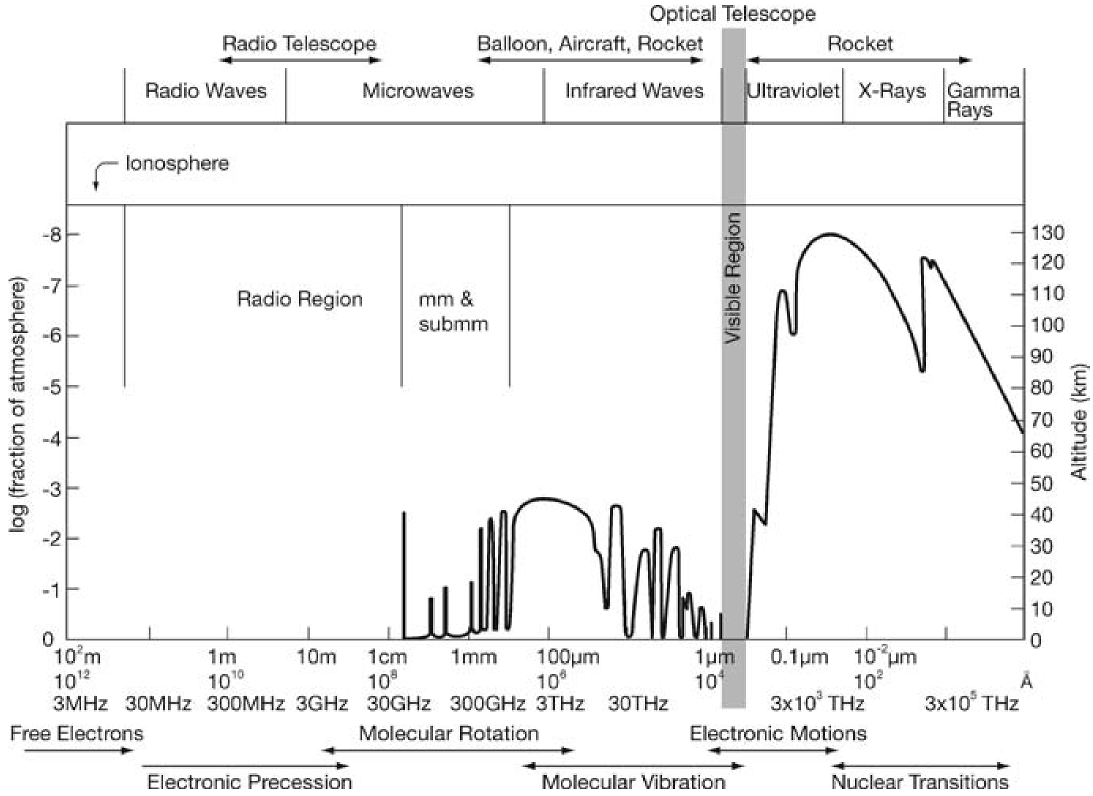

FIGURE B.1: The earths atmosphere is (fortunately) not transparent to all frequencies of radiation. This diagram shows the height in the atmosphere at which the transmission of radiation is attenuated by half (Rohlfs & Wilson, 2004).

GMCs are intrinsically cold objects, observations of GMCs, carried out from the ground, are generally limited to the radio and millimetre regimes where the atmosphere and interstellar dust is transparent.

It has been established that molecular clouds are composed primarily of molecular hydrogen. Unfortunately, H_2 is very difficult to observe directly due to its symmetry resulting in no electric dipole and the only allowed transitions occurring at high temperatures of ~ 700 K. Fortunately a wide range of molecules do emit radiation in the environments of molecular clouds that can be used as tracers of H_2. The next most prevalent molecule after H_2 is CO, which has a relative abundance of $^{12}CO/H_2 \simeq 10^{-6}$ (Blake et al., 1987), possesses dipole allowed rotational transitions in the millimetre regime and is easily excited into transmission due to its low critical density and excitation levels. Many more molecules exist in the ISM (Fig. B.2). For instance, molecules such as NH_3 have higher critical densities and require heavily shielded and dense environments to form and so preferentially trace dense cold gas. Detection and analysis of the radiation emitted by such molecules allows the derivation of a variety of physical properties such as optical depth, kinematics, temperature, density and mass.

The hydrogen that dominates the composition of GMCs also exists in an ionised (HII) state due

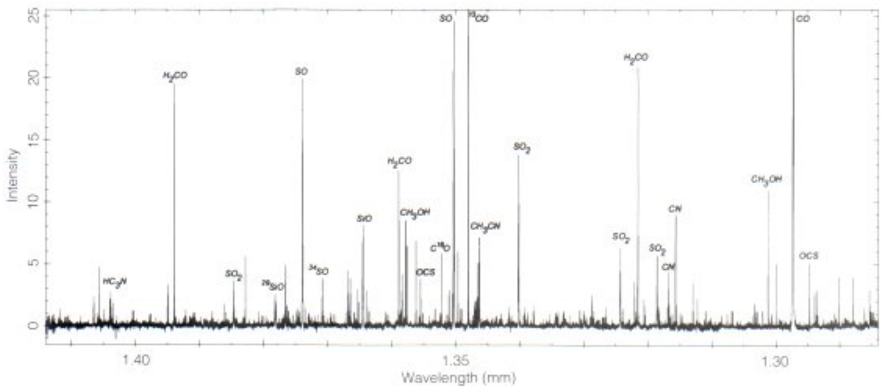

FIGURE B.2: A small frequency range of the observable window of the well known Orion GMC reveals many emission lines which provide a wealth of information about the molecular environment.

to photoionisation from the powerful radiation generated by massive stars. The free electrons and ions that exist within these ionised regions undergo electrostatic interactions producing continuum radiation in the radio regime of the electromagnetic spectrum. Observations of such radiation provides a direct indication of the presence of a massive star(s) and allows physical properties such as the optical depth, electron density, emission measure and ionised gas mass to be determined.

B.3 Definitions

Before proceeding further, it is important to introduce and clarify a number of fundamental definitions and concepts.

B.3.1 Intensity

Also known as the *specific intensity* or *brightness* (the three are used interchangeably) the intensity (I_ν) can be used to measure the infinitesimal power (dW) intercepted by an infinitesimal surface:

$$dW = I_\nu \cos\theta \, d\Omega_\mathrm{s} \, d\nu \tag{B.1}$$

where dW is the power in Watts, $d\Omega_\mathrm{s}$ is the surface area cm^2, $d\nu$ is the bandwidth in Hz. θ is the angle between the normal to the surface and the direction to $d\Omega_\mathrm{s}$ and finally I_ν is the specific intensity or brightness measured over a given solid angle (sr^{-1}) in units of W m^{-2} Hz^{-1} sr^{-1}. A useful property of the intensity is that for an extended source the intensity or surface brightness is independent of the distance as long as the radiation encounters no interference along its path.

B.3.2 Flux density

Flux is a scalar quantity whilst the flux density is a vector quantity or the amount of flux measured per unit of surface area. By integrating the intensity over the total solid angle subtended by the source of the emission (Ω_s) one may derive the flux density (S_ν) described by:

$$S_\nu = \int_{\Omega_s} I_\nu(\theta, \varphi) \cos\theta \, d\Omega \tag{B.2}$$

The flux density is measured in units of $\mathrm{W\,m^{-2}\,Hz^{-1}}$. In practice the flux density of radio sources is very small and so in radio astronomy the flux density is expressed in terms of *Jansky* (Jy) where $1\,\mathrm{Jy} = 10^{-26}\,\mathrm{W\,m^{-2}\,Hz^{-1}}$. The flux density of a source follows the expected inverse-square law and is dependent on the distance (D) as $1/D^2$. The total flux of a source is known as the luminosity, which is the total amount of electromagnetic energy radiated by a body per unit time.

B.3.3 Black body radiation

It is important to understand the concept of the radiation emitted from a black body as it underpins the majority of the theoretical framework described in this chapter. A black body refers to an object or system, which absorbs all radiation incident upon it and re-radiates energy that is characteristic of this radiating system only, not upon the type of radiation that is incident upon it. A black body has several important features:

- Radiation emitted by a black body is isotropic, homogeneous and unpolarised
- Black body radiation at a given wavelength depends only on the temperature (T)
- Any two blackbodies at the same temperature emit precisely the same radiation
- A black body emits more radiation than any other type of an object at the same temperature

Under the condition of thermal equilibrium black body radiation is modeled in terms of modes in an absorbing cavity to yield mathematical relationships that describe the distribution of intensity with frequency.

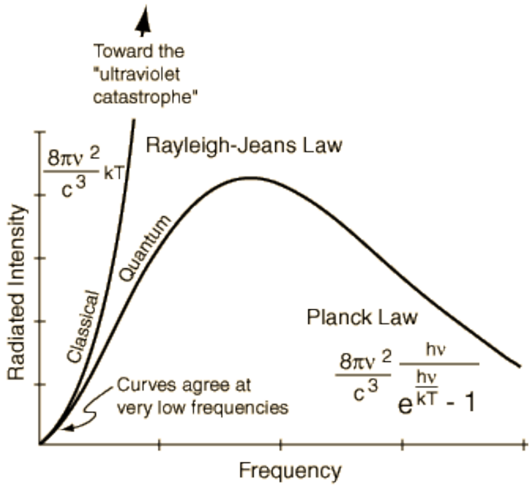

FIGURE B.3: The distribution of radiated intensity with frequency as described by the Planck Law. The Rayleigh-Jeans law approximates this distribution in the limit of low frequency. Note that the Planck and Rayleigh-Jean law's have been described in terms of spectral energy density $U_\nu(T) = \frac{4\pi}{c}B_\nu(T)$.

B.3.4 Thermodynamic equilibrium

The concept of thermodynamic equilibrium (TE) on a local (LTE) scale is an important assumption made throughout this work and greatly simplifies the analysis of radiation. In TE, the assumption is that all temperatures of interest are unchanging in time and uniform in space and so the net flow in heat is balanced. Although such a state is unlikely to apply to the entire content of most molecular clouds in which temperatures may vary widely (10–200 K), it is possible to use the assumption that on local volume scales, such as for individual clumps and cores, LTE may hold. Thermodynamic equilibrium is reached by the process of thermailisation by which the dominant form of interaction between bodies is collisions. Under the assumption of LTE a region can be modeled as a black body, which allows a number of well-known laws to be applied. If TE is not applicable then any subsequent analysis cannot apply Maxwell-Boltzmann statistics to describe the population of energy levels and as the absorption is no longer balanced by emission Kirchhoffs law (Eq. B.8) no longer applies and other complicating factors must be considered.

B.3.5 Application of black body radiation

By considering a black body in TE, the SED of the radiation that is emitted as a function of frequency is described by the Planck function (Fig. B.3). The brightness distribution (B_ν) depends only on thermodynamic temperature (T) of the surroundings and can be expressed as a function of frequency (ν) via *Planck's law*:

$$B_\nu(T) = \frac{2h\nu^3}{c^2} \frac{1}{\mathrm{e}^{h\nu/k_\mathrm{B}T} - 1} \tag{B.3}$$

or in terms of the wavelength (λ):

$$B_\lambda(T) = \frac{2hc^2}{\lambda^5} \frac{1}{\mathrm{e}^{hc/k_\mathrm{B}\lambda T} - 1} \tag{B.4}$$

where h is Planck's constant, c is the speed of light and k_B is the Boltzmann constant.

A very useful approximation simplifies Planck's law in the limiting case of low frequencies via the Rayleigh-Jeans approximation. The *Rayleigh-Jeans law* describes the black body curve in the classical limit ($h\nu < k_\mathrm{B}T$) however, it breaks down at high frequency known as the "ultraviolet catastrophe" (Fig. B.3) because it does not take into account quantum mechanical effects. Applying the Rayleigh Jeans approximation simplifies Planck's law in the following way:

$$\begin{aligned} &\mathrm{e}^{\left(\frac{h\nu}{k_\mathrm{B}T}\right)} \rightarrow 1 + \frac{h\nu}{k_\mathrm{B}T} \text{ for } h\nu < k_\mathrm{B}T \\ &B_\nu(T) = \frac{2h\nu^3}{c^2} \frac{k_\mathrm{B}T}{h\nu} = \frac{2k_\mathrm{B}T\nu^2}{c^2} \end{aligned} \tag{B.5}$$

The shape of the black body distribution is essentially the same at any temperature the peak intensity however shifts in such a way that at higher temperatures the peak is at shorter wavelengths. Solving the Planck distribution in terms of λ for $\delta B_\lambda/\delta\lambda = 0$ yields *Wien's displacement law* :

$$\lambda_\mathrm{peak}T = 0.002898 \text{ [K m]} \tag{B.6}$$

By summing the black body radiation over all wavelengths and half of the solid angle the total power emitted by a black body, per unit surface area is found to vary as the fourth power of the temperature *Stefan-Boltzmann law*:

$$F = \pi B(T) = \sigma_\mathrm{b} T^4 \tag{B.7}$$

where σ_b is the Stefan Boltzmann constant, F is the flux and T is the black body temperature.

In LTE the frequency-specific intensities of emitted (ε_ν) and absorbed (κ_ν) radiation by a perfect black body are not independent but related and a local temperature and can be defined such that emission is given by *Kirchhoffs law* :

$$\frac{\varepsilon_\nu}{\kappa_\nu} = B_\nu(T) \tag{B.8}$$

B.3.6 Population of energy levels

As will be discussed in more detail below, atoms and molecules exist in quantised energy, or excitation, levels. In TE the relative population of each excitation level is given by a combination of both the single excitation temperature, given by the Boltzmann distribution and the statistical weights that describe the probabilities of the different energy levels being populated. Thus, the population of energy levels is:

$$\frac{n_{\rm J}}{n_0} = \frac{g_{\rm J}}{g_0} {\rm e}^{-(E_{\rm J}-E_0)/k_{\rm B}T_{\rm ex}} \tag{B.9}$$

where $n_{\rm J}$ and n_0 is the number density in the upper and ground excited states, $g_{\rm J}$ and g_0 are the statistical weights of the upper and ground states and $T_{\rm ex}$ is the excitation temperature. The statistical weight, g, is often referred to as the degeneracy and is a result of the multiple quantum states that may exist in a particular energy state. The total angular momentum J may be oriented in space $2J + 1$ different ways, corresponding to the different values of the magnetic quantum number $M = 0, ... \pm J$. Thus the energy of any J level is degenerate by a factor $g_{\rm J} = 2J + 1$. For symmetric tops, K levels greater than zero are doubly degenerate, as the K and $+K$ levels have the same energy and also have degeneracy due to quantum mechanical symmetry considerations associated with the spins on the three identical atoms.

For a given temperature, the number of molecules will decrease exponentially with increasing energy level (J). As the temperature is increased the curve that describes the distribution becomes shallower and the higher J levels are populated with greater numbers of molecules (Fig. B.4). However, as the total degeneracy increases with J, the population decreases. The Boltzmann distribution describes the relative population of two states, the total number density (n) is the summation of all the filled states:

$$n = \sum_{i=0}^{\infty} n_{\rm i} \tag{B.10}$$

If the energy levels are populated according to the Boltzmann distribution the total number density of molecules may be inferred from the population in one energy level by combining the previous two equations:

$$n = n_0 \sum_{i=0}^{\infty} \frac{n_{\rm i}}{n_0} = n_0 \sum_{i=0}^{\infty} \frac{g_{\rm i}}{g_0} {\rm e}^{-E_{\rm i}/k_{\rm B}T} = \frac{n_0}{g_0} {\rm e}^{E_0/k_{\rm B}T} Q(T) \tag{B.11}$$

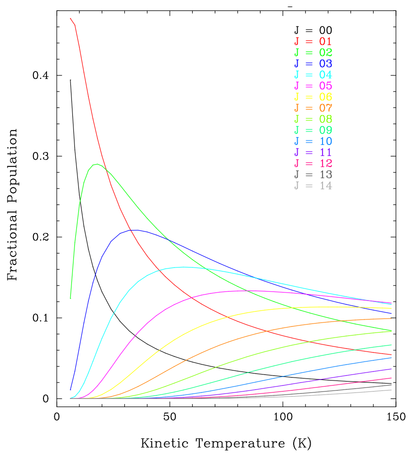

FIGURE B.4: For a molecule in LTE the Boltzmann distribution describes the level populations at the gas kinetic temperature, normalised by the partition function. The graph shows the relative populations of increasing excitation states of CO as a function of kinetic temperature. All populations have been normalised such that the sum over all levels equals unity.

where $Q(T)$ is the partition function, a sum over all energy states that normalises the distribution and is given by:

$$Q(T) = \sum_i g_{\rm i} {\rm e}^{-E_{\rm i}/k_{\rm B}T} \tag{B.12}$$

It is important to stress that the excitation temperature is the temperature at which we would expect to find a system with this ratio of level populations described by the Boltzmann distribution. However, it has no actual physical meaning except when in LTE and the excitation temperature can even be negative for a system with inverted levels (such as a maser). In LTE, where collisions dominate over radiation, the excitation temperature is equal to the kinetic temperature ($T_{\rm ex} = T_{\rm kin}$).

B.3.7 Brightness temperature

One of the important implications of the Rayleigh-Jeans law is that the brightness temperature ($T_{\rm b}$) and thermodynamic temperature of a black body are strictly proportional at low frequencies. The brightness temperature is the temperature a black body would have that corresponds to the same power per unit frequency interval per unit area, per unit solid angle as the celestial source and relates to the specific intensity via:

$$\begin{aligned} I_\nu = B_\nu(T) &= \frac{2k_{\rm B}T_{\rm b}\nu^2}{c^2} \\ T_{\rm b} &= \frac{c^2}{2k_{\rm B}\nu^2}B_\nu \end{aligned} \tag{B.13}$$

If the energy distribution (B_ν) is emitted by a black body and $h\nu \ll k_{\rm B}T$ then Eq. B.13 gives the thermodynamic temperature of the source, a value that is independent of ν.

B.4 Overview of emission mechanisms

Numerous physical processes occur within the ISM that give rise to detectable radiation via different emission mechanisms. These mechanisms separate into two main types: spectral line and continuum, which are broad terms that divide into further sub-categories. In either case, the emission of photons is a result of either the acceleration of electrons in bound-bound, bound-free, free-free and scattering processes or an abrupt change in the energy state of an atom or molecule in a vibration, electronic or rotational transition.

B.4.1 Spectral line emission

The many and varied atoms and molecules that form within the ISM can be stimulated into emitting photons with quantised energies and frequencies. The formation of these molecules may depend on certain environmental conditions, however different molecules require very different conditions to be freed from ice mantels (temperatures) and then different densities and temperatures to be excited into emission. Therefore, analysis of spectral line emission provides a powerful tool with which to study the various chemical and physical properties of the neutral ISM.

Spectral line emission is the result of transitions between two quantised energy states within an atom or molecule in an electronic, rotational or vibrational mode. The transition from the upper to lower energy state results in the emission of a photon with an energy equal to the difference in the two energy states ($\Delta E = E_{\rm u} - E_{\rm l}$) and in many cases there are sufficient atomic or molecular transitions to produce an observable line. The frequency of this emission is dependent on the type of transition and atomic structure and so allows the identification of the molecule or atom responsible.

Electronic transitions take place when an electron, bound within an atom or molecule, moves from a higher to lower energy level and emits radiation of a few electron volts (1 eV= 1.6×10^{-19} J) in the optical-ultraviolet regime. Vibrational transitions are a result of the stretching and relaxing of the molecular bonds that bind atoms into molecules and occur when nuclei are displaced from their equilibrium position and then oscillate about this position. Typical energies for vibrational transitions are 0.1–0.01 eV corresponding to lines in the infrared region of the spectrum. Rotational transitions occur when there is an abrupt change in the angular momentum of the molecule. The quantised rotational levels produce a measurable change in the

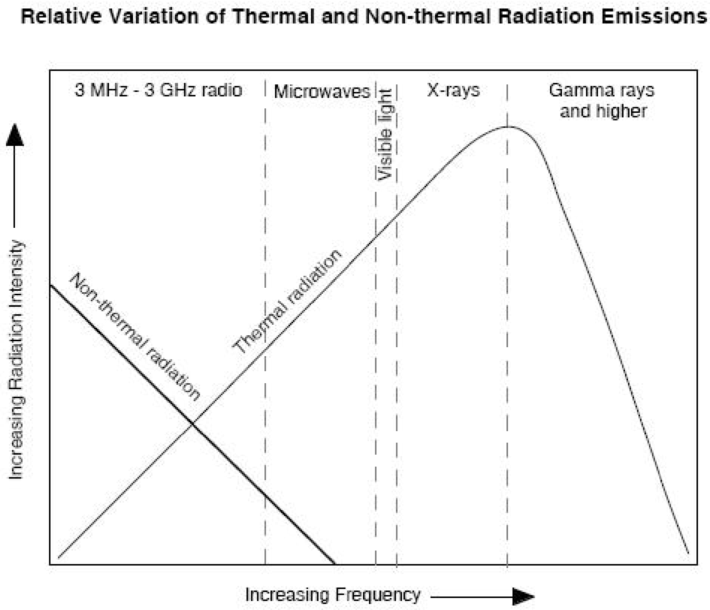

FIGURE B.5: The characteristic SED of thermal and non-thermal radio continuum emission (Rohlfs & Wilson, 2004).

electric field. In order to emit radiation via rotational transitions a molecule must be asymmetric meaning there is an uneven distribution of charge known as a permanent dipole moment (μ). Rotational transitions result in typical energies of $\cong 10^{-3}$ eV corresponding to emission lines in the centimetre and millimetre wavelengths.

B.4.2 Continuum emission

The physical processes that give rise to continuum emission can be split into two broad categories: thermal emission, which depends on the temperature of the emitter (black body and Bremsstrahlung), and non-thermal emission which has no dependence on temperature but rather properties such as magnetic field strength (synchrotron) and relative proportions of excited states (masers). Unlike spectral line emission, continuum emission is characterised by a broad and continuous SED.

The key distinguishing feature of thermal from non-thermal radiation is the shape of the SED. It is useful at this point to introduce the quantity known as the *spectral index* of the SED (α), which describes how the intensity changes as a function of frequency and is defined by:

$$S_\nu \propto \nu^\alpha \tag{B.14}$$

where α is the spectral index, S_ν is the flux density and ν is the frequency at which the flux density is measured. The SED of thermal emission increases with frequency ($\alpha > 0$) until at high frequencies it begins to drop off. Conversely, the SED of non-thermal emission decreases with increasing frequency ($\alpha < 0$) (Fig. B.5).

B.5 Molecular line fundamentals

Compared to atoms, molecules have complicated structure and the so the physics of their emission will be correspondingly more complex, involving positions and moments of multiple nuclei and electrons. This section provides the theory necessary to understand the mechanism of spectral line emission from molecules relevant to this study.

B.5.1 Types of molecules

Molecules are split into categories based on their structure and moments of inertia (I_{A}, I_{B}, I_{C}) about three principal axis of rotation (A, B, C). In this way, four types of molecules are classified: linear, symmetric top down, asymmetric top down and spherical top. This thesis is concerned with the spectral line emission generated by CO and NH_3 that have structure corresponding to linear and symmetric top categories respectively and so the discussion of these types of molecules is given in more depth below. For the sake of completeness molecules may also be classified as asymmetric top ($I_{\mathrm{A}} \neq I_{\mathrm{B}} \neq I_{\mathrm{C}}$) and spherical top ($I_{\mathrm{A}} = I_{\mathrm{B}} = I_{\mathrm{C}}$). The spectra of the former are difficult to interpret due to the lack of symmetry whilst the latter possess no electric dipole and so do not emit via rotational transitions. For more information see Townes & Schawlow (1955); Rohlfs & Wilson (2004).

B.5.2 Linear molecules: Carbon Monoxide

Linear molecules, such as CO, consist of a string of two or more atoms and are known as diatomic molecules. This results in two degenerate modes of rotation (about the A and B axis) and one that is negligible ($I_{\mathrm{B}} = I_{\mathrm{C}}$, $I_{\mathrm{A}} = 0$ or $I_{\mathrm{A}} \leqslant I_{\mathrm{B}} = I_{\mathrm{C}}$). It is impossible to distinguish between the two degenerate modes and so only one rotational quantum number J (where $J = 0, 1, 2, 3....$ $\Delta J = \pm 1$) is needed to describe the rotational motion of a linear molecule. The energy of a diatomic, linear molecule is described by a rigid rotor model:

$$E(J) = B_{\mathrm{e}} J(J+1) \tag{B.15}$$

where B_e is the rotation constant[1]. The difference between energy levels is governed by the selection rule $\Delta J = J_u - J_l = \pm 1$ where J_u and J_l are the upper and lower energy levels respectively. Thus the simple J =1-0 transition can be defined, ignoring the effects of centripetal distortion, as:

$$E_{J_l} \leftrightarrow E_{J_u} = 2B_e(J_u + 1) \tag{B.16}$$

Using these values it is possible to calculate the frequency at which a diatomic, rotational transition will occur. Taking the ^{12}CO (1-0) transition results in a frequency of 115.271 GHz and by applying $h\nu = k_B T$ the corresponding temperature is 5.5 K. This highlights just how easy it is to excite CO into emission.

B.5.3 Symmetric top molecules: ammonia

The NH_3 molecule consists of three hydrogen and one nitrogen atom arranged in a pyramid structure (Fig. B.6). This structure is an excellent example of a symmetric top molecule and has several important properties such as a large number of transitions sensitive to a wide range of excitation conditions, an inversion mode, spectral profile with hyperfine structure and high critical density ($\sim 10^4$cm^{-3} Stahler, S. W. & Palla, F. 2005) that make it an excellent dense molecular gas probe.

Two independent quantum numbers describe the rotation motion of symmetric top molecules (since two axes have equal moments of inertia). Instead of defining rotational quantum numbers for two independent axis one quantum number, J, is associated with the total angular momentum of the molecule and the other quantum number, K, describes the projection of the angular momentum onto the axis of symmetry. ammonia is a prolate symmetric top molecule and based on rigid rotor assumptions the rotational energy is:

$$E(J, K) = B_e J(J + 1) + (A_e - B_e)K^2 \tag{B.17}$$

and the above energy is governed by the selection rules $J = 0, 1, 2, ...$ and $K = -J, -J + 1, ..., -1, 0, 1, ..., J - 1, J$. These rotational transitions give rise to spectral lines in the far-infrared outside of the range of the observations presented here. Fortunately, the structure of the NH_3 molecule is conducive to quantum tunneling whereby the nitrogen atom tunnels through the potential barrier of the hydrogen atoms in an inversion transition.

[1] $B_e = \frac{h}{8\pi^2 I_B}$ for ^{12}CO B = 57635.968 MHz, ^{13}CO B = 55101.011 MHz and for C^{18}O B = 54891.420 MHz. These values have been taken from http://spec.jpl.nasa.gov/ and I_B. represents the moment of inertia about the B axis

ammonia is split into two distinct forms dependent on the orientation of the hydrogen spins which can be either $+1/2$ or $-1/2$. Aside from the $K = 0$ state there are eight possible orientations of the spin of the hydrogen nuclei: two states where all three hydrogen nuclei have the same spin, called *ortho-ammonia* ($K = 3n$, $n = 1, 2, 3, ...$) and six where the hydrogen nuclei have a combination of spins called *para-ammonia* ($K \neq 3n$, $n = 1, 2, 3, ...$).

B.5.3.1 Ammonia inversion transition

In addition to rotation the NH_3 molecule undergoes low energy vibrational motion that results in intense emission at radio wavelengths. The orientation of the nitrogen and hydrogen atoms results in the nitrogen atom experiencing a coulomb potential in the form of a double well, with one well on either side of the plane defined by the hydrogen atoms (Fig. B.6). Classically the hydrogen is confined to one of these wells but the low potential of the plane defined by the hydrogen atoms makes it probable for the nitrogen atom to tunnel quantum mechanically though the plane of the hydrogen atoms in an inversion mode. Thus, at radio wavelengths the transition, such as the NH_3 (1,1), is actually a transition of a NH_3 molecule that is in the $J = 1$, $K = 1$ rotational state in the ground vibrational state and the $J = 1$, $K = 1$ rotational level in the first and second excited inversion level. The two possible orientations of the nitrogen atom give rise to a positive and negative energy level known as an inversion doublet.

The inversion and rotation modes of the NH_3 molecule are not independent but interact (Fig. B.8). If there is rotation about the principal axis ($J > 0, K = J$) then the structure will be elongated (prolate, $I_A < I_B = I_C$) decreasing the distance between the hydrogen atoms which raises the potential barrier experienced by the nitrogen atom leading to an increase in the inversion energy and frequency as the rotation energy increases. Alternatively if there is significant angular momentum perpendicular to the principal axis $J > 0, K < J$ then the structure will be elongated (oblate, $I_A = I_B < I_C$) leading to a decrease in the potential barrier. If this were not the case then the inversion energy at all rotational levels of NH_3 would be the same and thus emit at the same frequency.

B.5.3.2 Hyperfine splitting

In addition to the inversion doublet described above the NH_3 spectra shows further splitting into what is known as hyperfine structure. This is a result of the interaction between the nitrogen nucleus and the electric potential of the molecule known as quadrupole splitting. The distribution of charge in the nitrogen nucleus is non-spherical which induces an electric quadrupole moment that interacts with the electric field of the electrons.

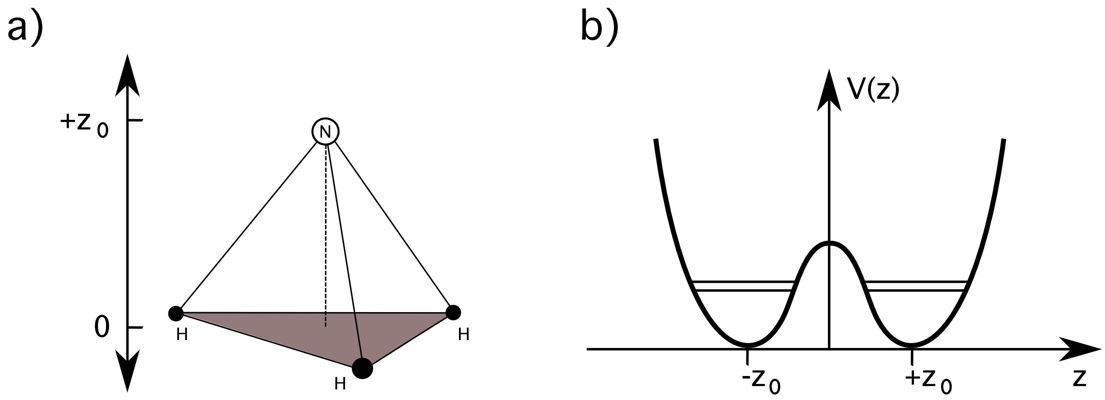

FIGURE B.6: The structure of the NH_3 molecule (left) results in the nitrogen atom experiencing a double potential well (right). The two lowest vibrational modes correspond to energies that may result in tunneling.

Each J, K inversion doublet splits into three levels characterised by the quantised nuclear spin of the nitrogen, $I = 1$, and the total angular momentum, $F = I + J$. Selection rules $\Delta F = 0$ for main lines and $\Delta F = \pm 1$ for satellite lines result in seven possible transitions with the main lines at $F = 0 \rightarrow 0, 1 \rightarrow 1, 2 \rightarrow 2$ and satellites at $F = 1 \leftrightarrow 0, 1 \leftrightarrow 2$. Due to the symmetry and inversion doubling, these satellites are on either side of the main line. If there is no change in the total angular momentum there is no shift in frequency and the emission belongs to the main line group. A change in the angular momentum of $\Delta F = \pm 1$ results in a shift of ± 0.61 and ± 0.93 MHz. Inversion transitions between these states results in a shift of the spectral lines of ± 0.61 and ± 1.54 MHz (Fig. B.7, top) respectively.

The relative intensities of these spectral features have been measured to high accuracy, the main lines contain 50% of the total flux (F= 0-0 1-1 2-2) and the two pairs of satellites (F= 1-0 1-2) contain 22.2 and 27.8% for the outer and inner respectively (Fig. B.7, bottom). This is an important property of the NH_3 spectrum and is used later in the determination of the optical depth.

These five hyperfine groups split still further due by weak magnetic interaction between the magnetic moments of the hydrogen and nitrogen nuclei. The resulting energy shifts due to this magnetic hyperfine splitting are spaced by only a few KHz and so are often unresolved in NH_3 observations as is the case in this work.

B.5.3.3 Ammonia inversion-rotation

Figure B.8 shows the energy level diagram for the inversion-rotation states of NH_3. Radiative transitions between K-ladders are normally forbidden by the selection rule $\Delta K = 0$. This is so because K is associated with the axis about which the molecule is symmetric and so has

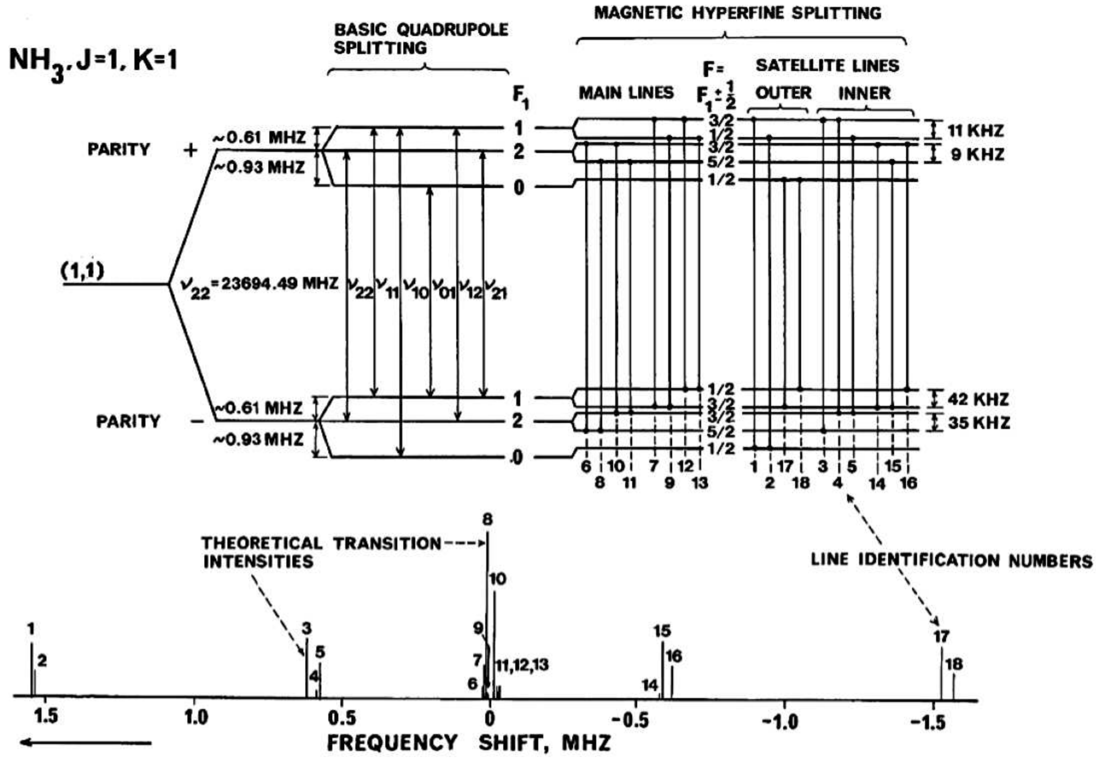

FIGURE B.7: The hyperfine splitting of the NH_3 $(J, K) = (1,1)$ transition and resultant spectral profile (Ho & Townes, 1983).

no net dipole moment in that direction. Thus, there is no interaction of this mode with the radiation. However, interactions between vibrational and rotational motions induces a small dipole moment perpendicular to the rotation axis giving rise to very slow $\Delta K = \pm 3$ transitions. Within each K-ladder the upper states ($J > K$) are called *non-metastable* because they decay rapidly down to the lowest *metastable* states via $\Delta J = 1$ transitions in the far-infrared (Ho & Townes, 1983). The lowest state in each K-ladder ($J = K$) are called metastable because they can only decay via the much slower octopole (10^9 s) $\Delta K = \pm 3$ transition (Ho & Townes, 1983). The population in the metastable states is almost exclusively excited by collisions and should reflect the kinetic temperature of the gas via the Boltzmann distribution.

B.5.4 Spectral line profiles

Several physical processes contribute to the shape of spectral line profiles of molecular emission. The first of these is *natural broadening*, which is the intrinsic width of the spectral line described by a Lorentzian profile. In an ensemble of emitting molecules, the uncertainty principle ($\Delta E \Delta t \approx \hbar$) causes variations in the lifetime of an excited state. This introduces an uncertainty in the energy released in any transition, leading to a spread in the frequency of the emitted or absorbed radiation.

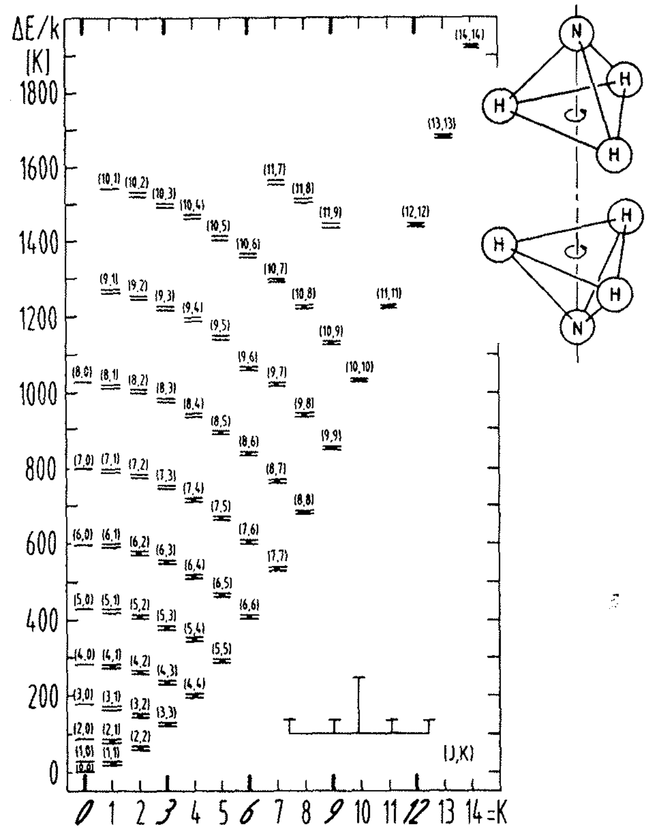

FIGURE B.8: Energy levels of ammonia in the lowest vibrational state (Wilson, Gaume & Johnston, 1993). The x-axis shows the quantum number K that corresponds to the z-component of the angular momentum. Transitions between the two spin states of the nitrogen atom cause the line splitting shown by the schematic spectra.

Global motions of the molecular gas relative to the observer is responsible for *Doppler shifting* the rest frequency of the molecular emission to different frequencies. This frequency shift is expressed as a velocity relative to the observer known as the local standard of rest (LSR) velocity via:

$$V_{\mathrm{LSR}} = c\frac{\nu_0 - \nu}{\nu_0} \tag{B.18}$$

where ν_0 is the rest frequency and ν is the observed frequency. This is a useful property of spectral line emission as it allows the investigation of the kinematics of a source. Within these moving volumes of gas, there are also chaotic motions of molecules which results in a small Doppler shift which widens the observed spectral line profile. *Thermal Doppler broadening* is the specific Doppler broadening of spectral line profiles due to thermal motion of molecules that in LTE are described by the Maxwell-Boltzmann distribution. Pure thermal broadening results in a Gaussian line shape with a full-width half-maximum (FWHM) given by:

$$\Delta\nu_{FWHM} = 2\sqrt{\ln(2)}\frac{\nu_0}{c}\sqrt{\frac{2k_{\mathrm{B}}T_{\mathrm{kin}}}{m}} \tag{B.19}$$

where m is the mass of the molecule. This may be expressed in terms of velocity by taking into account Eq. B.18 such that:

$$\Delta V(FWHM) = 2.35\sqrt{\frac{k_{\mathrm{B}}T_{\mathrm{kin}}}{m}} \tag{B.20}$$

Large-scale collective motions of groups of molecules also contribute significantly to the broadening of the line profile. This *turbulent Doppler broadening* is described by:

$$\Delta\nu_{FWHM} = 2\sqrt{\ln(2)}\frac{\nu_0}{c}\sqrt{\frac{2k_{\mathrm{B}}T_{\mathrm{kin}}}{m} + V_{\mathrm{t}}^2} \tag{B.21}$$

where V_{t}^2 is a constant called the micro-turbulent velocity. Finally collisions between molecules result in *pressure broadening* of the line profile. This occurs because the collisions between molecules interrupts the emission process and by shortening the characteristic time for the process increases the uncertainty in the energy emitted.

B.5.5 Astrophysical masers

As mentioned in the Chapter 1 Section 1.5.3 a number of astrophysical masers are commonly associated with star-forming regions. Whilst this work does not deal directly with the physics involved in the generation of maser emission, it is useful to be aware of the emission mechanism. For more information, see the review by Elitzur (1992).

Masers are a form of stimulated spectral line emission that occur in the ISM when a region of molecules (or atoms) absorb energy, be it in the form of radiation or collisions, which results in a population inversion with more molecules in the excited state than the ground state. The passage of a photon with the same frequency as the transitional frequency from upper to lower state can stimulate a transition between the upper and lower state releasing a photon. These stimulated photons have the same phase, frequency, polarisation, and direction of travel as the photons of the incident wave and in turn can go on to stimulates the emission of further photons. If the population density of the upper excitation level is larger than that of the lower level, the rate of stimulated emission exceeds absorption and the medium amplifies the propagating radiation rather than attenuating it. When the contribution of stimulated emission is included the absorption coefficient, optical depth and the standard attenuation term $e^{-\tau}$ becomes an amplification factor called the gain. This cascade scenario leads to an exponential increase in intensity

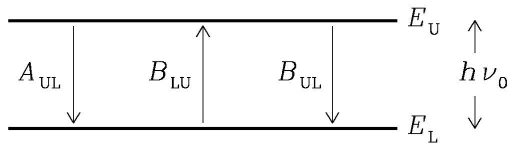

FIGURE B.9: The three Einstein coefficients describe spontaneous emission A_{ul}, stimulated emission B_{ul} and absorption B_{lu}.

resulting in very high brightness temperatures from 10^9 to 10^{14} K. This temperature does not represent the kinetic temperature and can easily saturate detectors.

Maser emission requires a large gain medium, which implies a substantial number of molecules along the line of sight. In order to attain this in the low-density environment of the ISM requires very large dimensions. In addition, this gain medium must be velocity coherent otherwise, the frequency of the radiation would become shifted by the Doppler effect and so unable to continue stimulating emission. This effect results in masers having multiple peaks as bodies of gas can have different coherent velocity along the same line of sight. These peaks can span 10s of km s^{-1} which suggests that there are significant supersonic turbulent motions within the material. The strong frequency dependence of stimulated emission means that the amplification only occurs in a very narrow frequency range that results in the line profiles of masers being narrower than the thermal line width.

B.5.6 Einstein coefficients

Einstein coefficients (Fig. B.9) are a convenient way of describing the quantum properties of spontaneous (A_{ul}) and stimulated (B_{ul}) emission and absorption (B_{lu}). Spontaneous emission is the spontaneous decay from a high energy level to a lower one and is described by the probability per unit time that an excited state will decay emitting $h\nu$ worth of energy $P_e = A_{ul}$. In the case of stimulated emission the energy state is induced to jump from higher to lower energy levels by the presence of electromagnetic radiation near to the frequency of the transition and the probability of this occurring is given by $P_s = B_{ul}U$. Absorption is the process by which a photon impacts an atom or molecules causing a jump from a lower to higher energy level. In the final two probabilities U is the flux density of the radiation field given by $U = 4\pi I/c$. In a stationary state (LTE) the number of emitted and absorbed photons must be equal so:

$$n_u A_{ul} + n_u B_{ul} = n_l B_{lu} U \tag{B.22}$$

where n_u and n_l is the number density of atoms in the upper and lower energy levels respectively. These Einstein coefficients are dependent as can be seen if we consider a system in TE :

$$U = \frac{A_{\mathrm{ul}}}{\frac{g_{\mathrm{l}}}{g_{\mathrm{u}}} \mathrm{e}^{\frac{h\nu_0}{k_{\mathrm{B}}T}} B_{\mathrm{lu}} - B_{\mathrm{ul}}} \tag{B.23}$$

In TE the spectral energy density U may be described by the Planck function by multiplying by $4\pi/c$:

$$U = \frac{4\pi}{c} B_\nu(T) = \frac{8\pi h\nu_0^3}{c^3} \frac{1}{\mathrm{e}^{\frac{h\nu_0}{k_{\mathrm{B}}T}} - 1} \tag{B.24}$$

this only applies if:

$$g_{\mathrm{l}} B_{\mathrm{lu}} = g_{\mathrm{u}} B_{\mathrm{ul}} \tag{B.25}$$

This is the first of the two relationships between the Einstein coefficients. The second is obtained by applying the Rayleigh-Jeans approximation (Eq. B.5) for low frequencies:

$$U = \frac{A_{\mathrm{ul}}}{B_{\mathrm{ul}}} \frac{k_{\mathrm{B}} T_{\mathrm{ex}}}{h\nu} = \frac{8\pi\nu^2 k_{\mathrm{B}} T_{\mathrm{ex}}}{c^3} \tag{B.26}$$

which can be solved for A_{ul} to give:

$$A_{\mathrm{ul}} = \frac{8\pi h\nu^3}{c^3} B_{\mathrm{ul}} \tag{B.27}$$

The Einstein coefficients are intrinsic properties of the particular transition and are related to the molecular properties via:

$$A_{\mathrm{ul}} = \frac{16\pi^3\nu^3}{3\varepsilon_0 h c^3} \left|\mu^2\right| \tag{B.28}$$

The Einstein coefficients have a specific form when considering an electric dipole for a transition between two rotational levels, such as CO, which is expressed as:

$$|\mu_J|^2 = \mu^2 \frac{J+1}{2J+3} \text{ for } \Delta J = 1 \tag{B.29}$$

where $\left|\mu^2\right|$ is the dipole matrix element for the particular transition, ε_0 is the permittivity of free space and ν is the frequency of the transition. For a more complex molecule such as the symmetric top NH_3 the inversion transitions between (J, K) and (J, K) dipole moment is given by:

$$|\mu_{JK}|^2 = \mu^2 \frac{K^2}{J(J+1)} \text{ for } \Delta J = 0 \; \Delta K = 0 \tag{B.30}$$

The following relationships relate the three Einstein coefficients:

$$B_{\mathrm{ul}} = \frac{c^3}{8\pi h\nu^3} A_{\mathrm{ul}} \text{ and } B_{\mathrm{lu}} g_{\mathrm{l}} = B_{\mathrm{ul}} g_{\mathrm{u}} \tag{B.31}$$

$$B_{\mathrm{lu}} = \frac{c^3}{8\pi h\nu^3} A_{\mathrm{ul}} \frac{g_{\mathrm{u}}}{g_{\mathrm{l}}} \tag{B.32}$$

These important results will be applied in the following sections.

B.6 Radio continuum emission

The following section presents a discussion of the thermal and non-thermal emission processes that give rise to continuum emission at radio wavelengths relevant to this work.

B.6.1 Thermal emission processes

There are two primary mechanisms that give rise to thermal continuum emission: black body radiation and Bremsstrahlung.

B.6.1.1 Thermal black body radiation

Any object has some level of thermal energy and so will radiate electromagnetic radiation as the energy imparted by heat results in the vibration of electrons that go on to generate thermal black body radiation.

When considering molecular clouds, heated dust is responsible for generating the majority of thermal black body radiation. This type of emission is particularly prevalent in the dusty environments that surround star formation regions where radiative heating of dust grains is expected to be important because of the high energy density of starlight and the high opacity of dust grains to starlight. A grain struck by a photon can leave the grain in an excited state, which can then spontaneously re-emit the energy. This radiation dominates the continuum radiation at higher frequencies (mid- to far- infrared, 5–100 μm, Fig. 2.2) and as described by Wiens law the hotter the dust the higher the peak frequency. The temperature, size and composition of the dust grains affect the shape of the SED. It should be noted that grains do not only cool by emitting thermal photons, they also cool via collisions with cold atoms or molecules, or through the ejection of

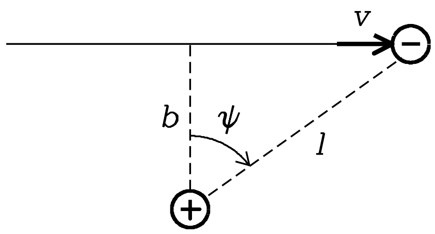

FIGURE B.10: Schematic of the electrostatic process that gives rise to Bremsstrahlung emission for a single electron. The fast moving negatively charged electron passes by a slow, heavy ion. Weak scattering in which the velocity vector of the electron only undergoes a very small change produces low energy radio photons.

atoms or molecules from the dust grain surface (sublimation). This sublimation can result in the release of complex molecules in compact regions known as hot molecular cores.

It is worth mentioning at this point emission from Polycyclic Aromatic Hydrocarbons (PAHs), which produce a family of five narrow emission bands at 3.3, 6.2, 7.7, 8.6 and 11.3 µm in the mid-infrared. PAHs have complex structure composed of hexagonal rings of Carbon and radicals (mainly hydrogen but possibly oxygen or nitrogen) and are excited into emission, via UV photons, in a vibration mode between the various molecular bonds. PAH emission is seen towards the PDRs that surround HII regions and highlight the boundary between the ionised and neutral environment.

B.6.1.2 Thermal Bremsstrahlung

The powerful radiation produced by massive stars has sufficient energy that when absorbed by atoms and molecules the host electrons have sufficient energy to overcome the coulomb attraction that binds them to the atom or molecule. In the case of GMCs, this results in the massive star generating a region of ionised plasma in which electrostatic interactions may take place.

This study is primarily concerned with the thermal continuum emission, which arises in such hot ionised gas (HII regions) excited by massive stars, called free-free or thermal Bremsstrahlung. Many different kinds of electrostatic interactions occur within HII regions, between various charged particles, but most do not emit significant amounts of radiation. A full derivation of theory from first principles would be impractical and so a more general description is given with citations to those results useful for radio astronomy.

The magnitude of the emitted radiation in an encounter between two charged particles (Fig. B.10) is described by the *Coulomb force*. The lightest ion is the hydrogen ion, a single proton, approximately two orders of magnitude larger than the electron mass, and so the acceleration of the electron will be significantly greater and dominate the radio emission process. The energy of a single ion-electron encounter is proportional to:

$$F_\perp = m_e \dot{v}_\perp = \frac{Z_e^2}{l^2}\cos\psi = \frac{Z_e^2 \cos^3\psi}{b^2} \tag{B.33}$$

where $\cos\psi = b/l$ and b is the impact parameter of the interaction, the minimum value of the distance l between the electron and ion. The *Larmor formula* (here in cgs units) can be applied to describe the power, P, radiated by a non-relativistic point charge as it accelerates.

$$P = \frac{2}{3}\frac{e^2 \dot{v}_\perp^2}{c^3} = \frac{2e^2}{3c^3}\frac{Z^2 e^4}{m_e^2}\left(\frac{\cos^3\psi}{b^2}\right) \tag{B.34}$$

The total energy emitted (W) by the interaction is:

$$W = \int_{-\infty}^{\infty} P\,dt \tag{B.35}$$

Since the change in energy is very small, the approximation that the electron velocity is nearly constant is valid. From the interaction diagram (Fig. B.10) it can be seen that:

$$v = \frac{dx}{dt} \text{ and } \tan\psi = \frac{x}{b} \tag{B.36}$$

so

$$v = \frac{b\,d\tan\psi}{dt} = \frac{b\sec^2\psi\,d\psi}{dt} = \frac{b\,d\psi}{\cos^2 dt} \tag{B.37}$$

and

$$dt = \frac{b}{v}\frac{d\psi}{\cos^2\psi} \tag{B.38}$$

The total pulse energy of a single interaction is:

$$W = \int_{-\infty}^{\infty} P\,dt = \frac{2}{3}\frac{Z^2 \mathrm{e}^6}{c^3 m_e^2 b^4}\int_{-\infty}^{\infty}\cos^6\psi\,dt \tag{B.39}$$

changing the variable of integration from t to ψ, invoking symmetry and evaluating the integral yields:

$$\int_0^{\pi/2} \cos^4\psi \, d\psi = \frac{3}{16}\pi \tag{B.40}$$

so the energy radiated by a single electron-ion interaction characterised by the impact parameter b and the velocity v is:

$$W = \frac{\pi Z^2 e^6}{4c^3 m_e^2}\left(\frac{1}{b^3 v}\right) \tag{B.41}$$

The radiation emitted by a single encounter of an electron and an ion depends on all its characteristic features be this the total radiated energy, average spectral density or the limiting frequency on the collision parameter (b) and velocity (v) of the encounter. The wide range of possible values of these parameters results in a broad distribution of energies and a continuum SED.

B.6.2 HII regions

HII regions have been introduced in Chapter 1 Section 1.5.5. Broadly speaking, three processes govern the physics and evolution of HII regions: photoionisation equilibrium, thermal balance and hydrodynamics.

Photoionisation equilibrium is the balance between photoionisation and recombination and determines the ionised structure of an HII region. Photoionisation of hydrogen commences when a high-mass star reaches such a high temperature that it produces photons with energies greater than the binding energy of hydrogen (13.6 eV). The subsequent region of ionised hydrogen (HII) will expand rapidly into the surrounding neutral medium until the total number of ionisations equals the total number of recombinations. The *Stromgren sphere* describes this state of equilibrium (Strömgren, 1939) by considering the simple spherical and homogenous case, it is possible to relate the luminosity and temperature of the exciting star(s) and the density of the surrounding hydrogen gas to determine the radius of the sphere where photoionisation equilibrium is reached:

$$R_s \approx \left(\frac{3N_{Ly}}{4\pi\alpha_H n_e^2}\right)^{1/3} \tag{B.42}$$

where N_{Ly} is the number of ionising photons per second (photons s^{-1}) also known as the *Lyman Continuum* (N_{Ly}) photons, n_e is the electron density (cm^{-3}) and α_H describes the hydrogen recombination rate ($\alpha_H = 2.7 \times 10^{-13}\, cm^{-3}\, s^{-1}$). The Lyman photon flux is highly dependent on the spectral type of the ionising star and only stars of spectral type B3 or earlier emit sufficient N_{Ly} photons to generate an HII region.

The radiation with energies just below the Lyman limit creates a PDR between the HII region and the rest of the molecular cloud. This shell of HI gas, with its photo-dissociating front, adds new complications to the dynamical evolution. In addition, hot stars produce large composite HII regions with PDRs, but intermediate mass stars produce only PDRs[2].

The thermal balance between heating and cooling within an HII region is dominated by the ejection of photoelectrons from hydrogen and helium and electron-ion impact excitation of metal ions. Thermal equilibrium is usually reached at temperatures of $\approx 10^4$ K two orders of magnitude higher than the initial temperature of the neutral interstellar gas (< 100 K). The ionising UV photons within the HII region create a factor of four increase in the number density within the HII region (as each H_2 molecule produces two protons and two electrons). Considering the equation of pressure of an ideal gas, $PV = nk_{\rm B}T$, it is clear that an increase in number density combined with a temperature difference drives the pressure expansion of the HII region into the natal molecular cloud. The HII region expands at $\sim 10\,\mathrm{km\,s^{-1}}$ and is capable of reversing infall onto the ionising star and with a typical sound speed in a molecular cloud of $\sim 200\,\mathrm{m\,s^{-1}}$ the expansion is supersonic and drives shocks into the molecular material.

Hydrodynamics includes shocks, ionisation and photodissociation fronts, outflows and winds from embedded stars and thermal expansion. These processes have a significant impact on the surrounding environment potentially sweeping up molecular material which may go on to fragment and form stars or inducing over-densities in the molecular gas to collapse (Chapter 1, Section 1.5.5).

The SED of HII regions is dictated by the optical depth which itself depends on the emission measure (integrated electron density) and electron temperature (Eq. B.52). At low frequencies $\tau \gg 1$, the HII region becomes opaque and its spectrum becomes that of a black body with temperature $T \approx 10^4$ K and its flux density varies with frequency as $S_\nu \propto \nu^2$. At higher frequencies, $\tau \ll 1$, the HII region is nearly transparent:

$$S_\nu \propto \frac{2k_B T \nu^2}{c^2}\tau \propto \nu^{-0.1} \tag{B.43}$$

The point at which an HII region goes from being optically thin to optically thick is the turnover frequency. The turnover frequency for a typical UC HII region with an emission measure of $\sim 10^8\,\mathrm{pc\,cm^{-6}}$ and size of 0.1 pc is approximately 5 GHz (Fig. B.11). It is clear that the optimal radio frequency with which to observe UC HII regions is at frequencies where the emission is optically thin above the turnover frequency. As an HII region evolves the electron density and emission measure will decrease resulting in the turnover frequency shifting to lower frequencies. This figure also highlights that observations designed to detect UC HII regions will not detect

[2]Diaz-Miller, Franco & Shore (1998) found that the minimum stellar temperature required to create a sizeable PDR is about 1.3×10^4 K.

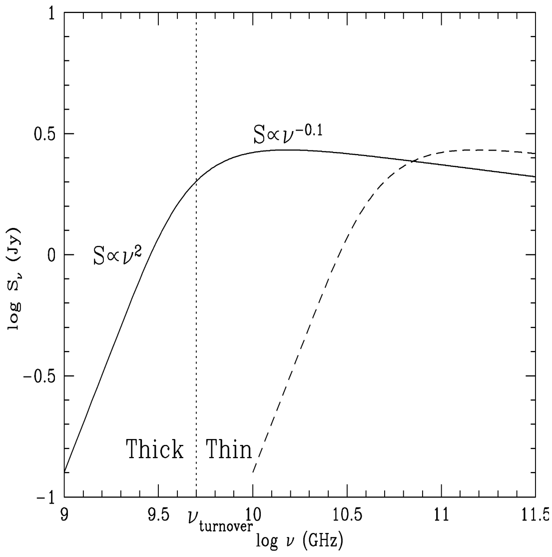

FIGURE B.11: Radio spectrum of thermal Bremsstrahlung emission from a spherical, homogenous and isothermal UC HII region. The turnover frequency corresponds to 5 GHz. The dashed line shows the SED of younger HII region that is smaller and denser (Kurtz, 2005).

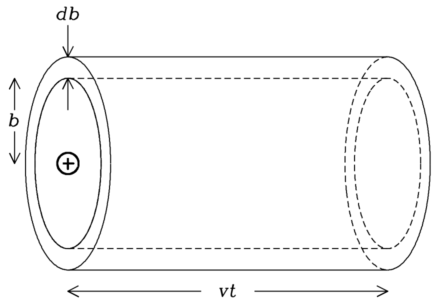

FIGURE B.12: The number of electrons with speeds v to $v + dv$ passing by a stationary ion and having impact parameters b to $b + db$ during the time interval t equals the number of electrons with speeds v to $v + dv$ in the cylindrical shell shown here.

the emission from the younger HC HII region phase. At a frequency of 5 GHz and above the optical depth of UC, compact and classical HII regions can be assumed to be optically thin.

B.7 Thermal Bremsstrahlung arising in an HII region

The interaction of a single electron and ion is described in Section B.6.1.2, in order to understand the emission associated with an HII region this description must be expanded upon to account for the numerous interactions, wide distribution of electron velocities and impact parameters that occur within an HII region. The distribution of velocities in LTE depends on the temperature (T) described by the Maxwell-Boltzmann distribution, whilst the distribution of the impact parameter depends on the electron and ion number density (N_e, N_i). The number of electrons passing any ion per unit time with impact parameter b to $b + db$ and speed v to $v + dv$ is:

$$N_e\,(2\pi b\,db)\,v f(v)\,dv \tag{B.44}$$

but because there are N_i ions per unit volume there is a total of:

$$N(v,b)\,dv\,db = (2\pi b\,db)[v f(v)\,dv]N_e N_i \tag{B.45}$$

The spectral power and frequency ν emitted isotropically per unit volume will be $4\pi\epsilon_\nu$, where ϵ_ν is the emission coefficient from radiative transfer, thus:

$$4\pi\epsilon_\nu = \int_{b=0}^{\infty}\int_{v=0}^{\infty} W_\nu(v,b)N(v,b)\,dv\,db \tag{B.46}$$

Substituting the results for $W_\nu(v,b)$ and $N(v,b)$ (Eq. B.45, B.41) gives:

$$\begin{aligned}4\pi\epsilon_\nu &= \int_{b=0}^{\infty}\int_{v=0}^{\infty}\left(\frac{\pi Z^2 e^6}{2c^3 m_e^2 b^2 v^2}\right)2\pi b\,db\,N_e N_i v f(v)\,dv\\ 4\pi\epsilon_\nu &= \frac{\pi^3 Z^2 e^6 N_e N_i}{c^3 m_e^2}\int_{v=0}^{\infty}\frac{f(v)}{v}\,dv\int_{b=0}^{\infty}\frac{db}{b}\end{aligned} \tag{B.47}$$

An issue that becomes apparent at this point is that the impact parameter will diverge logarithmically unless physical limits are placed on the impact parameter. The limits are set to b_{min} and b_{max}. Since the assumption has been made that there is a very small change in energy and considering LTE where only collisions are important a Maxwell-Boltzmann distribution can be adopted for the velocities such that:

$$f(v) = \frac{4v^2}{\sqrt{\pi}}\left(\frac{m}{2k_B T}\right)^{3/2}\exp\left(-\frac{mv^2}{2k_B T}\right) \tag{B.48}$$

with the velocity function defined it is possible to evaluate the integral over all electron speeds:

$$\int_{v=0}^{\infty}\frac{f(v)}{v}\,dv = \frac{4}{\sqrt{\pi}}\left(\frac{m_e}{2k_B T}\right)^{3/2}\int_{v=0}^{\infty} v\exp\left(-\frac{m_e v^2}{2k_B T}\right)dv \tag{B.49}$$

if $u = m_e v^2/(2k_B T)$ so $du = m_e v\,dv/(k_B T)$

$$\int_{v=0}^{\infty} \frac{f(v)}{v}\,dv = \frac{4}{\sqrt{\pi}}\left(\frac{m_\mathrm{e}}{2k_\mathrm{B}T}\right)^{3/2} \int_{u=0}^{\infty} \frac{k_\mathrm{B}T}{m_\mathrm{e}}\mathrm{e}^{-u}\,du = \frac{4}{\sqrt{\pi}}\left(\frac{m_\mathrm{e}}{2k_\mathrm{B}T}\right)^{1/2} \int_{u=0}^{\infty} \mathrm{e}^{-u}\,du$$
$$\int_{v=0}^{\infty} \frac{f(v)}{v}\,dv = \left(\frac{2m_\mathrm{e}}{nk_\mathrm{B}T}\right)^{1/2} \tag{B.50}$$

so that the emission coefficient may be expressed as:

$$\epsilon_\nu = \frac{\pi^2 Z^2 e^6 N_\mathrm{e} N_\mathrm{i}}{4c^3 m_\mathrm{e}^2}\left(\frac{2m_\mathrm{e}}{\pi k_\mathrm{B}T}\right)^{1/2} \ln\left(\frac{b_\mathrm{max}}{b_\mathrm{min}}\right) \tag{B.51}$$

This is the coefficient for thermal emission of an ionised gas cloud. The limits on the impact parameter (b_max, b_min) must be estimated to avoid the solution diverging. For b_max the sensible limit to apply is that of an impact parameter that is large but still emits in the radio regime $b_\mathrm{max} = v/2\pi\nu$ and the minimum impact parameter results in the maximum possible transfer of momentum or $b_\mathrm{min} \approx Ze^2/m_\mathrm{e}v^2 \approx Ze^2/3k_\mathrm{B}T$.

Since the assumption that the HII region is in LTE, Kirchhoffs law (Eq. B.8) describes the emission and absorption in the Rayleigh-Jeans limits as:

$$\kappa_\nu = \frac{\epsilon_\nu}{B_\nu(T)} = \frac{\epsilon_\nu c^2}{2k_\mathrm{B}T\nu^2} \tag{B.52}$$

and so:

$$\kappa_\nu = \frac{1}{\nu^2 T^{3/2}}\left[\frac{Z^2 e^6}{c} N_\mathrm{e} N_\mathrm{i} \frac{1}{\sqrt{2\pi (m_\mathrm{e} k_\mathrm{B})^3}}\right] \frac{\pi^2}{4} \ln\left(\frac{b_\mathrm{max}}{b_\mathrm{min}}\right) \tag{B.53}$$

B.7.1 Non-thermal radiation mechanisms

It is important to be aware of the characteristics and mechanisms that give rise to non-thermal continuum emission and in particular, how it can be distinguished from thermal continuum emission. In the context of this thesis, these differences are used to separate the thermal continuum emission generated by UC HII regions from stellar sources.

The process that give rise to non-thermal emission, as the name suggests, does not depend on the temperature of the medium but rather other factors such as magnetic field strength. Synchrotron radiation is found to dominate non-thermal emission and is the name given to emission that arises due to the acceleration of highly relativistic charged particles, usually electrons, as they spiral around magnetic field lines. This emission is highly polarised and can often be fitted with

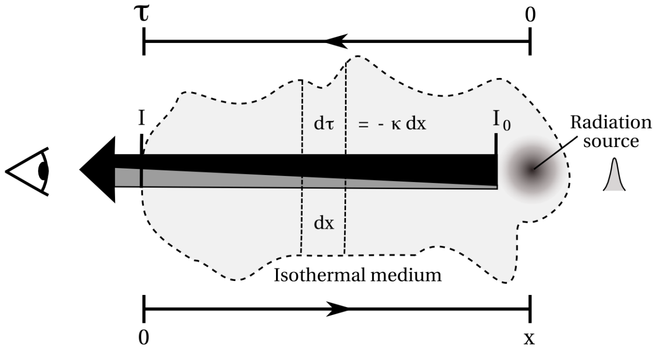

FIGURE B.13: Schematic of the transfer of radiation originating from a source with intensity I_0 through an isothermal medium of thickness dx and optical depth $d\tau$ to the observer with the intensity I.

a power law with a steep negative spectral index (i.e. $\alpha < -0.5$) i.e. a decreasing flux density with increasing frequency.

There are a number of sources that produce non-thermal emission including: colliding wind binary (Dougherty et al., 2003), pulsars (Lazaridis et al., 2008), supernova remnants (Gaensler et al., 1997) and active galactic nuclei (AGN) (Soria et al., 2010). By far the most prevalent source of non-thermal emission is the synchrotron emission associated with extragalactic radio galaxies (AGN: e.g. quasars, Seyfert galaxies and radio galaxies). The radio emission from most of these extragalactic sources is considerable weaker than Galactic radio sources with flux densities of < 0.1 Jy and is thought to be powered by a central super-massive black hole. This drives a highly collimated, high velocity jet in which interactions of relativistic electrons with magnetic fields generates synchrotron radiation.

B.8 Radiative transfer equation and brightness temperature

The physical processes that describe the origin of radiation has been described in Section B.5, this section addresses the way in which this radiation is processed as it passes through gas and dust within the ISM (Fig. B.13).

Whilst the intensity is independent of distance it will change if the radiation passes through a medium, such as a molecular cloud, in which absorption, emission and scattering processes can take place (Fig. B.13). This change in I_ν is described by the equation of radiative transfer:

$$\frac{dI_\nu}{ds} = -\kappa_\nu I_\nu + \varepsilon_\nu \tag{B.54}$$

where I_ν is the specific intensity of the radiation, κ_ν is the absorption coefficient (including scattering) and ε_ν is the emission coefficient both of which are dependent on the frequency. Equation B.54 is usually expressed in terms of the optical depth along the line of sight (τ_ν) between the object and observer, which is a measure of the fractional change in the intensity, as it passes through the ISM:

$$d\tau_\nu = -\kappa_\nu ds \tag{B.55}$$

substituting Equation B.55 into Equation B.54 and dividing both sides by κ_ν gives:

$$-\frac{1}{\kappa_\nu}\frac{dI_\nu}{ds} = \frac{dI_\nu}{d\tau_\nu} = I_\nu - B_\nu(T) \tag{B.56}$$

the solution to this equation is found by first multiplying by $\mathrm{e}^{-\tau_\nu}$ and integrating by parts to give:

$$I_\nu(s) = I_\nu(0)\mathrm{e}^{-\tau_\nu(s)} + \int_0^{\tau_\nu(s)} B_\nu(T(\tau))\mathrm{e}^{-\tau}\, d\tau \tag{B.57}$$

If the medium is isothermal then $T(\tau) = T(s) = T$ is constant and the integral may be computed to give:

$$I_\nu(s) = I_\nu(0)\mathrm{e}^{-\tau_\nu(s)} + B_\nu(T)(1 - \mathrm{e}^{-\tau_\nu(s)}) \tag{B.58}$$

For a large optical depth, that is $\tau_\nu(0) \to \infty$ in LTE this approaches the limit:

$$I_\nu = B_\nu(T) \tag{B.59}$$

When measuring the intensity a radio telescope is actually measuring the total intensity of both the sky and background source intensity. However, the desired intensity is that of the source ($I_\nu(s)$) over the intensity of the background ($I_\nu(0)$). To determine the source intensity the contribution from the background needs to be subtracted from the total intensity measured by a radio-telescope. The observed brightness I_ν for the optically thick case is equal to the black-body brightness distribution independent of the material. If the intensity is to be compared with the result obtained in the absence of a intervening medium $I_\nu(0)$, then:

$$\Delta I_\nu(s) = I_\nu(s) - I_\nu(0) = (B_\nu(T) - I_\nu(0))(1 - \mathrm{e}^{-\tau}) \tag{B.60}$$

This is the general solution to the radiative transfer equation assuming an isothermal and homogenous medium. The intensity of the detected radiation is the sum of the attenuated radiation from the source $I_\nu(0)\mathrm{e}^{-\tau_\nu}$ and the self attenuated radiation emitted by the medium $B_\nu(1-\mathrm{e}^{-\tau_\nu})$.

It is convenient to introduce the concept of brightness temperature (Eq. B.13) into the radiative transfer equation. If we assume the source of the emission is a black body, the brightness of the radiation (B_ν) at a particular frequency is dependent on the temperature of the source (T). In the case of low frequencies Rayleigh-Jeans approximation may be used (Eq. B.5) to give:

$$J_\nu(T) = \frac{c^2}{2k_\mathrm{B}\nu^2}B_\nu = \frac{h\nu}{k_\mathrm{B}}\frac{1}{(\mathrm{e}^{\frac{h\nu}{k_\mathrm{B}T_\mathrm{b}}}-1)} \tag{B.61}$$

where $J_\nu(T)$ is the observed intensity above the background. Inserting the brightness temperature into this equation gives:

$$T_\mathrm{b} = J_\nu(T) = \frac{h\nu}{k_\mathrm{B}}\frac{1}{(\mathrm{e}^{\frac{h\nu}{k_\mathrm{B}T}}-1)} \tag{B.62}$$

Inserting the brightness temperature (Eq. B.13) into the radiative transfer equation (Eq. B.54) gives:

$$J(T) = \frac{c^2}{2k_\mathrm{B}\nu^2}(B_\nu(T) - I_\nu(0))(1-\mathrm{e}^{-\tau_\nu(s)}) \tag{B.63}$$

Calibration procedures allow $J(T)$ to be expressed as a measured quantity referred to as the radiation temperature T_R^* or brightness temperature T_b. Realising that the brightness temperature is the intensity observed above the background intensity leads to the following important solution to the radiative transfer equation called the detection equation:

$$T_\mathrm{b} = T_0\left(\frac{1}{\mathrm{e}^{T_0/T_\mathrm{ex}}-1} - \frac{1}{\mathrm{e}^{\mathrm{T_0/T_{bg}}-1}}\right)(1-\mathrm{e}^{-\tau_\nu}) \tag{B.64}$$

where $T_0 = h\nu/k_\mathrm{B}$, T_ex and T_bg are the excitation and background temperature ($T_\mathrm{bg} = 2.7\,\mathrm{K}$). T_ex is the excitation temperature in the Rayleigh-Jeans limit and so Equation B.64 becomes:

$$T_\mathrm{b} = [T_\mathrm{ex} - T_\mathrm{bg}](1-\mathrm{e}^{-\tau_\nu}) \tag{B.65}$$

There are two special cases which simplify Equation B.65:

1. When the source is optically thick ($\tau \geqslant 1$), then: $\mathrm{e}^{-\tau_\nu} \leqslant 1$, and thus

$$T_{\mathrm{b}} \simeq T_{\mathrm{ex}} - T_{\mathrm{bg}} \tag{B.66}$$

and if $T_{\mathrm{ex}} \geqslant T_{\mathrm{bg}}$, then

$$T_{\mathrm{b}} \simeq T_{\mathrm{ex}} \tag{B.67}$$

2. When the source is optically thin ($\tau \leqslant 1$), the: $\mathrm{e}^{-\tau_\nu} \simeq 1 - \tau$, and thus

$$T_{\mathrm{b}} \simeq [T_{\mathrm{ex}} - T_{\mathrm{bg}}]\tau_\nu \tag{B.68}$$

and if $T_{\mathrm{ex}} \geqslant T_{\mathrm{bg}}$, then

$$T_{\mathrm{b}} \simeq T_{\mathrm{ex}}\tau_\nu \tag{B.69}$$

B.8.1 Radiative transfer with Einstein Coefficients

In the description above the radiative transfer equation is described using macroscopic emission and absorption coefficients. However, we must link the macroscopic and quantum properties of a radiating region to provide a description of the radiative transfer process at the molecular level. This can be achieved by applying Einstein coefficients to the equation of radiative transfer. Rather than fully derive how Einstein coefficients are applied to the radiative transfer equation the main result is quoted. A full derivation can be found in Rohlfs & Wilson 2004.

$$\frac{dI_\nu}{ds} = -\frac{h\nu_0}{c}\left(n_{\mathrm{l}}B_{\mathrm{lu}} - n_{\mathrm{u}}B_{\mathrm{ul}}\right) I_\nu\varphi(\nu) + \frac{h\nu_0}{4\pi}n_{\mathrm{u}}A_{\mathrm{ul}}\varphi(\nu) \tag{B.70}$$

where $\varphi(\nu)$ is the normalised line profile, assuming the absorption and emission line profiles are the same, described by $\varphi(\nu) = d\nu^{-1}$. Comparison of this equation to the original radiative transfer equation reveals that the emission and absorption coefficients (ϵ_ν and κ_ν) which describe the macro physics of the medium, can be described in terms of Einstein coefficients or the quantum physics of the molecules. By accounting for the original radiative transfer equation the absorption coefficient can be described in terms of either the upper or the lower population:

$$\kappa_\nu = -\frac{h\nu_0}{c}n_{\mathrm{l}}B_{\mathrm{lu}}\left(1 - \frac{g_{\mathrm{l}}}{g_{\mathrm{u}}}\frac{n_{\mathrm{u}}}{n_{\mathrm{l}}}\right)\varphi(\nu) \tag{B.71}$$

$$\kappa_\nu = -\frac{h\nu_0}{c} n_\mathrm{u} B_\mathrm{ul} \left(\frac{g_\mathrm{u}}{g_\mathrm{l}} n_\mathrm{l} - 1 \right) \varphi(\nu) \tag{B.72}$$

and the emission coefficient may be described as:

$$\varepsilon_\nu = \frac{h\nu_0}{4\pi} n_\mathrm{u} A_\mathrm{ul} \varphi(\nu) \tag{B.73}$$

Substituting Eq. B.9 and Eq. B.32 gives the following for the absorption coefficient of the lower population or alternatively by applying the Boltzmann equation for $g_\mathrm{u}/g_\mathrm{l}$ allows the absorption coefficient to be described by the upper energy level:

$$\begin{aligned} \kappa_\nu &= \frac{c^2}{8\pi} \frac{1}{\nu^2} \frac{g_\mathrm{u}}{g_\mathrm{l}} n_\mathrm{l} A_\mathrm{ul} \left[1 - \mathrm{e}^{(-\frac{h\nu_0}{k_\mathrm{B} T})} \right] \varphi(\nu) \\ \kappa_\nu &= \frac{c^2}{8\pi} \frac{1}{\nu^2} n_\mathrm{u} A_\mathrm{ul} \left[\mathrm{e}^{(-\frac{h\nu_0}{k_\mathrm{B} T})} - 1 \right] \varphi(\nu) \end{aligned} \tag{B.74}$$

Expanding on the definition of the optical depth (Eq. B.55) allows the absorption coefficient to be described in terms of optical depth as:

$$\begin{aligned} \tau_\nu &= \frac{c^2}{8\pi} \frac{1}{\nu^2} \frac{g_\mathrm{u}}{g_\mathrm{l}} n_\mathrm{l} A_\mathrm{ul} \left[1 - \mathrm{e}^{\left(-\frac{h\nu_0}{k_\mathrm{B} T}\right)} \right] \varphi(\nu)\, ds \\ \tau_\nu &= \frac{c^2}{8\pi} \frac{1}{\nu^2} n_\mathrm{u} A_\mathrm{ul} \left[\mathrm{e}^{\left(-\frac{h\nu_0}{k_\mathrm{B} T}\right)} - 1 \right] \varphi(\nu)\, ds \end{aligned} \tag{B.75}$$

B.9 Deriving physical properties: spectral line

In this work two approaches are required to derive the physical properties of the molecular environment from observations of the linear CO and symmetric-top NH_3 molecules due to the different molecular structure, energies and emission mechanisms. The analysis of molecular emission and derivation of physical properties follows the analysis of (Rohlfs & Wilson, 2004) and is valid under the assumption that:

- The emission originates from a medium in LTE
- Different isotopic species have the same excitation energy
- The optical depth in the ^{12}CO J =1-0 is large compared to unity

- The optical depth of ^{13}CO is small compared to unity
- The CO and NH_3 transitional lines are emitted from the same volume
- The line widths of the NH_3 (1,1) and (2,2) transitions are equal
- The beam filling factor (η_{ff}) is unity

B.9.1 Temperature

B.9.1.1 Excitation temperature

In order to derive the excitation temperature the optical depth must be known or assumed to be optically thick ($\tau > 1$). In the case of optically thick emission the detection Equation (Eq. B.64) may be rearranged for T_{ex} to give:

$$T_{\mathrm{ex}} = \frac{T_0}{\ln\left(\frac{T_0}{T_{\mathrm{b}} + \frac{T_0}{e^{T_0/T_{\mathrm{bg}}}}} + 1\right)} \tag{B.76}$$

Given the assumptions above, the ^{12}CO excitation and kinetic temperatures are equal ($T_{\mathrm{ex}} = T_{\mathrm{kin}}$). In practice it is often difficult or impossible to find an optically thick gas tracer within a single set of observations and the beam filling factor is less than unity. This is a particular problem with decreasing frequency as the beam size increases and so the derived excitation temperature does not hold any physical meaning. In the case of NH_3 $h\nu/k_{\mathrm{B}} = 1.13\,\mathrm{K}$ which is less than the background temperature[3].

An alternative to this method is required to determine T_{kin} for NH_3. Fortunately we can make use of the fact that radiative transitions between different K-ladders of NH_3 are forbidden meaning that the relative populations of different K-ladders is determined by collisions. Thus, an alternative method for estimating T_{kin} is to use the ratio of populations in different K-ladders. This is called the rotational temperature (T_{rot}).

B.9.1.2 Rotational temperature

The derivation of the rotational temperature for NH_3 is quite involved and so only an outline is given here for a detailed derivation see Ungerechts, Winnewisser & Walmsley (1986).

The NH_3 ($J = K$) inversion doublets are called metastable because they decay radiatively via slow (10^9 s) $\Delta K = \pm 3$ transitions (Ho & Townes, 1983). Consequently, the relative population

[3]For ^{12}CO $h\nu/k_{\mathrm{B}} = 5.53\,\mathrm{K}$.

of these states is strongly affected by collisions and so reflects the kinetic temperature (e.g. Walmsley & Ungerechts 1983). The rotational temperature describes the relative populations in different K-ladders of the NH_3 molecule, which in LTE, can be described by the Boltzmann distribution. Thus, for example if one considers only the (1,1) and (2,2) as the lower and upper excited states respectively then the population distribution is given by:

$$\begin{aligned} T_{\rm rot} &= \frac{-E_{\rm ul}}{k_{\rm B}} \frac{1}{\ln\left[\frac{N_{\rm u}}{N_{\rm l}} \frac{(2J_{\rm l}+1)}{(2J_{\rm u}+1)}\right]} \\ T_{\rm rot} &= \frac{-41.5}{\ln\left[\frac{3}{5}\frac{N_{\rm u}}{N_{\rm l}}\right]} \end{aligned} \tag{B.77}$$

The rotational temperature may be expressed in terms of the total optical depth by substituting for $\frac{N_{\rm u}}{N_{\rm l}}$. From the definition of optical depth:

$$\frac{\tau_{\rm u}}{\tau_{\rm l}} = \frac{\nu_{\rm u}^2}{\nu_{\rm l}^2} \frac{\Delta\nu_{\rm l}}{\Delta\nu_{\rm u}} \frac{T_{\rm exl}}{T_{\rm exu}} \frac{|\mu_{\rm u}|^2}{|\mu_{\rm l}|^2} \frac{g_{\rm u}}{g_{\rm l}} \times \exp\left\{\frac{-(E_{\rm u}-E_{\rm l})}{k_{\rm B}T_{\rm rot}}\right\} \tag{B.78}$$

where ν is the line rest frequency, $\Delta\nu$ is the line width, the excitation temperature is in the Rayleigh-Jeans limit and $|\mu(J,K)|^2 = \mu^2 K^2/[J(J+1)]$. The rotational temperature can be derived assuming equal excitation temperatures ($T_{\rm ex}$) and velocity line width ($\Delta\nu$) between the (1,1) and (2,2) transitions are equal. Substituting the appropriate values gives:

$$\begin{aligned} \frac{\tau_{2,2,\rm m}}{\tau_{1,1,\rm m}} &= 0.28 \times \exp\left\{\frac{-41.5}{T_{\rm rot}}\right\} \\ \mathrm{T_{rot}} &= \frac{41.5}{\ln\left[0.28\,(\tau_{1,1,\rm m}/\tau_{2,2,\rm m})\right]} \end{aligned} \tag{B.79}$$

The rotational temperature may also be expressed in terms of the antenna temperature of the (1,1) and (2,2) transitions by substituting the optical depth ratio in Eq. B.89 to give:

$$T_{\rm rot} = -41.5 \div \ln\left[\frac{-0.28}{\tau_{1,1,\rm m}} \ln\left\{1 - \frac{\Delta \mathrm{T}^*_{\rm A2,2,m}}{\Delta \mathrm{T}^*_{\rm A1,1,m}} \times (1 - \mathrm{e}^{-\tau_{1,1,\rm m}})\right\}\right] \tag{B.80}$$

where $\Delta T^*_{\rm A1,1,m}$ and $\Delta T^*_{\rm A2,2,m}$ is the main beam brightness temperatures of the NH_3 (1,1) and (2,2) main-line transition. Alternatively if the assumption is made that the emission is optically thin the rotational temperature can be found with only the main beam brightness temperatures Wilson, Gaume & Johnston (1993):

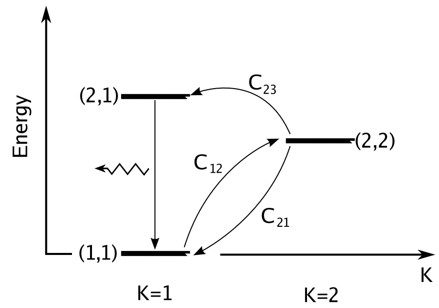

FIGURE B.14: Energy level diagram showing the collisional transition between the J, K = $(2,2), (2,1)$ and (2,2) energy levels. The quadrupole splitting of NH_3 is not shown and $C_x y$ is the collisional coefficient between levels.

$$T_{\rm rot} = \frac{41.5}{\ln\left[3.57\left(\Delta T^{*}_{\rm A1,1,m}/\Delta T^{*}_{\rm A2,2,m}\right)\right]} \tag{B.81}$$

B.9.1.3 Kinetic temperature

The mean kinetic temperature ($T_{\rm kin}$) is defined by the kinetic energy of a molecule and is given by:

$$\left\langle \frac{1}{2}mv^2 \right\rangle = \frac{3}{2}k_{\rm B}T_{\rm kin} \tag{B.82}$$

In a simple two-level system in LTE where radiative transitions are negligible the population of energy levels is defined by the Boltzmann distribution with the rotation and excitation temperature equal to the kinetic temperature. This is the case for CO however, in the case of NH_3 the population in the non-metastable levels may be non-negligible and so the approximation of a Boltzmann distribution defined by the rotational temperature between the NH_3 (1,1) and (2,2) levels may not be valid.

Although the (2,2) and (1,1) populations are not linked by radiative transitions, collisions can cause a transfer of population from the (2,2) levels to the (2,1) levels and by radiative decay to the (1,1) levels. The very fast decay from (2,1) to (1,1) causes $T_{\rm rot}$ to be an underestimate of $T_{\rm kin}$ (Walmsley & Ungerechts, 1983).

$$\frac{n_{22}}{n_{11}} = \frac{C_{12}}{(C_{21}+C_{23})} = \frac{C_{12}}{C_{21}}\frac{1}{(1+C_{23}/C_{21})} \tag{B.83}$$

where C_{23}, C_{21} and C_{12} are the collisional rate coefficients between the $J, K = (2,2 \rightarrow 2,1)$, $(2,2 \rightarrow 1,1)$ and $(1,1 \rightarrow 2,2)$ levels respectively.

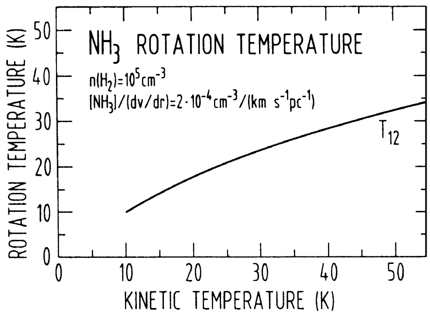

FIGURE B.15: A plot of the kinetic temperature as a function of rotational temperature obtained from the column densities of the (1,1) and (2,2) NH_3 lines (Rohlfs & Wilson, 2004).

The equation of detailed balance relates the collisional excitation and de-excitation rates, C_{lu} and C_{ul}, as follows:

$$C_{\mathrm{lu}} = \frac{g_{\mathrm{u}}}{g_{\mathrm{l}}} C_{\mathrm{ul}} \mathrm{e}^{-E_{\mathrm{ul}}/k_{\mathrm{B}}T_{\mathrm{kin}}} \tag{B.84}$$

The relative populations of two states is given by the Boltzmann equation at the rotational temperature:

$$\frac{N_{\mathrm{l}}}{N_{\mathrm{u}}} \frac{C_{\mathrm{lu}}}{C_{\mathrm{ul}}} = \left(\frac{g_{\mathrm{l}}}{g_{\mathrm{u}}} \mathrm{e}^{E_{\mathrm{lu}}/k_{\mathrm{B}}T_{\mathrm{rot}}}\right)\left(\frac{g_{\mathrm{u}}}{g_{\mathrm{l}}} \mathrm{e}^{-E_{\mathrm{lu}}/k_{\mathrm{B}}T_{\mathrm{kin}}}\right) = \frac{\mathrm{e}^{T_0/k_{\mathrm{B}}T_{\mathrm{rot}}}}{\mathrm{e}^{T_0/k_{\mathrm{B}}T_{\mathrm{kin}}}} \tag{B.85}$$

Empirical results reveal that at low temperatures ($< 15\,\mathrm{K}$) the rotation and kinetic temperature are approximately equivalent; however, they begin to deviate at higher temperature and thus analytic expressions underestimate the rotation temperature for kinetic temperatures above 40 K (Fig. B.15 (Walmsley & Ungerechts, 1983; Ho & Townes, 1983). For $T_{\mathrm{kin}} < T_0$ a relationship between rotational and kinetic temperature may be calculated by consideration of (1,1), (2,2) and (2,1) states only (Swift, Welch & Di Francesco, 2005; Walmsley & Ungerechts, 1983) and (Danby et al., 1988) show that $C_{\mathrm{lu}}/C_{\mathrm{ul}} = 0.82\mathrm{e}^{(-21.45/T_{\mathrm{kin}})}$, such that:

$$\begin{aligned} T_{\mathrm{rot}} &= \frac{T_{\mathrm{kin}}}{1 + \frac{T_{\mathrm{kin}}}{41.5}\ln\left[1 + 0.82\mathrm{e}^{\left(\frac{-21.45}{T_{\mathrm{kin}}}\right)}\right]} \text{ [K]} \\ T_{\mathrm{kin}} &= T_{\mathrm{rot}} \times \left(1 + \frac{T_{\mathrm{kin}}}{41.5}\right) \times \ln\left(1 + 0.82 \times \mathrm{e}^{(-21.45/T_{\mathrm{kin}})}\right) \end{aligned} \tag{B.86}$$

B.9.2 Optical depth

In the case of the ^{13}CO transition the optical depth is derived by assuming the excitation temperature is equal to the ^{12}CO excitation temperature. Rearranging Equation B.64 for the optical depth and substituting the appropriate values:

$$\tau_0^{13} = -\ln\left[1 - \frac{T_{\rm b}^{13}}{5.3}\left\{\left[\exp\left(\frac{5.3}{T_{\rm ex}}\right) - 1\right]^{-1} - 0.16\right\}^{-1}\right] \tag{B.87}$$

In the case of NH_3 the optical depth may be derived directly using the hyperfine spectral profile. This is because the relative intensities for the various hyperfine components are known (cf. Townes & Schawlow 1955). Applying Equation1 from Ho & Townes (1983) the ratio of temperatures of the main and satellite lines ($\Delta T^*_{\rm A(J,K,m)}$ and $\Delta T^*_{\rm A(J,K,s)}$) is:

$$\frac{\Delta T^*_{\rm A(J,K,m)}}{\Delta T^*_{\rm A(J,K,s)}} = \frac{\eta_{\rm b}\left[J_\nu(T_{\rm ex}) - J_\nu(T_{\rm bg})\right]\left[1 - {\rm e}^{(-\tau_{\rm J,K,m})}\right]}{\eta_{\rm b}\left[J_\nu(T_{\rm ex}) - J_\nu(T_{\rm bg})\right][1 - {\rm e}^{(-\tau_{\rm J,K,s})}]} \tag{B.88}$$

Since the observations are of the same transition the beam filling factor ($\eta_{\rm b}$) and excitation temperature are approximately equal and so:

$$\frac{\triangle T^*_\alpha({\rm J,K,m})}{\triangle T^*_\alpha({\rm J,K,s})} = \frac{1 - {\rm e}^{-\tau({\rm J,K,m})}}{1 - {\rm e}^{-\alpha\tau({\rm J,K,m})}} \tag{B.89}$$

where $\tau({\rm J,K,m})$ is the optical depth of the main line component and α is the expected ratio of intensity for the satellite compared to the main component ($\alpha = 0.28$ and 0.22 for the (1,1) satellites) under optically thin conditions. An implicit assumption is that the beam filling factors are equal as are the excitation temperatures for the different hyperfine components. This is a reasonable assumption because of the very close energy separations and the small probability of special excitation mechanisms that differentiate between the hyperfine components (Ho & Townes, 1983).

B.9.3 Column density

Integrating over the line of sight results in the column density ($N_{\rm l} = \int n\, ds$) of molecules in the corresponding state and taking $\varphi(\nu)$ to be the normalised line profile usually assumed to be Gaussian allows Equation B.75 to be expressed as:

$$\begin{aligned}\tau_\nu &= \frac{c^2}{8\pi}\frac{1}{\nu^2}\frac{g_u}{g_l}\frac{N_l}{dv}A_{ul}\left[1-\mathrm{e}^{\left(-\frac{h\nu_0}{k_B T}\right)}\right]\\ \tau_\nu &= \frac{c^2}{8\pi}\frac{1}{\nu^2}\frac{N_u}{dv}A_{ul}\left[\mathrm{e}^{\left(-\frac{h\nu_0}{k_B T}\right)}-1\right]\end{aligned} \tag{B.90}$$

This contains the column density in the lower and upper level (N_l and N_u). Rearranging for the N_l and substituting $\frac{d\nu}{\nu} = \frac{v}{c} \Rightarrow d\nu = \frac{c}{\nu}dv$, integrating over the velocity range and rearranging Equation B.90, which yields the total column density of the lower level:

$$N_l = \frac{8\pi\nu^3}{c^3 A_{ul}}\frac{g_l}{g_u}\left[1-\mathrm{e}^{h\nu/k_B T}\right]^{-1}\int \tau_\nu dv \tag{B.91}$$

This can total column density in the lower level be related to the column density over all levels via the Boltzmann (Eq. B.9) and the partition function, $Q(T)$ (Eq. B.12):

$$N_l = \frac{g_l}{Q(T)}N_{tot}\mathrm{e}^{-hBJ(J+1)/k_B T} \tag{B.92}$$

Where the partition function takes into account the energy of a diatomic rigid rotor $-E$ with the energy of a rigid rotor Eq. B.16 and can be expressed as:

$$Q(T) = \sum_{J=0}^{\infty} g_J \mathrm{e}^{-hB_e J(J+1)/k_B T} \approx \frac{k_B}{hB_e}\left(\frac{T+hB_e}{3k_B}\right) \tag{B.93}$$

Finally by substituting for the spontaneous emission coefficient (A_{ul}) Eq. B.28 into Equation B.91 and using equations Eq. B.92 and Eq. B.93 the total column density can be determined:

$$N_{tot} = \frac{3k_B}{8\pi^3 B_e \mu^2}\frac{\mathrm{e}^{hB_e J(J+1)/k_B T}}{(J+1)}\frac{(T+hB_e/3k_B)}{1-\mathrm{e}^{-h\nu/k_B T}}\int \tau_\nu dv \tag{B.94}$$

where μ is the permanent dipole moment[4]. The ^{13}CO molecule is generally chosen to determine the column density. Taking into account constants[5] allows the column density equation to be simplified to:

$$N_{tot\,(^{13}CO)} = 2.6 \times 10^{14}\frac{T_{ex}\int \tau_{13}(v)dv}{1-\mathrm{e}^{\frac{-5.3}{T_{ex}}}} \tag{B.95}$$

[4]See http://spec.jpl.nasa.gov/

[5]The rotational constant (B = 55.101 GHz), permanent dipole moment (μ = 0.112 debye) and frequency (ν = 110.221 GHz).

where the integrated optical depth may be approximated by:

$$T_{\text{ex}} \int_{-\infty}^{\infty} \tau(\nu)\, d\nu \cong \frac{\tau_0}{1 - \mathrm{e}^{-\tau_0}} \int_{-\infty}^{\infty} T_{\text{mb}}(\nu)\, d\nu \tag{B.96}$$

The column density of NH_3 may be derived in the same way by taking into account the different partition function, emission mechanism, permanent dipole moment (Eq. B.30) and the appropriate Einstein coefficient. Applying these and accounting for constants[6] results in the column density of molecules in the upper level:

$$N_{\text{u}} = \frac{1.6 \times 10^{13} \Delta V \tau_{(1,1,\text{m})}}{\mathrm{e}^{T_0/T_{\text{ex}}} - 1} \tag{B.97}$$

where ΔV is the line width in km s^{-1} and $\tau_{(1,1,\text{m})}$ is the main line optical depth. The column density N_u refers to the upper transition level, we make use of the Boltzmann equation to estimate the total column density N(1, 1) assuming that both levels are evenly populated:

$$N_{\text{NH}_3(1,1)} = N_{\text{u}} + N_{\text{l}} = N_{\text{u}}(1 + \mathrm{e}^{h\nu/kT_{\text{ex}}}) \tag{B.98}$$

Now that the total column density for the (1,1) transition is known, the total column density over all rotational transitions can be derived by assuming a Boltzmann distribution and the partition function (statistical weight of (2,2) to (1,1) is 5/3). The total column density of NH_3 within the clumps is then derived using the following equation, assuming that only metastable levels are populated (see Ungerechts, Winnewisser & Walmsley 1986 Eq. A15):

$$N_{(\text{NH}_3)} = N(1,1)\left(\frac{1}{3}\mathrm{e}^{23.4/T_{\text{rot}}} + 1 + \frac{5}{3}\mathrm{e}^{-41.5/T_{\text{rot}}} + \frac{14}{3}\mathrm{e}^{-101.5/T_{\text{rot}}}\right) \tag{B.99}$$

B.9.4 Mass

The mass may be determined by considering the geometry of the emission and number density derived above.

$$M = A N_{\text{m}} X \mu_{\text{m}} m_{\text{H}_2} \tag{B.100}$$

where A is the physical area of the emission, N_{m} is the column density of the observed molecular transition, X is the abundance ratio between the observed molecule and H_2, μ_{m} is the mean molecular weight of the gas and m_{H_2} is the mass of molecular hydrogen.

[6]Permanent dipole moment (μ = 1.468 debye) and frequency (ν = 23.694 GHz).

Molecular clouds are composed of mainly H_2 and He and so in order to derive the mass of a molecular cloud from a molecular transition an assumption must be made as to the relative abundance of the observed molecule and H_2. The following assumption is that the relative abundance of the observed molecule, be it CO or NH_3 relative to H_2 and He is uniform.

B.9.5 Virial mass and parameter

Molecular clouds are supported against gravitational collapse by various mechanisms, such as turbulence, thermal gas pressure, and magnetic fields. Observations show that the line widths of molecular clouds are much wider than their thermal line widths and so transonic or supersonic turbulence must be the main source of kinetic energy and support in molecular clouds (Larson, 1981; Williams, Blitz & McKee, 2000).

The virial mass of a molecular cloud is defined as the mass for which a molecular cloud is in virial equilibrium, i.e. when the internal kinetic energy K equals half the gravitational energy $U(2K + U = 0)$. The stability of molecular clumps against collapse can be tested by calculating the virial mass, which we derive using the standard equation (e.g. Evans 1999):

$$M_{\rm vir} \simeq 210R\langle \Delta V^2 \rangle \tag{B.101}$$

where R is the clump radius (pc) and ΔV is the FWHM line width (km s^{-1}). The virial parameter α of a molecular cloud is the ratio of its virial mass ($M_{\rm vir}$) to its mass (M). It describes the ratio of the internal supporting energy to the gravitational energy such that $\alpha_{\rm vir} = M_{\rm vir}/M$. Therefore, for $M > M_{\rm vir}$ ($\alpha < 1$), $2K + U < 0$ and the molecular cloud is gravitationally bound, potentially unstable and may collapse. For $M < M_{\rm vir}$ ($\alpha > 1$), $2K + U > 0$ and the molecular cloud is not gravitationally bound.

B.10 Deriving physical properties: radio continuum

Complicated geometries present difficulties in the interpretation of the physical properties such as density and surface brightness along a particular line of sight. Analysis of the radio data presented in this thesis is limited to the peak properties of the source averaged over the size of the observing beam such as in Wood & Churchwell (1989b); Molinari et al. (1996); Rohlfs & Wilson (2004).

B.10.1 Optical depth

The peak optical depth (τ) can be estimated if the peak main beam brightness temperature is known using $T_\mathrm{b} = T_\mathrm{e}(1 - \mathrm{e}^{-\tau})$ assuming the telescope beam is uniformly filled with ionised gas. The electron temperature of the ionised gas within HII regions has been shown to vary between 6800-13000 K (Spitzer & Savedoff, 1950; Caswell & Haynes, 1987). The electron temperature towards regions in G305 is unknown and so we assume a value of $T_\mathrm{e} = 10^4$ K throughout the rest of this analysis. This assumption results in an uncertainty of $\sim 20\%$ in the derived optical depth and $< 10\%$ in the physical properties derived below. The peak optical depth may be written as:

$$\tau = -\ln\left(1 - \frac{T_\mathrm{b}}{10^4}\right) \tag{B.102}$$

B.10.2 Emission measure

The Emission Measure (EM) of an HII region is defined as the integral of the product of the electron and proton density (N_e) along the line of sight:

$$EM = \int_0^{s/pc} (N_\mathrm{e})^2 \, \mathrm{d}\,(s) \;\; [\mathrm{pc\,cm^{-6}}] \tag{B.103}$$

The peak emission measure may be derived by substituting numerical values in the expression of the radio optical depth (Eq. B.53) to give:

$$EM = \frac{\tau}{8.235 \times 10^{-2} T_\mathrm{e}^{-1.35} \nu^{-2.1}} \;\; [\mathrm{pc\,cm^{-6}}] \tag{B.104}$$

where T_e is the electron temperature, assumed to be 10^4 K, ν is the frequency in GHz.

B.10.3 Electron density

The emission measure is related to the electron density through Equation B.103 and so the peak electron density (n_e) may be expressed as:

$$n_\mathrm{e} = \sqrt{\frac{EM}{\Delta s}} \;\; [\mathrm{cm^{-3}}] \tag{B.105}$$

where Δs is the optical path length through the peak and is defined as the geometrical average of the two axes of the source after applying the correction of Panagia & Walmsley (1978).

B.10.4 Mass

The ionised gas mass, M_{HII} of a source derived via a peak analysis by assuming a spherical geometry and is given by:

$$M_{\mathrm{HII}} = n_{\mathrm{e}} m_{\mathrm{p}} \frac{4}{3} \pi r^3 \tag{B.106}$$

where n_{e} is the electron density, m_{p} is the proton mass and r is the radius of the source.

B.10.5 Lyman flux

The total ionising photon flux of the Lyman continuum (N_{Ly}) is independent of source geometry and is determined using the modified equation (7) presented in Carpenter, Snell & Schloerb (1990):

$$N_{\mathrm{Ly}} = 7.7 \times 10^{43} S_{\mathrm{int}} D^2 \nu^{0.1} \ [\mathrm{s}^{-1}] \tag{B.107}$$

where N_{Ly} is the total number of Lyman photons emitted per second, S_{int} is the integrated radio flux (mJy), D is the distance to the source (3.8 ± 0.6 kpc) and ν is the frequency of the observation (GHz). This value of the ionising flux should be considered a lower limit due to dust absorption of the UV flux and the under estimated integrated flux.

The spectral type of the ionising star responsible for an HII region may be estimated by comparing the Lyman continuum flux to the derived value of the total number of ionising photons generated by massive stars tabulated by Panagia (1973). This is under the assumption that the radio emission observed is caused by a single zero age main sequence (ZAMS) star, no UV flux is absorbed by dust and that the HII region is ionisation bounded. Whilst the most massive star will dominate the Lyman flux if there are multiple stars that make a significant contribution to the ionising flux the spectral type will be later than we have estimated. Conversely, if there is significant absorption by dust and/or the nebular is not ionisation bounded the spectral type may be earlier than our estimate. This leads to an error in the spectral classification of approximately half a spectral type (e.g. Wood & Churchwell 1989a).

Appendix C

Appendix C

C.1 ^{12}CO pathfinder

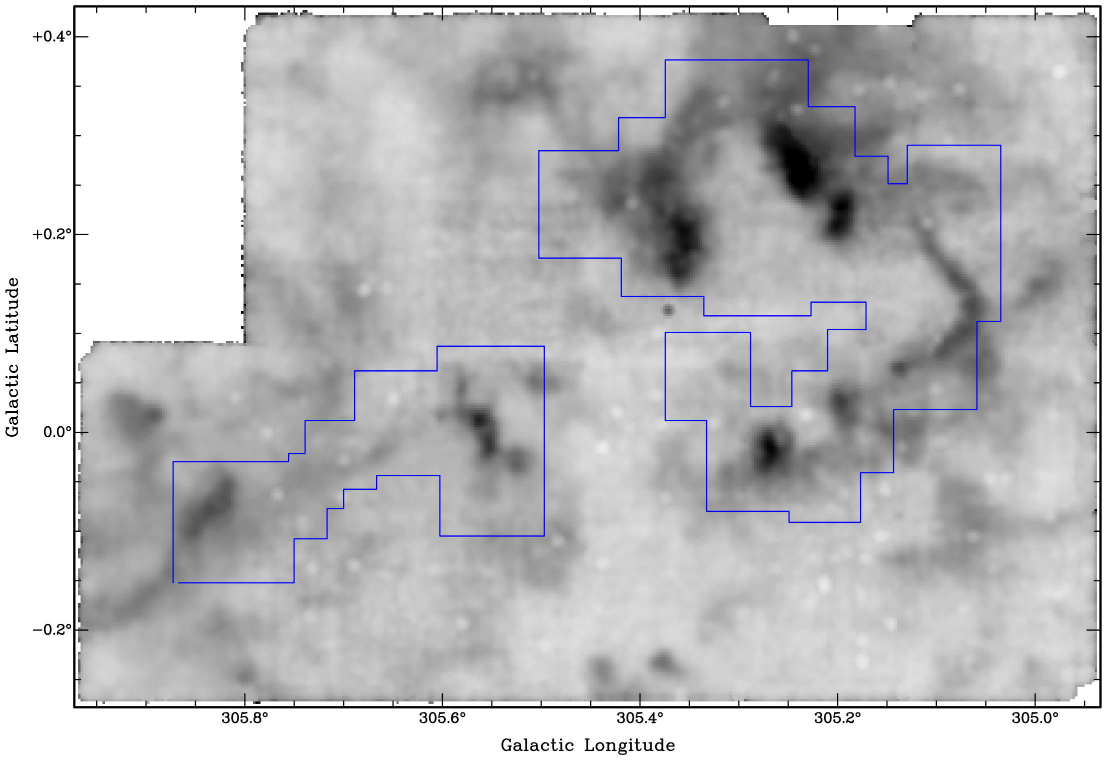

FIGURE C.1: The low sensitivity ^{12}CO pathfinder performed in the test phase of a new fast mapping mode with Mopra. The blue outline shows the mapped region in the CO observations presented in Chapter 3.

C.2 H_2O maser peak spectra

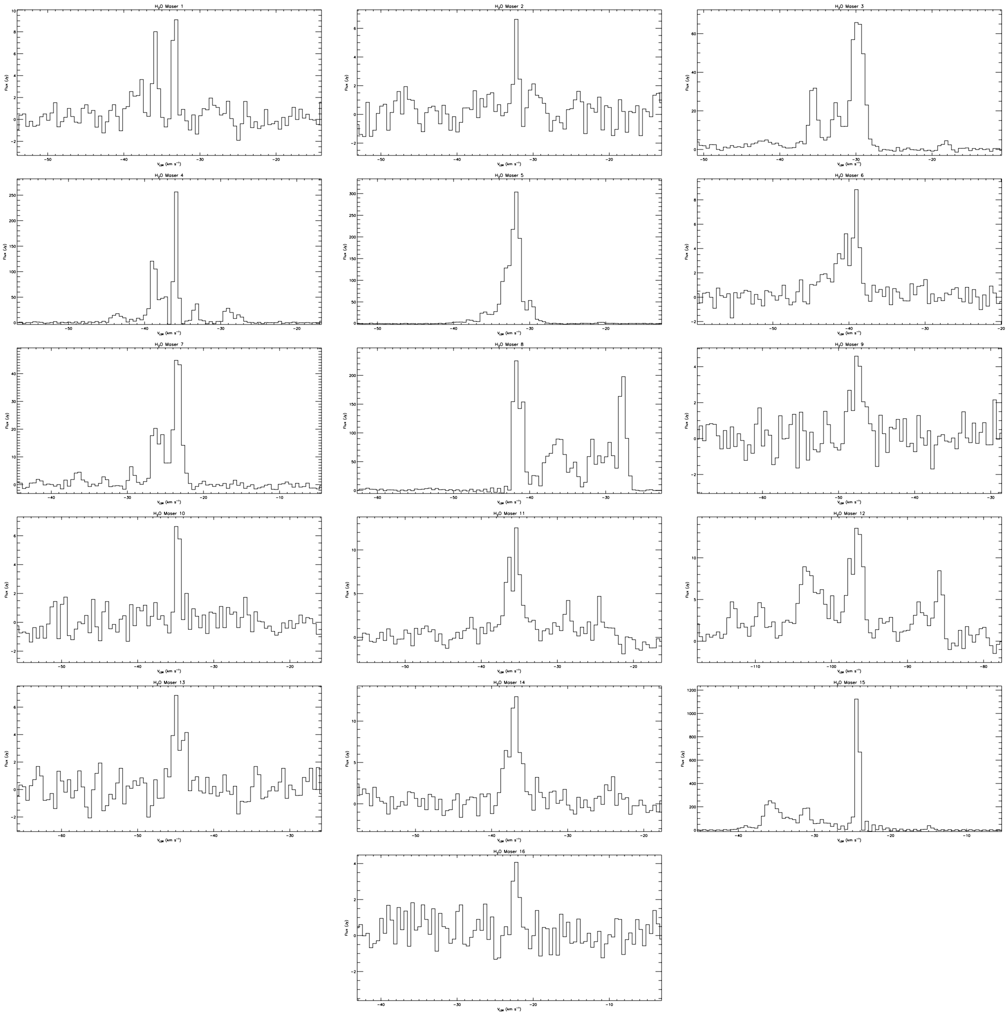

FIGURE C.2: Peak spectra of the 16 H_2O masers towards G305.

C.3 CO clump catalogue

Clump	Clump	Peak			Dimension				Peak
Number	Name	Galactic		V_{LSR}	Δl	Δb	R	Δv	T_{mb}
		(l)	(b)	(km s^{-1})	($''$)	($''$)	(pc)	(km s^{-1})	(K)
1	G305.24+0.26	305.24	0.26	-38.8	295.34	324.52	2.42	5.71	15.55
2	G305.56+0.02	305.56	0.02	-39.7	222.51	156.10	1.50	3.69	14.00
3	G304.94+0.55	304.94	0.55	-34.6	385.20	261.13	2.46	2.87	14.26
4	G305.26-0.03	305.26	-0.03	-32.4	410.77	332.67	2.77	4.60	13.26
5	G305.27-0.02	305.27	-0.02	-32.4	169.69	140.30	1.23	5.53	12.83
6	G305.55-0.01	305.55	-0.01	-37.9	156.76	202.59	1.47	5.30	11.45
7	G305.19+0.01	305.19	0.01	-31.4	265.25	128.08	1.47	5.13	11.71
8	G305.82-0.05	305.82	-0.05	-35.1	138.68	244.36	1.42	3.56	11.02
9	G305.24-0.03	305.24	-0.03	-28.2	196.72	157.68	1.35	2.96	10.67
10	G305.27-0.04	305.27	-0.04	-33.3	172.82	163.42	1.36	3.43	11.76
11	G305.22-0.02	305.22	-0.02	-28.7	225.29	184.05	1.56	5.75	10.83
12	G305.36+0.21	305.36	0.21	-35.1	193.42	195.29	1.61	5.49	12.19
13	G305.26+0.3	305.26	0.30	-38.3	263.55	251.26	1.93	5.63	10.45
14	G305.36+0.17	305.36	0.17	-38.8	201.83	234.07	1.67	4.57	11.62
15	G304.88+0.61	304.88	0.61	-34.6	325.70	245.82	2.05	2.37	12.14
16	G305.37+0.19	305.37	0.19	-35.1	227.52	173.72	1.52	4.36	11.17
17	G305.2+0.23	305.20	0.23	-39.7	202.61	284.60	1.73	6.17	10.83
18	G305.36+0.23	305.36	0.23	-38.3	162.67	191.26	1.35	2.91	10.38
19	G305.85-0.07	305.85	-0.07	-34.6	156.71	250.79	1.45	3.43	9.83
20	G305.19+0.03	305.19	0.03	-36.5	271.44	232.99	1.82	5.57	9.29

TABLE C.1: Physical properties of the 57 detected ^{13}CO clumps. Columns are: Identifier, Name, FWHM, Radius, average line-center optical depth of ^{13}CO, excitation temperature derived from ^{12}CO, H_2 column density, H_2 density assuming spherical geometry, $\sum_c$ surface mass density, mass, virial mass and virial parameter.

Clump Number	Clump Name	Peak Galactic (l)	Peak Galactic (b)	Peak V_{LSR} (km s^{-1})	Dimension Δl ($''$)	Dimension Δb ($''$)	Dimension R (pc)	Dimension Δv (km s^{-1})	Peak T_{mb} (K)
21	G305.21+0.21	305.21	0.21	-42.9	177.11	117.13	1.06	3.27	9.62
22	G305.14+0.07	305.14	0.07	-36.0	266.28	246.83	1.87	4.27	9.38
23	G305.35+0.21	305.35	0.21	-40.1	185.04	170.11	1.26	2.94	9.45
24	G305.38+0.24	305.38	0.24	-38.3	136.46	187.94	1.27	4.02	9.40
25	G305.2+0.21	305.20	0.21	-41.5	153.84	163.75	1.26	4.26	9.05
26	G304.92+0.5	304.92	0.50	-32.4	130.69	96.67	0.88	3.19	13.81
27	G305.37+0.26	305.37	0.26	-35.1	168.68	326.19	1.77	4.78	9.10
28	G304.9+0.55	304.90	0.55	-33.7	175.74	172.11	1.27	2.52	8.71
29	G305.2-0.01	305.20	-0.01	-30.1	114.42	127.25	0.95	3.94	8.40
30	G305.31+0.33	305.31	0.33	-38.8	532.73	235.91	2.50	5.44	8.76
31	G305.17+0.22	305.17	0.22	-42.4	287.01	152.95	1.53	4.64	8.00
32	G305.44+0.25	305.44	0.25	-38.3	336.10	254.41	1.70	4.31	9.00
33	G305.39+0.25	305.39	0.25	-39.2	165.99	150.03	1.25	5.58	8.74
34	G305.31-0.04	305.31	-0.04	-33.3	141.29	119.86	0.98	4.17	8.64
35	G305.41+0.2	305.41	0.20	-34.2	223.05	175.53	1.33	2.97	7.95
36	G305.52-0.03	305.52	-0.03	-37.9	155.09	112.25	0.95	6.02	7.60
37	G305.16+0.25	305.16	0.25	-38.3	146.02	168.65	1.07	3.67	8.12
38	G305.35+0.24	305.35	0.24	-40.6	143.50	182.59	1.00	2.73	7.69
39	G305.18-0.02	305.18	-0.02	-31.9	227.12	149.48	1.41	6.83	7.21
40	G305.77-0.08	305.77	-0.08	-41.1	161.94	191.19	1.31	3.83	6.76
41	G305.82-0.1	305.82	-0.10	-41.1	229.97	270.19	1.79	4.73	7.05
42	G305.87-0.09	305.87	-0.09	-34.6	135.10	136.20	0.96	3.16	10.90
43	G305.79-0.09	305.79	-0.09	-41.1	132.25	114.63	0.93	4.68	7.14
44	G305.55-0.06	305.55	-0.06	-41.5	85.10	101.21	0.70	2.49	7.26

TABLE C.1: Physical properties of the 57 detected ^{13}CO clumps. Columns are: Identifier, Name, FWHM, Radius, average line-center optical depth of ^{13}CO, excitation temperature derived from ^{12}CO, H_2 column density, H_2 density assuming spherical geometry, $\sum_c$ surface mass density, mass, virial mass and virial parameter.

Clump Number	Clump Name	Peak			Dimension				Peak
		Galactic		V_{LSR}	Δl	Δb	R	Δv	T_{mb}
		(l)	(b)	(km s^{-1})	($''$)	($''$)	(pc)	(km s^{-1})	(K)
45	G305.06+0.11	305.06	0.11	-36.9	303.72	316.25	1.90	6.94	7.14
46	G305.22-0.06	305.22	-0.06	-33.3	146.68	78.96	0.78	2.23	6.50
47	G305.11+0.2	305.11	0.20	-41.1	190.65	249.56	1.09	4.84	6.29
48	G305.32+0.28	305.32	0.28	-42.0	152.31	145.76	0.91	3.25	6.48
49	G305.39+0.17	305.39	0.17	-35.6	133.12	111.71	0.87	2.63	6.74
50	G305.61+0.01	305.61	0.01	-35.1	129.59	94.81	0.58	2.09	6.14
51	G305.11+0.25	305.11	0.25	-39.2	147.88	78.20	0.76	4.72	6.14
52	G305.08+0.16	305.08	0.16	-41.1	148.87	212.83	0.94	3.67	6.19
53	G305.74-0.04	305.74	-0.04	-39.7	225.40	140.68	1.25	4.54	5.26
54	G305.55-0.04	305.55	-0.04	-40.6	79.38	97.21	0.66	2.69	6.14
55	G305.19+0.2	305.19	0.20	-40.6	284.89	112.00	1.06	4.66	6.10
56	G305.15+0.21	305.15	0.21	-17.7	153.75	129.96	0.81	2.10	5.86
57	G305.4+0.18	305.40	0.18	-34.2	91.63	95.82	0.66	3.14	5.81

TABLE C.1: Physical properties of the 57 detected ^{13}CO clumps. Columns are: Identifier, Name, FWHM, Radius, average line-center optical depth of ^{13}CO, excitation temperature derived from ^{12}CO, H_2 column density, H_2 density assuming spherical geometry, $\sum_c$ surface mass density, mass, virial mass and virial parameter.

C.3.1 CO clump spectra

Below the 62 clump averaged ^{12}CO ^{13}CO and ^{13}COspectra are displayed.

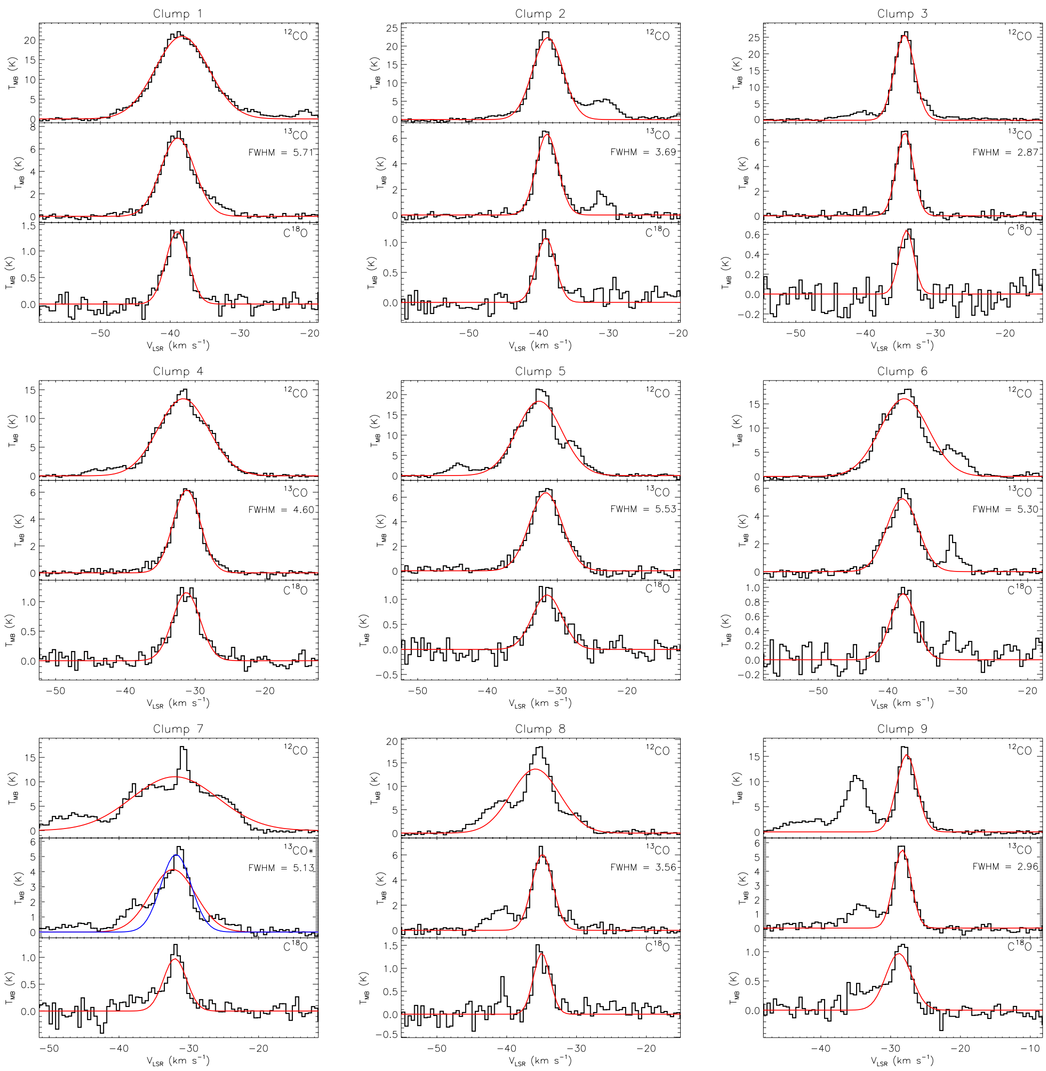

FIGURE C.3: Clump averaged spectra of the 61 detected CO clumps towards G305. Clumps have been integrated spatially over the clump area defined by CLUMPFIND and Hanning smoothed to provide a sensitivity of ~ K per ~ km s^{-1}channel. Gaussian fitting is applied each transition , shown as red overplots.

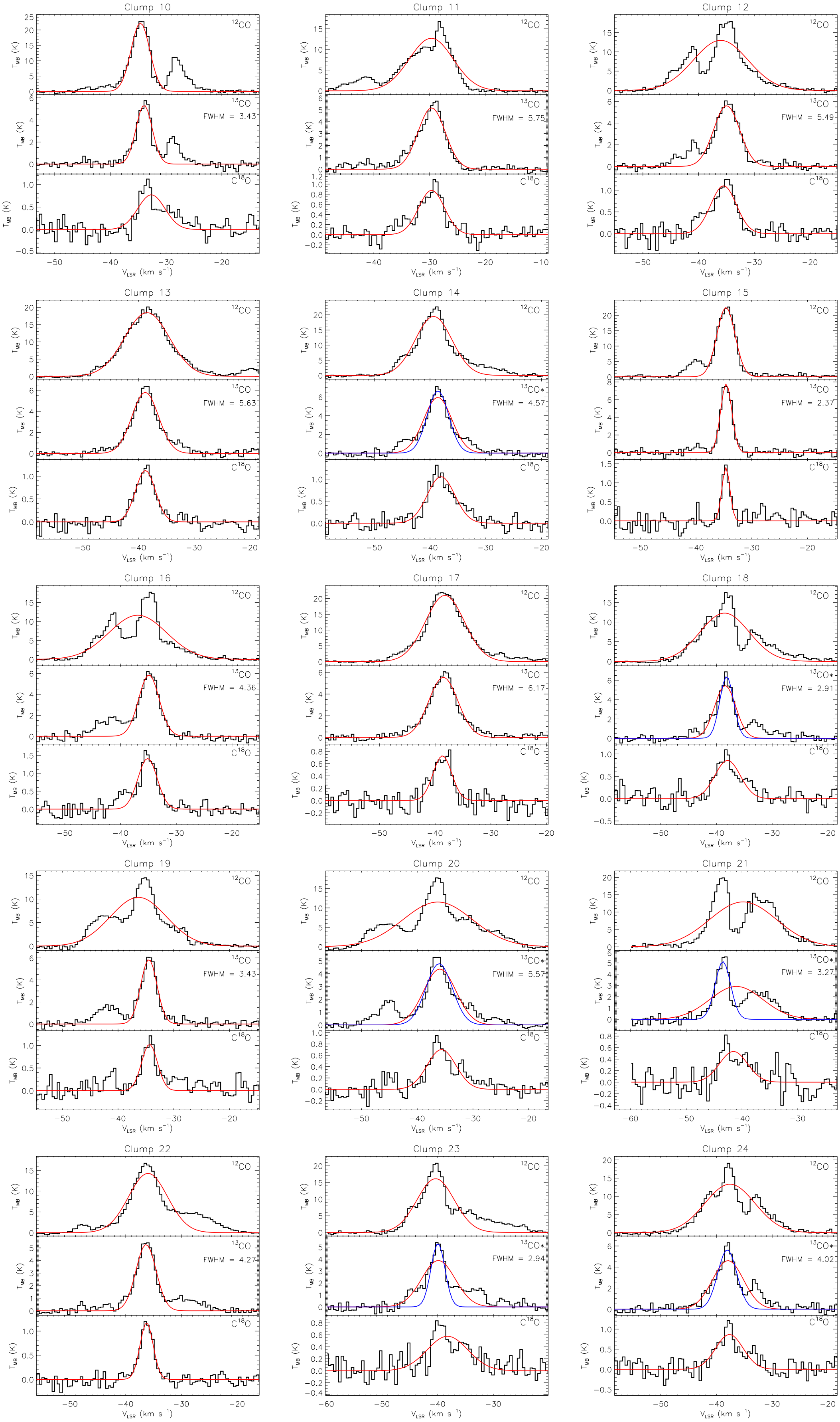
Clump 10
^{12}CO
^{13}CO
FWHM = 3.43
C^{18}O
Clump 11
^{12}CO
^{13}CO
FWHM = 5.75
C^{18}O
Clump 12
^{12}CO
^{13}CO
FWHM = 5.49
C^{18}O
Clump 13
^{12}CO
^{13}CO
FWHM = 5.63
C^{18}O
Clump 14
^{12}CO
^{13}CO*
FWHM = 4.57
C^{18}O
Clump 15
^{12}CO
^{13}CO
FWHM = 2.37
C^{18}O
Clump 16
^{12}CO
^{13}CO
FWHM = 4.36
C^{18}O
Clump 17
^{12}CO
^{13}CO
FWHM = 6.17
C^{18}O
Clump 18
^{12}CO
^{13}CO*
FWHM = 2.91
C^{18}O
Clump 19
^{12}CO
^{13}CO
FWHM = 3.43
C^{18}O
Clump 20
^{12}CO
^{13}CO*
FWHM = 5.57
C^{18}O
Clump 21
^{12}CO
^{13}CO*
FWHM = 3.27
C^{18}O
Clump 22
^{12}CO
^{13}CO
FWHM = 4.27
C^{18}O
Clump 23
^{12}CO
^{13}CO*
FWHM = 2.94
C^{18}O
Clump 24
^{12}CO
^{13}CO*
FWHM = 4.02
C^{18}O
T_{MB} (K)
V_{LSR} (km s^{-1})

FIGURE C.3

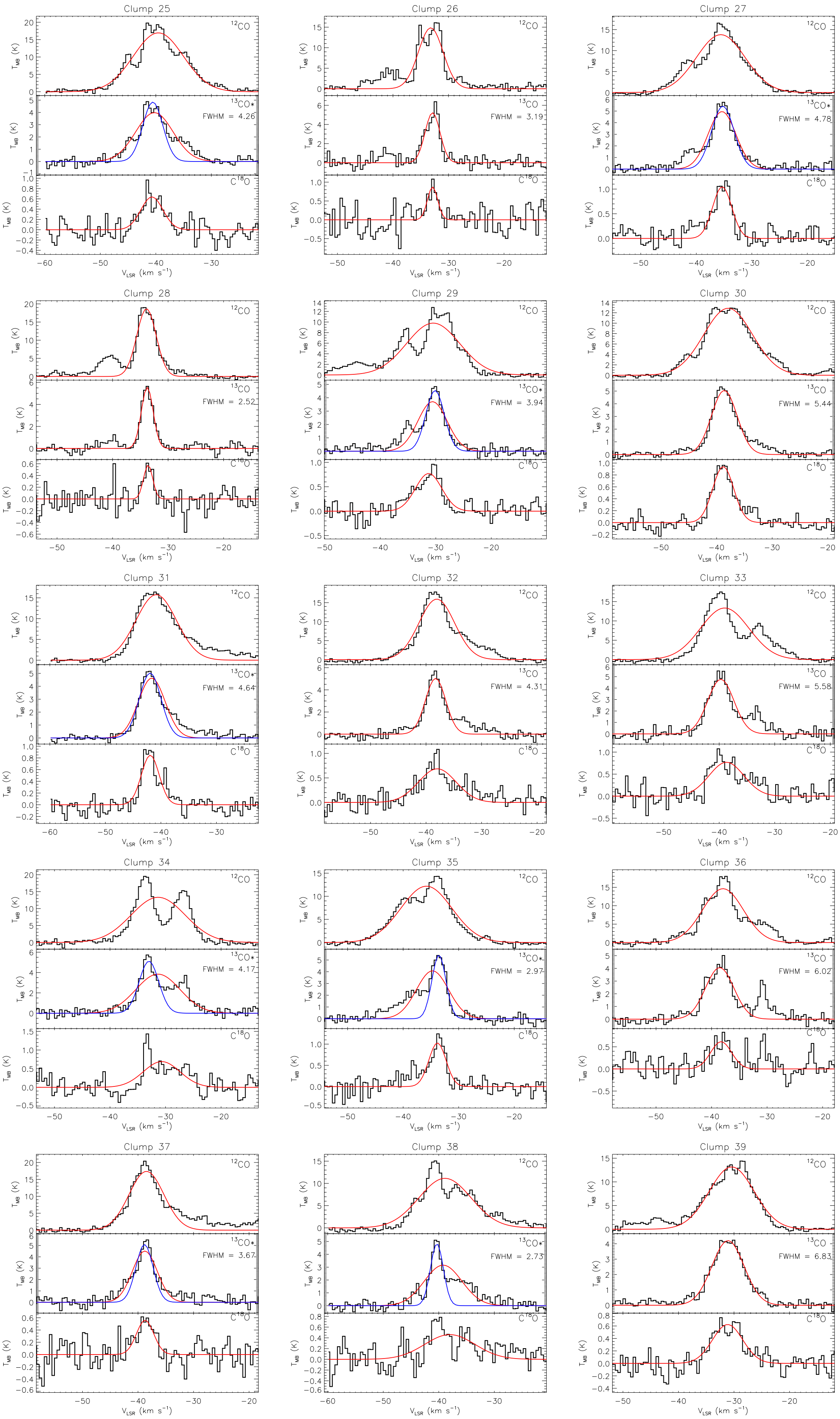
Clump 25
^{12}CO
^{13}CO*
FWHM = 4.26
C^{18}O
Clump 26
FWHM = 3.19
Clump 27
FWHM = 4.78
Clump 28
FWHM = 2.52
Clump 29
FWHM = 3.94
Clump 30
FWHM = 5.44
Clump 31
FWHM = 4.64
Clump 32
FWHM = 4.31
Clump 33
FWHM = 5.58
Clump 34
FWHM = 4.17
Clump 35
FWHM = 2.97
Clump 36
FWHM = 6.02
Clump 37
FWHM = 3.67
Clump 38
FWHM = 2.73
Clump 39
FWHM = 6.83
T$_{MB}$ (K)
V$_{LSR}$ (km s^{-1})

FIGURE C.3

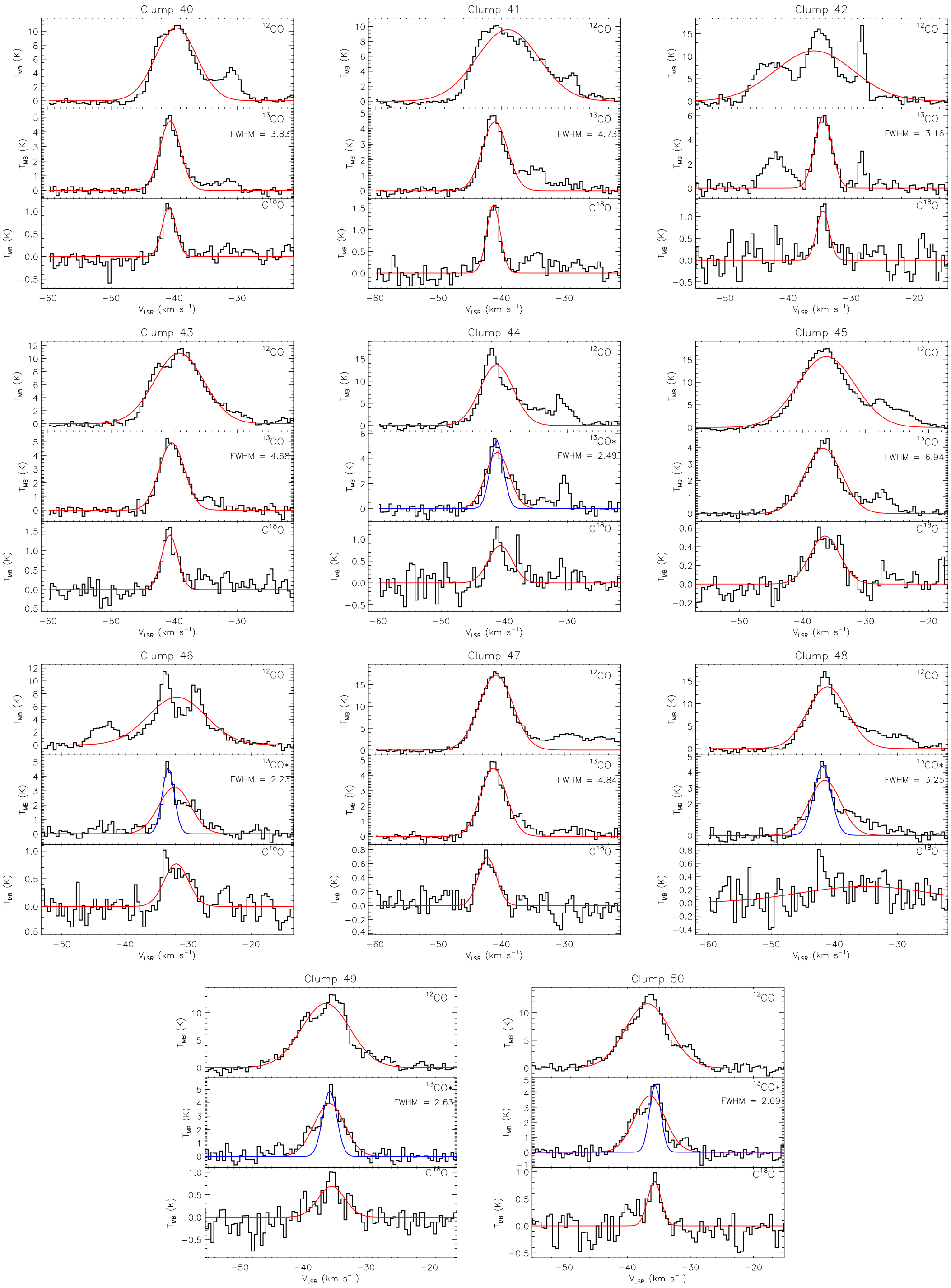
Clump 40
Clump 41
Clump 42
Clump 43
Clump 44
Clump 45
Clump 46
Clump 47
Clump 48
Clump 49
Clump 50
^{12}CO
^{13}CO
C^{18}O
FWHM = 3.83
FWHM = 4.73
FWHM = 3.16
FWHM = 4.68
FWHM = 2.49
FWHM = 6.94
FWHM = 2.23
FWHM = 4.84
FWHM = 3.25
FWHM = 2.63
FWHM = 2.09
T_{MB} (K)
V_{LSR} (km s^{-1})

FIGURE C.3

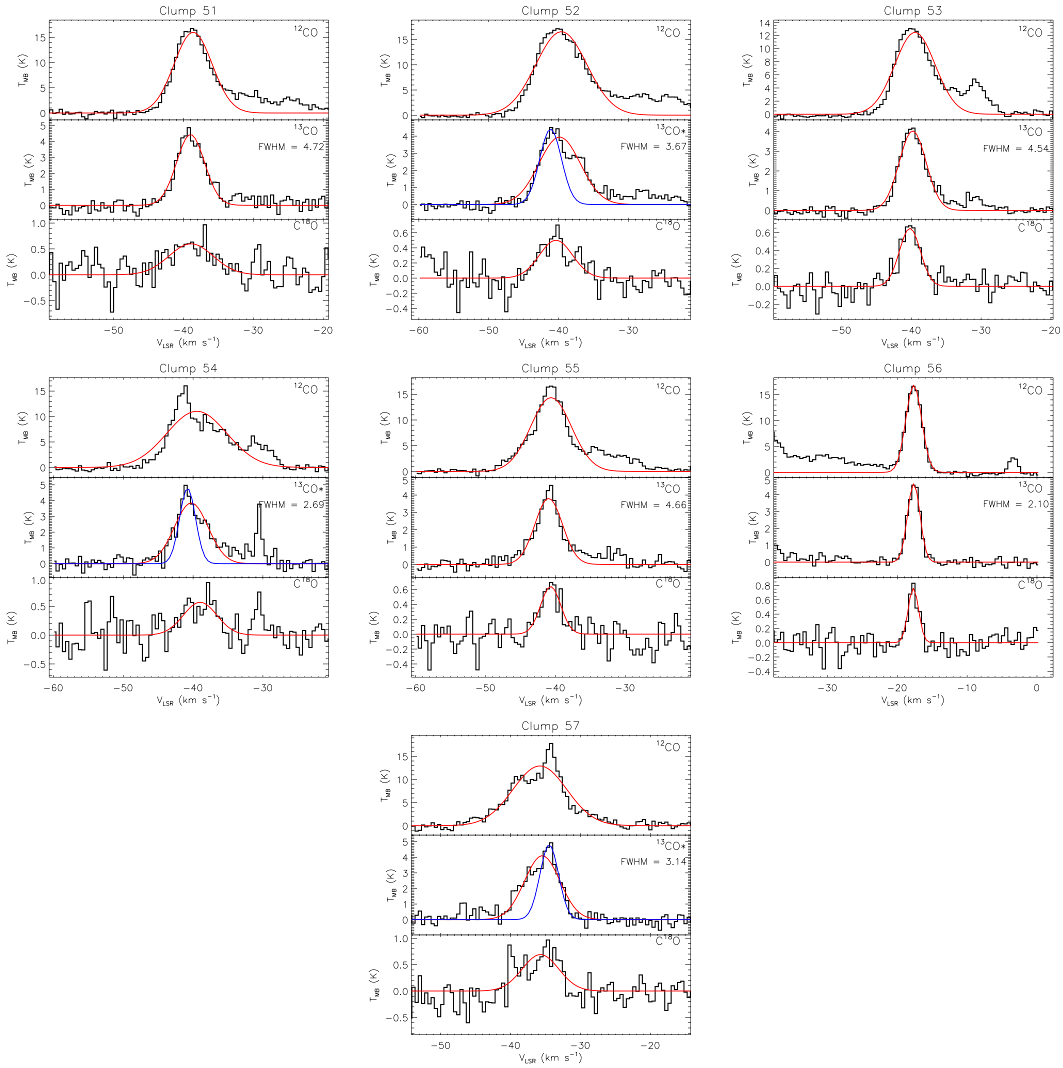
Clump 51
Clump 52
Clump 53
Clump 54
Clump 55
Clump 56
Clump 57
FWHM = 4.72
FWHM = 3.67
FWHM = 4.54
FWHM = 2.69
FWHM = 4.66
FWHM = 2.10
FWHM = 3.14
T_MB (K)
V_LSR (km s^-1)

FIGURE C.3

C.3.2 CO clump physical properties

Clump No.	Clump Name	τ (^{13}CO)	T_{ex} (K)	N_{H_2} 10^{22}(cm^{-2})	n_{H_2} 10^{3}(cm^{-3})	$\sum_c$ 10^{2}(M$_\odot$ pc^{-2})	M 10^{3}(M$_\odot$)	M_{vir} 10^{3}(M$_\odot$)	α_{vir}
1	G305.24+0.26	0.46 ± 0.03	21.34 ± 0.21	5.27 ± 0.43	5.5 ± 2.7	12.0 ± 3.9	22.0 ± 1.8	12.0 ± 2.0	0.58 ± 0.10
2	G305.56+0.02	0.34 ± 0.02	21.56 ± 0.20	3.18 ± 0.27	5.4 ± 2.6	7.1 ± 2.3	5.0 ± 0.4	5.0 ± 0.8	0.99 ± 0.18
3	G304.94+0.55	0.41 ± 0.02	23.80 ± 0.29	2.74 ± 0.21	2.8 ± 1.4	6.1 ± 2.0	12.0 ± 0.9	6.4 ± 1.0	0.55 ± 0.10
4	G305.26-0.03	0.67 ± 0.06	17.01 ± 0.29	3.33 ± 0.30	3.1 ± 1.5	7.5 ± 2.5	18.0 ± 1.7	12.0 ± 1.8	0.64 ± 0.12
5	G305.27-0.02	0.45 ± 0.03	18.76 ± 0.22	4.25 ± 0.37	8.8 ± 4.2	9.5 ± 3.1	4.5 ± 0.4	6.1 ± 1.0	1.36 ± 0.25
6	G305.55-0.01*	0.44 ± 0.03	17.73 ± 0.23	3.24 ± 0.33	5.6 ± 2.7	7.3 ± 2.4	4.9 ± 0.5	7.0 ± 1.1	1.43 ± 0.28
7	G305.19+0.01*	0.60 ± 0.05	15.11 ± 0.26	3.06 ± 0.35	5.3 ± 2.6	6.9 ± 2.3	4.7 ± 0.6	6.8 ± 1.6	1.46 ± 0.38
8	G305.82-0.05	0.55 ± 0.04	15.56 ± 0.33	2.73 ± 0.29	4.9 ± 2.4	6.1 ± 2.0	3.9 ± 0.4	4.6 ± 0.8	1.18 ± 0.23
9	G305.24-0.03	0.57 ± 0.04	17.92 ± 0.21	2.24 ± 0.21	4.2 ± 2.0	5.0 ± 1.7	2.9 ± 0.3	3.6 ± 0.6	1.25 ± 0.24
10	G305.27-0.04	0.35 ± 0.02	21.76 ± 0.19	2.76 ± 0.25	5.2 ± 2.5	6.2 ± 2.0	3.6 ± 0.3	4.2 ± 0.7	1.17 ± 0.22
11	G305.22-0.02	0.66 ± 0.05	15.95 ± 0.24	3.08 ± 0.31	5.0 ± 2.4	6.9 ± 2.3	5.3 ± 0.5	8.1 ± 1.3	1.54 ± 0.29
12	G305.36+0.21	0.48 ± 0.03	19.09 ± 0.22	4.00 ± 0.35	6.3 ± 3.0	9.0 ± 2.9	7.3 ± 0.6	8.0 ± 1.3	1.10 ± 0.20
13	G305.26+0.3	0.45 ± 0.03	20.35 ± 0.21	3.88 ± 0.37	5.1 ± 2.5	8.7 ± 2.9	10.0 ± 1.0	9.9 ± 1.6	0.96 ± 0.18
14	G305.36+0.17*	0.41 ± 0.03	19.14 ± 0.22	4.32 ± 0.40	6.6 ± 3.2	9.7 ± 3.2	8.5 ± 0.8	6.9 ± 1.2	0.81 ± 0.16
15	G304.88+0.61	0.49 ± 0.03	20.13 ± 0.38	2.50 ± 0.22	3.1 ± 1.5	5.6 ± 1.8	7.4 ± 0.7	4.4 ± 0.7	0.59 ± 0.11
16	G305.37+0.19	0.47 ± 0.03	17.76 ± 0.24	3.46 ± 0.34	5.8 ± 2.8	7.8 ± 2.6	5.6 ± 0.6	6.0 ± 1.0	1.07 ± 0.21
17	G305.2+0.23	0.35 ± 0.02	21.24 ± 0.21	4.05 ± 0.39	5.9 ± 2.9	9.1 ± 3.0	8.6 ± 0.8	9.7 ± 1.5	1.13 ± 0.21
18	G305.36+0.23*	0.49 ± 0.03	18.67 ± 0.21	3.08 ± 0.28	5.8 ± 2.8	6.9 ± 2.3	4.0 ± 0.4	3.6 ± 0.7	0.90 ± 0.19
19	G305.85-0.07	0.75 ± 0.06	14.32 ± 0.31	2.51 ± 0.28	4.4 ± 2.1	5.6 ± 1.9	3.7 ± 0.4	4.5 ± 0.8	1.21 ± 0.25

TABLE C.2: Identifiers and observed properties of the 57 detected ^{13}CO clumps reported by Clumpfind. An asterisks above the clump number indicates where XS has been used to fit a Gaussian to the clump averaged ^{13}CO spectral profile.

Clump No.	Clump Name	τ (^{13}CO)	T_{ex} (K)	N_{H_2} 10^{22}(cm^{-2})	n_{H_2} 10^{3}(cm^{-3})	$\sum_c$ 10^{2}(M$_\odot$ pc^{-2})	M 10^{3}(M$_\odot$)	M_{vir} 10^{3}(M$_\odot$)	α_{vir}
20	G305.19+0.03*	0.41 ± 0.03	14.99 ± 0.27	3.15 ± 0.38	4.4 ± 2.1	7.0 ± 2.4	7.3 ± 0.9	9.2 ± 1.7	1.25 ± 0.28
21	G305.21+0.21*	0.34 ± 0.02	20.15 ± 0.19	3.06 ± 0.34	7.4 ± 3.6	6.9 ± 2.3	2.4 ± 0.3	3.1 ± 0.6	1.30 ± 0.30
22	G305.14+0.07	0.45 ± 0.04	17.00 ± 0.23	2.32 ± 0.24	3.1 ± 1.5	5.2 ± 1.7	5.7 ± 0.6	7.2 ± 1.2	1.27 ± 0.25
23	G305.35+0.21*	0.34 ± 0.02	18.37 ± 0.23	2.93 ± 0.33	5.9 ± 2.9	6.6 ± 2.2	3.3 ± 0.4	3.4 ± 0.7	1.02 ± 0.23
24	G305.38+0.24*	0.42 ± 0.03	18.36 ± 0.25	3.34 ± 0.33	6.7 ± 3.2	7.5 ± 2.5	3.8 ± 0.4	4.6 ± 0.9	1.22 ± 0.26
25	G305.2+0.21*	0.31 ± 0.02	21.54 ± 0.18	3.39 ± 0.35	6.8 ± 3.3	7.6 ± 2.5	3.8 ± 0.4	4.9 ± 0.9	1.28 ± 0.28
26	G304.92+0.5	0.49 ± 0.03	15.89 ± 0.53	2.31 ± 0.24	6.7 ± 3.2	5.2 ± 1.7	1.3 ± 0.1	2.5 ± 0.4	2.02 ± 0.41
27	G305.37+0.26*	0.48 ± 0.04	17.01 ± 0.25	3.11 ± 0.33	4.5 ± 2.2	7.0 ± 2.3	6.9 ± 0.8	7.7 ± 1.4	1.12 ± 0.24
28	G304.9+0.55	0.40 ± 0.03	19.09 ± 0.32	1.71 ± 0.17	3.4 ± 1.7	3.8 ± 1.3	1.9 ± 0.2	2.9 ± 0.5	1.49 ± 0.29
29	G305.2-0.01*	0.53 ± 0.04	15.27 ± 0.25	2.08 ± 0.24	5.5 ± 2.7	4.7 ± 1.6	1.3 ± 0.2	3.4 ± 0.7	2.55 ± 0.59
30	G305.31+0.33	0.65 ± 0.05	15.95 ± 0.24	2.69 ± 0.30	2.7 ± 1.3	6.0 ± 2.0	12.0 ± 1.3	12.0 ± 2.0	1.04 ± 0.20
31	G305.17+0.22*	0.41 ± 0.03	17.35 ± 0.23	2.84 ± 0.33	4.7 ± 2.3	6.4 ± 2.1	4.7 ± 0.6	6.4 ± 1.2	1.37 ± 0.30
32	G305.44+0.25	0.43 ± 0.03	16.96 ± 0.38	2.43 ± 0.29	3.6 ± 1.8	5.4 ± 1.8	4.9 ± 0.6	6.6 ± 1.1	1.34 ± 0.27
33	G305.39+0.25	0.41 ± 0.03	17.52 ± 0.31	3.00 ± 0.33	6.1 ± 3.0	6.7 ± 2.3	3.3 ± 0.4	6.3 ± 1.0	1.92 ± 0.38
34	G305.31-0.04*	0.39 ± 0.03	16.57 ± 0.28	3.37 ± 0.39	8.7 ± 4.3	7.6 ± 2.6	2.3 ± 0.3	3.7 ± 0.7	1.62 ± 0.36
35	G305.41+0.2*	0.51 ± 0.04	15.15 ± 0.29	2.63 ± 0.32	5.0 ± 2.4	5.9 ± 2.0	3.3 ± 0.4	3.6 ± 0.7	1.09 ± 0.25
36	G305.52-0.03	0.41 ± 0.04	15.21 ± 0.35	2.60 ± 0.34	6.9 ± 3.4	5.8 ± 2.0	1.7 ± 0.2	5.2 ± 0.9	3.12 ± 0.68
37	G305.16+0.25*	0.37 ± 0.03	17.11 ± 0.28	2.49 ± 0.32	5.9 ± 2.9	5.6 ± 1.9	2.0 ± 0.3	3.6 ± 0.7	1.76 ± 0.41
38	G305.35+0.24*	0.44 ± 0.04	15.92 ± 0.24	2.05 ± 0.25	5.2 ± 2.6	4.6 ± 1.6	1.4 ± 0.2	2.5 ± 0.5	1.72 ± 0.42
39	G305.18-0.02	0.53 ± 0.05	15.90 ± 0.25	2.55 ± 0.30	4.6 ± 2.2	5.7 ± 1.9	3.6 ± 0.4	8.7 ± 1.4	2.44 ± 0.49
40	G305.77-0.08	0.73 ± 0.07	13.45 ± 0.27	1.61 ± 0.19	3.1 ± 1.5	3.6 ± 1.2	1.9 ± 0.2	4.5 ± 0.7	2.35 ± 0.48
41	G305.82-0.1	0.79 ± 0.07	12.90 ± 0.31	2.08 ± 0.26	3.0 ± 1.5	4.7 ± 1.6	4.7 ± 0.6	7.6 ± 1.3	1.63 ± 0.35
42	G305.87-0.09	0.60 ± 0.05	13.89 ± 0.43	3.13 ± 0.38	8.3 ± 4.1	7.0 ± 2.4	2.0 ± 0.3	2.7 ± 0.5	1.35 ± 0.29
43	G305.79-0.09	0.90 ± 0.08	13.53 ± 0.27	2.13 ± 0.25	5.8 ± 2.8	4.8 ± 1.6	1.3 ± 0.2	3.9 ± 0.6	3.06 ± 0.62
44	G305.55-0.06*	0.46 ± 0.04	13.95 ± 0.30	2.09 ± 0.27	7.6 ± 3.7	4.7 ± 1.6	0.7 ± 0.1	1.6 ± 0.3	2.19 ± 0.52
45	G305.06+0.11	0.34 ± 0.03	18.25 ± 0.21	2.52 ± 0.31	3.4 ± 1.7	5.6 ± 1.9	6.4 ± 0.8	12.0 ± 1.9	1.87 ± 0.38
46	G305.22-0.06*	0.66 ± 0.06	12.54 ± 0.30	1.46 ± 0.19	4.8 ± 2.3	3.3 ± 1.1	0.6 ± 0.1	1.6 ± 0.4	2.52 ± 0.66
47	G305.11+0.2	0.35 ± 0.03	17.72 ± 0.21	2.10 ± 0.25	4.9 ± 2.4	4.7 ± 1.6	1.8 ± 0.2	4.8 ± 0.8	2.71 ± 0.55

TABLE C.2

Clump No.	Clump Name	τ (^{13}CO)	T_{ex} (K)	N_{H_2} 10^{22}(cm^{-2})	n_{H_2} 10^3(cm^{-3})	$\sum_c$ 10^2(M$_\odot$ pc^{-2})	M 10^3(M$_\odot$)	M_{vir} 10^3(M$_\odot$)	α_{vir}
48	G305.32+0.28*	0.37 ± 0.03	15.74 ± 0.25	1.59 ± 0.21	4.4 ± 2.2	3.6 ± 1.2	0.9 ± 0.1	2.7 ± 0.6	2.89 ± 0.72
49	G305.39+0.17*	0.52 ± 0.04	14.51 ± 0.31	1.99 ± 0.27	5.8 ± 2.9	4.5 ± 1.5	1.1 ± 0.2	2.1 ± 0.4	1.95 ± 0.49
50	G305.61+0.01*	0.55 ± 0.05	14.15 ± 0.27	1.76 ± 0.23	7.7 ± 3.8	3.9 ± 1.4	0.4 ± 0.1	1.1 ± 0.3	2.64 ± 0.75
51	G305.11+0.25	0.37 ± 0.03	17.31 ± 0.22	1.95 ± 0.24	6.5 ± 3.2	4.4 ± 1.5	0.8 ± 0.1	3.2 ± 0.5	4.11 ± 0.84
52	G305.08+0.16*	0.34 ± 0.03	17.84 ± 0.21	2.52 ± 0.32	6.8 ± 3.3	5.6 ± 1.9	1.6 ± 0.2	3.1 ± 0.6	1.99 ± 0.48
53	G305.74-0.04	0.43 ± 0.04	14.75 ± 0.25	1.51 ± 0.20	3.1 ± 1.5	3.4 ± 1.2	1.7 ± 0.2	5.2 ± 0.8	3.09 ± 0.65
54	G305.55-0.04*	0.44 ± 0.04	13.85 ± 0.30	2.32 ± 0.34	8.9 ± 4.5	5.2 ± 1.8	0.7 ± 0.1	1.6 ± 0.3	2.26 ± 0.59
55	G305.19+0.2	0.34 ± 0.03	17.20 ± 0.23	1.59 ± 0.21	3.8 ± 1.9	3.6 ± 1.2	1.3 ± 0.2	4.5 ± 0.7	3.56 ± 0.75
56	G305.15+0.21	0.34 ± 0.03	16.96 ± 0.23	2.14 ± 0.28	6.7 ± 3.3	4.8 ± 1.6	1.0 ± 0.1	1.5 ± 0.3	1.55 ± 0.38
57	G305.4+0.18*	0.36 ± 0.03	15.08 ± 0.27	2.22 ± 0.29	8.5 ± 4.2	5.0 ± 1.7	0.7 ± 0.1	1.9 ± 0.4	2.77 ± 0.67

TABLE C.2

Appendix D

Appendix D

D.1 Small-scale radio sources

Source Index	Source Name	Dimensions Observed maj (”)	min (”)	Observed flux density Peak (mJy beam^{-1}) $f_{5.5}$	$f_{8.8}$	Integrated (mJy) $f_{5.5}$	$f_{8.8}$	Spectral Index (α)
0	G305.375+00.112	unresolved		2.9 ± 0.3	2.2 ± 0.3	3.3	2.6	−0.2
1	G305.384+00.119	unresolved		1.2 ± 0.3	1.5 ± 0.3	1.5	1.9	0.7
2^{st}	G305.342+00.078	unresolved		0.9 ± 0.1	1.6 ± 0.2	1.0	1.9	1.7
3^{st}	G305.361+00.056	unresolved		1.8 ± 0.3	2.5 ± 0.3	2.4	2.9	0.6
4	G305.303+00.112	unresolved		7.4 ± 0.3	6.7 ± 0.2	9.3	7.9	−0.4
5	G305.439+00.083	unresolved		3.1 ± 0.3	4.4 ± 0.1	3.8	5.7	0.8
6	G305.430+00.113	unresolved		0.9 ± 0.1	1.0 ± 0.1	0.9	1.0	0.4
7	G305.541+00.134	unresolved		0.7 ± 0.3	0.6 ± 0.1	1.0	0.6	−1.4
8^{uc}	G305.362+00.150	2.40 ± 0.05	3.0 ± 0.05	24.0 ± 0.8	26.0 ± 0.9	29.0	34.0	–
9^{uc}	G305.368+00.213	4.20 ± 0.09	4.2 ± 0.08	28.0 ± 1.1	15.0 ± 1.0	62.0	54.0	–
10^{brc}	G305.244+00.224	3.60 ± 0.66	4.8 ± 0.36	1.7 ± 0.2	0.9 ± 0.1	5.5	1.7	–
11^{st}	G305.142+00.098	unresolved		3.5 ± 0.1	3.0 ± 0.1	4.2	3.4	−0.4
12	G305.193+00.359	unresolved		2.5 ± 0.3	1.3 ± 0.1	3.1	1.8	−0.6
13	G305.185+00.346	unresolved		1.2 ± 0.3	0.9 ± 0.1	1.6	1.1	−1.4
14	G305.204+00.465	3.60 ± 1.04	6.0 ± 0.23	3.1 ± 0.4	1.5 ± 0.2	8.8	2.5	–
15	G305.563+00.220	unresolved		2.0 ± 0.2	1.6 ± 0.2	2.3	1.8	−0.2
16	G305.512+00.235	unresolved		1.7 ± 0.1	1.5 ± 0.1	1.8	1.4	−0.2

TABLE D.1: Identifiers and observed properties of the 71 detected compact radio sources. For sources that fall below the detection limit at 8.8 GHz we present the upper limit $3 \times \sigma$ value where σ is the rms noise. Superscript above the source index indicates the nature of the source as derived in Section. 4.6, *st* corresponds to stellar, *uc* to UC HII candidate and *brc* to BRC sources with no superscript are background.The spectral index is derived from the 1 GHz split dataset and presented for unresolved sources only.

Source Index	Source Name	Dimensions Observed maj (")	min (")	Observed flux density Peak (mJy beam^{-1}) $f_{5.5}$	$f_{8.8}$	Integrated (mJy) $f_{5.5}$	$f_{8.8}$	Spectral Index
17^{uc}	G305.562+00.013	6.00 ± 1.51	5.4 ± 1.00	7.3 ± 0.8	3.4 ± 0.4	31.4	12.1	–
18	G305.537+00.014	unresolved		2.0 ± 0.1	1.7 ± 0.2	2.0	1.7	−0.1
19	G305.523−00.006	unresolved		4.2 ± 0.2	3.0 ± 0.2	5.3	4.7	−0.2
20^{uc}	G305.553−00.012	4.20 ± 0.18	3.6 ± 0.16	8.4 ± 0.7	5.3 ± 0.4	16.0	9.6	–
21	G304.787−00.009	4.20 ± 0.13	3.0 ± 0.10	3.0 ± 0.2	0.5$^{\uparrow}$	6.5	0.5$^{\uparrow}$	–
22	G304.782−00.026	unresolved		20.5 ± 0.5	21.1 ± 1.1	23.9	24.9	0.1
23	G304.776−00.023	unresolved		2.6 ± 0.3	3.3 ± 0.2	2.9	3.5	1.0
24	G304.895+00.128	unresolved		3.2 ± 0.1	2.8 ± 0.2	3.7	3.3	−0.3
25	G304.944+00.411	unresolved		3.4 ± 0.3	3.2 ± 0.3	3.8	3.5	−0.1
26^{uc}	G304.930+00.552	3.00 ± 0.53	4.2 ± 0.4	2.4 ± 0.3	1.3 ± 0.1	7.3	0.8	–
27	G305.706+00.501	unresolved		3.3 ± 0.2	0.5$^{\uparrow}$	4.4	0.5$^{\uparrow}$	−3.4
28	G305.679+00.019	unresolved		1.0 ± 0.1	0.8 ± 0.1	1.2	0.8	−0.8
29	G305.714−00.102	unresolved		4.8 ± 0.1	3.4 ± 0.3	6.1	4.2	−0.4
30	G305.698−00.135	4.20 ± 4.84	6.0 ± 0.36	9.7 ± 1.4	4.8 ± 0.1	30.0	14.0	–
31	G305.663−00.150	2.17 ± 0.10	1.46 ± 0.1	1.3 ± 0.1	0.8 ± 0.1	2.3	0.8	–
32	G305.729−00.176	unresolved		3.9 ± 0.2	2.7 ± 0.2	4.9	3.5	−0.6
33	G305.672−00.191	3.00 ± 0.26	4.8 ± 0.14	4.0 ± 0.3	2.0 ± 0.2	6.8	3.9	–
34	G305.672−00.223	unresolved		1.9 ± 0.1	0.9 ± 0.1	2.6	1.4	−1.8
35	G305.477+00.381	unresolved		0.9 ± 0.1	0.8 ± 0.1	1.0	0.8	−0.1
36	G305.494−00.110	unresolved		1.1 ± 0.1	0.5$^{\uparrow}$	1.9	0.5$^{\uparrow}$	−2.4
37^{uc}	G305.200+00.019	2.40 ± 0.16	2.4 ± 0.13	7.2 ± 0.5	7.0 ± 0.8	9.2	8.6	–
38	G305.405+00.504	unresolved		2.2 ± 0.1	1.8 ± 0.1	2.5	2.2	−0.1
39	G305.414+00.514	unresolved		1.3 ± 0.1	0.8 ± 0.1	1.4	0.8	−1.2
40	G305.752+00.410	unresolved		1.3 ± 0.1	0.8 ± 0.1	1.7	0.9	−1.3
41	G305.132+00.502	unresolved		1.6 ± 0.1	1.7 ± 0.1	1.8	2.0	0.2
42	G304.843+00.085	unresolved		1.9 ± 0.1	0.5$^{\uparrow}$	2.1	0.5$^{\uparrow}$	−0.2

TABLE D.1: continued.

Source Index	Source Name	Dimensions Observed		Observed flux density				Spectral Index
				Peak (mJy beam^{-1})		Integrated (mJy)		
		maj (”)	min (”)	$f_{5.5}$	$f_{8.8}$	$f_{5.5}$	$f_{8.8}$	(α)
43	G304.861+00.051	unresolved		2.4 ± 0.1	1.2 ± 0.1	3.1	1.8	−1.0
44	G305.389+00.235	unresolved		1.3 ± 0.1	0.9 ± 0.1	1.5	1.4	−0.1
45	G305.572+00.264	unresolved		0.8 ± 0.1	0.5 ± 0.2	0.8	0.7	−0.1
46	G305.694−00.322	unresolved		3.0 ± 0.1	1.5 ± 0.1	3.9	1.8	−1.0
47	G305.410−00.287	unresolved		0.8 ± 0.1	0.8 ± 0.1	0.7	0.8	−0.3
48	G305.198−00.271	unresolved		1.1 ± 0.1	0.9 ± 0.1	1.4	1.2	−0.1
49	G304.845−00.216	unresolved		2.1 ± 0.3	1.2 ± 0.3	2.6	1.4	−1.0
50	G304.819−00.152	unresolved		1.1 ± 0.2	1.3 ± 0.2	1.3	1.6	0.4
51	G304.803+00.222	unresolved		1.7 ± 0.1	2.0 ± 0.2	2.1	2.5	0.6
52	G305.669+00.428	unresolved		1.0 ± 0.3	$0.5^{\uparrow}$	1.5	$0.5^{\uparrow}$	−1.2
53	G305.714+00.353	unresolved		0.8 ± 0.1	$0.5^{\uparrow}$	0.9	$0.5^{\uparrow}$	−1.3
54	G305.200+00.448	unresolved		0.8 ± 0.3	$0.5^{\uparrow}$	1.1	$0.5^{\uparrow}$	−1.4
55	G304.851+00.502	unresolved		0.9 ± 0.2	$0.5^{\uparrow}$	0.7	$0.5^{\uparrow}$	−0.4
56^{st}	G305.302+00.052	unresolved		1.1 ± 0.2	1.2 ± 0.2	1.3	1.5	0.1
57	G304.818+00.235	unresolved		0.8 ± 0.1	0.9 ± 0.1	0.8	0.9	0.2
58	G305.291−00.094	unresolved		0.5 ± 0.1	$0.5^{\uparrow}$	0.6	$0.5^{\uparrow}$	−0.8
59^{st}	G305.335+00.074	unresolved		1.5 ± 0.1	1.5 ± 0.1	1.7	2.2	0.5
60^{st}	G305.522+00.063	unresolved		0.8 ± 0.1	$0.5^{\uparrow}$	1.0	$0.5^{\uparrow}$	−0.6
61	G305.499+00.050	unresolved		0.5 ± 0.1	$0.5^{\uparrow}$	0.6	$0.5^{\uparrow}$	−0.8
62	G305.385−00.147	unresolved		0.5 ± 0.2	$0.5^{\uparrow}$	0.7	$0.5^{\uparrow}$	−0.3
63^{st}	G305.091−00.095	unresolved		0.5 ± 0.1	$0.5^{\uparrow}$	0.5	$0.5^{\uparrow}$	0.1
64	G305.047−00.120	unresolved		0.5 ± 0.1	0.5 ± 0.1	0.6	0.7	−0.1
65	G305.558+00.459	unresolved		0.6 ± 0.1	$0.5^{\uparrow}$	0.7	$0.5^{\uparrow}$	−0.8
66	G305.076+00.396	unresolved		0.7 ± 0.1	0.6 ± 0.1	0.8	0.7	−0.8
67^{st}	G305.631+00.000	unresolved		0.9 ± 0.1	1.2 ± 0.2	1.1	1.5	0.7
68	G305.466+00.374	unresolved		0.6 ± 0.3	0.6 ± 0.1	1.1	1.1	−0.5
69	G305.284+00.365	unresolved		0.5 ± 0.1	$0.5^{\uparrow}$	0.6	$0.5^{\uparrow}$	−0.2
70	G305.596−00.211	unresolved		0.6 ± 0.2	$0.5^{\uparrow}$	0.8	$0.5^{\uparrow}$	−0.2

TABLE D.1

Bibliography

Aikawa Y., Ohashi N., Inutsuka S.-i., Herbst E., Takakuwa S., 2001, ApJ, 552, 639

Anderson L. D., Bania T. M., Balser D. S., Rood R. T., 2011, ApJS, 194, 32

Anglada G., Villuendas E., Estalella R., Beltrán M. T., Rodríguez L. F., Torrelles J. M., Curiel S., 1998, AJ, 116, 2953

Arce H. G., Borkin M. A., Goodman A. A., Pineda J. E., Halle M. W., 2010, ApJ, 715, 1170

Arce H. G., Shepherd D., Gueth F., Lee C.-F., Bachiller R., Rosen A., Beuther H., 2007, Protostars and Planets V, 245

Arzoumanian D. et al., 2011, A&A, 529, L6

Ascenso J., Alves J., Lago M. T. V. T., 2009, Apss, 324, 113

Bachiller R., 1996, ARAA, 34, 111

Bacmann A., Lefloch B., Ceccarelli C., Castets A., Steinacker J., Loinard L., 2002, A&A, 389, L6

Bastian N., Covey K. R., Meyer M. R., 2010, ARAA, 48, 339

Baume G., Carraro G., Momany Y., 2009, MNRAS, 398, 221

Benjamin R. A. et al., 2003, pasp, 115, 953

Bergin E. A., Maret S., van der Tak F. F. S., Alves J., Carmody S. M., Lada C. J., 2006, ApJ, 645, 369

Bergin E. A., Tafalla M., 2007, ARAA, 45, 339

Berry D. S., Reinhold K., Jenness T., Economou F., 2007, in Astronomical Society of the Pacific Conference Series, Vol. 376, Astronomical Data Analysis Software and Systems XVI, R. A. Shaw, F. Hill, & D. J. Bell, ed., pp. 425–+

Bertelli G., Bressan A., Chiosi C., Fagotto F., Nasi E., 1994, aaps, 106, 275

Beuther H., Leurini S., Schilke P., Wyrowski F., Menten K. M., Zhang Q., 2007, A&A, 466, 1065

Beuther H., Schilke P., Sridharan T. K., Menten K. M., Walmsley C. M., Wyrowski F., 2002, A&A, 383, 892

Bica E., Ortolani S., Momany Y., Dutra C. M., Barbuy B., 2004, MNRAS, 352, 226

Bisbas T. G., Wünsch R., Whitworth A. P., Hubber D. A., Walch S., 2011, ApJ, 736, 142

Blaauw A., 1964, ARAA, 2, 213

Blake G. A., Sutton E. C., Masson C. R., Phillips T. G., 1987, ApJ, 315, 621

Blitz L., 1991, in NATO ASIC Proc. 342: The Physics of Star Formation and Early Stellar Evolution, C. J. Lada & N. D. Kylafis, ed., p. 3

—, 1993, in Astronomical Society of the Pacific Conference Series, Vol. 376, Protostars and Planets III, E. H. Levy & J. I. Lunine, ed., pp. 125–161

Blitz L., Shu F. H., 1980, ApJ, 238, 148

Bloemhof E. E., Reid M. J., Moran J. M., 1992, ApJ, 397, 500

Bonnell I. A., Bate M. R., Clarke C. J., Pringle J. E., 1997, MNRAS, 285, 201

—, 2001, MNRAS, 323, 785

Bonnell I. A., Vine S. G., Bate M. R., 2004, MNRAS, 349, 735

Borkin M., Arce H., Goodman A., Halle M., 2008, in Astronomical Society of the Pacific Conference Series, Vol. 394, Astronomical Data Analysis Software and Systems XVII, R. W. Argyle, P. S. Bunclark, & J. R. Lewis, ed., p. 145

Brand J., Blitz L., 1993, A&A, 275, 67

Breen S. L. et al., 2007, mnras, 377, 491

Brooks K. J., Storey J. W. V., Whiteoak J. B., 2001, MNRAS, 327, 46

Calzetti D., Sheth K., Churchwell E., Jackson J., 2009, in The Evolving ISM in the Milky Way and Nearby Galaxies

Carpenter J. M., Snell R. L., Schloerb F. P., 1990, ApJ, 362, 147

Caswell J. L., 1998, MNRAS, 297, 215

—, 2009, PASA, 26, 454

Caswell J. L., Batchelor R. A., Forster J. R., Wellington K. J., 1989, Australian Journal of Physics, 42, 331

Caswell J. L., Haynes R. F., 1987, aap, 171, 261

Cesaroni R., Churchwell E., Hofner P., Walmsley C. M., Kurtz S., 1994, aap, 288, 903

Cesaroni R., Walmsley C. M., Churchwell E., 1992, A&A, 256, 618

Chomiuk L., Povich M. S., 2011, AJ, 142, 197

Chrysostomou A., Bacciotti F., Nisini B., Ray T. P., Eislöffel J., Davis C. J., Takami M., 2008, A&A, 482, 575

Churchwell E., 1975, in Lecture Notes in Physics, Berlin Springer Verlag, Vol. 42, H II regions and related topics, T. L. Wilson & D. Downes, ed., pp. 245–+

—, 2002, araa, 40, 27

Churchwell E. et al., 2009, pasp, 121, 213

Clark J. S., Porter J. M., 2004, aap, 427, 839

Cohen M. et al., 2007, mnras, 374, 979

Collings M. P., Dever J. W., Fraser H. J., McCoustra M. R. S., Williams D. A., 2003, ApJ, 583, 1058

Comeron F., Torra J., 1996, aap, 314, 776

Condon J. J., Griffith M. R., Wright A. E., 1993, AJ, 106, 1095

Conti P. S., Crowther P. A., 2004, MNRAS, 355, 899

Cornwell T. J., 1988, A&A, 202, 316

Crowther P. A., Conti P. S., 2003, MNRAS, 343, 143

Crowther P. A., Schnurr O., Hirschi R., Yusof N., Parker R. J., Goodwin S. P., Kassim H. A., 2010, MNRAS, 408, 731

Crutcher R. M., 1999, ApJ, 520, 706

—, 2005, in Astronomical Society of the Pacific Conference Series, Vol. 343, Astronomical Polarimetry: Current Status and Future Directions, A. Adamson, C. Aspin, C. Davis, & T. Fujiyoshi, ed., p. 111

Curtis E. I., Richer J. S., 2010, MNRAS, 402, 603

Curtis E. I., Richer J. S., Swift J. J., Williams J. P., 2010, MNRAS, 408, 1516

Cyganowski C. J. et al., 2008, AJ, 136, 2391

Dale J. E., Bonnell I., 2011, MNRAS, 414, 321

Dale J. E., Bonnell I. A., 2012, MNRAS, 422, 1352

Dale J. E., Bonnell I. A., Whitworth A. P., 2007, MNRAS, 375, 1291

Dame T. M., 2007, apjl, 665, L163

Danby G., Flower D. R., Valiron P., Schilke P., Walmsley C. M., 1988, mnras, 235, 229

Danks A. C., Dennefeld M., Wamsteker W., Shaver P. A., 1983, A&A, 118, 301

Danks A. C., Wamsteker W., Shaver P. A., Retallack D. S., 1984, A&A, 132, 301

Davies B. et al., 2012, MNRAS, 419, 1871

Davies B., Hoare M. G., Lumsden S. L., Hosokawa T., Oudmaijer R. D., Urquhart J. S., Mottram J. C., Stead J., 2011, MNRAS, 416, 972

de Pree C. G., Mehringer D. M., Goss W. M., 1997, apj, 482, 307

de Pree C. G., Rodriguez L. F., Goss W. M., 1995, Rev. Mex. Astron. Astrofis, 31, 39

de Wit W. J., Testi L., Palla F., Zinnecker H., 2005, A&A, 437, 247

Deharveng L. et al., 2010, A&A, 523, A6

Deharveng L., Zavagno A., Caplan J., 2005, A&A, 433, 565

Diaz-Miller R. I., Franco J., Shore S. N., 1998, ApJ, 501, 192

Dobbs C. L., Burkert A., Pringle J. E., 2011, MNRAS, 413, 2935

Dougherty S. M., Clark J. S., Negueruela I., Johnson T., Chapman J. M., 2010, A&A, 511, A58

Dougherty S. M., Pittard J. M., Kasian L., Coker R. F., Williams P. M., Lloyd H. M., 2003, A&A, 409, 217

Dutra C. M., Bica E., Soares J., Barbuy B., 2003, aap, 400, 533

Dyson J. E., Williams D. A., 1997, Physics of the interstellar medium. Institute of Physics Publishing Bristol and Philidelphia

Eden D. J., Moore T. J. T., Plume R., Morgan L. K., 2012, ArXiv e-prints

Elia D. et al., 2010, A&A, 518, L97

Elitzur M., 1992, ARAA, 30, 75

Ellingsen S. P., Voronkov M. A., Cragg D. M., Sobolev A. M., Breen S. L., Godfrey P. D., 2007, in IAU Symposium, Vol. 242, IAU Symposium, J. M. Chapman & W. A. Baan, ed., pp. 213–217

Elmegreen B. G., 1979, ApJ, 231, 372

—, 1998, in Astronomical Society of the Pacific Conference Series, Vol. 148, Origins, C. E. Woodward, J. M. Shull, & H. A. Thronson Jr., ed., p. 150

—, 2007, in IAU Symposium, Vol. 237, IAU Symposium, B. G. Elmegreen & J. Palous, ed., pp. 384–389

Elmegreen B. G., Lada C. J., 1977, apj, 214, 725

Evans N. J., Shirley Y. L., Mueller K. E., Knez C., 2002, in Astronomical Society of the Pacific Conference Series, Vol. 267, Hot Star Workshop III: The Earliest Phases of Massive Star Birth, P. Crowther, ed., p. 17

Evans, II N. J., 1999, ARAA, 37, 311

Evans, II N. J. et al., 2009, ApJS, 181, 321

Fazio G. G., Hora, 2004, ApJS, 154, 10

Felli M. et al., 2007, A&A, 476, 373

Foster J. B. et al., 2011, ApJS, 197, 25

Franco J., Kurtz S. E., Garcia-Segura G., Hofner P., 2000, Apss, 272, 169

Fukui Y., Iwata T., Mizuno A., Bally J., Lane A. P., 1993, in Protostars and Planets III, E. H. Levy & J. I. Lunine, ed., pp. 603–639

Gaensler B. M., Manchester R. N., Staveley-Smith L., Tzioumis A. K., Reynolds J. E., Kesteven M. J., 1997, ApJ, 479, 845

Gao Y., Solomon P. M., 2004, ApJ, 606, 271

Genzel R., Downes D., 1977, aaps, 30, 145

Georgelin Y. M., Boulesteix J., Georgelin Y. P., Le Coarer E., Marcelin M., 1988, aap, 205, 95

Goss W. M., Shaver P. A., 1970, Australian Journal of Physics Astrophysical Supplement, 14, 1

Gould R. J., Salpeter E. E., 1963, ApJ, 138, 393

Graves S. F. et al., 2010, MNRAS, 409, 1412

Green J. A. et al., 2009, mnras, 392, 783

—, 2012, MNRAS, 2351

Guan X., Wu Y., Ju B., 2008, MNRAS, 391, 869

Harju J., Lehtinen K., Booth R. S., Zinchenko I., 1998, aaps, 132, 211

Harju J., Walmsley C. M., Wouterloot J. G. A., 1993, aaps, 98, 51

Hartmann L., Ballesteros-Paredes J., Bergin E. A., 2001, ApJ, 562, 852

Hatchell J., Dunham M. M., 2009, A&A, 502, 139

Hatchell J., Fuller G. A., Richer J. S., 2007, A&A, 472, 187

Haworth T. J., Harries T. J., 2012, MNRAS, 420, 562

Heiderman A., Evans, II N. J., Allen L. E., Huard T., Heyer M., 2010, ApJ, 723, 1019

Herbig G. H., 1962, ApJ, 135, 736

Hill T. et al., 2011, A&A, 533, A94

Hindson L., Thompson M. A., Urquhart J. S., Clark J. S., Davies B., 2010, mnras, 408, 1438

Hindson L., Thompson M. A., Urquhart J. S., Faimali A., Clark J. S., Davies B., 2012, MNRAS, 421, 3418

Ho P. T. P., Townes C. H., 1983, araa, 21, 239

Hoare M. G. et al., 2005, in IAU Symposium, Vol. 227, Massive Star Birth: A Crossroads of Astrophysics, R. Cesaroni, M. Felli, E. Churchwell, & M. Walmsley, ed., pp. 370–375

Hopkins P. F., Quataert E., Murray N., 2011, MNRAS, 417, 950

Hosokawa T., Inutsuka S.-i., 2005, ApJ, 623, 917

Intema H. T., van der Tol S., Cotton W. D., Cohen A. S., van Bemmel I. M., Röttgering H. J. A., 2009, A&A, 501, 1185

Jackson J. M., Finn S. C., Chambers E. T., Rathborne J. M., Simon R., 2010, ApJL, 719, L185

Jackson J. M. et al., 2006, ApJS, 163, 145

Jones I. G., Watkinson A., Egau P. C., Percival T. M., Skellern D. J., Graves G. R., 1984, Proceedings of the Astronomical Society of Australia, 5, 574

Kennicutt, Jr. R. C., 1998, ARAA, 36, 189

Kennicutt, Jr. R. C., Evans, II N. J., 2012, ArXiv e-prints

Kennicutt, Jr. R. C., Tamblyn P., Congdon C. E., 1994, ApJ, 435, 22

Kenny H. T., Taylor A. R., 2007, ApJ, 662, 1231

Kroupa P., 2001, MNRAS, 322, 231

Krumholz M. R., 2011, in American Institute of Physics Conference Series, Vol. 1386, American Institute of Physics Conference Series, E. Telles, R. Dupke, & D. Lazzaro, ed., pp. 9–57

Krumholz M. R., Klein R. I., McKee C. F., Offner S. S. R., Cunningham A. J., 2009, Science, 323, 754

Krumholz M. R., Matzner C. D., McKee C. F., 2006, ApJ, 653, 361

Krumholz M. R., McKee C. F., 2008, Nature, 451, 1082

Krumholz M. R., McKee C. F., Tumlinson J., 2009, ApJ, 693, 216

Krumholz M. R., Tan J. C., 2007, ApJ, 654, 304

Kuiper R., Klahr H., Beuther H., Henning T., 2010, ApJ, 722, 1556

Kurtz S., 2002, in Astronomical Society of the Pacific Conference Series, Vol. 267, Hot Star Workshop III: The Earliest Phases of Massive Star Birth, P. Crowther, ed., pp. 81–+

—, 2005, in IAU Symposium, Vol. 227, Massive Star Birth: A Crossroads of Astrophysics, R. Cesaroni, M. Felli, E. Churchwell, & M. Walmsley, ed., pp. 111–119

Kurtz S., Churchwell E., Wood D. O. S., 1994, ApJS, 91, 659

Kurtz S., Hofner P., 2005, AJ, 130, 711

Kurtz S. E., Watson A. M., Hofner P., Otte B., 1999, apj, 514, 232

Kwan J., 1979, ApJ, 229, 567

Lacy J. H., Knacke R., Geballe T. R., Tokunaga A. T., 1994, ApJL, 428, L69

Lada C. J., 1985, ARAA, 23, 267

Lada C. J., Forbrich J., Lombardi M., Alves J. F., 2012, ApJ, 745, 190

Lada C. J., Kylafis N. D., eds., 1999, The Origin of Stars and Planetary Systems. NATO ASIC

Lada C. J., Lada E. A., 2003, ARAA, 41, 57

Lada C. J., Lombardi M., Alves J. F., 2010, ApJ, 724, 687

Ladd N., Purcell C., Wong T., Robertson S., 2005, PASA, 22, 62

Langer W. D., Penzias A. A., 1990, ApJ, 357, 477

Larson R. B., 1981, MNRAS, 194, 809

Lazaridis K., Jessner A., Kramer M., Stappers B. W., Lyne A. G., Jordan C. A., Serylak M., Zensus J. A., 2008, MNRAS, 390, 839

Lefloch B., Lazareff B., 1994, A&A, 289, 559

Leger A., Puget J. L., 1984, aap, 137, L5

Leisawitz D., 1989, in Bulletin of the American Astronomical Society, Vol. 21, Bulletin of the American Astronomical Society, p. 1189

Leistra A., Cotera A. S., Liebert J., Burton M., 2005, AJ, 130, 1719

Longmore S. N., Burton M. G., Barnes P. J., Wong T., Purcell C. R., Ott J., 2007a, MNRAS, 379, 535

Longmore S. N., Burton M. G., Keto E., Kurtz S., Walsh A. J., 2009, mnras, 399, 861

Longmore S. N., Maercker M., Ramstedt S., Burton M. G., 2007b, mnras, 380, 1497

Lumsden S. L., Hoare M. G., Oudmaijer R. D., Richards D., 2002, MNRAS, 336, 621

Luna A., Mayya Y. D., Carrasco L., Rodríguez-Merino L. H., Bronfman L., 2009, in Revista Mexicana de Astronomia y Astrofisica Conference Series, Vol. 37, Revista Mexicana de Astronomia y Astrofisica Conference Series, pp. 32–37

Lundstrom I., Stenholm B., 1984, aaps, 58, 163

Mac Low M.-M., Klessen R. S., 2004, Reviews of Modern Physics, 76, 125

Martins F., Hillier D. J., Paumard T., Eisenhauer F., Ott T., Genzel R., 2008, A&A, 478, 219

Martins F., Schaerer D., Hillier D. J., 2005, A&A, 436, 1049

Massey P., 2003, in IAU Symposium, Vol. 212, A Massive Star Odyssey: From Main Sequence to Supernova, K. van der Hucht, A. Herrero, & C. Esteban, ed., p. 316

Mauerhan J. C., Van Dyk S. D., Morris P. W., 2011, AJ, 142, 40

McKee C. F., Offner S. S. R., 2010, ApJ, 716, 167

McKee C. F., Tan J. C., 2003, ApJ, 585, 850

Menten K., 1991, in Astronomical Society of the Pacific Conference Series, Vol. 16, Atoms, Ions and Molecules: New Results in Spectral Line Astrophysics, A. D. Haschick & P. T. P. Ho, ed., pp. 119–+

Miao J., White G. J., Thompson M. A., Nelson R. P., 2009, ApJ, 692, 382

Milam S. N., Savage C., Brewster M. A., Ziurys L. M., Wyckoff S., 2005, ApJ, 634, 1126

Moffat A. F. J., 1983, aap, 124, 273

Moffat A. F. J. et al., 1998, A&A, 331, 949

Molinari S. et al., 2010a, in 38th COSPAR Scientific Assembly, Vol. 38, pp. 2488–+

Molinari S., Brand J., Cesaroni R., Palla F., 1996, aap, 308, 573

Molinari S. et al., 2010b, pasp, 122, 314

Moore T. J. T., Bretherton D. E., Fujiyoshi T., Ridge N. A., Allsopp J., Hoare M. G., Lumsden S. L., Richer J. S., 2007, MNRAS, 379, 663

Mücke A., Koribalski B. S., Moffat A. F. J., Corcoran M. F., Stevens I. R., 2002, ApJ, 571, 366

Murray N., Rahman M., 2010, ApJ, 709, 424

Myers P. C., Benson P. J., 1983, ApJ, 266, 309

Nguyen Luong Q. et al., 2011, A&A, 529, A41

Nürnberger D. E. A., Bronfman L., Yorke H. W., Zinnecker H., 2002, aap, 394, 253

Oey M. S., Lamb J. B., 2011, ArXiv e-prints

Offner S. S. R., McKee C. F., 2011, ApJ, 736, 53

Ossenkopf V., Klessen R. S., Heitsch F., 2001, A&A, 379, 1005

Padoan P., Kritsuk A., Norman M. L., Nordlund Å., 2005, ApJL, 622, L61

Panagia N., 1973, AJ, 78, 929

Panagia N., Walmsley C. M., 1978, aap, 70, 411

Parsons H., Thompson M. A., Chrysostomou A., 2012, MNRAS submitted

Pascale E. et al., 2008, ApJ, 681, 400

Pilbratt G. L. et al., 2010, A&A, 518, L1

Pillai T., Kauffmann J., Wyrowski F., Hatchell J., Gibb A. G., Thompson M. A., 2011, A&A, 530, A118

Pineda J. E., Rosolowsky E. W., Goodman A. A., 2009, ApJL, 699, L134

Polychroni D., Moore T. J. T., Allsopp J., 2012, ArXiv e-prints

Povich M. S. et al., 2009, apj, 696, 1278

—, 2011, apjs, 194, 14

Preibisch T. et al., 2011, ApJS, 194, 10

Price S. D., Egan M. P., Carey S. J., Mizuno D. R., Kuchar T. A., 2001, AJ, 121, 2819

Pringle J. E., Allen R. J., Lubow S. H., 2001, MNRAS, 327, 663

Purcell C. R., 2006, PhD thesis, The University of New South Wales

Purcell C. R., Hoare M. G., Diamond P., 2008, in Astronomical Society of the Pacific Conference Series, Vol. 387, Massive Star Formation: Observations Confront Theory, H. Beuther, H. Linz, & T. Henning, ed., pp. 389–+

Purcell C. R. et al., 2009, A&A, 504, 139

Rathborne J. M., Johnson A. M., Jackson J. M., Shah R. Y., Simon R., 2009, ApJS, 182, 131

Retallack D. S., 1979, New Zealand Journal of Science, 22, 545

Rich J. W., de Blok W. J. G., Cornwell T. J., Brinks E., Walter F., Bagetakos I., Kennicutt, Jr. R. C., 2008, AJ, 136, 2897

Robitaille T. P., Whitney B. A., 2010, Astrophysical Journal, 710, L11

Rohlfs K., Wilson T. L., 2004, Tools of radio astronomy. Springer

Roman-Duval J., Jackson J. M., Heyer M., Rathborne J., Simon R., 2010, ApJ, 723, 492

Rownd B. K., Young J. S., 1999, AJ, 118, 670

Roy A. et al., 2011, ApJ, 727, 114

Russeil D., Georgelin Y. M., Amram P., Gach J. L., Georgelin Y. P., Marcelin M., 1998, aaps, 130, 119

Salpeter E. E., 1955, Astrophysical Journal, 121, 161

Sault R. J., Teuben P. J., Wright M. C. H., 1995, in Astronomical Society of the Pacific Conference Series, Vol. 77, Astronomical Data Analysis Software and Systems IV, Shaw R. A., Payne H. E., Hayes J. J. E., eds., p. 433

Sault R. J., Wieringa M. H., 1994, aaps, 108, 585

Scannapieco C. et al., 2011, ArXiv e-prints

Schneider N., Brooks K., 2004, PASA, 21, 290

Shaver P. A., Goss W. M., 1970, Australian Journal of Physics Astrophysical Supplement, 14, 133

Shepherd D. S., Churchwell E., 1996a, ApJ, 472, 225

—, 1996b, ApJ, 457, 267

Shu F. H., Adams F. C., Lizano S., 1987, ARAA, 25, 23

Smith L. F., Biermann P., Mezger P. G., 1978, aap, 66, 65

Smith N., Brooks K. J., 2008, The Carina Nebula: A Laboratory for Feedback and Triggered Star Formation, Astronomical Society of the Pacific, pp. 138–+

Smith N., Whitney B. A., Conti P. S., de Pree C. G., Jackson J. M., 2009, mnras, 399, 952

Smith R. J., Clark P. C., Bonnell I. A., 2008, MNRAS, 391, 1091

Soria R., Pakull M. W., Broderick J. W., Corbel S., Motch C., 2010, MNRAS, 409, 541

Spitzer, Jr. L., Savedoff M. P., 1950, ApJ, 111, 593

Stahler, S. W. & Palla, F., ed., 2005, The Formation of Stars. Wiley-VCH

Strömgren B., 1939, ApJ, 89, 526

Sugitani K., Fukui Y., Ogura K., 1991, apjs, 77, 59

Swift J. J., Welch W. J., Di Francesco J., 2005, ApJ, 620, 823

Tachihara K., Onishi T., Mizuno A., Fukui Y., 2002, A&A, 385, 909

Taylor G. B., Carilli C. L., Perley R. A., eds., 1999, Synthesis Imaging in Radio Astronomy II, Vol. 180. Astronomical Society of the Pacific

Thompson M. A., Urquhart J. S., Moore T. J. T., Morgan L. K., 2012, MNRAS, 421, 408

Thompson M. A., Urquhart J. S., White G. J., 2004, aap, 415, 627

Tieftrunk A. R., Megeath S. T., Wilson T. L., Rayner J. T., 1998, aap, 336, 991

Townes C. H., Schawlow A. L., 1955, Microwave Spectroscopy. Dover Books on Physics and Chemistry

Ungerechts H., Winnewisser G., Walmsley C. M., 1986, A&A, 157, 207

Urquhart J. S., Busfield A. L., Hoare M. G., Lumsden S. L., Clarke A. J., Moore T. J. T., Mottram J. C., Oudmaijer R. D., 2007a, A&A, 461, 11

Urquhart J. S. et al., 2007b, A&A, 474, 891

—, 2009, ArXiv e-prints

Urquhart J. S., Hoare M. G., Lumsden S. L., Oudmaijer R. D., Moore T. J. T., 2008, in Astronomical Society of the Pacific Conference Series, Vol. 387, Massive Star Formation: Observations Confront Theory, H. Beuther, H. Linz, & T. Henning, ed., pp. 381–+

Urquhart J. S. et al., 2010, PASA, 27, 321

—, 2011, MNRAS, 418, 1689

van der Walt J., 2005, MNRAS, 360, 153

van Dishoeck E. F., Blake G. A., 1998, ARAA, 36, 317

Vázquez R. A., Baume G., 2001, A&A, 371, 908

Vázquez-Semadeni E., 2010, in Astronomical Society of the Pacific Conference Series, Vol. 438, Astronomical Society of the Pacific Conference Series, R. Kothes, T. L. Landecker, & A. G. Willis, ed., p. 83

Vázquez-Semadeni E., Gazol A., Scalo J., 2000, ApJ, 540, 271

Vázquez-Semadeni E., Gómez G. C., Jappsen A. K., Ballesteros-Paredes J., González R. F., Klessen R. S., 2007, ApJ, 657, 870

Vázquez-Semadeni E., Ryu D., Passot T., González R. F., Gazol A., 2006, ApJ, 643, 245

Viti S., Collings M. P., Dever J. W., McCoustra M. R. S., Williams D. A., 2004, MNRAS, 354, 1141

Walborn N. R., Blades J. C., 1997, ApJS, 112, 457

Walborn N. R., Maíz-Apellániz J., Barbá R. H., 2002, AJ, 124, 1601

Walmsley C. M., Ungerechts H., 1983, aap, 122, 164

Walsh A. J. et al., 2011, MNRAS, 416, 1764

Walsh A. J., Burton M. G., 2006, mnras, 365, 321

Walsh A. J., Burton M. G., Hyland A. R., Robinson G., 1998, mnras, 301, 640

Walsh A. J., Chapman J. F., Burton M. G., Wardle M., Millar T. J., 2007, MNRAS, 380, 1703

Walsh A. J., Lo N., Burton M. G., White G. L., Purcell C. R., Longmore S. N., Phillips C. J., Brooks K. J., 2008, Publications of the Astronomical Society of Australia, 25, 105

Wang J., Townsley L. K., Feigelson E. D., Broos P. S., Getman K. V., Román-Zúñiga C. G., Lada E., 2008, apj, 675, 464

Whiting M. T., 2012, MNRAS, 421, 3242

Whitworth A., 1979, MNRAS, 186, 59

Whitworth A. P., Bhattal A. S., Chapman S. J., Disney M. J., Turner J. A., 1994, MNRAS, 268, 291

Williams J. P., Blitz L., McKee C. F., 2000, Protostars and Planets IV, 97

Williams J. P., de Geus E. J., Blitz L., 1994, apj, 428, 693

Williams J. P., McKee C. F., 1997, ApJ, 476, 166

Wilson T. L., Gaume R. A., Johnston K. J., 1993, apj, 402, 230

Wilson W. E. et al., 2011, ArXiv e-prints

Wolfire M. G., Cassinelli J. P., 1987, ApJ, 319, 850

Wood D. O. S., Churchwell E., 1989a, apj, 340, 265

—, 1989b, apjs, 69, 831

Wu Y., Zhang Q., Yu W., Miller M., Mao R., Sun K., Wang Y., 2006, aap, 450, 607

Xie T., Mundy L. G., Vogel S. N., Hofner P., 1996, ApJL, 473, L131

Yorke H. W., Sonnhalter C., 2002, ApJ, 569, 846

Zavagno A., Deharveng L., Comerón F., Brand J., Massi F., Caplan J., Russeil D., 2006, A&A, 446, 171

Zavagno A., Pomarès M., Deharveng L., Hosokawa T., Russeil D., Caplan J., 2007, A&A, 472, 835

Zhang Q., Hunter T. R., Brand J., Sridharan T. K., Molinari S., Kramer M. A., Cesaroni R., 2001, ApJL, 552, L167

Zinnecker H., Yorke H. W., 2007, ARAA, 45, 481